Star Formation and Quenching in Galaxies: Groups, Clusters, and Mergers

by

Andrew Matthew McGregor Reeves

A thesis
presented to the University of Waterloo
in fulfillment of the
thesis requirement for the degree of
Doctor of Philosophy
in
Physics

Waterloo, Ontario, Canada, 2023

Examining Committee Membership

The following served on the Examining Committee for this thesis. The decision of the Examining Committee is by majority vote.

External Examiner:	Allison Man Assistant Professor, Dept. of Physics and Astronomy University of British Columbia
Supervisor:	Michael Hudson Professor, Dept. of Physics and Astronomy University of Waterloo
Internal Members:	James Taylor Associate Professor, Dept. of Physics and Astronomy University of Waterloo
	Niayesh Afshordi Professor, Dept. of Physics and Astronomy University of Waterloo
Internal-External Member:	Achim Kempf Professor, Dept. of Applied Mathematics University of Waterloo

Author's Declaration

This thesis consists of material all of which I authored or co-authored: see Statement of Contributions included in the thesis. This is a true copy of the thesis, including any required final revisions, as accepted by my examiners.

I understand that my thesis may be made electronically available to the public.

Statement of Contributions

I am the sole author of Chapters 1 and 5, which were written under the supervision of Michael Hudson. The other three chapters of this manuscript were written for publication and are listed below. In particular, Chapters 2 and 3 represent largely unchanged versions of papers published in the Monthly Notices of the Royal Astronomical Society (MNRAS).

Chapter 2: **Reeves A. M. M.**, Balogh M. L., van der Burg R. F. J., Finoguenov A., Kukstas E., McCarthy I. G., Webb K., et al., 2021. The GOGREEN survey: Dependence of galaxy properties on halo mass at $z > 1$ and implications for environmental quenching. *Monthly Notices of the Royal Astronomical Society*, 509, pp.3364-3384. doi:10.1093/mnras/stab1955.

The main co-author of the paper resulting in Chapter 2 was my supervisor for the project, Michael Balogh, who provided ideas and much guidance. I performed the majority of the writing and analysis. Data, many group and one-on-one discussions, and edit contributions came from the GOGREEN (Galaxies in Rich Early ENvironments) collaboration (see Chapter 2 for full author list), with notable reduced data contributions by Remco van der Burg and Kristi Webb. Significant work went into synthesizing the varied, sometimes divergent, feedback and suggestions, and some of the spectroscopic target selection and data collection was performed by me during three observing runs, two at Gemini North and one at Gemini South. This and related GOGREEN data work additionally led to the following publications for which I am a co-author (in order of publication date): Chan et al. (2019), Old et al. (2020), van der Burg et al. (2020), Webb et al. (2020), Balogh et al. (2021), Chan et al. (2021), McNab et al. (2021), Baxter et al. (2022), Kukstas et al. (2023), Baxter et al. (submitted), and Pintos-Castro et al. (in prep).

Chapter 3: **Reeves A. M. M.**, Hudson M. J., Oman K. A., 2023. Constraining quenching timescales in galaxy clusters by forward-modelling stellar ages and quiescent fractions in projected phase space. *Monthly Notices of the Royal Astronomical Society*, Volume 522, Issue 2, pp.1779-1799. doi:10.1093/mnras/stad1069.

Chapter 4: **Reeves A. M. M.**, Hudson M. J. How many stars form in major mergers? Submitted, *Monthly Notices of the Royal Astronomical Society*.

The work described in Chapter 3 is co-authored by my supervisor Michael Hudson, as well as Kyle Oman, who provided a convenient orbit library and helpful feedback. The to-be-published work in Chapter 4 is co-authored with Michael Hudson. I've performed the majority of the writing and analysis of these two projects, with Michael Hudson supervising and providing ideas, guidance, and feedback for both of these projects.

Abstract

This thesis studies the impact of galaxy environment on star formation and 'quenching', by using simple physically-motivated models that can be fit using available observed quantities. Quenching refers to the close to total suppression, whether gradual or abrupt, of star formation in a galaxy, and remains a challenging process to understand due to the many tangled non-linear physical processes involved in galaxy formation. By examining the effects of specific environments on star formation, we are effectively given naturally controlled experiments. In particular, this work addresses gaps in our understanding of quenching during and prior to ('pre-processing') infall into galaxy groups and clusters, as well as the poorly studied star formation burst that occurs when one galaxy merges with another.

The first section of this thesis presents observed properties of galaxies of the GOGREEN $1 < z < 1.5$ galaxy groups. Using publicly available COSMOS and SXDF, with supporting GOGREEN spectroscopic data for confirming group properties, I use background subtraction to determine stellar mass functions of groups at $z > 1$ for the first time. I see enhanced quenching in higher mass galaxies in these groups compared to galaxies in the average field population. Using this result and previously published work measuring the quiescent fraction of galaxies for GOGREEN $1 < z < 1.5$ clusters, as well as similar measurements at lower redshifts, I find a halo mass dependence of quiescent fraction excess when controlled for stellar mass, with logarithmic slope, $\mathrm{d(QFE)/dlog}(M_{\mathrm{halo}}) \sim 0.24 \pm 0.04$ at all redshifts. I find this trend is qualitatively reproduced in the BAHAMAS hydrodynamical simulation at $z \sim 1$, but not the increasing quenched fraction with stellar mass trend. I then interpret my observational results using two toy accretion-quenching models. From this analysis, time until quenching in a group/cluster appears to be shorter for larger halos, with a particularly intense dependence required if there is no pre-processing. Our results strongly support a scenario where environmental quenching begins in low-mass $< 10^{14} M_{\odot}$ at $z > 1$.

The second section turns to infall quenching and preprocessing in $z \sim 0$ galaxy clusters using SDSS data. Numerous works have looked at low redshift clusters using quiescent fractions and star formation rates, but struggle to break degeneracies in infall quenching timescales or come to agreement. To address this, I build on a string of works by Kyle Oman and Michael Hudson, which employ statistical infall time in projected phase space information from N-body simulations, by adding an additional observable: spectroscopically derived mass-weighted stellar ages (MWAs). I then forward model the MWAs and quiescent fractions in projected phase space using star-formation histories from the stochastic UniverseMachine model, finding overall infall quenching times of ~ 4 Gyr after first pericentre. The use of MWAs enables breaking degeneracy in a two-parameter

model, yielding both time of quenching onset and SFR suppression timescale for our stellar mass bins $9 < \log(M_\star/\mathrm{M}_\odot) < 10$ and $10 < \log(M_\star/\mathrm{M}_\odot) < 10.5$. The results of this modeling suggest quenching begins close to, or just after first pericentre, but the suppression timescale is relatively long (~ 2.3 Gyr versus $\tau \lesssim 1$ Gyr) for the higher stellar mass bin, indicating ram-pressure stripping is not complete on first pericentric passage. Prior works required short suppression timescales to maintain the SFR bimodality, but we show that the use of stochastic star formation histories removes the need for this constraint.

The third section determines the mass of stars created when two galaxies merge, a long-standing unknown due to not having large and pure samples of post-merger galaxies until this past year (2022). In particular, I forward model the difference in stellar age between post-coalescence mergers and a control sample, controlling for stellar mass, environmental density, and redshift. We find an age difference of up to 3 Gyr, best fit by a stellar mass burst fraction of 0.18 ± 0.02, consistent with some previously published measurements, but much higher than found in hydrodynamical simulations. Our model is robust to choice of analytic star formation history as well as differences in burst duration. Using published SFRs of Luminous InfraRed Galaxies (LIRGs), we estimate a burst duration of 120–250 Myr, which is consistent with simulations and longer than is estimated for post-starbursts in the literature. We find our stellar mass burst fraction is consistent with the amount of molecular gas reported for very close pairs (pre-coalescence) in the literature. Additionally, we find that the difference between published cold gas measurements for pre- and post-coalescence is consistent with our estimated stellar mass burst fraction, lending credence to our approach.

Acknowledgements

I would like to thank my supervisor, Michael Hudson, for taking me on as a graduate student part-way through my PhD and helping me get back on track. You've been a great pleasure to work with and your encouragement, thoughtful methodology, and expertise have really helped me grow as a researcher.

I would like to thank Michael Balogh and the GOGREEN collaboration as a whole, who I worked with for my first research project. I learned much from our many conversations and it was an incredible experience and opportunity to be able to collect data at the Gemini telescopes with Kristi Webb and Remco van der Burg. Special thanks to Michael Balogh for the opportunity to work with the GOGREEN collaboration. Thank you also James Taylor, Niayesh Afshordi, and Achim Kempf, for serving on my PhD committee, as well as for your feedback and advice.

Thank you to all the other grad students I studied alongside of, I'm sorry for not mentioning everyone by name here. Extra fun and a broader community very much helped with sanity, especially our weekly virtual hangouts during the isolating depths of the COVID-19 pandemic.

And I can't forget, thank you to the OrganizeUW union drive and all the organizers for your amazing work towards organizing a grad student and sessional lecturer labour union. You are an inspiration and proof that a better, more just, and caring world is possible.

Thank you to my family in Atlantic Canada, particularly my parents Jon and Bethany Reeves, for your support of my interests, despite them being different than yours and some uncertainty as to what it meant to study science/astrophysics. I also would like to thank my in-laws, the Klassens, for their encouragement and support through the latter half of this degree and especially for your help during the pandemic. It made a world of difference.

Thank you to the members of the Athena Community Astronomy Club for giving me a place to explore my teenage fascination with space and science generally and for being great friends. And thank you also to my childhood friends in PEI for putting up with my special interest/nerdiness. It's been amazing to be able to stay in touch and to see what an awesome bunch of guys you've become. Thank you also to my friends here in Ontario as well for your encouragement.

And, finally and most importantly, a special thank you to my wife, Karen. It's been a wild few years, getting married during a global pandemic and now completing this PhD! I honestly couldn't have done this without your love, support, and many prayers. And since they seem to fit here best, I'd also like to thank our two sweet black cats Kya and Luna for

their unconditional love and emotional support, with special thanks to Kya for snuggles while working and helping to keep working from home interesting.

This work was financially supported by the Ontario graduate scholarship program and a one-year QEII Graduate Scholarship in Science and Technology. The work was primarily conducted at the University of Waterloo, which sits on the traditional lands of the so-called 'Neutral', Haudenosaunee, and Anishinaabeg peoples, and originally primarily the Mississaugas, who inhabited the upper Grand River prior to displacement due to European settlement. I acknowledge this land was later granted to the Six Nations as part of the Haldimand Tract which spans six miles on each side of the Grand River, and should legally be considered, according to Crown agreements which are recognized by the Canadian state, their rightful territory to use and govern. The large variety of telescopes from which the data this thesis is based upon are all over the world, including sacred native Hawaiian land, and are an incredible technological feat made possible by countless workers, communities, and international collaborations who make and support these telescopes and service their staff.

Dedication

I dedicate my thesis to the members and friends of the Athena Community Astronomy Club in Summerside, Prince Edward Island, without which my passion for astronomy and science would have been a very lonely pursuit during my teenage years. I am eternally grateful for their kindness, generosity, and the time we have spent sharing the joy of exploring the night sky together. May you all have lots of clear skies and I hope we will find opportunity to share many of them together in the years to come.

Table of Contents

List of Figures

List of Tables

Chapter 1

Introduction

Looking out into our vast Universe, we see faint islands of starlight amidst a dark expanse. In the past century we've gone from the discovery of galaxies as separate systems from our Milky Way (by e.g. Hubble, 1925, 1926, 1929), to an understanding of the buildup of primarily dark matter structure through the Lambda Cold Dark Matter (ΛCDM) model. It is amidst such large-scale structure that galaxies form and evolve, including the Milky Way (Mo et al., 2010).

Through the back-and-forth dialectic between increasingly deep systematic observations of galaxies with modelling/simulation work, astronomers have developed an impressive general understanding of galaxy formation. Despite this, correctly and simultaneously modelling various aspects of galaxy formation in detail across both different environments and across cosmic time remains a considerable challenge (Naab & Ostriker, 2017).

Many open questions remain. In particular, understanding the buildup of stellar mass in the Universe requires a clear picture of the mechanisms behind the 'quenching' (suppression or shutdown) of star formation. To address this problem, in this thesis I focus on premature quenching of galaxies due to environmental factors – primarily group and cluster environment – and the impact of mergers. In this introduction, I will discuss star formation and quenching in galaxies, with particular focus on what we know about environmental quenching mechanisms, as well as star formation enhancement and quenching during galaxy mergers.

1.1 Growth of structure in the Universe

The standard Lambda Cold Dark Matter (ΛCDM) model is now well established as a descriptive and accurate model for the large-scale evolution and buildup of structure in the Universe. The model is a parametrization of a Friedmann–Lemaître–Robertson–Walker spacetime in General Relativity, which expands rapidly from a hot dense state (the Big Bang) into the massive expanse we see 13.8 Gyr later as the observable Universe. The present-day Universe is dominated by a negative energy density component referred to as 'dark energy' (69% of our Universe's total mass-energy density), Λ, and a cold (slow velocities relative to the speed of light) 'dark matter' component (26%), with regular baryonic matter forming only a small ($\sim 5\%$) fraction of the matter-energy density of the Universe (Planck Collaboration et al., 2020). Dark energy is only detectable by its effect on the expansion rate of the Universe – namely that this expansion is accelerating. Dark matter on the other hand, gravitationally behaves like regular matter, except to the best of current knowledge, it does not interact with regular matter or itself through the other known forces of nature – electromagnetism, the weak nuclear force, and the strong nuclear force.

In the context of galaxy formation, ΛCDM describes how gravitationally-bound dark matter halos build up hierarchically through a combination of smooth accretion of surrounding matter, as well as merging with other halos (White & Rees, 1978; van den Bosch, 2002). This has been thoroughly studied using N-body simulations of galaxy scale dark matter halos up to large cosmological volumes (Navarro et al., 1997; Springel, 2005). Inside these dark matter halos, baryonic physics, such as radiative cooling and feedback from stars and accreting supermassive black holes (e.g. White & Frenk, 1991; Finlator & Davé, 2008; Bouché et al., 2010; Schaye et al., 2010; Davé et al., 2012; Bower et al., 2017; Qu et al., 2017) drive the formation and evolution of galaxies within this gravitationally-dominant component.

Within the largest virialized structures in the Universe, galaxy clusters, galaxy evolution is heavily influenced by whether galaxies are centrals or satellites (i.e. subhalos) of another larger dark matter halo. Most galaxies in the present-day Universe are found in small-medium-sized groups of galaxies, with a much smaller proportion ($\sim 10\%$, see McGee et al., 2009) in clusters which can have upwards of 1000 galaxies. Galaxies and groups of galaxies tend to follow large-scale structures called filaments, with galaxy clusters forming at the nodes of these filaments; the filamentary environment and history of galaxies within it may additionally impact a galaxy's evolution. For galaxies in clusters, their prior history as subhalos and within filaments can significantly impact their stellar mass and gas properties. Understanding this history and its impact on galaxy formation is essential to understanding

the baryon cycle in clusters, as $\gtrsim 30\%$ of galaxies are accreted as groups (McGee et al., 2009; De Lucia et al., 2012).

1.2 Gas physics and star formation in galaxies

In this section, gas physics, star formation, and their connections will be introduced. For readers unfamiliar with the subject area, a common and useful simplification is to view a galaxy as being a reservoir of stars, cold gas, and hot gas, with transitions between these. Inflows/outflows into/out of the galaxy's halo are also allowed. For an illustration of an example gas regulation model (Lilly et al., 2013), see Fig. 1.1.

1.2.1 Hot gas of the circumgalactic medium

Key to galaxy formation is the ability of hot halo gas to cool into molecular gas clouds, from which stars can form. In massive cluster-sized halos, their formation through accretion leads to shock heating of intracluster gas (Gunn & Gott, 1972). Such heating leads to kinetic temperatures of $T_{\rm vir} \gtrsim 10^7$K, leaving the gas fully ionized, primarily able to cool via the emission of x-ray photons emitted during collisions of electrons and atomic nuclei – bremsstrahlung radiation. In halos with lower virial temperatures, $10^4{\rm K} < T_{\rm vir} < 10^6{\rm K}$, electrons and ions can recombine, emitting photons, or neutral atoms can be collisionally excited before settling back to their ground state. The efficiency of this cooling process (and the exact distribution of wavelengths of radiation emitted) depends strongly on the metallicity/molecules present. For halos with gas cooler than $T_{\rm vir} \sim 10^4$, gas is generally neutral, significantly suppressing cooling; cooling can then only occur through collisions causing excitation/de-excitation of fine/hyperfine structure lines or rotational and vibrational lines for metals and molecules, respectively (Mo et al., 2010).

Since the primary cooling processes in halos are due to two-body particle interactions, as described above, cooling is most effective in higher density regions. For a uniform spherical cloud of an ideal gas in virial equilibrium in a $10^{11}{\rm M}_\odot$ galaxy forming at $z = 3$, will have a cooling time $t_{\rm cool} \sim 7 \times 10^8$yr (Mo et al., 2010). If nothing were to stop or slow this cooling process, we would end up with an 'overcooling' problem where there would be far less hot halo gas remaining in halos than what we observe (especially true for massive halos) and ΛCDM would predict a much higher stellar mass content than we see in the present-day Universe (White & Rees, 1978).

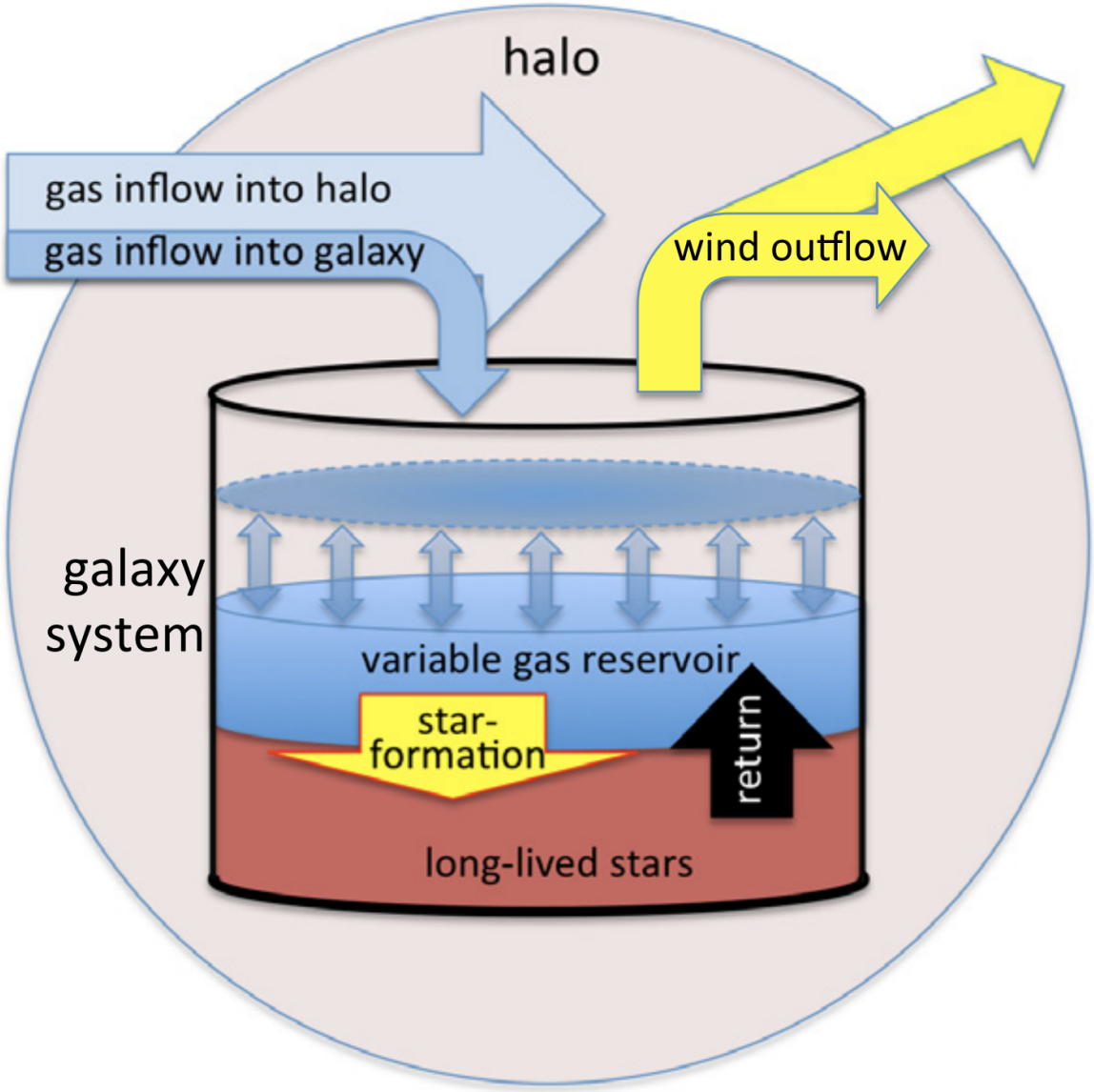

Figure 1.1: Illustration of a gas regulation model, adapted from fig. 2 in Lilly et al. (2013). Such models have frequently been used for decades to understand and produce toy models of galaxy evolution. Not depicted in this illustration is the cooling of hot halo gas onto the galaxy.

Halo mergers can shock heat halo gas, delaying further cooling, but the timescales between major mergers is too long and their prevalence too low to explain why the gaseous halo fails to cool into the centre of the halo. A strong UV background at high redshifts may also suppress gas cooling in halos with $T_{\rm vir} \lesssim 10^5$K in forming low-mass ($R_{\rm vir} \sim 3 \times 10^8 {\rm M}_\odot$ at $z \sim 15$) galaxies (e.g. Navarro et al., 1997). Throughout much of cosmic history though, it is generally agreed that some mixture of energetic feedback from internal processes are preventing the gas from cooling too fast in dark matter halos, primarily supernovae winds and active galactic nuclei (Naab & Ostriker, 2017). Active galactic nuclei in brightest cluster galaxies (BCGs) are especially important for providing the energy to maintain group and cluster circumgalactic medium (CGM) temperatures (McNamara & Nulsen, 2007; McCarthy et al., 2010), which prevents star formation in BCGs and maintains a CGM that is important in the quenching of satellite and newly infalling galaxies (Naab & Ostriker, 2017).

1.2.2 Cold interstellar medium: the fuel for star formation

Gas that has cooled from a galaxy's surrounding CGM, into its core or disk, forms the cold interstellar medium (ISM). This repository of cold gas is the reservoir that directly fuels star formation. In a typical star-forming late-type galaxy, the cold ISM can be well over 50 per cent of the total baryonic (gas + stars) mass below stellar masses of $10^{10}{\rm M}_\odot$ and decreases with stellar mass, down to ~ 10 per cent at stellar masses of $10^{10}{\rm M}_\odot$ (Saintonge & Catinella, 2022). Of this, ~ 75 per cent is atomic (primarily HI) gas by mass, with the rest in molecular form (primarily H_2) and dust (only ~ 1 per cent of the gas mass). Early-type galaxies, the vast majority of which are not star forming, are effectively depleted of their cold ISM (which is < 3 per cent of their total baryonic mass). Although of crucial importance to our understanding of galaxy evolution, an empirically-motivated model is still lacking for how exactly gas is exchanged between the ISM and surrounding CGM (Saintonge & Catinella, 2022).

As the gas in the ISM cools, it can collapse into giant molecular clouds, which form stars when they collapse under their own self-gravity. For this reason, there is a well-known correlation between a galaxy's molecular gas mass density and star formation rate (SFR) known as the Kennicutt-Schmidt scaling relation (Kennicutt, 1998; Bigiel et al., 2008). There is a well known increasing trend for star forming galaxies of SFR with stellar mass, called the star forming main sequence. Unsurprisingly, the star formation rates and position of galaxies on the star forming main sequence is strongly correlated with cold gas content. It appears that the shape of the main sequence is primarily set by the dependence of H_2 gas mass on galaxy mass. Star forming galaxies just above the main

sequence have higher molecular gas fractions, while those below the main sequence have lower fractions. The scatter is explainable by one of the following competing ideas: (a) galaxies have smooth SFHs from their gas inflows and outflows in equilibrium (Lilly et al., 2013) but have a spread in formation times of ~ 1.4 Gyr (e.g. Speagle et al., 2014), or (b) galaxies have highly variable star formation rates due to stochastic accretion of baryonic matter temporarily triggering star-formation (Tacchella et al., 2016). Notably, there is no evidence for a significant population of gas-rich quiescent galaxies – the vast majority are gas-poor (Cappellari et al., 2011; Saintonge et al., 2017).

The cold gas depletion time for a galaxy, defined as the ratio between gas mass and SFR, is frequently used to characterize the typical timescale over which star formation would continue, assuming no recycling or fresh inflows of cold gas. It is ~ 4 Gyr for an average star-forming spiral galaxy (Saintonge et al., 2017), decreasing with increasing redshift (Tacconi et al., 2013; Saintonge et al., 2013). These comparatively short timescales compared to the age of the Universe are used as supportive evidence for replenishing mechanisms, primarily steady accretion of gas onto galaxies, without which essentially no galaxies would continue to be star-forming today. Calculating and examining quantities of cold gas, star formation, and such timescales in different environments can yield insights into the physical mechanisms affecting star formation.

1.2.3 Star formation properties of galaxies

Since we can only see a momentary snapshot of a galaxy, we rely on various indirect tracers of star formation rate. Such indirect tracers are sensitive to the recent star formation over a given timescale (Kennicutt, 1998). Observables such as the Hα line emission, for example, trace the gas ionized by star formation over the timescale for which a molecular cloud lasts before dispersing (on the order of ~ 10 Myr). Others, which use UV slope or photometric colour to trace the composition of stellar populations, which redden as younger stars die out over tens of Myr (UV slope) up to multiple Gyr (overall photometric colour). Some, like the depth of the D4000 ratio, the ratio in flux between either side of the Balmer break, is a good proxy for stellar population age and therefore can trace the past star formation histories of galaxies (Balogh et al., 1999, 2021). More elaborate methods for fitting the star formation histories of galaxies by fitting synthetic stellar populations are also often utilized to infer information about the past star formation of galaxies (e.g. Leja et al., 2017b). Refinement of these various methods continues, as understanding of the impact of various properties continues to steadily improve (e.g. dust and metallicity), or as underlying assumptions are tested, such as of the Initial Mass Function (what fraction of stars of a given mass form, which may evolve with redshift, see e.g. Conroy et al., 2009a)).

An important feature of galaxy evolution is the global evolution of star formation through cosmic time. It is well established that the star formation rate density had its peak, or 'cosmic noon', at $z \sim 1-2$, and has declined since by a factor of ~ 10 (Madau & Dickinson, 2014). With decreasing redshift, the relative contribution to the global star formation rate density shifts towards lower stellar mass galaxies (Damen et al., 2009), a specific example of 'downsizing' (for a noteable early work finding this, see Cowie et al., 1996). The accumulated stellar mass formed in the global population of galaxies results in the build up of the global stellar mass function with time, with galaxies piling up close to an approximate maximum stellar mass of $\sim 10^{12}\mathrm{M}_{\odot}$, with lower stellar mass galaxies forming a $\sim$ power law distribution (Schechter, 1976).

Just as importantly, as hinted at earlier when discussing the inability of hot halo gas to cool, star formation is rather inefficient, with at most ~ 25 per cent of baryonic mass in halos converted to stars. This efficiency peaks at or just under 10^{12} $\mathrm{M}_{\odot}$ and declines as a power-law slope with decreasing or increasing stellar mass away from this (Moster et al., 2013). Resolved observations of galaxies also indicate low star forming efficiencies down to molecular gas scales (Kennicutt & Evans, 2012), as seen in detailed maps of stellar mass and molecular gas density (e.g. Leroy et al., 2008). Common explanations for this inefficiency in star formation within the galactic disc is often ascribed to stellar winds (Springel & Hernquist, 2003) and turbulence (Mac Low & Klessen, 2004).

One of the most important features in the study of galaxy evolution is the distribution of galaxies in the SFR–stellar mass (SFR-M_*) plane. At a fixed stellar mass, the SFR of galaxies is bimodal, with two distinct clumps: bluer star-forming galaxies and redder quiescent galaxies. In stellar mass there is a general increasing trend in SFR, for the blue cloud this is referred to as the star-forming main sequence. The star-forming main sequence has been observed up to $z \sim 6$, with the mean SFR steadily shifting higher towards higher redshifts by a factor of $\sim (1+z)^2$, with a scatter of ~ 0.2–0.3 dex (Lilly et al., 2013; Speagle et al., 2014; Whitaker et al., 2014; Tomczak et al., 2016). The source of this bimodality, its persistence across cosmic time and across different environments, and what causes galaxies to transition from star forming to quiescent in these various contexts, remains a long-standing major open area of galaxy research, which this thesis aims to address.

1.3 Quenching of star formation

Quenching can take place through a variety of mechanisms, often divided into intrinsic (internal) or external ('environmental') mechanisms (Baldry et al., 2006; Peng et al., 2010).

There is of course, interplay/overlap between the two classes of mechanisms, but they are generally studied separately for simplicity. This separation can be strongly motivated by the seminal work of Peng et al. (2010), who show using an empirical model that the differential effects of stellar mass (i.e. internal) quenching and environmental quenching are separable up to $z \sim 1$, although competing interpretations have been discussed (De Lucia et al., 2012; Pintos-Castro et al., 2019). This picture may also break down at high redshift, when galaxy formation may have been heavily dominated by the high rate of major mergers (Rodriguez-Gomez et al., 2015a).

Similarly, galaxies can be classified into either central or satellite galaxies (van den Bosch et al., 2008; Peng et al., 2012). Satellite galaxies are those for which their dark matter halo is a subhalo in a larger dark matter halo, whereas central galaxies are at the centre of their local gravitational potential well. This distinction is important since gas in a halo cools onto the central and not onto satellites. Satellites on the other hand can be affected by both internal and external mechanisms.

It has been shown through extensive study that the fraction of quiescent galaxies is observed to increase strongly with galaxy stellar mass (e.g. Kauffmann et al., 2003; Baldry et al., 2006), increase with environmental density (e.g. Peng et al., 2010) – especially for the densest environments of groups and clusters (see e.g. Gómez et al., 2003; McGee et al., 2011; van der Burg et al., 2020, for example work showing this from $z \sim 0$ to $z > 1$), and decline with redshift (Muzzin et al., 2013b). Although the large body of observational work examining the environmental dependence of quenching across a range of redshifts does provide discriminating tests of models (e.g. Weinmann et al., 2010; McGee et al., 2014; Hirschmann et al., 2016), linking intuitive theoretical models of the underlying physical mechanisms in a consistent (and unique) way to the observed trends remains a challenge.

I now summarize the dominant mechanisms, which will be referred to throughout the studies of quenching covered in this thesis.

1.3.1 Internal quenching mechanisms

Galaxies have not converted all their baryonic matter in their halos into stars – much of their baryons remain in the hot gas halo. The expectation for this gas in massive galaxies, groups, and clusters, to rapidly cool early in the Universe's history has for many years been referred to as the 'overcooling' problem (Benson, 2010). The primary physical mechanisms to stop this process in isolated galaxies are forms of internal feedback: either the winds of young and exploding stars (Keller et al., 2014) for low-mass galaxies or outflows from feeding supermassive black holes at the centres of more massive galaxies, referred to as

active galactic nuclei (AGN) (Harrison, 2017). This can then lead to heating and/or ejection of the cold gas, suppressing or completely quenching star formation.

AGN in particular have emerged as a highly important mechanism for the regulation of halo temperatures, preventing rapid cooling and considered a likely solution to the overcooling problem (Benson, 2010). AGN feedback appears to be an important factor in the suppression of star formation rate only for galaxies with stellar masses greater than $\sim 2 \times 10^{10} M_{\odot}$ (Werner et al., 2019) and especially important for the most massive galaxies/halos, as mentioned earlier for BCGs and galaxy clusters. This feedback provides the needed heating such that the hot halo gas of massive central galaxies isn't able to cool throughout much of the history of the Universe (McNamara & Nulsen, 2012). This process appears effective for halos, even up to the size of the most massive galaxy clusters.

Finally, even if additional gas is able to cool, there is a mechanism that can prevent this cold gas from fragmenting and forming stars in early type galaxies: 'morphological quenching'. Such quenching, at least in simulations (Martig et al., 2009), occurs when a galaxy transitions from a stellar disc to a spheroid and the cold disc gas is stabilized via turbulence in the gas. A common source of the this turbulence and the overall morphological transformation is thought to be due to mergers (Martig et al., 2009). This quenching process appears to be relevant to quenching of disc galaxies as well – with observational studies indicating large dense bulges are a necessary but not always sufficient condition for quenching (e.g. Fang et al., 2013).

1.3.2 Environmental quenching mechanisms

Overview of mechanisms

A number of environmental mechanisms can come into play as galaxies interact with each other or become satellites within a larger halo. These processes are generally labeled with rather violent names, such as 'starvation' or 'strangulation', where shutoff of accretion of additional cold gas causes a galaxy to quench (see Fig. 1.2 for a simplified illustration of this common quenching scenario contrasted with some kind of gas stripping scenario). I now lay out some key environmental mechanisms affecting the hot and cold gas, leading to quenching.

Galaxies passing near each other can experience 'harassment' – changes in internal structure due to gravitational affects. This may trigger collapse of cold gas in the galaxy, enhancing star formation or AGN and potentially leading to early quenching. Interacting galaxies can also gravitationally strip material off of each other during close passes, as

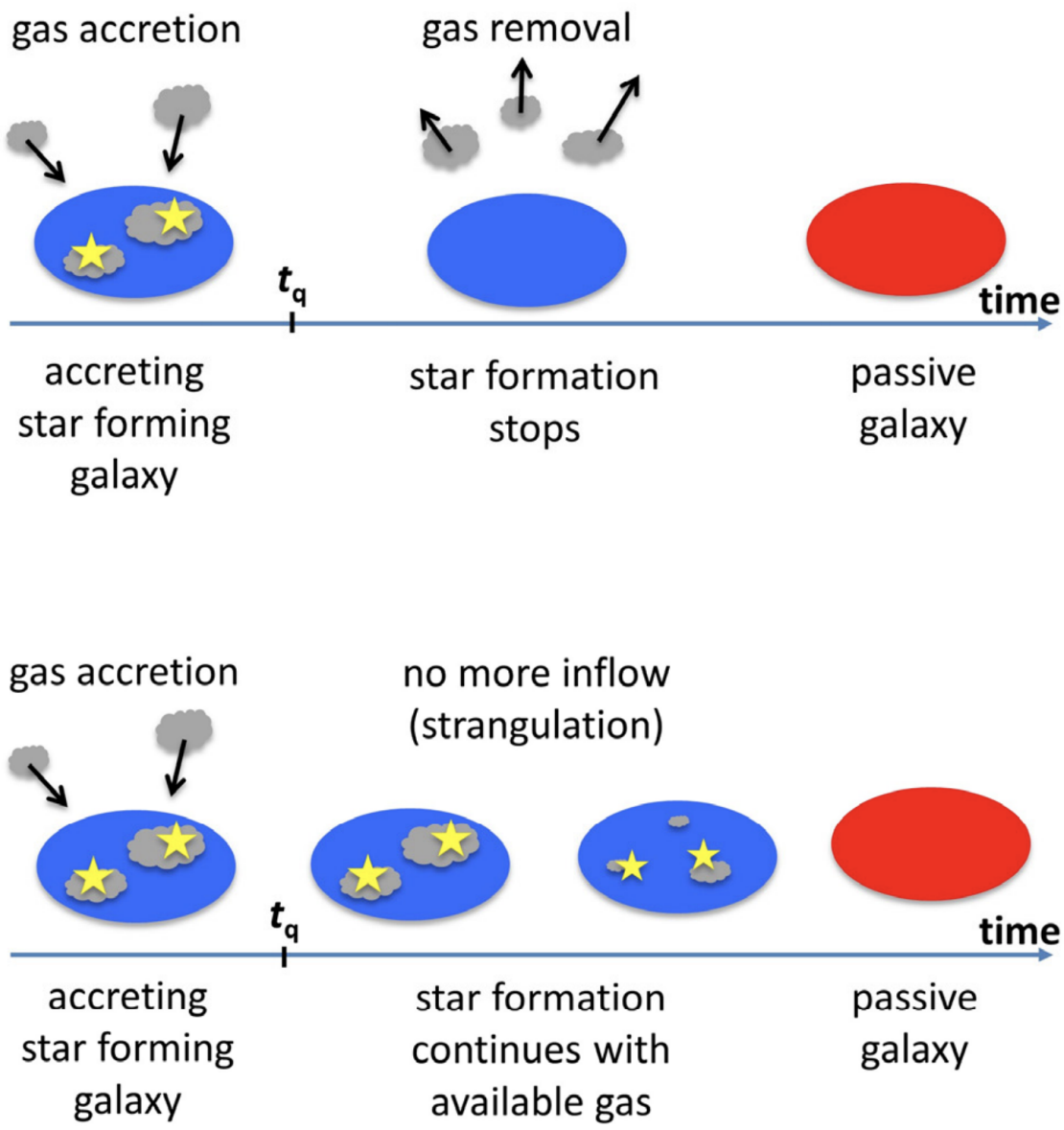

Figure 1.2: Illustration of two contrasting quenching mechanisms, adapted from fig. 1 of Peng et al. (2015). A galaxy accreting new gas and steadily forming stars prior to time of onset of a quenching mechanism, t_q In the top example, gas is suddenly stripped, stopping star formation and resulting in rapid quenching. In the bottom illustration a strangulation scenario is depicted, where inflow of new gas is cut off, followed by steady depletion of the available gas until star formation has used up or expelled all available gas.

seen in tidal tails and bridges (Toomre & Toomre, 1972). If cold gas is tidally stripped in this way, it can lead to starvation. Finally, interacting pairs of galaxies may merge, which is a particularly violent event for a galaxy, believed to potentially trigger starbursts and quenching shortly thereafter (see introductory Sec. 1.4 for further detail). This is sometimes referred to as 'cannibalism' when a central galaxy accretes a smaller, less massive galaxy. Mergers are most common in dense environments, particularly within galaxy groups, and to a lesser extent galaxy clusters, which have much higher velocity dispersions and therefore experience few satellite-satellite mergers (Lin et al., 2010).

Galaxies that become satellites of a larger halo, either in a significantly more massive galaxy halo or within a group/cluster of galaxies, can experience a number of additional mechanisms impacting their star formation.

When a galaxy falls into a larger halo, such a galaxy is no longer the deepest gravitational potential in their immediate environment, which can lead to a starvation/strangulation scenario after several gigayears (first proposed by Larson et al., 1980). This occurs due to both the cut off of cosmological inflows of additional gas and stoppage of the galaxy's hot gas halo from being able to cool, e.g. by its removal (Kereš et al., 2005; Dekel & Birnboim, 2006a). The starvation timescale is generally assumed to simply be the (linear) gas depletion time, defined as how long it will take to deplete the cold gas mass at time of infall, given the current rate of star formation. At $z \sim 0$, this timescale is approximately ~ 4 Gyr for a $\log(M_\star/\mathrm{M}_\odot) \sim 10.3$ stellar mass galaxy. Although cold gas fractions are known to increase with redshift, star formation rates are much higher at high redshift, leading to depletion times (Popping et al., 2015a) that steadily decrease with redshift. This timescale is often assumed to simply decrease with the dynamical timescale.

Ram pressure stripping is one of the most commonly cited quenching mechanisms for quenching in clusters, first studied analytically in the context of galaxy infall into clusters by Gunn & Gott (1972). If it is stronger than the restoring gravitational force by the galaxy on the cold gas in the intragalactic medium, this cold gas can be stripped. Cold gas stripping could explain the long-observed fact that cold gas is significantly depleted in cluster galaxies (Haynes et al., 1984), with as many as two thirds HI deficient near the cluster core where most galaxies are no longer on their first or second infall (Chung et al., 2009; Serra et al., 2012). Galaxies with cold gas being stripped can be observed in UV and visual wavelengths – such galaxies are termed 'jelly-fish' galaxies, after how they appear with streams of stripped gas left behind them (Smith et al., 2010; Ebeling et al., 2014). The ram pressure force experienced by an infalling galaxy is proportional to the density of the intracluster medium and the velocity squared. This effect is well illustrated by the fact that Roberts et al. (2021) observed almost all jellyfish galaxies in projected phase space occurring close to cluster centre ($r < 0.5R_{200c}$) and at high velocities ($v \gtrsim 2\sigma_v$, where

e.g. $\sigma_v \sim 1000$ km/s is a typical galaxy cluster velocity dispersion). Consistent with this, jellyfish are rare in groups but comparatively common in galaxy clusters (making up as many as 20 per cent of galaxies currently in $z \sim 0$ clusters Roberts et al., 2021), making it clear that ram pressure as a cause of quenching is likely much more important in clusters. As well, from this discussion it's clear that the location of quenching onset due to ram pressure stripping will depend on location, with simulation works such as Zinger et al. (2018) finding that stripping of a galaxy's hot halo gas as far out as 2–3$R_{\rm vir}$ and cold gas stripping only occurring at $r < 0.5R_{\rm vir}$.

In the observational literature on infall quenching, starvation and ram pressure stripping are often discussed as if they are opposite extremes, with starvation being the longer timescale and ram pressure stripping of cold gas being $<$ 1 Gyr (see e.g. Cortese et al., 2021, for explanation of this timescale). Unfortunately this simple picture appears to only be true for significant stripping of *both* cold disc gas and complete removal of hot halo gas available for cooling. Although the hot halos of galaxies cannot be directly observed, hydrodynamical simulations and semi-analytic models have been developed to explore the impacts on the hot and cold gas components. Ram pressure stripping more often is likely partial, especially by first pericentre (Cortese et al., 2021). Cold gas is not always stripped (depending on orbital parameters and cluster mass) and the hot halo is generally not fully stripped. Specifically, e.g. McCarthy et al. (2008a) found $\sim$ 30 percent of hot halo gas can remain after as long as 10 Gyr (see also Bahé & McCarthy, 2015). It is unclear how much gas removal would be needed to prevent further gas cooling onto the galaxy's disc. Additionally, in a process called 'overconsumption', stellar winds in star forming galaxies can push gas out of the disc, particularly in lower mass galaxies, which can then be stripped away rather than cool back onto the disc, shortening quenching times (McGee et al., 2014). Determining the role of ram pressure stripping on both hot and cold gas clearly at the very least requires a careful analysis that is able to constrain both the duration of quenching, but also the location of quenching onset.

The importance of these various mechanisms across environment, redshift, and galaxy mass, remain a challenge to model consistently. Determining the relative importance of each in these different contexts remains a very active area of investigation.

Observations of quenching in groups and clusters

Groups and clusters of galaxies are particularly interesting environments to study galaxy evolution as they act as a giant 'calorimeters', in principle containing an observable record of all galaxy formation energy inputs and outputs over the history of the Universe (e.g. Gonzalez et al., 2007; Balogh et al., 2017). This makes them a valuable 'laboratory' for

probing galaxy astrophysics, particularly in relation to gas physics and the quenching of star formation.

Galaxies in clusters are almost all quiescent at $z \sim 0$, with a decreasing quiescent fraction at higher redshifts, (an effect first noted for redder galaxy colours in Butcher & Oemler, 1978, 1984). The quiescent fraction in groups has for some time been believed to lie between those of clusters and the general 'field' population of galaxies (Kimm et al., 2009). It appears that denser environments accelerate quenching for galaxies. E.g. Kodama & Bower (2001) show that the average decline in star formation rate is greater in clusters than the field evolution with cosmic time, but it is important to note that this is driven by the enhanced quiescent fraction, since the star forming bimodality is preserved between cluster and field at a given redshift, from $z \sim 0$ to $z > 1$ (Wetzel et al., 2013; Old et al., 2020). The strong correlation between galaxy morphology and quenching – with quiescent galaxies generally being early-type (elliptical) galaxies – also holds for galaxy groups and especially clusters. Morphology-density relations have long been noted (Dressler, 1980) and have since been confirmed up to $z \sim 1$ (e.g. Smith et al., 2005). The statistical connection between morphology and quenching suggests a common underlying mechanism, but a satisfying picture that quantifies the effect from a given process or combination of processes remains elusive.

Part of the uncertainty around quenching in galaxy clusters is quantifying quenching at higher redshifts (e.g. $z > 1$) in different environments, especially for less massive (fainter) galaxies, $\log(M_\star/\mathrm{M}_\odot) \lesssim 10.5$ still being debated at the onset of the research carried out in this thesis. Some studies found a strong deficit of faint red/quiescent galaxies in $z > 1$ clusters (De Lucia et al., 2007; Stott et al., 2007; Gilbank et al., 2008), while others found little-to-no evolution of the faint-end of red/quiescent galaxies since $z \sim 1.3$ (Andreon, 2008; Crawford et al., 2009). Such studies struggled to make the most of observations of limited surveys of galaxies in clusters at $z \geq 1$, which had insufficient survey depth and small samples. This strongly motivated the deep multi-band GOGREEN group and cluster galaxy survey (Balogh et al., 2017, 2021), of which my first paper in this thesis is based upon (see Chapter 2. I will touch upon the findings of the GOGREEN survey further in the Conclusions chapter (Chapter 5), including how my Chapter 2 findings contribute to a new picture of quenching in groups and clusters at $z > 1$.

Complicating our ability to disentangle various quenching mechanisms in groups and clusters is that galaxies may experience partial or full quenching prior to entering such an environment. Such a scenario where a galaxy is in a denser environment prior to entering a larger group/cluster is often referred to as 'pre-processing'. Determining the extent and timing of quenching in groups and clusters and separating it from pre-processing, in a consistent way across the history of the Universe, has been a persistent challenge

to our understanding of quenching (Wetzel et al., 2013), primarily due to observational limitations of groups and clusters and their surrounding environments at higher redshifts (needed to break degeneracies in modeling), as well difficulty distinguishing between prior secular evolution of central galaxies and their time spent as satellites. Work by McGee et al. (2009) found $\geq$ 30 per cent of galaxies in present-day clusters ($M_{\rm halo} \geq 10^{14}{\rm M}_{\odot}$) were in $M_{\rm halo} \geq 10^{13}{\rm M}_{\odot}$ halos prior to accretion, with the fraction increasing to $\sim$ 50 per cent for the most massive ($M_{\rm halo} \geq 10^{14}{\rm M}_{\odot}$) clusters (with similar findings by De Lucia et al., 2012). Whether a galaxy will start infall-induced quenching as soon as it becomes a satellite for the first time or whether it starts upon infall into a sufficiently massive halo remains unclear. The role of some form of pre-processing is indeed important at $z \sim 0$, but at higher redshifts has been less clear. My work presented in Chapter 2 explores this via modelling for groups and clusters at $z > 1$ and my work in Chapter 3 touches on this problem at $z \sim 0$ (see also Conclusions in Chapter 5).

Even for galaxy clusters, where quenching is clearly very enhanced and now well characterized, a persistent debate over the location and timescale of infall quenching remains. The seminal work of Wetzel et al. (2013), for example, models the timescale from when a galaxy crosses the virial radius of a larger halo and becomes a satellite for the first time, which may be much earlier than when a galaxy becomes a satellite of the final cluster halo. From fitting quiescent fractions in $z \sim 0$ groups and galaxies, they find quenching times of 2–4 Gyr, primarily depending on the stellar mass of a galaxy (much shorter timescales for higher stellar mass galaxies), followed by a rapid < 1 Gyr star formation rate decline. Such a rapid decline in star formation rate may at least in part come from ram-pressure stripping of galaxies, which is most extreme near cluster centre (Jaffé et al., 2018; Vulcani et al., 2018; Roberts et al., 2021). Other works, which model using a surrounding infall population as a proxy for pre-processed infalling galaxies, such as the series of works by Oman and collaborators (Oman & Hudson, 2016; Oman et al., 2021), find gentler quenching ($\sim 5.5-6$ Gyr since first virial crossing) infall quenching and no dependence on stellar mass. Overall, works at $z \sim 0$ find a wide range of overall quenching timescales, 2–7 Gyr, indicating strong model dependence (e.g. De Lucia et al., 2012; Moster et al., 2018; Rhee et al., 2020). Careful constraints of delayed-then-rapid model quenching timescales is also often problematic due to degeneracies in the model parameters and general reliance in the literature on a single observable (quiescent fraction). My work in Chapter 3 addresses this problem for $z \sim 0$ clusters.

1.4 Star formation enhancement and quenching due to galaxy mergers

Since merging in the ΛCDM cosmological framework is an essential part of galaxy formation, studying mergers is of critical importance for understanding the build-up of stellar mass in galaxies, including the processes governing star formation and quenching of galaxies. Although far more common early in the Universe's history (Conselice et al., 2003; Hopkins et al., 2010), they still play an important role in the long term evolution of galaxies in the present-day Universe, especially in groups (Lin et al., 2010). As well, although widely studied both observationally and theoretically, particularly for close galaxy pairs, probing the after-effects of merging on galaxy evolution remains difficult, as it has only recently become possible to identify large samples of post-mergers that are both complete (over a survey region) and highly pure (at $z \sim 0$ in e.g. Bickley et al., 2021, 2022). Because of this limitation, much exploration remains to understand how mergers impact star formation and quenching.

The standard picture of the merger sequence is as follows. A pair of galaxies destined to merge will pass by or through each other $\sim 2-3$ times during an inspiral phase over timescales of up to several Gyr (Kitzbichler & White, 2008; Jiang et al., 2014) before coalescing into a single galaxy with a single nucleus shortly after (McElroy et al., 2022). The timeline for this process shown for a representative pair of galaxies in Fig. 1.3. Close passes (causing gravitational tides and torques) and final merger can cause radical morphological transformations, particularly in the case of major mergers (Darg et al., 2010). N-body simulations (e.g. Toomre & Toomre, 1972) and hydrodynamical simulations (e.g. Hopkins et al., 2013; Garrison-Kimmel et al., 2018) largely agree with observations as to what morphologies are produced by mergers, for both ongoing merging and coalesced post-merger remnants. Galaxies' stellar and gas kinematics are significantly disrupted, resulting in features such as tidal bridges between the two galaxies as they pass close to each other, and a long and curving tidal tail of escaping material on the far side (e.g. Toomre & Toomre, 1972). As a pair of galaxies finally coalesce, their stellar matter undergoes a gravitational process called violent relaxation, where the galaxy's kinematics rapidly become virialized (supported by random internal orbits/motions instead of rotationally supported). In the ~ 1 Gyr from the start of coalescence, tidal streams and shells of stellar material are frequently visible, with shells in massive ellipticals visible in imaging for up to ~ 2 Gyr (Pop et al., 2018). A realistic illustration of the timeline of this morphological transformation for pairs of merging simulated galaxies across stages of the merging process is shown in Fig. 1.4, for both a major merger and minor merger (figure adapted from fig. 2 of Nevin et al., 2023).

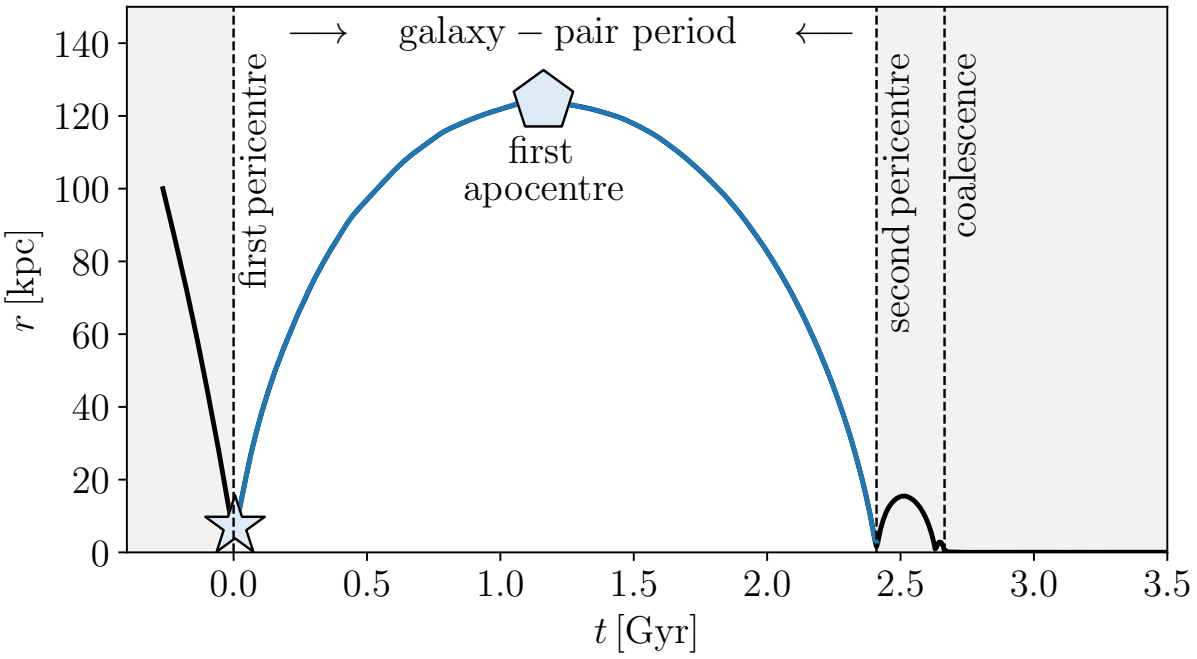

Figure 1.3: Representative plot of the radial separation of a pair of simulated merging galaxies with respect to time, fig. 2 of Moreno et al. (2019), who use the GIZMO/'Feedback in Realistic Environments'(FIRE)-2 simulation codes. Exact duration of the first few orbital passes between two merger galaxies depends on initial relative velocity (fairly high in this plot), as well as the relative mass of the two galaxies. Coalescence shortly after second pericentre is fairly typical.

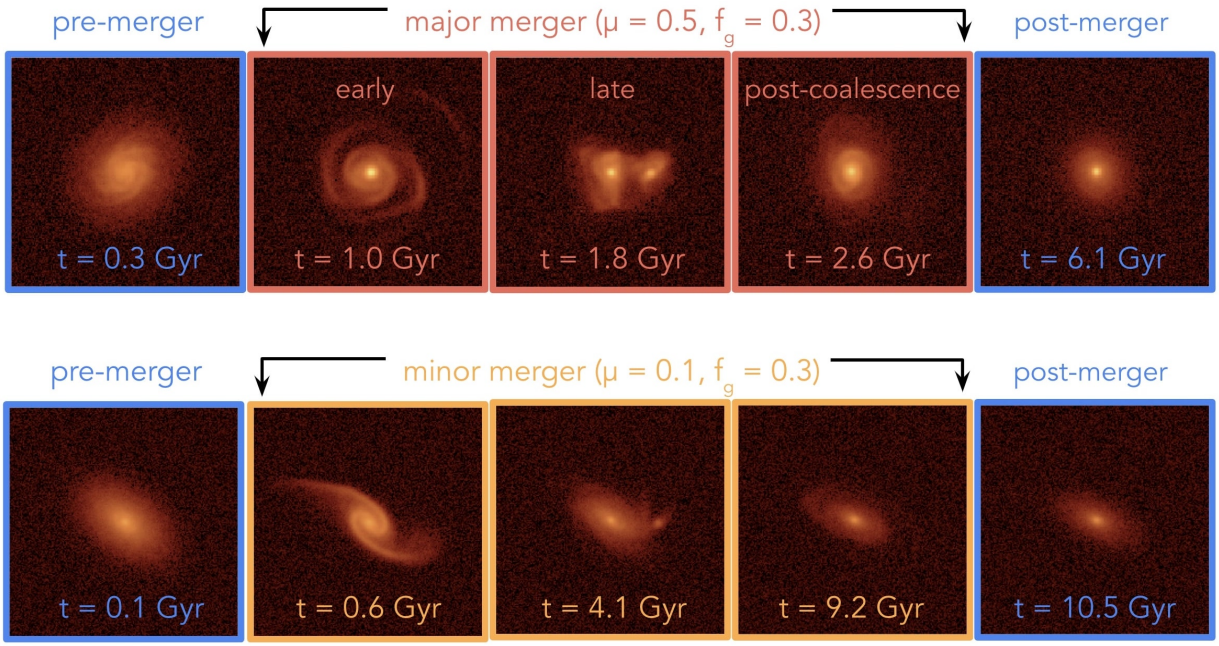

Figure 1.4: Illustration of merger stages for `SUNRISE/GADGET-3` simulated galaxies, adapted from Nevin et al. (2023). Stages shown are prior to galaxy-galaxy interactions (isolated pre-merger galaxy), early and late inspiral as the pair go through several close passes/pass-throughs of each other, and post-coalescence where the galaxies have merged into a single indistinguishable object with one nucleus but with noticeable morphological disruptions, and then after some time becomes a galaxy with no evidence of recent disruptions (isolated galaxy). Specifically, the top (bottom) panels track a simulated galaxy and show how its morphology changes as a function of time/merger stage, due to a major (minor) merger. Both cases have a cold gas fraction of $f_{\rm g} = 0.3$, with mass ratio $\mu \equiv M_1/M_2$.

The inspiral phase may enhance molecular gas fractions (Violino et al., 2018; Moreno et al., 2019) and clearly enhances star formation by a factor of $\sim 1.5-2$ in close galaxy pairs (< 20 kpc, e.g. Patton et al., 2013). The merging process appears to trigger strong inflows of cold gas to the centre of the galaxies (Mihos & Hernquist, 1996), believed to culminate in a starburst upon coalescence (Kauffmann & Haehnelt, 2000) and/or also accrete onto the SMBH, triggering AGN feedback (including quasars Sanders et al., 1988; Kauffmann & Haehnelt, 2000; Canalizo & Stockton, 2001; Hopkins et al., 2013). Some simulation works disagree with a starbust scenario, such as Hani et al. (2020), who examined mergers in the hydrodynamical simulation IllustrisTNG, only finding a modest factor of ~ 2 SFR enhancement during/after coalescence. Simulations and numerical models (Noguchi, 1987, 1988; Hernquist, 1989; Barnes & Hernquist, 1991, 1996a) generally agree on induced cold gas flow during inspiral due to the cold disc gas losing angular momentum during the merging process. Such studies found that close passes during inspiral result in the formation of a stellar bar and separate gas bar feature, but with the gas lagging behind due it being collisional. This rotational lag of a few degrees, results in it being gravitationally torqued by the stellar bar, draining angular momentum, resulting in gas flowing to the centre of the galaxy (Hopkins et al., 2008a; Hopkins, 2012). As the galaxies coalesce, the accumulated cold gas in the centres of both galaxies merge and is compressed, triggering a starburst. Feedback from supernova winds or AGN, or preventative means, such as induced turbulence, may rapidly quench a post-merger galaxy (e.g. Hopkins et al., 2008a). A rapid quenching scenario seems implied at least for a sizable (~ 20 per cent) proportion of post-mergers, by e.g. morphologically-identified merger remnants being 30-60 times more likely to be 'post-starburst' galaxies (Ellison et al., 2022).

Post-starburst galaxies (or 'E+A'/'K+A'; hereafter referred to as PSBs) are galaxies that have just undergone a rapid transition from star forming to quiescent. A characteristic tell-tale signature of such galaxies is a lack of nebular emission lines, indicating a low SFR, as well as strongly pronounced population of type A stars (leading to characteristic strong Balmer absorption lines), which only live up to ~ 1 Gyr (González Delgado et al., 1999) and so indicate a star-formation burst in the last ~ 1 Gyr. In practice, it may be hard to classify post-starbursts beyond ~ 300 Myr (Snyder et al., 2011). Because of their strong association with tidal features and disturbed morphologies (from $\sim$ 50–90% of galaxies Yang et al., 2008; Brown et al., 2009; Pracy et al., 2009; Pawlik et al., 2016; Sazonova et al., 2021, with deeper surveys finding a higher fraction), they are often speculated or interpreted to primarily be post-merger galaxies, at least in the low-redshift Universe (Quintero et al., 2004; Bekki et al., 2005; Yang et al., 2008; Pracy et al., 2012, 2013). It is worth noting that a sufficiently rapidly quenched galaxy, such as may occur from ram-pressure stripping in cluster environments, can easily be classified as a post-starburst from

spectra despite not having had a starburst (Snyder et al., 2011).

Much semi-analytic modeling (Cox et al., 2008), as well as detailed hydrodynamical simulations of merging galaxies (e.g. the FIRE-2 simulation, which has ~ 1 pc resolution Moreno et al., 2019), have been carried out. Despite such detailed and extensive modelling, it remains poorly observationally constrained how much hot and cold gas there is during and shortly after coalescence, let alone how it evolves. Even the amount of stellar mass formed during a possible starburst from merging has only been constrained indirectly in one way in the literature (Hopkins et al., 2008c). Because of this, the exact amount of feedback from star formation/supernovae and AGN in models and hydrodynamical simulations remains somewhat speculative and poorly constrained. Addressing these observational limitations is crucial to furthering progress in modeling/simulations that is anchored to the physical (observable) Universe.

1.5 This thesis

This thesis seeks to shed led on the mechanisms behind the quenching of galaxies by examining the role of environment on star formation in galaxies. This is done through data analysis of observationally-derived datasets and simulation results, as well as simplified empirical models to explain the observationally-derived results.

In Chapter 2, I verify galaxy groups and their members at $1 < z < 1.5$. I measure various properties and perform statistical background-subtraction to measure and fit their stellar mass functions for quiescent and star-forming galaxies. By comparing to field galaxies and adding in GOGREEN cluster results, I explore the dependence of quenching on halo mass empirically and with a simple infall quenching model.

In Chapter 3, I forward-model the observed effects of infall quenching on stellar ages and quiescent fraction in projected phase space for SDSS galaxies in the local Universe. With the model I constrain when quenching starts and how long it takes, as well as perform a thorough comparison to other infall quenching models in the literature.

In Chapter 4, I forward-model the star-formation burst of galaxy mergers using a dataset of morphologically identified galaxy mergers. Using stellar ages and star-formation rates of close pairs, I constrain the excess stellar mass formed during the inspiral phase prior to merging as well as for the burst occurring at time of coalescence. I provide a constraint on the duration of the starburst and explore consistency of such a burst with available gas observations.

Finally, in Chapter 5, I summarize the findings of the preceding Chapters and describe their contribution to the understanding of quenching. The chapter concludes with potential improvements as well as directions where further work is needed.

Chapter 2

Enhanced quenching in GOGREEN galaxy groups at redshift 1.0 to 1.5 and a dependence on halo mass

2.1 Introduction

It is well established in the standard Lambda Cold Dark Matter (ΛCDM) cosmology that gravitationally bound dark matter haloes build up hierarchically through a combination of smooth accretion of surrounding matter, as well as merging with smaller structures (White & Rees, 1978; Navarro et al., 1997; Qu et al., 2017). Complex baryonic physics, such as radiative cooling and feedback from stars and accreting supermassive black holes (e.g. White & Frenk, 1991; Finlator & Davé, 2008; Bouché et al., 2010; Schaye et al., 2010; Davé et al., 2012; Bower et al., 2017) drives the formation of galaxies within this gravitationally dominant component.

Up to at least $z \sim 2.5$, galaxy populations exhibit a bimodality in their star formation rate (SFR) distribution (e.g. Bell et al., 2004b; Brinchmann et al., 2004; Brammer et al., 2011; Muzzin et al., 2012) and a corresponding bimodality in the distribution of rest-frame colours (e.g. Strateva et al., 2001; Baldry et al., 2004; Bell et al., 2004a; Williams et al., 2009; Foltz et al., 2018; Muzzin et al., 2013b; Taylor et al., 2015). Observations of these two populations at different redshifts show that the number density and shape of the stellar mass function (SMF) for quiescent (red) galaxies has evolved dramatically, while the SMF of star-forming (blue) galaxies has remained nearly unchanged since $z \sim 3.5$ (e.g. Faber et al., 2007; Muzzin et al., 2013b; McLeod et al., 2021). This indicates that the latter

population eventually stops forming stars, in a process generically called 'quenching'. The distinct bimodality in the colour and SFR distribution is generally assumed to imply that this quenching must be fairly rapid (e.g. Balogh et al., 2004b; Wetzel et al., 2012), although see Chapter 3.4 where we demonstrate that this assumption is not necessarily true.

The fraction of quiescent galaxies increases strongly with stellar mass, for $M_{\rm stellar} > 10^9$ $M_\odot$ (e.g. Kauffmann et al., 2003, 2004; Brinchmann et al., 2004; Baldry et al., 2006; Weinmann et al., 2006; Kimm et al., 2009; Muzzin et al., 2012; van der Burg et al., 2018). At fixed stellar mass, the quiescent fraction declines with increasing redshift, and is higher in denser environments. This has been thoroughly demonstrated in works studying dense environments of rich groups and clusters in the local $z \sim 0$ Universe (Kauffmann et al., 2004; Gómez et al., 2003; Balogh et al., 2004a; Hou et al., 2014), as well as intermediate $0 < z < 1$ redshifts (De Lucia et al., 2004; Wilman et al., 2005; Cooper et al., 2006; McGee et al., 2011; Giodini et al., 2012; van der Burg et al., 2018; Just et al., 2019) and at $z > 1$ (Muzzin et al., 2012; Balogh et al., 2014; Nantais et al., 2016; Guglielmo et al., 2019; Strazzullo et al., 2019; van der Burg et al., 2020). At low redshifts, the dependence of the quiescent fraction on stellar mass and environment is largely separable (Baldry et al., 2006; Peng et al., 2010; Kovač et al., 2014; Balogh et al., 2016; van der Burg et al., 2018). This has been interpreted to indicate that the dominant physical mechanisms are also separable (e.g. Peng et al., 2010). However, this is not necessarily the case (De Lucia et al., 2012; Pintos-Castro et al., 2019), and most physically-motivated models invoked to explain environment quenching have a dependence on stellar mass (e.g. McGee et al., 2014; Fillingham et al., 2015; Quilis et al., 2017; Wright et al., 2019).

The environmental dependence of quenching provides a particularly interesting and discriminating test of models (e.g. Weinmann et al., 2010; McGee et al., 2014; Hirschmann et al., 2016). Comparison of data with models is challenging, however, in part because there are many different, commonly used definitions of environment. These include local density (Cooper et al., 2006; Peng et al., 2010; Sobral et al., 2011; Darvish et al., 2016; Davidzon et al., 2016; Lemaux et al., 2019; Kawinwanichakij et al., 2017; Papovich et al., 2018), group/cluster virial masses and cluster centric distance (Poggianti et al., 2006; Oman et al., 2013; Muzzin et al., 2014; Paccagnella et al., 2016; van der Burg et al., 2018, 2020), and status as central or satellite in halo (Muzzin et al., 2012; Mok et al., 2013; Balogh et al., 2016). The quiescent fraction at fixed stellar mass correlates with environment in most cases, but the interpretation of the physical mechanisms behind the observed trends remains elusive, in part because of the difficulty linking these observations to theoretical models.

To interpret the environmental dependence of the quiescent fraction, numerous works have used simple accretion models where galaxies take some amount of time to fully quench,

once they enter a new environment. To reproduce the observations at $z \sim 0$ requires long timescales, of at least $\sim 2-7$ Gyr (e.g. De Lucia et al., 2012; Wheeler et al., 2014). To reconcile this with the bimodality in observed SFRs, which requires a rapid transition, it is frequently assumed to be a long delay time during which the galaxy properties remain uninfluenced by their environment, before rapid quenching sets in (Wetzel et al., 2013; Oman & Hudson, 2016). These timescales are shorter at higher redshift, scaling approximately with the dynamical time (Tinker & Wetzel, 2010; Tinker et al., 2013; Balogh et al., 2016; Foltz et al., 2018). However, all these timescales are relative to an assumed starting point associated with a change in environment. In general this is not well defined, and depends upon assumptions about the physical mechanisms at work.

A physically relevant definition of environment in ΛCDM models is the mass of the host halo, and location within it. The environment of a galaxy undergoes a large change when it is accreted into a more massive halo and first becomes a satellite, as it orbits within that new halo. A simple objective definition of this accretion time is the moment when a galaxy crosses R_{200}[1] for the first time (Balogh et al., 2000). However, simulations suggest environment first becomes important when satellites are cut off from cosmological accretion, which can happen well outside R_{200} (Behroozi et al., 2014; Bahé & McCarthy, 2015; Pallero et al., 2019). On the other hand, for processes like ram pressure stripping that require a dense intracluster medium, the more relevant starting point could be well inside R_{200} (e.g. Muzzin et al., 2014). Moreover, the starting time for environmental effects depends on when in the merger history hierarchy the galaxy is accreted, according to one of the above definitions. One consideration is the accretion onto the main progenitor of the final halo. Alternatively, the physically relevant definition could be the first time a galaxy is accreted onto any more massive halo and hence first becomes a satellite. The latter is often referred to as "pre-processing"; observations and simulations both indicate that pre-processing may be important for a significant proportion of galaxies and that at least some cluster galaxies had their star formation quenched in $M_{\rm halo} \geq 10^{13}{\rm M}_{\odot}$ groups prior to being accreted into massive clusters (Zabludoff & Mulchaey, 1998; Kawata & Mulchaey, 2008; Berrier et al., 2009; McGee et al., 2009; De Lucia et al., 2012; Hou et al., 2014; Pallero et al., 2019; Donnari et al., 2021).

To make progress requires observations of galaxies spanning a wide range in stellar mass and redshift, within a range of well-characterized environments that can be directly linked to theory. This can be achieved with samples of groups and clusters with reliable halo mass estimates. The GOGREEN survey (Balogh et al., 2017, 2021) was designed with this

[1] R_{Δ} can be defined for a halo as the radius within which the average density is Δ times either the critical density of the Universe or Δ times the background density. We use the former definition in this work.

goal, and provides a sample of 21 galaxy systems at $1 < z < 1.5$ with deep photometry and extensive spectroscopy, ranging from groups to the most massive clusters. The groups are a subset of those identified from the deep X-ray and spectroscopic observations in the COSMOS and SXDF regions (Finoguenov et al., 2010; Leauthaud et al., 2012; Giodini et al., 2012; Gozaliasl et al., 2019). COSMOS groups at $z < 1$ have already been studied in some detail. For example, Giodini et al. (2012) measured stellar mass functions for quiescent and star-forming galaxies (separated using NUV-R colours) in these systems. Among other things, they found that the fraction of quiescent galaxies increases with halo mass, and decreases with increasing redshift, though this was not examined as a function of stellar mass. In the present paper we build upon this work, taking advantage of deeper X-ray data and additional spectroscopy to extend the group sample to $1 < z < 1.5$. We also make use of significantly improved photometry (deeper/more bands) to separate quiescent/star-forming galaxies and measure their stellar mass functions and quiescent fractions. Combined with the GOGREEN sample, and lower redshift comparison samples, this allows for an improved picture of quenching as a function of both stellar and halo mass, over the redshift range $0 < z < 1.5$.

The structure of the paper is as follows. In §2.2 we describe the spectroscopic and photometric data sets, as well as the group catalogues, that we use for the measurements. Results are presented in §2.3. In §2.4, we discuss our measurements in the context of the literature, compare to the BAHAMAS hydrodynamical simulation, and explore a toy model to constrain pre-processing scenarios. We then conclude and summarise in §2.5. In Appendix A, we include additional details of calibrations and robustness checks, present the spectroscopically targeted GOGREEN groups and stacked velocity dispersion measurement, as well as provide supplemental plots to our analysis and discussion of halo mass trends.

Uncertainties are given at the 1-σ (Gaussian) level, unless stated otherwise. Logarithms with base 10 ($\log_{10}$) are written simply as "log" throughout this work. All magnitudes are given in the AB magnitude system, all (RA, DEC) coordinates are given using the J2000 system, and a Chabrier (2003) initial mass function (IMF) is assumed throughout, unless specified as otherwise. As well, a flat ΛCDM cosmology with $H_0 = 70$ km s^{-1} Mpc^{-1}, $\Omega_m = 0.3$, and $\Omega_\Lambda = 0.7$, is assumed. Halo masses and radii are given as either (M_{500c}, R_{500c}) or (M_{200c}, R_{200c}), where c refers to the critical density of the Universe at a given redshift. Conversions of mass and radius between $500c$ and $200c$ were done using concentration parameters estimated using the redshift-dependent relation defined in Muñoz-Cuartas et al. (2011). Finally, whenever the term "field" is used, we are referring to an average sample of the Universe, which includes all environments.

2.2 Datasets and sample selections

The core analysis of this work is based on 21 X-ray selected groups at $1 < z < 1.5$, in the COSMOS and SXDF survey regions. We rely on the excellent photometric redshifts, calibrated with extensive spectroscopy, and statistical background subtraction to analyse the galaxy populations in these groups. The following subsections summarise the data and sample selections, including comparison samples at lower redshift and higher halo mass.

2.2.1 Photometric data

Imaging and catalogues

For COSMOS we use the UltraVISTA (McCracken et al., 2012; Muzzin et al., 2013a) survey as the source of the photometry and catalogues. The first data release (DR1, v4.1) provides a K-selected catalogue in 38 photometric bands, covering 1.62 deg^2 and with a 5σ ($2.1''$ aperture) limiting magnitude of $K_s = 23.9$AB. The 95% stellar mass-completeness limit is 10^{10} M$_\odot$ at $z = 1.5$. The catalogues include photometric redshifts and rest-frame $U-V$ and $V-J$ colours, computed using EAZY (Brammer et al., 2010). The photometric redshifts are accurate to $\delta z/(1+z) = 0.013$ (68% confidence limits), with a catastrophic outlier fraction of 1.6% (Muzzin et al., 2013a). The catalogues also include stellar masses and population parameters, which were obtained using the spectral energy distribution fitting code FAST (Kriek et al., 2009) with the Bruzual & Charlot (2003) models. A subset of the COSMOS field is covered by the ultra-deep stripes of UltraVISTA DR3. This catalogue includes 50 photometric bands and covers a non-contiguous 0.8465 deg^2, with a 5σ ($2''$ aperture) limiting magnitude of $K_s = 24.9$AB[2]. A magnitude $K_s = 23.5$ is reached at the 90% confidence limit and the 95% mass-completeness limit is $10^{9.58}$ M$_\odot$ at $z = 1.5$. We use DR3 catalogues for the subset of groups that fall entirely within one of the stripes of that survey; otherwise we use DR1.

For SXDF we use the SPLASH-SXDF 28-band catalogue (Mehta et al., 2018). The subset of the SXDF field with all available filters covers 0.708 deg^2, with a $5\sigma(2'')$ limiting magnitude of $K = 25.32$ (Mehta et al., 2018). By comparing with UltraVISTA DR3, we expect this survey to be 95% complete above a stellar mass limit of $10^{9.4}$ M$_\odot$ at $z = 1.5$. Photometric redshifts, their uncertainties, and stellar mass estimates were calculated by the SPLASH team using LePhare (Arnouts et al., 1999; Ilbert et al., 2006). Photometric

[2]The official UltraVISTA DR3 data release document can be accessed here: https://www.eso.org/sci/observing/phase3/data_releases/uvista_dr3.pdf

redshift uncertainties are reported in terms of their χ^2 fit, $\Delta\chi^2 = 1.0$ for upper and lower 68% confidence limits. We rely on the rest-frame U, V, and J colours to classify galaxies, and we compute these using the SPLASH-SXDF v1.6 photometric catalogue, with EAZY. Redshifts were fixed to the SPLASH-SXDF photometric redshifts or spectroscopic redshift, if available.

A small correction (< 0.06) is made to the photometric redshifts in the range $1 < z < 1.5$, to correct a redshift-dependent bias that is observed upon comparison with a spectroscopic sample, as described in Appendix A.3. Details of the various spectroscopic redshift catalogues used for this, as well as description of how they informed our photometric redshift selection of group members and groups, can be found in Appendix A.4.

Galaxy selection

We select galaxies from the UltraVISTA DR1 catalogue of Muzzin et al. (2013a), closely reproducing the selection used by Muzzin et al. (2013b) to calculate the stellar mass function evolution. Specifically, we select objects identified as galaxies (rather than stars), with uncontaminated photometry and $K_s < 23.4$. We impose an additional cut of S/N > 7 in the K_s photometry. We perform a similar selection for UltraVISTA DR3, except to $K_s < 24.9$. For galaxies in the SPLASH-SXDF we select galaxies with the same $S/N > 7$ criterion, and $K_s < 23.7$, corresponding to the 5σ depth of that survey. Stars in SXDF are excluded from the sample using the "STAR_FLAG" parameter, which is based on whether the photometry is best-fit to a stellar or galaxy template, with an additional restriction that the object does not belong to the stellar sequence in BzK colour-colour space.

Finally, we make a survey-dependent stellar mass cut to ensure complete, unbiased galaxy samples. For $1 < z < 1.5$ groups in UltraVISTA DR1, the shallowest of the survey regions, we select galaxies with $\log M_{\rm stellar}/{\rm M}_\odot > z_{\rm group} + 8.5$, corresponding to the mass completeness limit shown in Figure 2 of Muzzin et al. (2013b). For groups in the deeper UltraVISTA DR3 and SXDF we conservatively select galaxies with $M_{\rm stellar} > 10^{9.6}$ M$_\odot$, corresponding to the $z = 1.5$ completeness limit of DR3.

Classification of quiescent and star-forming galaxies

We identify quiescent[3] ("red") and star-forming ("blue") galaxies using rest-frame UVJ colour-colour cuts, following Muzzin et al. (2013b). To ensure consistency between the

[3]Equivalently referred to in some of the literature as 'passive' or 'quenched'.

three photometric catalogues we use, we apply small systematic shifts to the $U-V$ and $V-J$ colours of galaxies in UltraVISTA DR1 and SXDF, to match those of UltraVISTA DR3. Specifically, we calculate the average difference in these colours between surveys, using galaxies at $1 < z < 1.5$ and with stellar masses above 10^{10} $M_{\odot}$. This results in a shift of $\Delta(V-J) = 0.08$ and $\Delta(U-V) = -0.05$ for UltraVISTA DR1; for SXDF the corresponding shifts are 0.10 and 0.15, respectively. We then use the following selection, slightly modified from Muzzin et al. (2013b) (which worked with the original UltraVISTA DR1 colours), to identify quiescent galaxies at $1 < z < 1.5$:

$$U - V > 1.26, V - J < 1.58, \tag{2.1}$$
$$U - V > (V - J) \times 0.88 + 0.47, \tag{2.2}$$

We illustrate these cuts on the rest-frame $U-V$ vs $V-J$ distribution in Figure 2.1.

We also consider a lower redshift comparison sample of groups, at $0.5 < z < 0.7$, selected entirely from UltraVISTA DR1 (see §2.2.2). Noting that the UVJ colour-colour cut is weakly redshift dependent (Williams et al., 2009; Whitaker et al., 2011; Muzzin et al., 2013b) we instead adopt for these galaxies exactly the selection of Muzzin et al. (2013b) at $0.0 < z < 1.0$, namely:

$$U - V > 1.3, V - J < 1.5, \tag{2.3}$$
$$U - V > (V - J) \times 0.88 + 0.69\,. \tag{2.4}$$

Group selection

The COSMOS groups and SXDF groups we use for our analyses were identified in Gozaliasl et al. (2019) and Finoguenov et al. (2010), respectively. Each group in the catalogue has a quality flag ranging from 1 (best) to 5 (worst), although the precise meaning of these flags is different in the two surveys. We update quality flags for a subset of groups in the two group catalogues based on information from our GOGREEN spectroscopy, which increases the number of available spectroscopically confirmed groups. We then select only groups with quality flags < 3, defined in Gozaliasl et al. (2019) to have both X-ray detections, photometric overdensity of galaxies, and at least one spectroscopically-confirmed member [4].

[4] In Table 2.1, group COSMOS-30317 is listed as having no spectroscopic members. This discrepancy with Gozaliasl et al. (2019) may be either due to a different cut in redshift or a difference in the spectroscopic catalogues being used.

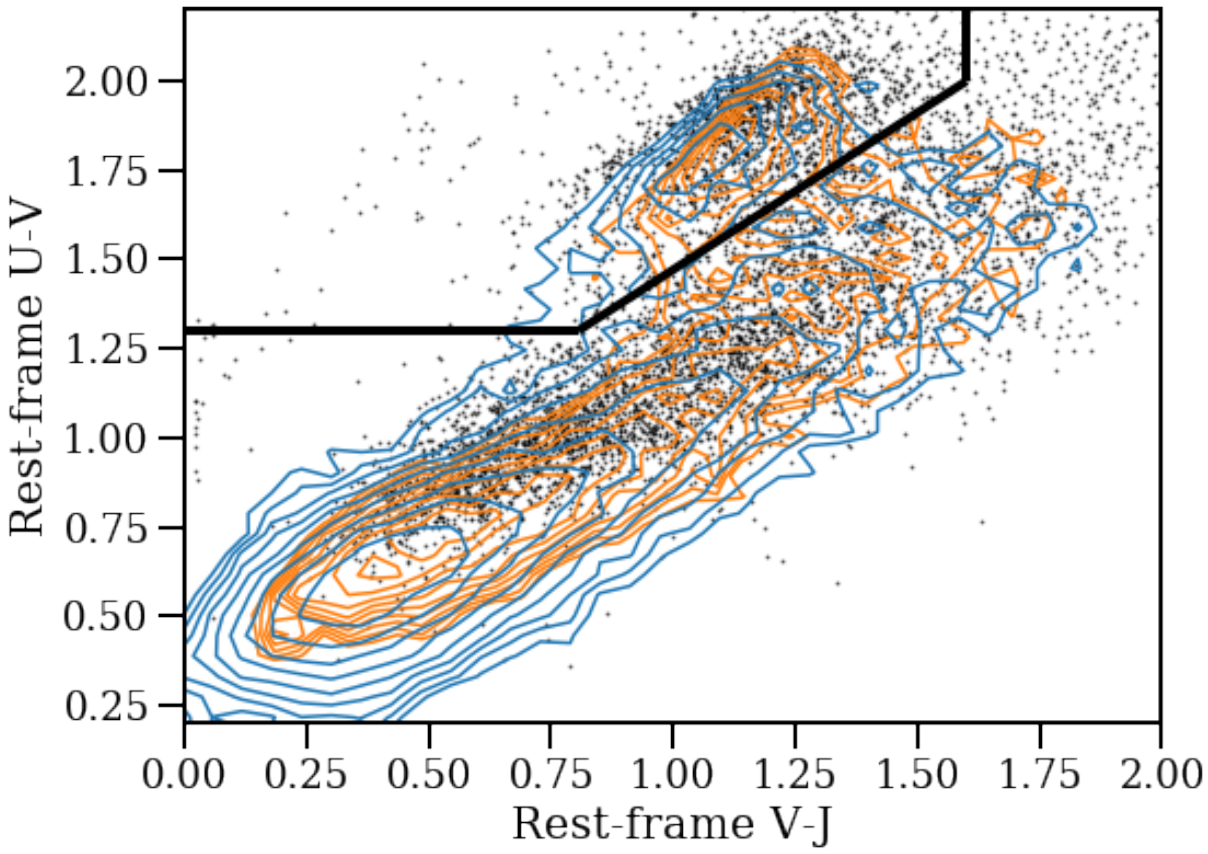

Figure 2.1: Rest-frame $U - V$ vs $V - J$ colour distributions for galaxies in the SXDF (black points), UltraVISTA DR1 (orange contours) and DR3 (blue contours), with the colour-colour cuts dividing quiescent and star-forming galaxies (solid black line). Small zeropoint adjustments have been made to SXDF and DR1, as described in the text. For the purposes of this figure, galaxies are limited to $1 < z < 1.5$ and $\log(M_{\rm stellar}/{\rm M}_{\odot}) > 10$.

With this selection we have an initial sample of 21 groups at $1 < z < 1.5$: nine in UltraVISTA DR1, eight in DR3, and four in SXDF. The properties of these groups are presented in Table 2.1. All of these groups have halo masses estimated to be in the range $13.6 < \log(M_{\rm halo}/{\rm M}_\odot) < 14.0$, with an average of $\log(M_{\rm halo}/{\rm M}_\odot) \approx 13.8$. For each group we calculate $R_{200c}(z)$ (using Hearin et al., 2017) corresponding to this average mass (e.g. $R_{200c} = 1.044'$ in projection at $z = 1.25$).

The masses are based on the weak lensing calibrations of the $L_{\rm X} - M_{\rm halo}$ relations in COSMOS (Leauthaud et al., 2010). The mentioned biases in the Planck 2015 paper (Planck Collaboration et al., 2016b) are relevant only for the hydrostatic mass estimates (see also Smith et al., 2016, for detailed discussion of the biases in the Planck 2015 paper). For the SZ confirmation on similar galaxy groups (near our redshift and halo mass range), there is one such measurement, at z=2 (Gobat et al., 2019). As an alternative indicator of halo mass, we calculate the richness, $\lambda_{10.2,{\rm R<1Mpc}}$, defined as the number of photometrically background-subtracted galaxies within a 1 Mpc radius above a stellar mass of $10^{10.2}$ ${\rm M}_\odot$. In Figure 2.2 we show the correlation between these richness values and the M_{200c} masses from X-ray fluxes for our group sample. This is compared with more massive clusters from van der Burg et al. (2020), discussed in §2.2.2 below. For that sample, we use halo masses based on the dynamical analysis of Biviano et al. (2021). Although the uncertainties on individual richness measurements are large, this comparison confirms that the group sample is systematically less rich than the cluster sample, at the level expected from their mass estimates. Only one of the groups has a richness $\lambda_{10.2,R<1{\rm Mpc}} < 1$, significantly lower than expected of a truly overdense system.

The subset of $1 < z < 1.5$ groups with GOGREEN spectroscopy affords the opportunity to study these groups in some more detail, and to test the robustness of the statistical background subtraction. This analysis is presented in Appendix A.4.3. Where it is possible to calculate a robust velocity dispersion, we report these values in Table 2.1. The dynamical halo mass, $M_{200c,{\rm dyn}}$ (column 8 of Table 2.1), is then derived using the relation in Saro et al. (2013). Two groups – SXDF64 and SXDF87 – have dynamical masses significantly higher than that based on their X-ray emission, and formally above our arbitrary threshold for low-mass haloes, of 10^{14} ${\rm M}_\odot$. To be conservative, therefore, we exclude these two groups from the rest of our analysis, though we have confirmed that our results are not sensitive to this choice.

The mean and median redshift of the group sample (1.179 and 1.170, respectively) is somewhat lower than that of the field sample (1.236 and 1.39). We have verified that our conclusions are unchanged if we divide the group and field samples into two redshift bins and conclude that our findings are not sensitive to this difference.

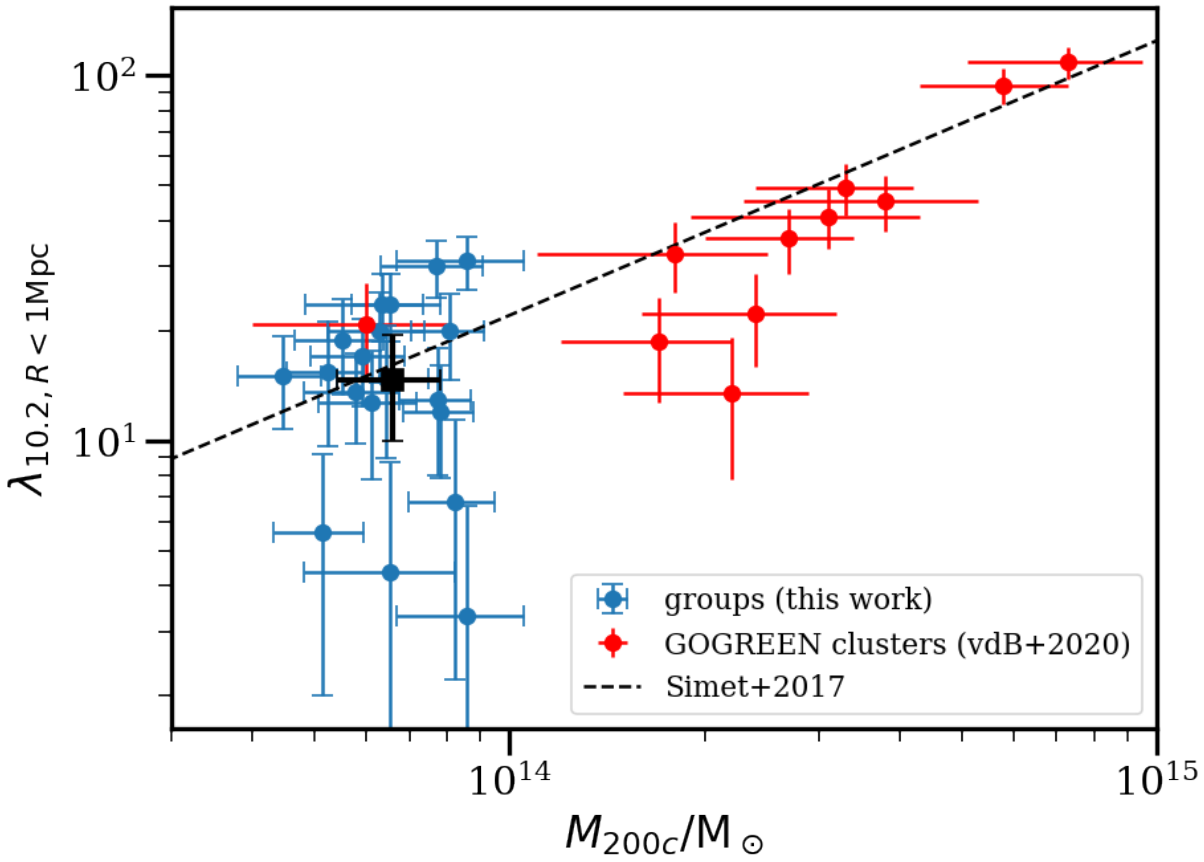

Figure 2.2: Richness as a function of halo mass for groups in this work (blue points; mean of sample shown with the square black point) and the GOGREEN clusters (red points). The richness, $\lambda_{10.2,\mathrm{R<1Mpc}}$, is the number of background-subtracted galaxies that have stellar masses above $10^{10.2}$ $\mathrm{M}_\odot$ within 1 Mpc, following van der Burg et al. (2020). Halo masses for the groups are derived from the X-ray fluxes, while for the clusters they are based on a spectroscopic dynamical analysis from Biviano et al. (2021). The richness-halo mass relation fit for clusters at $0.1 < z < 0.33$ from Simet et al. 2017 is shown for comparison as a dashed line. Note that one of the groups has a formally negative richness, and lies off the bounds of this figure.

Name	RA (°)	Dec (°)	z	flag	$\log\left(\frac{M_{200c,\mathrm{X}}}{\mathrm{M}_\odot}\right)$	K_s limit	$\log\left(\frac{M_{200c,\mathrm{dyn}}}{\mathrm{M}_\odot}\right)$	$\sigma_v(\mathrm{km\,s^{-1}})$	N_{spec}	$\lambda_{10.2,\mathrm{R<1Mpc}}$
COSMOS-30221	150.56200	2.50309	1.197	0	13.80	24.9	$12.90 \pm {}^{0.30}_{0.39}$	200 ± 50	9	23.6 ± 5.0
COSMOS-20267	150.44487	2.75393	1.138	1	13.91	24.9	–	–	2	20.0 ± 5.3
COSMOS-30307	149.73943	2.34139	1.028	1	13.72	24.9	–	–	3	15.4 ± 5.7
COSMOS-20028	149.46916	1.66856	1.316	0	13.89	24.9	$13.33 \pm {}^{0.19}_{0.38}$	285 ± 75	10	30.0 ± 5.4
COSMOS-20057	150.45229	1.91046	1.179	1	13.81	24.9	–	–	1	23.7 ± 5.0
COSMOS-10155	150.59137	2.53778	1.138	1	13.89	24.9	–	–	3	12.0 ± 4.1
COSMOS-30317	150.12646	1.99926	1.019	1	13.65	24.9	–	–	0	15.0 ± 4.2
COSMOS-20072	149.86012	1.99973	1.179	1	13.92	23.9	–	–	3	6.8 ± 4.6
COSMOS-20199	150.70682	2.29253	1.095	1	13.70	23.9	–	–	5	-6.5 ± 2.6
COSMOS-20198	149.59607	2.43788	1.168	1	13.81	23.9	–	–	3	14.8 ± 5.8
COSMOS-20243	150.26115	2.76857	1.315	1	13.80	23.9	–	–	1	20.0 ± 5.6
COSMOS-10063	150.35902	1.93521	1.172	0	13.74	23.9	–	–	9	18.85 ± 5.5
COSMOS-10105	150.38295	2.10278	1.163	1	13.79	23.9	–	–	5	12.7 ± 4.9
COSMOS-20125	150.62077	2.16754	1.404	0	13.81	23.9	–	–	8	4.4 ± 4.4
COSMOS-10223	150.05064	2.47520	1.260	1	13.76	23.9	–	–	4	13.6 ± 3.7
COSMOS-30323	150.22540	2.55061	1.100	2	13.71	23.9	–	–	3	5.6 ± 3.6
SXDF49XGG	34.49962	−5.06489	1.091	0	13.77	25.3	$13.25 \pm {}^{0.22}_{0.27}$	255 ± 50	14	17.0 ± 4.6
SXDF64XGG*	34.33188	−5.20675	0.916	0	13.76	25.3	$14.20 \pm {}^{0.18}_{0.21}$	530 ± 80	8	–
SXDF76aXGG	34.74613	−5.30411	1.459	0	13.93	25.3	$14.06 \pm {}^{0.38}_{0.54}$	520 ± 180	6	31.1 ± 5.2
SXDF76bXGG	34.74743	−5.32348	1.182	0	–	25.3	$12.98 \pm {}^{0.33}_{0.45}$	210 ± 65	7	3.3 ± 3.3
SXDF87XGG*	34.53602	−5.06303	1.406	0	13.89	25.3	$14.44 \pm {}^{0.19}_{0.223}$	700 ± 110	9	–

Table 2.1: Group names correspond to those in Gozaliasl et al. (2019) and Finoguenov et al. (2010) for COSMOS and SXDF, respectively; names in boldface are those included in the GOGREEN (Balogh et al., 2021) spectroscopic survey. SXDF76XGG has been split into "a" and "b" to identify the foreground group; the original X-ray mass estimate for $M_{200c,X}$ has been retained only for the higher redshift system. Group redshifts are taken from the original catalogues, except where GOGREEN spectroscopy is available to provide an improved measurement (see Appendix A.4.3). Column 5 is the group quality flag. A flag value of 0 denotes a group with confirmed redshift from GOGREEN (Balogh et al., 2021). Other flag numbers are based on the Gozaliasl et al. (2019) catalogue: 1 for secure X-ray emission with well-defined centre and at least one spectroscopic member, and 2 for a system that has some X-ray contamination from foreground or background systems. Column 6 gives the group halo mass estimates from the original catalogues, derived from observed X-ray luminosities. Column 7 gives the K_s-band limiting magnitude for the survey from which each group is drawn, as described in the text. Column 9 gives the (spectroscopic) velocity dispersion we determined for our GOGREEN targeted groups in Appendix A.4.3, and column 8 shows the corresponding dynamical masses. Column 9 gives the number of spectroscopic group galaxies in each group, within a radius of $2R_{200c}$. The final column gives the richness for groups in our photometric sample, with richness defined as the number of group members with $\log(M_{\mathrm{stellar}}/\mathrm{M}_\odot) > 10.2$ found within a 1 Mpc circular aperture (see Figure 2.2 for a comparison of these values with the GOGREEN clusters sample from van der Burg et al. (2020)). The two groups indicated with a $*$ are excluded from the analysis in this paper, as their dynamical masses suggest they may exceed our threshold definition for low-mass haloes.

2.2.2 Comparison samples

Higher halo masses at $1 < z < 1.5$

We contrast our low halo-mass systems at $1 < z < 1.5$ with eleven higher mass clusters in the same redshift range from GOGREEN. Our measurements are similar to those in van der Burg et al. (2020), but recalculated to include only galaxies within R_{200c}. Halo masses are determined dynamically (Biviano et al., 2021), and we show the correlation between these and the cluster richness in Figure 2.2. This sample is divided into two bins of halo mass, though the highest mass bin contains only two clusters at the lower end of the target redshift range: SPT-CL J0546-5345 ($z = 1.068$) and SPT-CL J2106-5844 ($z = 1.126$). We note that several clusters (SpARCS-1051, SpARCS-1638, SpARCS-1034, SpARCS-0219) have low richness values more typical of our groups.

Intermediate redshift $0.5 < z < 0.7$

The galaxy populations in the X-ray selected groups at $z < 1$ have been extensively studied, notably by Giodini et al. (2012). We use a similar sample but redo the analysis to ensure consistent methodology when comparing with our higher redshift sample. Specifically, we select fourteen groups in the redshift range $0.5 < z < 0.7$ from the COSMOS field, and use the UltraVISTA DR1 catalogue. Since the average rest-frame UVJ colours and photometric redshifts do not noticeably differ between UltraVISTA DR1 and DR3, we do not make the adjustments to colours or photometric redshifts that we applied to the higher redshift sample. The groups are required to be robustly identified (quality flags < 3) and in the halo mass range $13.6 < \log(M_{\rm halo}/{\rm M}_{\odot}) < 14.0$. The average halo mass of the sample is $\log(M_{\rm halo}/{\rm M}_{\odot}) \approx 13.78$, comparable to the mass of our higher redshift group sample. The photometric redshift selection, and statistical background subtraction, is done in an analogous way to that for the $1 < z < 1.5$ sample.

For higher mass clusters at this redshift we use the published measurements and uncertainties in the stellar mass functions for 21 clusters selected based on their Sunyaev-Zeldovich (SZ) signal, from the Planck all sky survey, from van der Burg et al. (2018). These clusters span the halo mass range $14.5 < \log(M_{\rm halo}/{\rm M}_{\odot}) < 15.1$. These were analysed in a very similar way to the clusters from van der Burg et al. (2020) that we use at higher redshift.

The field sample we compare with at this redshift is comprised of all UltraVISTA DR1 galaxies with photometric redshifts in the range $0.5 < z < 0.7$.

Low redshift $0.01 < z < 0.2$

At $0.01 < z < 0.2$ we use the SDSS-DR7 measurements from (Omand et al., 2014). Galaxy groups are selected from the Yang et al. (2012) friends-of-friends catalogue. Halo masses were determined through abundance matching, using the total group luminosity to rank them. We select haloes in the same mass ranges as at other redshifts, without any evolution correction; the final sample includes 13806/3282/483 haloes in the low/intermediate/high mass bins. All galaxies associated with a halo are included as members, with no additional selection based on clustercentric radius. Stellar masses are computed following the procedure described in Brinchmann et al. (2004), with a small (10 per cent) correction to convert from a Kroupa (2001) to a Chabrier (2003) initial mass function using Madau & Dickinson (2014). Quiescent galaxies are identified as those with specific star formation rates $\mathrm{sSFR} < -0.24 \log(M_{\mathrm{stellar}}/\mathrm{M}_{\odot}) - 8.50$, chosen to lie below and parallel to the star-forming main sequence identified in Omand et al. (2014).

2.3 Results

2.3.1 Stellar mass functions

The photometric redshift uncertainties in both UltraVISTA and SPLASH-SXDF are still large enough that galaxies cannot be unambiguously identified as members of groups or clusters. We therefore rely on statistical background subtraction, using our representative field sample, to calculate the stellar mass functions.

The number of group members of a given type (quiescent or star-forming), and within a given stellar mass bin, is calculated as the number of galaxies N_C within a circular aperture A_C around the group centre, and with photometric redshifts such that $|z - z_g| < \Delta z$ relative to the group redshift, z_g, minus the corresponding average number of galaxies in the field within that same aperture and redshift slice. For each galaxy sub-population (e.g. quiescent or star-forming) the average number of galaxies per group that we find is described by the following expression:

$$\phi(M) = \frac{1}{N_G} \sum_{g} \left[N_{C,z_g}(M) - N_{\mathrm{survey},z_g}(M) \times \left(\frac{A_C}{A_{\mathrm{survey}}} \right) \right], \tag{2.5}$$

where N_G is the number of groups, g is a given group, N_{survey}, A_{survey} are the number of field galaxies and the total area of the survey from which each group is drawn, respectively.

We use $M = M_{\rm stellar}$ in the above expression for brevity. The aperture size is chosen to be R_{200c}, and a photometric redshift cut of $\Delta z = 0.126$ was chosen for all three survey regions (see Appendix A.3.2 for explanation of this cut choice). As well, since the area of a group aperture at a given redshift is negligible relative to the rest of the given survey region at that redshift, we refer to the overall survey area/volume as the "field".

The error on the number of background-subtracted galaxies in a group is given by summing in quadrature the Poisson counting error and the Poisson error term for the field contribution ($A_C/A_{\rm survey}$), which simplifies to $\sigma \approx \sqrt{N_C(M)}$. The total error for the number of galaxies in a given mass bin is then

$$\sigma(M) = \frac{1}{\phi(M)} \sqrt{\sum_g N^2_{C,z_g}(M)}, \tag{2.6}$$

where N_{C,z_g} is the number of galaxies in the circular aperture, C, around a given group, g, at redshift z_g.

In Figure 2.3 we present the background-subtracted stellar mass functions for the full sample of $1 < z < 1.5$ groups, and separately for the quiescent and star-forming populations. Each bin is weighted by the number of contributing groups, such that the resulting values are the average number of galaxies per group, per dex in stellar mass.

The stellar mass functions are fit with Schechter (1976) functions of the form

$$\Phi(M) = \frac{dN}{dM} dM = \Phi^* \left(\frac{M}{M^*}\right)^{\alpha} e^{-M/M^*} dM, \tag{2.7}$$

where M is the stellar mass, M^* is the characteristic mass where the Schechter function transitions between a power law and an exponential cut-off, and α is the logarithmic slope of the faint-end power-law. We fit all three parameters, separately for each sample, by minimizing the χ^2. Where needed, we arbitrarily increase the uncertainties to ensure $\chi^2/\nu = 1$ for the best fit model, where ν is the number of degrees of freedom. This is only important for the quiescent population, for which a single Schechter function does not provide a good fit ($\chi^2/\nu = 2.56$); uncertainties are therefore increased by a factor ~ 1.6. With this adjustment we calculate the 68% confidence limits from the χ^2 distribution and determine all parameter combinations that provide a χ^2 within these limits. All points are included in the fits, including those with contributions from fewer than the maximum number of groups. The best fit parameters and their uncertainties are given in Table 2.2, and the mass functions are shown in Figure 2.3.

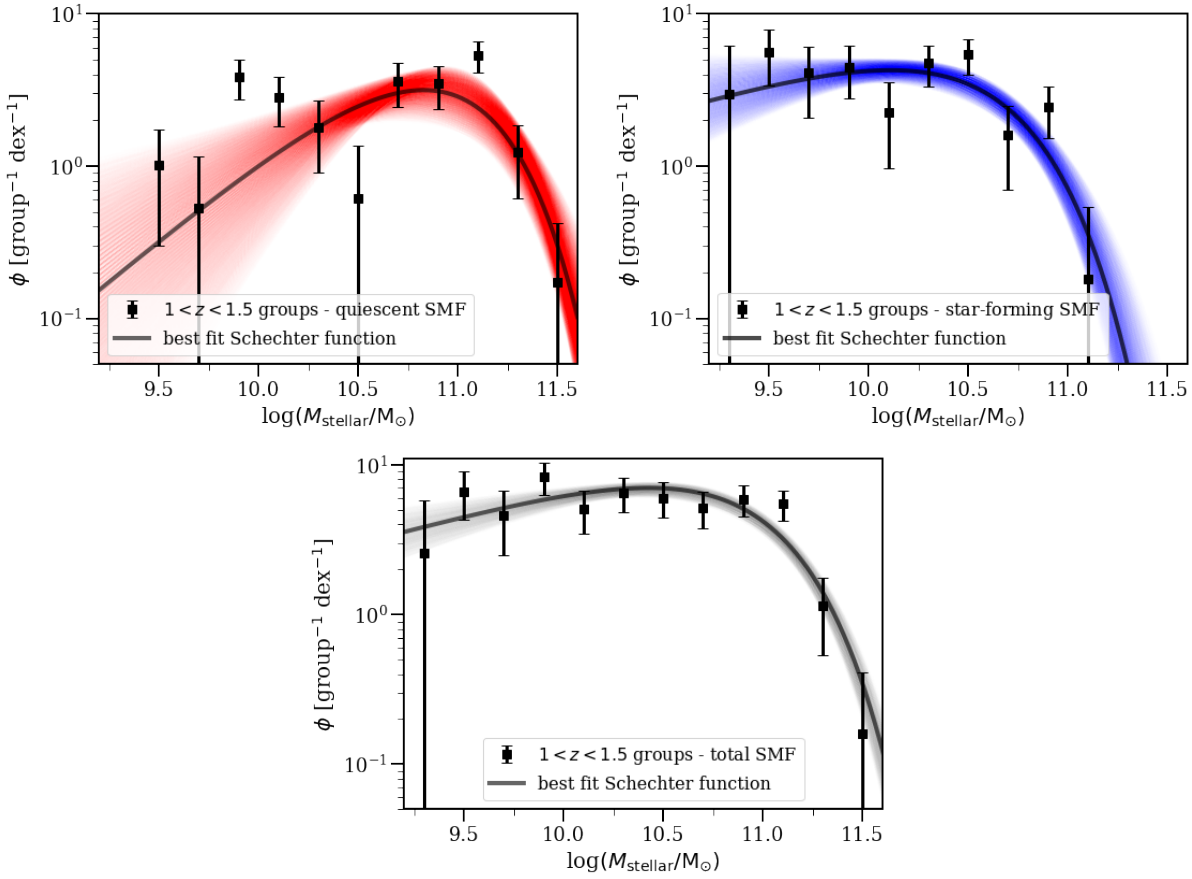

Figure 2.3: Background-subtracted stellar mass function of quiescent (top panel), star-forming (middle), and total (bottom) group galaxies at $1 < z < 1.5$. Overlaid on each plot are the Schechter function fits to the group data (solid line), normalized to match the number of group galaxies per dex (bin size $\Delta \log(M_{\rm stellar}/{\rm M}_\odot) = 0.2$), and with shaded regions indicating the 68% confidence interval on the fit parameters, computed as described in the text. Error bars shown represent the Poisson shot noise.

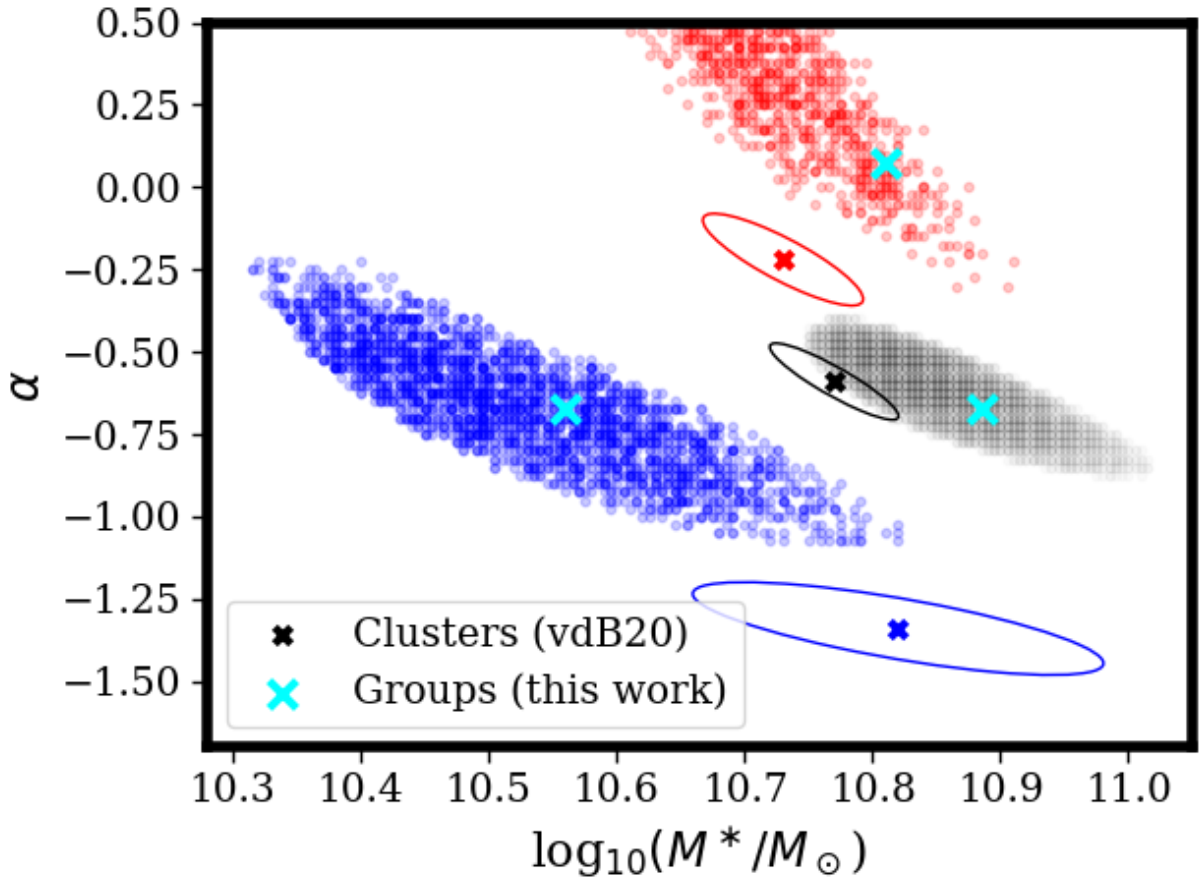

Figure 2.4: We show two of the Schechter function fit parameters for the $1 < z < 1.5$ galaxy group population, for the total sample (black), the quiescent galaxies (red) and the star-forming galaxies (blue). Points represent draws of parameters within the 68 per cent confidence limits of the fits. The cyan crosses indicate the best fit parameters. The α parameter for the quiescent population is effectively unbounded: high values of $\alpha > 2$ provide acceptable fits within 2σ. The crosses with solid ellipses represent the fit parameters and 68 per cent confidence limits for the massive cluster population at the same redshifts, from van der Burg et al. 2020.

Groups

Population	$\log(M^*/\mathrm{M}_\odot)$	α	ϕ^* [group^{-1} dex^{-1}]
Quiescent	$10.8^{+0.2}_{-0.3}$	$0.1^{+0.7}_{-0.4}$	$8.9^{+13.6}_{-6.2}$
Star-forming	$10.6^{+0.2}_{-0.2}$	$-0.7^{+0.5}_{-0.4}$	$8.6^{+24.0}_{-6.7}$
Total	$10.9^{+0.1}_{-0.1}$	$-0.7^{+0.2}_{-0.2}$	$14.0^{+15.3}_{-7.8}$

Field

Population	$\log(M^*/\mathrm{M}_\odot)$	α	ϕ^* [10^{-3} Mpc^{-3} dex^{-1}]
Quiescent	$10.63^{+0.04}_{-0.03}$	$0.06^{+0.07}_{-0.07}$	$1.42^{+0.28}_{-0.24}$
Star-forming	$10.82^{+0.03}_{-0.04}$	$-1.27^{+0.02}_{-0.02}$	$1.31^{+0.33}_{-0.27}$
Total	$10.90^{+0.04}_{-0.04}$	$-1.12^{+0.03}_{-0.03}$	$1.98^{+0.60}_{-0.46}$

Table 2.2: Best fit Schechter function parameters and their 68% confidence limits, for the low-mass halo (group) population and the combined field (UltraVISTA DR1, DR2, and SXDF). The normalization parameter for the group galaxies Schechter fits, ϕ^*, reproduces the curves in Figure 2.3; it has units of number of galaxies per group per dex.

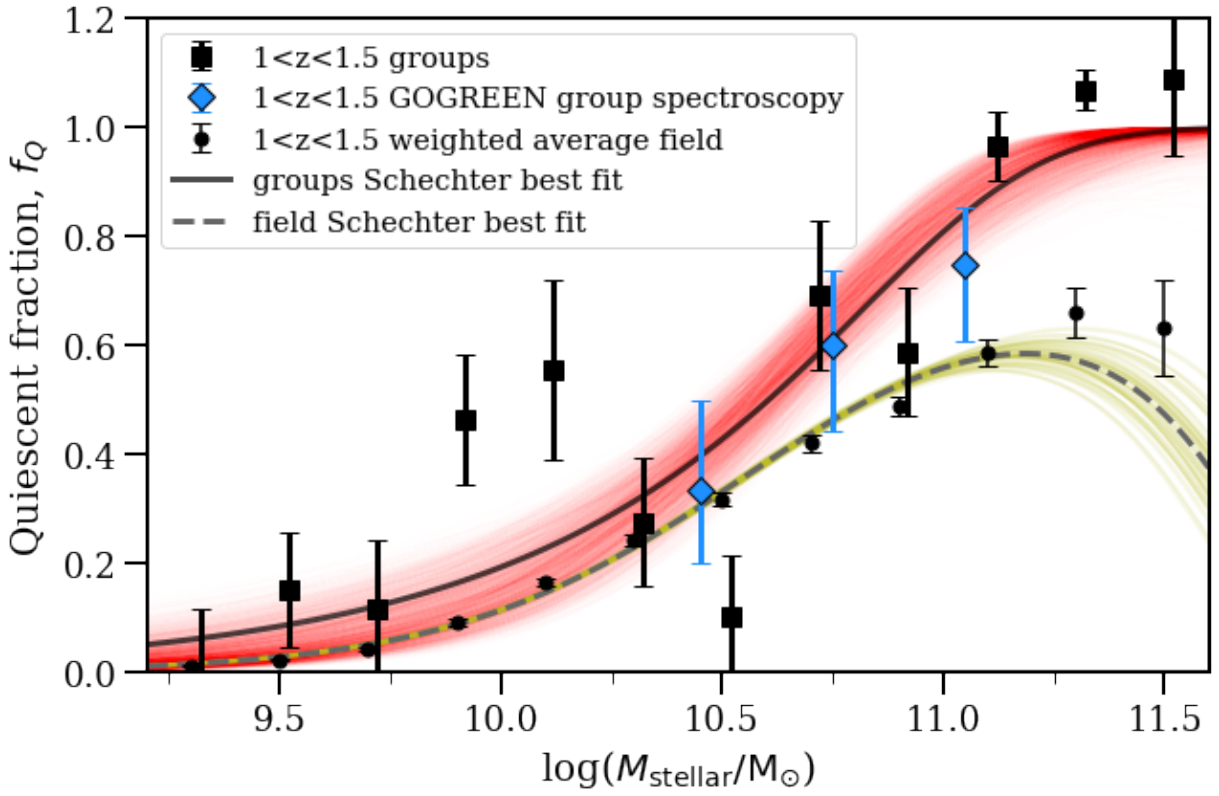

Figure 2.5: Measured quiescent fractions for the group (large black squares, offset slightly horizontally for clarity) and field (small black points). The red shaded region reflects fits drawn from the 68% confidence limits on the fits to the quiescent and star-forming stellar mass functions (constrained to be within the 68% confidence limits on the total stellar mass function fit). The quiescent fraction for the field derived from Schechter fits for the field is also shown, as the black dashed curve with yellow shading showing the 68% confidence limits. Points with $f_Q > 1$ are a result of uncertainty on the statistical background subtraction, which can lead to a formally negative abundance of star-forming galaxies. We also show the quiescent fraction for the spectroscopic group members (blue diamonds), i.e. within $2R_{200c}$.

The parameters M^* and α are compared with the corresponding fits to the GOGREEN massive cluster population from van der Burg et al. (2020), in Figure 2.4. The shape of the total stellar mass function is in excellent agreement with that measured in more massive clusters. Both the quiescent and star forming populations prefer a higher α slope than the clusters, but the Schechter function fit parameter combinations in the two samples are still consistent at the 2σ level. Importantly, we do not observe the excess of low-mass quiescent group members that is seen at low redshifts (Peng et al., 2010) and we rule out a steep ($\alpha < -1$) low-mass slope for this population at the 99 per cent confidence level.

2.3.2 Quiescent fraction and quiescent fraction excess

We use the stellar mass functions in the previous section to compute the quiescent fraction, defined as:

$$f_Q(M) \equiv \frac{N_{\rm Q}(M)}{N_{\rm Q}(M) + N_{\rm SF}(M)}, \tag{2.8}$$

where $N_{\rm Q}$ and $N_{\rm SF}$ are the number of quiescent and star-forming galaxies, respectively, as identified in UVJ colour space (see §2.2.1).

We show f_Q as a function of stellar mass for our group sample in Figure 2.5. Uncertainties on the binned data are computed assuming the quiescent and star-forming stellar mass populations are independent. However, we correctly account for the covariance when deriving the quiescent fraction from the Schechter function fits, which are overlaid as the shaded region. We calculate this by taking random draws from fits within the 68% confidence limits of the quiescent and star-forming populations, and only keep those for which the sum is in agreement with the total SMF within the same 68% confidence. There is a strong dependence on stellar mass, with f_Q increasing from near zero to unity over the full range. For high stellar masses, $M_{\rm stellar} > 10^{11}$ M$_\odot$, f_Q is systematically larger in the group sample than the field. At lower masses the excess is both smaller and statistically not significant. To complement this comparison, we also consider the quiescent fraction for the spectroscopic members of the seven GOGREEN groups (i.e. excluding the two with high dynamical masses, that are excluded from all our analysis). This has the advantage that it does not rely on statistical background subtraction. However, the smaller sample size means we can only consider three stellar mass bins, and we also include all spectroscopic group members within $2R_{200c}$, a larger aperture than for the photometric sample. These spectroscopic members are from GOGREEN and any of the available surveys described in §A.4.1. As shown in the Figure, the quiescent fractions for this spectroscopic subsample are fully consistent with our full group sample.

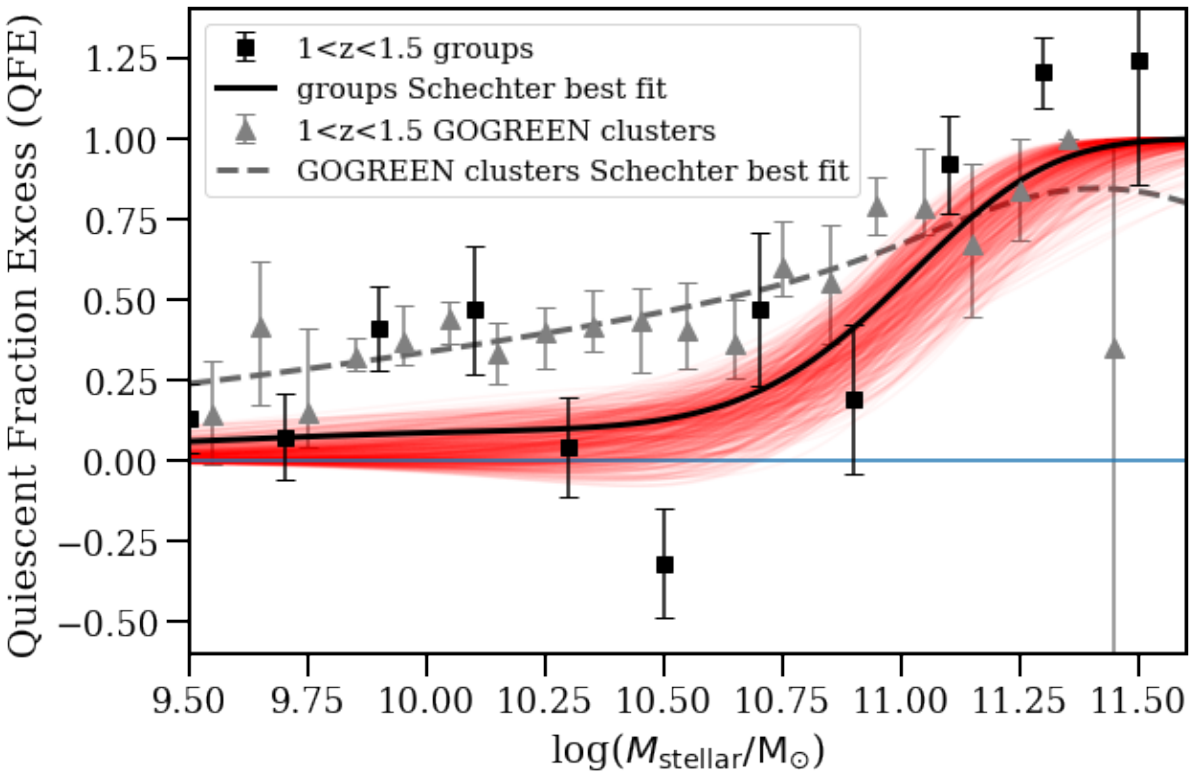

Figure 2.6: Quiescent fraction excess is shown as a function of stellar mass for our $1 < z < 1.5$ galaxy group sample (black squares). The quiescent fraction excess is significantly nonzero only for $M \gtrsim 10^{11}$ $M_\odot$. The red shaded region represents the 68% confidence limits derived from the Schechter function fits to our stellar mass functions. Quiescent fraction excess values (grey triangles) and best fit line (gray dashed line) are also plotted for the GOGREEN $1 < z < 1.5$ clusters in (van der Burg et al., 2020). The clusters show a strong trend in QFE with stellar mass, particularly above $\log(M^*/M_\odot) \approx 10.75$. Additionally, the clusters display significant quiescent fraction excess at lower stellar masses, with a trend in the data consistent with an approximately flat relation for $\log(M_{\rm stellar}/M_\odot) < \log(M^*/M_\odot)$.

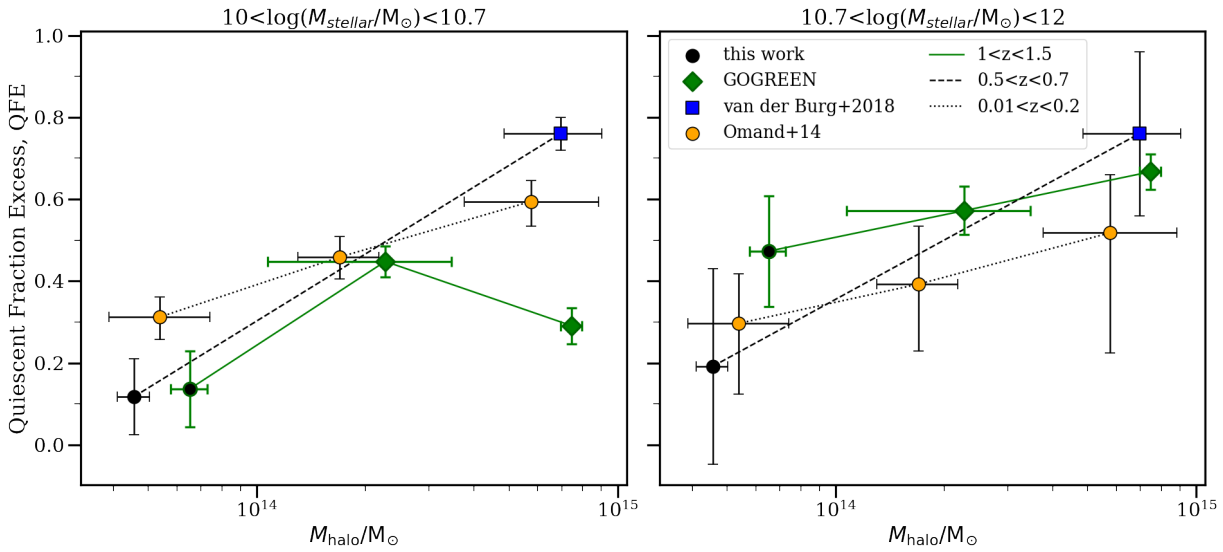

Figure 2.7: Quiescent fraction excess (QFE) shown as a function of halo mass (M_{200c}), $M_{\rm halo}/{\rm M}_\odot$, for two galaxy stellar mass bins, and for samples at three different redshift ranges, as indicated. Our new measurements at $1 < z < 1.5$ are shown as the green points connected by a green solid line, with the groups' point indicated by a black circle rather than a green diamond (GOGREEN clusters). The other samples are described in §2.2.2; we note the black circle for $0.5 < z < 0.7$ is specifically calculated in this work as well. The halo-mass dependence of the QFE has a similar slope at all redshifts and stellar mass bins, of ~ 0.24 (see text for details). See Figure A.8 for a more detailed breakdown of both f_Q and QFE by stellar mass.

To better characterize any difference in f_Q in groups relative to the field, we calculate the quiescent fraction excess (QFE)[5]. This is defined as

$$\mathrm{QFE} \equiv \frac{f_{Q,\mathrm{cluster}} - f_{Q,\mathrm{field}}}{1 - f_{Q,\mathrm{field}}}, \tag{2.9}$$

where $f_{Q,\mathrm{field}}$ and $f_{Q,\mathrm{cluster}}$ are the fractions of quiescent galaxies in the field and cluster, respectively. In a naive infall interpretation, this quantity represents the fraction of galaxies accreted from the field that have been transformed into quiescent galaxies to match the observed group population (e.g. van den Bosch et al., 2008; Peng et al., 2010; Wetzel et al., 2012; Balogh et al., 2016; Bahé et al., 2017). We note that QFE< 0 is a physical solution even in the presence of environmental quenching processes, since the field is defined as the global population, including massive haloes; there will therefore be a halo mass scale below which most "field" galaxies reside in more massive haloes.

The QFE values for our group sample are shown as a function of stellar mass in Figure 2.6. The average QFE is significantly greater than zero and shows an increasing trend with stellar mass, similar to those for the $1 < z < 1.5$ clusters in van der Burg et al. (2020), also shown in Figure 2.6. These results are also similar to those published by Balogh et al. (2016), for groups at a slightly lower redshift $0.8 < z < 1$, though we find a larger QFE at the highest stellar masses. Interestingly, both groups and clusters are consistent with a mass-independent QFE below M^* (QFE ≈ 0 for groups, QFE $\approx 0.35 - 0.40$ for clusters) and a significant jump in QFE towards QFE ≈ 1 above M^*.

2.3.3 The halo mass dependence of galaxy quenching

We now present QFE as a function of halo mass and stellar mass, in Figure 2.7. The group and cluster samples at each redshift are described in §2.2.2, as are the definitions of the field samples. Motivated by the results in Figure 2.6 we show the results in two stellar mass bins, below and above the jump in QFE. Our conclusions are unchanged if we use a smaller binning, which we demonstrate in Appendix A.5.

In general we find the QFE increases with increasing stellar mass and halo mass, with at most modest redshift evolution when those parameters are fixed. Most notably, the

[5]We choose the terminology, QFE, for consistency with recent prior works (Wetzel et al., 2012; Bahé et al., 2017; van der Burg et al., 2020) and a more intuitive meaning than a variety of other synonymous terms used in the literature. Other terms synonymous with QFE used in the literature include "transition fraction" (van den Bosch et al., 2008), "conversion fraction" (Balogh et al., 2016; Fossati et al., 2017), and "environmental quenching efficiency" (Peng et al., 2010; Wetzel et al., 2015; Nantais et al., 2017; van der Burg et al., 2018).

dependence of QFE on the logarithm of halo mass appears to be similar in all stellar mass and redshift bins. To further quantify this, we fit a linear regression model to QFE as a function of $M_{\rm halo}$ for all the data, with a single slope but different intercepts for each redshift and stellar mass bin. We find a slope of $m = 0.24 \pm 0.04$ with a reduced χ^2 of ~ 1.06 indicating an acceptable fit. The points that appear most discrepant with this simple scaling are for the highest halo masses in the stellar mass range $10^{10} < M_{\rm stellar}/{\rm M}_{\odot} < 10^{10.7}$. The QFE for the GOGREEN data are actually lower than that measured at intermediate halo masses at the same redshift, though they are consistent at the 1.6σ level as determined by a two-tailed split-Gaussian hypothesis test. Though this appears to differ from the simple scaling derived above, we note that this approximate independence of QFE on halo masses above $\sim 2 \times 10^{14} M_{\rm halo}$ is in fact consistent with what we observe at other redshift and stellar mass bins, and also with the simulation predictions discussed below, in §2.4.1. Although there are only two clusters contributing to this bin, sample variance is unlikely to be large enough to explain the large difference between this measurement and the measurement of similarly massive clusters at lower redshift, given the observed homogeneity of cluster systems (e.g. Trudeau et al., 2020). On the other hand, the QFE observed in the massive Planck-selected clusters at $0.5 < z < 0.7$ is significantly higher than even the $z = 0$ sample at the same mass, and implies a steeper logarithmic slope than we fit for the sample as a whole. It is possible that this reflects a bias resulting from the SZ-selection, or a difference in the field samples near those clusters, but we do not have a good explanation for the result. It would be useful to include more cluster samples at intermediate redshift in a future analysis.

2.4 Discussion

It is well known that the quiescent fraction of galaxies in clusters shows a general decrease with increasing redshift (e.g. Butcher & Oemler, 1984; Haines et al., 2013) and quiescent populations of galaxies are now well studied for clusters at $z > 1$ (e.g. Brodwin et al., 2013; Nantais et al., 2016; Lee-Brown et al., 2017; Kawinwanichakij et al., 2017; Foltz et al., 2018; Strazzullo et al., 2019; Trudeau et al., 2020; van der Burg et al., 2020). In this work we have used the wide halo mass range of the GOGREEN and COSMOS/SXDF cluster catalogues to demonstrate (Figure 2.7) that QFE correlates (increases) with both stellar mass and halo mass at $1 < z < 1.5$.

A compilation of QFE values (integrated over a broad stellar mass range) for low halo mass "groups" at various redshifts was presented by Nantais et al. (2016). We show an updated version of their figure including our background-subtracted group measurements in

Figure 2.8, for all galaxies with $M_{\rm stellar} > 10^{10}$ M$_\odot$. Overall, our work is broadly consistent with the published literature: even within low-mass haloes the galaxy population exhibits enhanced quenching relative to the field. A possible redshift trend of QFE with redshift may be apparent in this compilation. However, we resist drawing any strong conclusions from a further quantitative comparison, given significant methodological differences between studies. Moreover, the stellar mass dependence of QFE complicates any physical interpretation of these integrated values.

Our results build on the earlier work of van der Burg et al. (2020), who measured the stellar mass function of the GOGREEN cluster sample and found that, while the fraction of quiescent galaxies is much higher in the clusters than the field, the shape of the stellar mass function for quiescent galaxies is identical in both environments. The same is true for the star-forming population. This is a puzzling result and it indicates that, unlike at low redshift, environmental quenching is *not* separable from the stellar mass dependence. This is reflected in the fact that the QFE strongly increases with increasing stellar mass, from $\sim 30\%$ at $\sim 10^{10}$ M$_\odot$ to $\sim 80\%$ at $> 10^{11}$ M$_\odot$, in contrast with studies in the local Universe. A possible explanation for this, as described in van der Burg et al. (2020), is that the quenching mechanism in these $z > 1$ clusters is an accelerated version of the same process affecting field galaxies.

However, this interpretation would naively lead to the prediction that cluster galaxies should be substantially older than field galaxies, which contradicts the findings of Webb et al. (2020). In that work, SFHs were measured for 331 quiescent galaxies in the same GOGREEN cluster and field samples, using the PROSPECTOR Bayesian inference code (Leja et al., 2017b; Johnson et al., 2019a) to fit the photometric and spectroscopic observations[6]. They find that galaxies in clusters in the stellar mass range $10^{10} - 10^{11.8}$ M$_\odot$ are older than field galaxies, but only by $\lesssim 0.3$ Gyr.

As dark matter haloes grow, it is unclear exactly how or when environmental quenching processes become important (e.g. Bahé et al., 2013). In particular, if environmental processes are important in low-mass haloes, the quenching of star formation may take place long before galaxies are finally accreted onto massive clusters. In the following two subsections, we first explore how well hydrodynamic simulations reproduce our observations and then we use what we have learned about the halo mass dependence of the quiescent fraction at $1 < z < 1.5$ to explore the extent to which pre-processing could reconcile the van der Burg et al. (2020) and Webb et al. (2020) results.

[6]The full posteriors of Webb et al. (2020)'s PROSPECTOR fits are available from the Canadian Advanced Network for Astronomical Research (CANFAR), at `www.canfar.net/storage/list/AstroDataCitationDOI/CISTI.CANFAR/20.0009/data`; DOI:10.11570/20.0009.

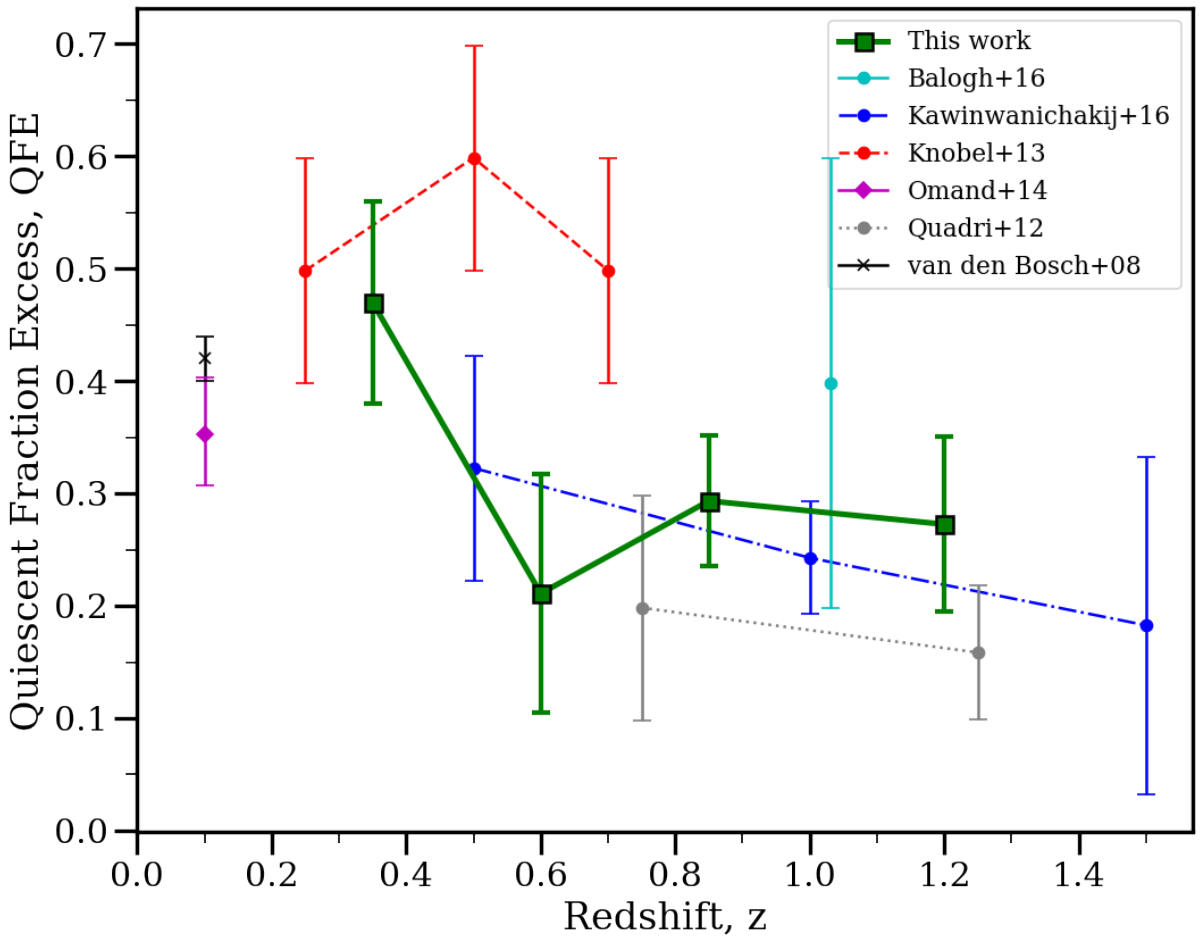

Figure 2.8: Compilation of quiescent fraction excess measurements as a function of redshift for groups of galaxies, adapted from Nantais et al. (2016). Lines connect points from the same study. Our sample (green squares) include all galaxies with $M_{\rm stellar} > 10^{10}$ $M_{\odot}$, the 95% stellar mass completeness limit at $z = 1.5$. Overall the compilation appears to indicate a gradual redshift evolution of QFE. We caution, however, that the different analyses shown here are not fully consistent in their methodology or sample selections.

2.4.1 Comparison with BAHAMAS hydrodynamic simulation predictions

We begin considering the physical implications of our result by determining the extent to which these correlations are naturally predicted by hydrodynamic simulations. For this we use the BAHAMAS cluster simulations (McCarthy et al., 2017, 2018), which were run with the standard Planck 2013 cosmology (Ade et al., 2014), using $2{\times}1024^3$ particles in a large cosmological volume, 400 Mpc h^{-1} on a side. Dark matter and (initial) baryon particles masses of $\approx 4.44 \times 10^9\ h^{-1}\ \mathrm{M}_\odot$ and $8.11 \times 10^8\ h^{-1}\ \mathrm{M}_\odot$ are used, respectively. These simulations implement various subgrid physics models, including metal-dependent radiative cooling in the presence of a uniform photoionising UV/X-ray background, star formation stellar evolution and chemical enrichment, and stellar and AGN feedback (see Schaye et al., 2010, and references therein for a detailed description of the subgrid implementations). Consistent with our work and compiled literature results, a Chabrier (2003) IMF is assumed. The parameters of these prescriptions were adjusted to reproduce the observed Kennicutt-Schmidt law, the observed galaxy stellar mass function (GSMF), and the amplitude of group/cluster gas mass fraction–halo mass relation at $z \sim 0$. Thus, these simulations are distinguished from some others by the fact that they are deliberately calibrated to ensure the correct total baryon content in haloes. This is important when considering environmental effects on group scales where, for example, hydrodynamic interactions with the hot gas may be important.

We select all BAHAMAS groups with halo masses $\log(M_{200c}/\mathrm{M}_\odot) > 13.2$ (no explicit upper halo mass limit). The group selection is based on a Friends-of-Friends group-finding algorithm applied to two separate snapshots of the BAHAMAS simulation, at $z = 0$ and $z = 1.25$, respectively. For each identified group, all galaxies within R_{200c} (in 3D space) are considered to be group members. For each group, the field sample is taken to be all galaxies outside $2.5R_{200c}$. To separate quiescent from star-forming galaxies, we use the sSFR threshold from Franx et al. (2008): $\mathrm{sSFR} > 0.3/t_{H(z)}$, where $t_{H(z)}$ is the Hubble time at a given redshift. At $z \sim 1.25$ $t_{H(z)} \sim 5$ Gyr, so this corresponds to $\mathrm{sSFR} > 6{\times}10^{-11}$ yr^{-1}. Although this is different from the UVJ selection made in the data, we have confirmed that the qualitative trends of f_Q and QFE are stable for large variations in the choice of star-forming threshold – a multiplicative factor of 2-3 to the sSFR cut does not qualitatively change our conclusions.

We focus our attention primarily on the QFE trends with halo mass in BAHAMAS, shown in Figure 2.9 for the same stellar mass bins as in Figure 2.6. The quiescent fractions themselves, and an alternative stellar mass binning, are provided in Appendix A.5. We first consider the high stellar mass sample, in the right panel. The BAHAMAS predictions

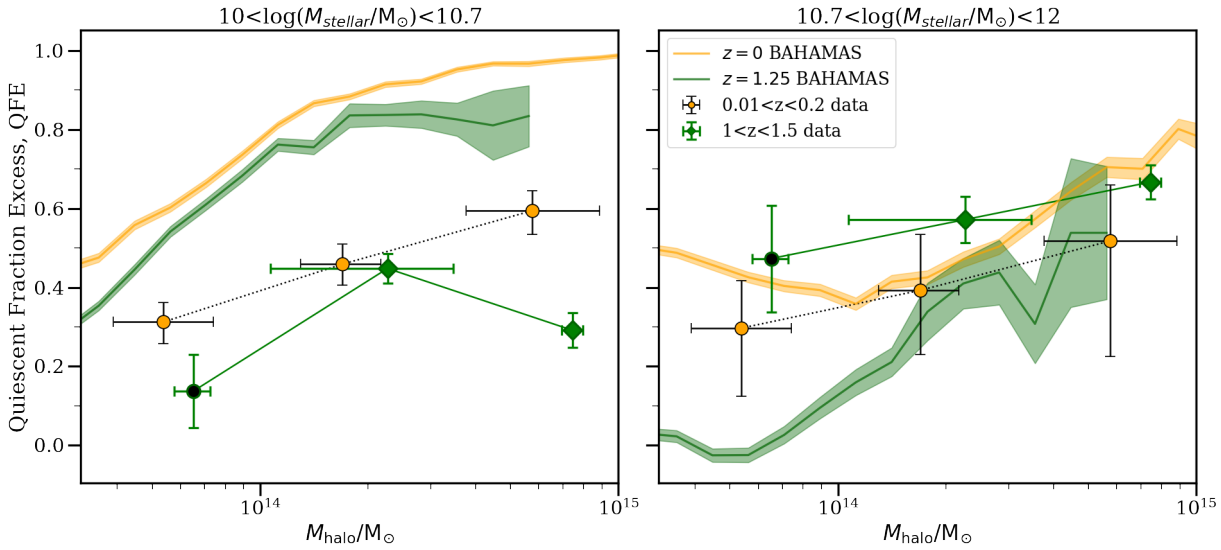

Figure 2.9: We show the quiescent fraction excess from the BAHAMAS hydrodynamic simulation as a function of stellar and halo mass, $M_{\rm halo}/{\rm M}_\odot$ at two redshift snapshots as indicated. The corresponding data from Figure 2.7 are reproduced here for comparison. In the simulations, both f_Q and QFE decrease with increasing stellar mass, in stark contrast with the data. However, the correlation with halo mass and redshift is qualitatively similar to the trends observed in the data. See Figure A.9 for a more detailed breakdown of both f_Q and QFE by stellar mass.

at $z = 0$ are in quite good agreement with the data, reproducing both the absolute value of the QFE and its dependence on halo mass. The simulations predict that this halo mass dependence becomes significantly steeper at $z \sim 1$, in contrast with the observations. There is reasonable agreement at high halo masses ($M_{\rm halo} > 10^{14}$ M$_\odot$), though the modest redshift evolution is in the opposite sense to the observations. On group scales, however, the models predict no significant QFE at $z \sim 1$, significantly below our measured QFE $= 0.48 \pm 0.15$.

Turning now to the lower stellar mass bin, $10 < \log(M_{\rm stellar}/{\rm M}_\odot) < 10.7$, the model generally predicts a steep increase in QFE with halo mass, before flattening around $M_{\rm halo} \sim 2 \times 10^{14}$ M$_\odot$. The overall shape of the trend – steep then flat – appears similar to our data, just shifted upwards. Over the whole mass range, the dependence of QFE on halo mass has a logarithmic slope of ~ 0.3 at both redshifts (i.e. a factor of 10 increase in halo mass results in an increase of ~ 0.3 in QFE), remarkably similar to our measurement in §2.3.3. The sense and magnitude of the redshift evolution is also in good agreement with the observations. Despite these successes, the absolute value of the QFE itself is too high, for all halo masses at both $z = 0$ and $z = 1.25$. This reflects the difficulties faced by many simulations and models, and is likely due to an incomplete understanding of feedback (Kukstas et al., 2023). The result is also sensitive to choices in how quiescent galaxies are defined, and the aperture within which star formation rates and masses are measured in the simulations (e.g. Furlong et al., 2015; Donnari et al., 2019, 2021). The fact that the simulations predict a halo mass dependence of QFE that is similar to what we observe over a wide range in redshift and halo mass is encouraging, and suggests that they may be correctly capturing the relevant physics associated with the impact of large scale structure growth on galaxy evolution, even if the feedback prescriptions themselves are not sufficiently accurate to reproduce the observed dependence of QFE on stellar mass.

2.4.2 Toy models

As described earlier, simple toy models of galaxy clusters at $1 < z < 1.5$, in which environmental quenching occurs after accretion onto the main progenitor, are unable to simultaneously match the observed quiescent fractions and relative ages of quiescent galaxies (van der Burg et al., 2020; Webb et al., 2020). In particular, van der Burg et al. (2020) note that the stellar mass-dependence of environmental quenching needs to be similar to that of the quenching process in the general field to result in the observed SMFs, and they propose that clusters experience an early accelerated form of that same phenomenon during the protocluster phase. However, Webb et al. (2020) find mass-weighted ages in cluster galaxies that are only slightly older than field galaxies. Webb et al. (2020) then use

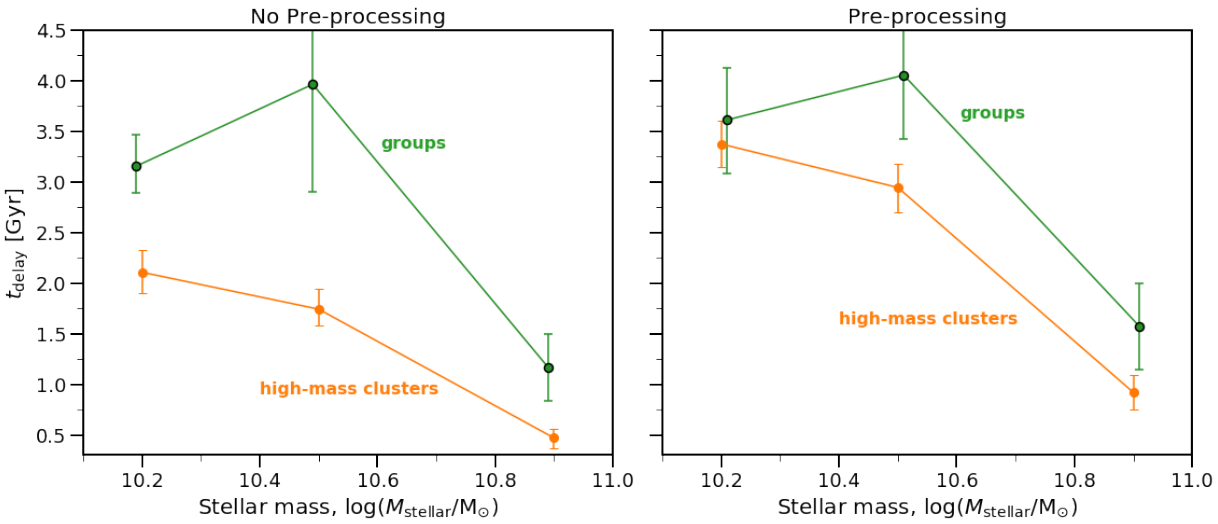

Figure 2.10: The time delay parameter values for our pre-processing and no pre-processing toy models are plotted as a function of stellar mass (points with error bars) for both groups (green) and clusters (orange). These time delays are directly constrained by the group/cluster quiescent fractions in each stellar mass bin; the uncertainties are a result of uncertainties on the observed quiescent fractions (i.e. propagated through the model).

a simple infall model to demonstrate that neither a simple head-start to formation time for the cluster galaxies nor a simple quenching time delay (i.e. time since infall into a cluster) alone can explain both the enhanced quiescent fraction and very similar mass-weighted ages (MWAs) for the cluster and field populations.

Our results, which show how galaxy populations correlate with environment in haloes with masses well below that of massive clusters, suggest that "pre-processing" is likely to be important. The BAHAMAS simulations include a more complete treatment of halo growth and hydrodynamic processes, including pre-processing in a physically motivated way. The fact that those simulations predict a similar trend of QFE with halo mass to that observed is encouraging, and suggests that the failures of the toy models discussed above may lie in their simplified definitions of accretion time. We aim in this section to fit and contrast two toy models, one with pre-processing and one without, using the quiescent fraction excess in a range of halo masses at $1 < z < 1.5$. We can then use these models to predict group/cluster galaxies' average stellar mass-weighted ages and compare to values derived from GOGREEN observations.

Toy model descriptions

The infall-based quenching model we use here is the same as that in Webb et al. (2020), but with changes to the accretion history. More explicitly, we use the Schreiber et al. (2015) SFR evolution for star-forming galaxies. When galaxies are quenched their SF is immediately truncated. We track the number of star-forming and quiescent galaxies from $z = 10$ to $z = 1.2$ and then compare galaxies which have stellar masses between 10^{10}–10^{12} $M_{\odot}$ at $z = 1.2$. Galaxies that are self-quenched are modelled using the self-quenching efficiency proposed by Peng et al. (2010), i.e.: the quenching probability is $\propto \mathrm{SFR}/M_{\mathrm{stellar}}$, using the SFR for a galaxy of stellar mass M_{stellar}. We also assume that the shape of star-forming SMFs in our model do not differ between field and clusters, as found by van der Burg et al. (2020). Finally, it is assumed that all galaxies can undergo satellite quenching, with star-forming galaxies in clusters completely quenching after a t_{delay} amount of time has elapsed from the time of first "infall", which we will define below.

For this quenching model there are therefore two parameters. The self-quenching efficiency normalization is set by reproducing the observationally measured field quiescent fraction (i.e. with t_{delay} fixed to $t_{\mathrm{delay}} = 0$). The t_{delay} parameter is then iteratively fit to reproduce the fraction of quiescent galaxies in a given cluster (see specifics described further in §2.4.2). As this represents quenching in excess of the field population, the delay time corresponds most directly to the QFE. If $t_{\mathrm{delay}} = 0$, all cluster galaxies would be quenched; increasing the parameter reduces the QFE as fewer galaxies have been in the cluster long enough to quench. Finally, we neglect mergers, which are included in van der Burg et al. (2020), for simplicity.

To explore whether simple pre-processing alleviates tension between quiescent fraction and ages, we consider two extreme definitions of galaxy "infall time". The first defines infall as the first time a central galaxy becomes a satellite, using the models of McGee et al. (2009) (which were applied to N-body dark matter simulations) as published in Balogh et al. (2016). In their findings, this amounts to a roughly constant accretion rate, with clusters starting their accretion $\sim$ 0.5 Gyr before groups. For the other extreme we assume galaxies are only accreted once they cross the virial radius of the most massive progenitor halo, using the halo mass accretion rate in Bouché et al. (2010). We assume that the number of infalling galaxies in a given timestep is proportional to the mass accreted in a given timestep. We will refer to these two models as the "pre-processing model" and "no pre-processing model", respectively.

For simplicity, we only compare our "groups" sample (lowest halo-mass bin) with the high-mass clusters (highest halo mass bin) at $1 < z < 1.5$ presented in our results section (see §2.3.3).

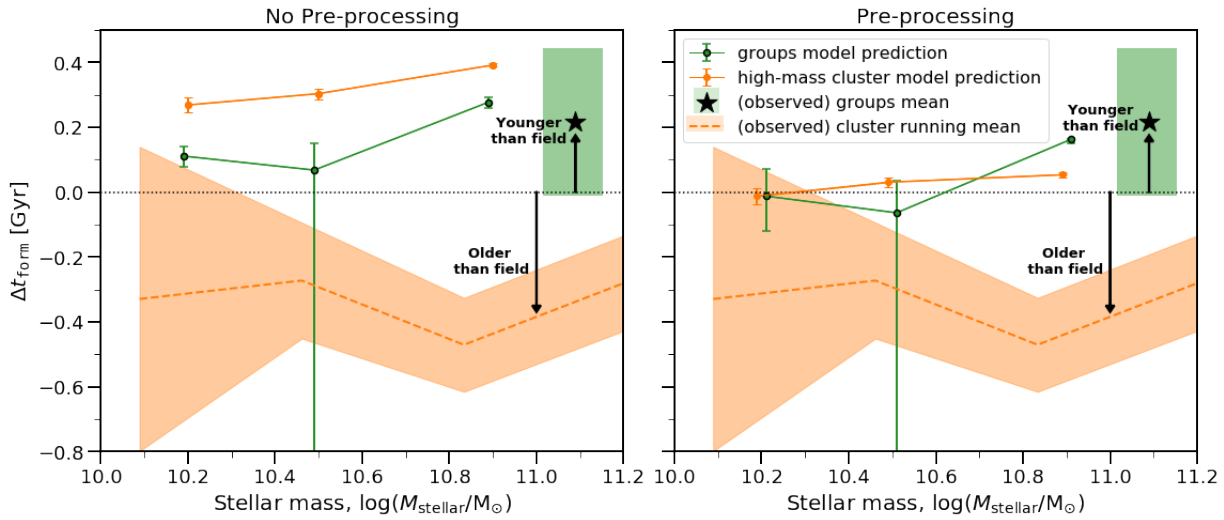

Figure 2.11: Using our fit $t_{\rm delay}$ values (Figure 2.10), we predict the difference in average formation time between the groups/high-mass clusters and the field. For a given galaxy in a given sample, $t_{\rm form}$ is defined as $t_{\rm obs}-$MWA, where MWA is the mass-weighted age from the stellar population synthesis modelling of quiescent galaxies in the GOGREEN spectroscopic sample (Webb et al., 2020). Model prediction values are shown with simple points with errorbars and connecting lines for the groups and clusters in green and orange, respectively. Observationally-derived average values are also shown, with the high-mass clusters running average shown as the dashed orange line (shaded regions for the bootstrapped standard deviation on the mean) and the groups are shown as a single point (black star) with green shaded region. The horizontal width of the green groups shaded region is the bootstrapped standard deviation on the mean stellar mass. Quiescent galaxies in groups are younger than those in clusters, ruling out the predictions of our simple model without pre-processing. Although the time delay exhibits a strong dependence on stellar mass, the dependence of mean MWA on stellar mass in our models is weak. The MWA has a significant halo mass dependence only for the no pre-processing model. For a plot showing the $t_{\rm obs}-$MWA values for individual galaxies in all samples, see Figure A.7.

Toy model results

We start by considering the stellar mass dependence of the $t_{\rm delay}$ parameter, in Figure 2.10. This parameter is effectively calculated from the observed quiescent fraction excess (see §2.4.2), which has a strong stellar mass trend; thus, $t_{\rm delay}$ similarly shows a strong trend with stellar mass, such that $t_{\rm delay}$ decreases with increasing stellar mass in both models. As well, we observe the expected difference between the pre-processing and no pre-processing infall models. Pre-processing models require a longer $t_{\rm delay}$ to reproduce the same quiescent fraction, given that first accretion happens earlier. The values of $t_{\rm delay}$ that we find are broadly consistent with similar work at these redshifts (e.g. Balogh et al., 2016), and with measurements at lower redshift (e.g. Wetzel et al., 2013) assuming they evolve proportionally to the dynamical time. As we are primarily interested in the trends with stellar and halo mass, we do not comment further on the absolute value of this parameter.

Most relevant to our discussion here, we find that the halo mass dependence of $t_{\rm delay}$ depends on the accretion model. In the no pre-processing case there is a significant dependence on halo mass. Shorter delay times are needed in higher mass clusters, to reproduce our observations that the quiescent fractions are higher in those systems. In the pre-processing model, galaxies accreted into a cluster effectively get a head-start, and this largely accounts for the difference in quiescent fraction. Thus, we find that in a pre-processing model, the observed dependence of QFE on halo mass (at fixed stellar mass) can be explained with a $t_{\rm delay}$ that has at most a weak dependence on halo mass. In this case the variation in QFE with halo mass derives primarily from the fact that the accretion time distribution is a function of halo mass (see e.g. De Lucia et al. (2012) for further discussion of this).

We now try to break this degeneracy by considering the mass-weighted ages of the quiescent galaxies in the two models. To show this, we define a formation time, $t_{\rm form} = t_{\rm obs} - {\rm MWA}$, which is the difference between the age of the Universe (at a given galaxy's observed redshift) and the determined MWA value. This value reflects how long after the Big Bang it took until the mass-weighted bulk of stars had formed. We show our MWA predictions in the form of the difference in $t_{\rm form}$ between groups/clusters and the field in Figure 2.11. The no pre-processing model predicts $t_{\rm form}$ should increase (ie: MWA decreases) with increasing halo mass, by about $\sim 150 - 200$ Myr between the lowest and highest halo masses shown here. In contrast, the pre-processing model predicts no significant dependence of MWA on halo mass.

We now compare these predictions directly with observed measurements[7] of MWA from

[7]Specifically, here we show the medians of the posteriors.

Webb et al. (2020), shown in Figure 2.11. The running mean $t_{\rm form}$ for the highest halo mass sample ("high-mass clusters") is shown; for the group sample, which includes only 15 quiescent galaxies, we show the mean and standard deviation (green shaded region) of the whole stellar mass range ($10 < \log(M_{\rm stellar}/{\rm M}_\odot) < 12$). A more detailed version of this Figure, showing age measurements for individual galaxies in all samples, is given in Appendix A.4.4.

The no pre-processing model predicts that quiescent galaxies in groups should be ~ 200 Myr *older* than galaxies in clusters. Although our sample of group galaxies is small, it is inconsistent with this prediction: if anything, the quiescent group galaxies are *younger* than their counterparts in more massive systems. The data are more consistent with the pre-processing model. In this case, dependence on halo mass is weak, but in the observed direction for the highest stellar mass bin we consider, which also corresponds most closely to the mean stellar mass of our data.

In summary, including pre-processing does a reasonable job of explaining the halo mass dependence of quiescent galaxy ages, with a $t_{\rm delay}$ parameter that is nearly independent of halo mass. This is broadly consistent with a picture where the environmental quenching is caused by the same physical mechanism in groups and clusters. The data suggest, however, that quiescent galaxies in clusters may be even older than can be explained in the pre-processing model. A likely explanation for this, since halos in a large scale overdensity form before those of the same mass in a low density environment, would be if galaxies in rich proto-cluster environments undergo earlier quenching than primordial environments for group galaxies, as discussed in van der Burg et al. (2020) and Webb et al. (2020). It seems increasingly likely that a significant portion of the GOGREEN cluster galaxy population was subject to an accelerated quenching mechanism at $z \sim 3-4$. This is additionally compatible with recent high redshift work showing that quiescent galaxies exist at redshifts as high as e.g. $z \sim 3-5$ (Valentino et al., 2020; Forrest et al., 2020).

2.5 Conclusions

We use photometric redshifts and statistical background subtraction to measure stellar mass functions of galaxies in low mass haloes at $1 < z < 1.5$ ("groups"). These groups are selected from COSMOS and SXDF surveys, based on X-ray and sparse spectroscopy. We compute the quiescent fraction (f_Q) and quiescent fraction excess (QFE) for these systems, as a function of stellar mass. The result is then compared with higher mass clusters at $1 < z < 1.5$ from the GOGREEN survey (Balogh et al., 2021), and a compilation of lower

redshift samples at $0 < z < 0.2$ and $0.5 < z < 0.7$ that span a similar range of halo mass as our $1 < z < 1.5$ samples.

Observationally, we find:

- Excess quenching in $1 < z < 1.5$ groups relative to the field, with an overall QFE of $\sim 20\%$ for galaxies with $\log(M_{\rm stellar}/{\rm M}_\odot) > 10$.
- Unlike at low redshift, environmental quenching is *not* separable from the stellar mass dependence. This can be seen as an increase of the QFE in groups, from $\sim 10\%$ below M^* to $\sim 100\%$ above M^*. A similar trend is present in more massive clusters, where the QFE increases from $\sim 40\%$ to $\sim 85\%$.
- When controlling for stellar mass, both f_Q and QFE correlate (increase) with halo mass. Observations at all redshifts and stellar masses are consistent with a single logarithmic slope of ${\rm d(QFE)}/{\rm d}\log(M_{\rm halo}) \sim 0.24 \pm 0.04$.

In our discussion, we compare to the BAHAMAS hydrodynamical simulation and also with toy models in which galaxies quench star formation upon infall, after some time delay. For the latter we contrast a pre-processing model, where galaxies begin this quenching time delay upon infall into any larger halo, and a no pre-processing model in which the time delay only begins when the galaxy is accreted into the main progenitor.

From this analysis, we find:

- The BAHAMAS hydrodynamic simulation reproduces the trend of quiescent fraction excess with halo mass seen in the data. Specifically they show a steep increase in QFE with halo mass, which then flattens to a near constant value for halo masses $M_{\rm halo} \gtrsim 2{\times}10^{14}\ {\rm M}_\odot$. When fit with a straight line, the average trend is ${\rm d(QFE)}/{\rm d}\log(M_{\rm halo}) \sim 0.30$, which compares well with the observed $0.24{\pm}0.04$. This suggests the simulation may be capturing the relevant physics behind the role of large scale structure growth on galaxy evolution.
- Both the quiescent fraction and the quiescent fraction excess predicted by BAHAMAS decreases with increasing stellar mass, opposite to what is observed. This probably indicates an incomplete model of subgrid feedback and/or star formation at galaxy scales in the BAHAMAS simulation.
- From the toy models, we find the time delay until quenching begins must depend on stellar mass, reflecting the strong dependence of group/cluster quiescent fractions on stellar mass. In the absence of pre-processing, this delay time also has a strong dependence on halo mass, decreasing with increasing mass.

- We find pre-processing reduces the discrepancy with the observed halo mass dependence of quiescent galaxy mass-weighted ages. Specifically, assuming quenching occurs when a galaxy first becomes a satellite increases the average age of quiescent cluster galaxies, relative to a model without pre-processing. However, the data suggest that quiescent galaxies in clusters at $1 < z < 1.5$ may still be older than can be explained in this simple pre-processing model.

These observations further demonstrate that galaxy evolution depends on more than just stellar mass, in a nontrivial way that is still not fully captured by models. The environment, at least through the host halo mass, plays an important role at all redshifts $z < 1.5$. This effect, however, is not separable from the dependence on stellar mass. Moreover, it is important even in low-mass haloes at $z \sim 1$, and thus likely not solely due to extreme physics like ram pressure stripping of cold gas reservoirs. The most natural physical mechanism that is expected to operate on all scales probed in this work is the shutoff of cosmological accretion onto satellites, and the subsequent overconsumption of gas reservoirs (e.g. McGee et al., 2014). This physics should be included with reasonable fidelity in hydrodynamic simulations, and it is encouraging that the BAHAMAS simulations are able to reproduce the observed halo-mass dependence, even while there remain problems on small-scales. Forthcoming, homogeneous surveys with large telescopes – particularly those with highly multiplexed spectroscopy – will make these statements much more precise and useful for constraining models. Observations of high redshift protoclusters, with JWST and other facilities, will determine whether or not there are additional effects that accelerate star formation quenching in these environments, as hinted at indirectly by our data.

Chapter 3

Constraining quenching timescales in galaxy clusters by forward-modelling stellar ages and quiescent fractions in projected phase space

3.1 Introduction

Galaxies have long been known to exhibit a bimodality in their star formation rates (SFRs) such that the population of bluer galaxies with higher SFRs make up the 'star-forming main sequence' and the redder galaxies with lower SFRs forming the quiescent 'red sequence' (e.g. Bell et al., 2004a; Brinchmann et al., 2004; Brammer et al., 2011; Muzzin et al., 2012). The quiescent fraction increases strongly with increasing galaxy stellar mass, likely due to some internal ('mass') quenching process, as well as increasing with the density of its surrounding environment (e.g. Cooper et al., 2007; Peng et al., 2010), due to some environmental quenching process(es). Despite significant exploration of quenching trends and their statistical relation to internal and environmental properties, it remains a matter of debate which quenching mechanisms are responsible for the bulk of quenching in the densest environments across cosmic time, particularly galaxy clusters (Naab & Ostriker, 2017; Wechsler & Tinker, 2018).

Galaxies falling into groups or clusters may have their star formation affected by a number of physical processes. Initially, upon infall into a cluster, a galaxy may experience enhanced star formation, due to ram pressure compressing and triggering collapse of a

galaxies' cold gas reservoir (see e.g. Jaffé et al., 2018; Vulcani et al., 2018; Roberts et al., 2021). If strong enough, ram pressure can strip the cold gas in star-forming galaxies, triggering relatively abrupt quenching (normally < 1 Gyr is assumed to be indicative of this scenario, see e.g. Boselli et al., 2016; Fossati et al., 2018). Alternatively, numerous studies support stripping of just the hot halo gas could be leading to a 'strangulation' scenario, where a star-forming galaxy continues forming stars using its cold gas reservoir, but since its cold gas supply is not replenished, the galaxy then quenches once it runs out of cold gas (such as argued by Larson et al., 1980; Balogh et al., 2000; Bekki et al., 2002; Boselli & Gavazzi, 2006; McGee et al., 2009; Taranu et al., 2014; Paccagnella et al., 2016). Such a scenario is often simply parameterized by a 'delayed-then-rapid' quenching prescription (Wetzel et al., 2013), with a range of time until quenching (after 'infall' – definitions for which vary) of $2 - 7$ Gyr preferred by observations at $z = 0$ (see also e.g. De Lucia et al., 2012; Moster et al., 2018; Rhee et al., 2020; Oman et al., 2021, among numerous others). Other effects, like harassment from galaxies passing near each other, as well as mergers, can affect the star formation in a galaxy (Boselli & Gavazzi, 2006). Complicating this picture is the 'pre-processing' of galaxies in host haloes of a lower mass groups prior to their infall into a cluster, which can additionally enhance the quiescent fraction in clusters compared to accreting isolated galaxies from the field. Although widely recognized as playing an important role in explaining the environmental dependence of star formation, work remains in characterizing the significance of pre-processing for quenching, where exactly it occurs, and how it evolves with redshift (Fujita, 2004; McGee et al., 2009; De Lucia et al., 2012; Webb et al., 2020). It is at least clear that quenching is significantly enhanced relative to the field at least up to $z \sim 1.5$ in rich galaxy groups (Gerke et al., 2007; Wetzel et al., 2012; Mok et al., 2013; Reeves et al., 2021) and clusters (van der Burg et al., 2018; Pintos-Castro et al., 2019; van der Burg et al., 2020).

Constraining timescales using forward modelling of observable quantities in projected phase space (PPS) in clusters can provide significant information for discerning when and where different physical quenching mechanisms may be dominant. In observational works, galaxy properties have shown a strong link to their position in PPS (for a variety of distinct examples see e.g. Mahajan et al., 2011; Smith et al., 2012; Muzzin et al., 2014; Jaffé et al., 2015; Noble et al., 2016; Gavazzi et al., 2018; Jaffé et al., 2018; Kelkar et al., 2019; Kim et al., 2020; Rhee et al., 2020; Roberts et al., 2021). Little detailed forward modelling work has been done on constraining quenching timescales in PPS, aside from that developed in the series of papers by Oman, Hudson and collaborators (Oman et al., 2013; Oman & Hudson, 2016; Oman et al., 2021). The second and third of these papers use the quiescent fraction of cluster galaxies in PPS coordinates as well as corresponding distribution of infall times inferred from N-body simulations. The PPS coordinates used in this context,

namely the radial distance from cluster center and line-of-sight velocity offset from its host system, only carry magnitude (i.e. no sign) information in practice, as it's generally not possible to distinguish between a satellite receding towards a background host or a background satellite receding away from a foreground host. This method provides a nearby interloper population on the cluster outskirts (outside some 3D radial cut) against which to compare cluster satellites. This has an advantage over using a generic field population: using these interlopers in the cluster outskirts provides an already pre-processed infalling galaxy sample, allowing better isolation of cluster physics from the physics involved in pre-processing.

Whereas many previous works that modeled environmental quenching have relied on quiescent fractions, observational indicators that are sensitive to the star formation history over longer timescales should provide more information. Luminosity- or mass-weighted ages (MWAs) in particular not only provide complementary quantitative information about the star formation history of galaxies, but are also insensitive to whether a given galaxy's star formation history is assumed to be smooth or stochastic (see discussion in Section 3.4.2).

Studies using spectroscopic indicators of stellar age have long established that more massive galaxies, or, more accurately, galaxies with deeper potential wells, have older ages (Nelan et al., 2005; Graves et al., 2007). Dependence on environment is weaker: early studies focused on the age difference between field and cluster ellipticals after controlling for mass or velocity dispersion (Thomas et al., 2005; Bernardi et al., 2006). Radial trends of the stellar ages of galaxies within clusters (at fixed velocity dispersion) were found (Smith et al., 2006) with a stronger environmental dependence on the ages of dwarf galaxies (Smith et al., 2012).

Studies of stellar age in PPS are less common. Pasquali et al. (2019) considered luminosity-weighted stellar ages in zones of PPS around low redshift clusters, finding ages that are older by ~ 2 Gyr for the innermost lower-velocity regions of PPS compared to the outermost regions. Recently, Khullar et al. (2022) studied D4000-derived ages in PPS in $0.3 < z < 1.1$ clusters, again finding older ages for PPS regions associated with the core of the cluster (see also Kim et al., 2022).

There has been even less effort modelling the effect of quenching on the stellar ages. Taranu et al. (2014) used infalling subhalo orbits from N-body simulations to forward-model the age-sensitive Balmer line Lick indices as a function of cluster-centric radius. Their models preferred long quenching timescales occurring for galaxies that have passed within $\sim 0.5 r_{200c}$ (i.e. preferring slow 'strangulation' over rapid ram-pressure stripping).

As little work has been done forward modelling spectroscopically-derived ages in clusters and none has been carried out in full PPS with a large sample (but see Upadhyay

et al., 2021, for a first attempt with a sample of 11 galaxies in the Coma cluster), the goal of this work is to extend the modelling of Oman & Hudson (2016) and Oman et al. (2021), who studied the quiescent fraction, $f_{\rm Q}$, in PPS. Oman et al. (2021) found that using $f_{\rm Q}$ alone is not sufficient to constrain both the time of quenching onset and the timescale over which quenching occurs on average and so they marginalized over this latter parameter to find the average time at which 50 per cent of infalling star-forming galaxies have quenched. Extending this and similar work could make use of, for example, the entire sSFR distribution, but as we will describe, the shape of the quiescent bump is sensitive to observational systematics, while the depth of the green valley is sensitive to choice of star formation history (smooth versus stochastic). In this paper, we will focus on extending Oman et al. (2021) by forward modelling the observed MWAs of galaxies in PPS, in addition to using quiescent fractions. This additional observable will enable joint constraints on both the time of onset of infall quenching and the timescale for the duration of quenching preferred by both observables, for the population of galaxies as a whole.

Our paper is structured as follows. In Section 3.2, we describe how we parameterise PPS and the SDSS-based datasets, from which we get our $f_{\rm Q}$ and mean MWAs. We then, in Section 3.3, introduce our forward modelling approach (including sources of star formation histories and infall histories) and present our quiescent fraction and mean MWA modelling results in PPS as well as the constraints on quenching timescales they provide. In Section 3.4, we discuss the robustness of our results, how they compare to literature, and what they imply for the dominant infall quenching processes. We then conclude in Section 3.5.

Unless otherwise specified, the following assumptions and conventions are used. Uncertainties are estimated from the $16^{\rm th}$-$84^{\rm th}$ percentile interval (equivalent to 1-σ for a Gaussian-distributed variable). Logarithms with base 10 ($\log_{10}$) are written simply as 'log' throughout this work. A flat ΛCDM cosmology consistent with the Planck 2015 cosmological parameters (Planck Collaboration et al., 2016a) is assumed, namely $H_0 = 68$ km s^{-1} Mpc^{-1}, $\Omega_m = 0.31$, and $\Omega_\Lambda = 0.69$. We define a virial overdensity at $z = 0$ in this work as ~ 360 times the background density, $\Omega_m \rho_c$, corresponding to the density of a recently virialized spherical top-hat solution (see e.g. Bryan & Norman, 1998) [1]. A Chabrier (2003) initial mass function (IMF) is assumed throughout.

[1]For a commonly used virial overdensity definition of $200\rho_c$, this corresponds to $M_{200c}/M_{\rm vir} \approx 0.81$ and $r_{200c}/r_{\rm vir} \approx 0.73$ (Oman et al., 2021), assuming a concentration parameter of $c_{200} = r_{200c}/r_s \approx 5$ (where r_s is the NFW profile scale radius), a typical value for clusters (Ludlow et al., 2014).

3.2 Data and Simulations

3.2.1 PPS selection and conventions

We adopt the convention of Oman et al. (2013) for selecting objects in PPS to allow direct comparison to observations: there are two sets of cluster-centred coordinates: (r, v) for the 2×3D physical phase space coordinates and (R, V) for the normalized PPS coordinates. Specifically, the PPS coordinates consist of the distance to cluster centre perpendicular to the line-of-sight and the velocity component along the line of sight, which we choose to be the Cartesian Z-axis of a given simulation dataset. The projected radius between the cluster centre and a galaxy is then

$$R = \left(\frac{1}{r_{\rm vir,3D}}\right)\sqrt{(r_X - r_{X,\rm cls})^2 + (r_Y - r_{Y,\rm cls})^2} \tag{3.1}$$

and the projected velocity relative to the motion of the cluster centre of mass is

$$V = \left(\frac{1}{\sigma_{\rm 3D}}\right)\left|(v_Z - v_{Z,\rm cls}) + H(Z - Z_{\rm cls})\right|. \tag{3.2}$$

Using an absolute value for the projected velocity definition captures an assumption that the distances to clusters and satellites are not measured with enough accuracy to determine the sign of their relative velocity. The additional H term corrects for the Hubble flow. To allow easy comparison between clusters, for both simulations and observations, we have normalized the PPS coordinates. For ease of comparison to Oman & Hudson (2016) and Oman et al. (2021), radial coordinates are normalized by dividing by the 3D virial radius of the cluster, $r_{\rm vir,3D}$, and velocity coordinates by the 3D velocity dispersion, $\sigma_{\rm 3D}$, of a given cluster. As we are averaging over many clusters in both the orbit library and observed sample, we can assume that clusters are approximately spherically symmetric. This in turn allows relation of the 3D velocity dispersion to the observable 1D velocity dispersion by $\sigma_{\rm 3D} \approx \sigma_{\rm 1D}/\sqrt{3}$. We note that in order to ensure consistency between the normalization factors used for R and V, they should not be independent, i.e. the velocity dispersion should be derived from the virial radius or vice-versa. See Section 3.2.4 for details of how these are calculated for the SDSS data.

3.2.2 Infall histories: N-body simulation orbit library

We use the PPS orbital libraries from Oman et al. (2021); they base their methodology on Oman & Hudson (2016) to produce a catalogue of orbit parameter probability distributions

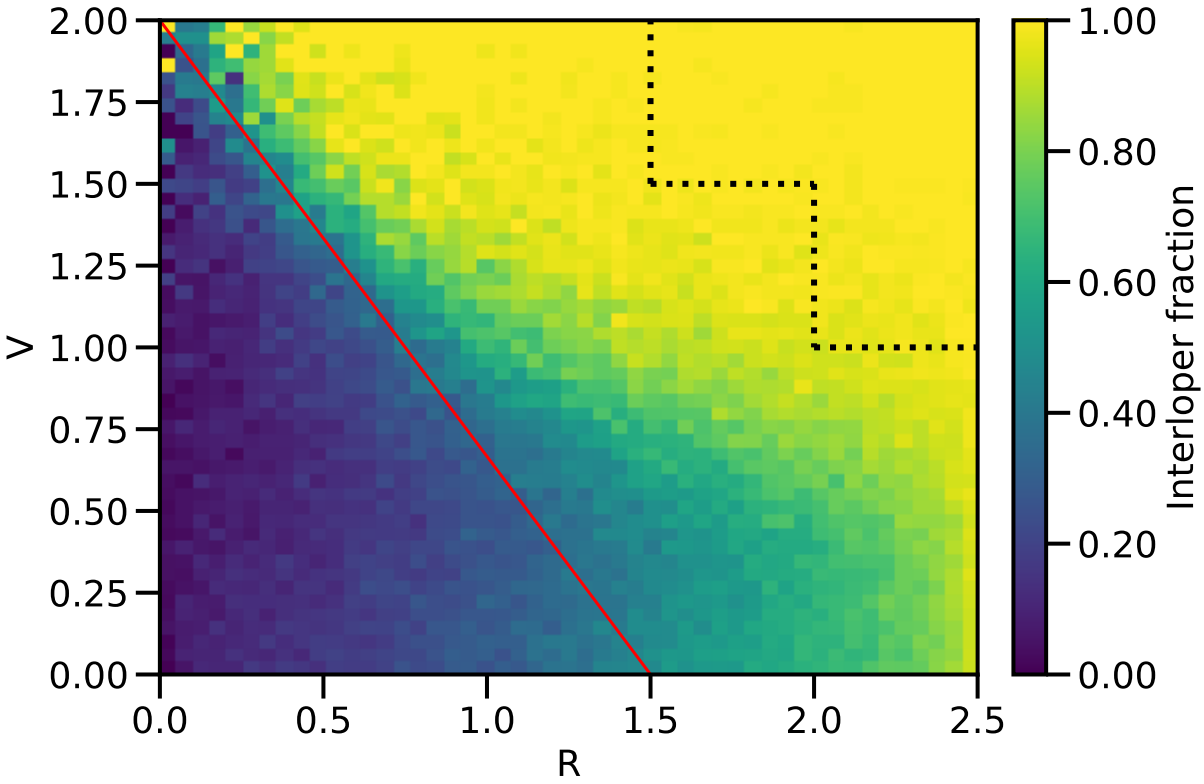

Figure 3.1: The fraction of interlopers in (R,V) projected phase space bins determined using the orbital library from Oman et al. (2021). R is distance from cluster centre, in units of $r_{\rm vir,3D}$ and V is the velocity offset from cluster centre, with units of $\sigma_{\rm 3D}$. The red diagonal line, $V = -(4/3)R + 2$, guides the eye as to where ~ 50 per cent of galaxies are interlopers, aside from a portion around $(R, V) \sim (1.2, 0.4)$, which has many galaxies at or close to their first apocentre after entering the cluster. The dotted line delineates a region in the upper right that is heavily dominated by the interloper population, which we use to compare between SDSS and UniverseMachine interlopers.

from an N-body simulation. As described in Oman et al. (2021), the 'level 0' voids-in-void-in-voids simulation (VVV; Wang et al., 2020) is used, which has a box size of 500 h^{-1}Mpc on a side, mass resolution elements of 10^9 $h^{-1}\mathrm{M}_\odot$, and a force softening scale of 4.6 h^{-1}kpc. They run the simulation to scale factor $a = 2$, corresponding to redshift $z = -0.5$ or ~ 10 Gyr into the future (i.e. negative lookback times), allowing them to find the time of first pericentre for > 99.9 per cent of resolved satellite galaxies. Host halo masses and satellite halo masses are estimated using the ROCKSTAR halo finder; infall times and times of first pericentre are derived from halo merger trees generated by the CONSISTENT TREES utility. These merger trees include all haloes with > 30 particles, corresponding to $M_{\rm vir} \gtrsim 4 \times 10^{10}$ $\mathrm{M}_\odot$, allowing resolution of $M_{\rm vir} \sim 2.5 \times 10^{11}$ $\mathrm{M}_\odot$ haloes, which host the lowest stellar mass galaxies in our observed sample – $M_\star \sim 10^{9.5}$ $\mathrm{M}_\odot$ (at least until they are stripped of $\gtrsim 85$ per cent of their halo mass).

Satellites are identified as haloes within a 3D aperture of 2.5 $r_{\rm vir}$ at $z = 0$ for $\log(M_{\rm vir}/\mathrm{M}_\odot) > 12$ host systems (although we only use hosts with $\log(M_{\rm vir}/\mathrm{M}_\odot) > 14$ in this work). Satellite primary progenitors/descendants are traced backward/forward through time and orbits relative to the $z = 0$ primary progenitor/descendent of their host are recorded. The time of first pericentre is not interpolated (it is very challenging to do this properly and is unnecessary for our purposes), so it is worth noting here that this results in non-uniform output times, with a median timestep of 220 Myr and a maximum timestep of 380 Myr, sufficient to resolve the characteristic quenching and stripping timescales fit in Oman et al. (2021). Worth noting is that the satellite halo mass, $M_{\rm sat}$, is its maximum mass at $z \geq 0$, since maximum halo mass is better correlated with stellar mass in 'moderately stripped' satellites; see e.g. Conroy et al. (2006) and Appendix A of Wetzel et al. (2013) for further elaboration on this.

For the orbit library itself, since satellites are all galaxies within $2.5r_{\rm vir}$, interlopers are then naturally defined as all galaxies that fall within $2.5r_{\rm vir}$ in projection, but outside $2.5r_{\rm vir}$ in 3D. Only a vanishingly small fraction, $\ll 1$ per cent, of interlopers would have been classified as satellites at an earlier time. All satellites have a recorded time of first infall into the final cluster ($2.5r_{\rm vir}$ in 3D) and time of first pericentre ($t_{\rm fp}$) in the final cluster; we only use $t_{\rm fp}$ in our modelling and analysis. We make use of their relative abundance compared to selected satellites to define the probability that an 'observed' galaxy is an interloper. For the sake of illustration and intuition for the reader, we plot the statistical fraction of galaxies that are interlopers at a given position in PPS, rather than cluster satellites, in Fig. 3.1. In the plot it's clear that at both high R and V the vast majority of galaxies are interlopers and vice-versa for lower R and V. We note that around $(R, V) = (1.5-2, 0-0.5)$ there are many galaxies on their first infall into a cluster, whereas galaxies at around $(R, V) = (0-0.5, 1-2)$ are primarily galaxies at their first

pericentre. Over several orbits galaxies settle to low (R, V). As well, we plot a straight line indicating where approximately 50 per cent of galaxies are interlopers – this should provide a helpful rule-of-thumb for the reader in the plots of various quantities in PPS that will follow.

3.2.3 Star formation histories: the UniverseMachine

For individual galaxies' SFR histories we use the UniverseMachine semi-analytic model (Behroozi et al., 2019) which parametrises galaxy SFRs as a function of halo potential well depth, redshift, and assembly history. Their halo potentials and assembly history are derived from the *Bolshoi-Planck* dark matter simulation (Klypin et al., 2016; Rodríguez-Puebla et al., 2016), which features a periodic comoving volume $250h^{-1}$ Mpc on a side with 2048^3 ($\sim 8 \times 10^9$) particles. The simulation employs a flat ΛCDM cosmology compatible with Planck15 results (Planck Collaboration et al., 2016a), with stored snapshots equally spaced in $\log(a)$ (180 intervals). The rockstar halo finder (Behroozi et al., 2013a) and Consistent Trees (Behroozi et al., 2013b) are used to construct merger trees, the same codes used in the construction of the merger trees for the orbit library employed in this work (Section 3.2.2).

For our purposes, it was important that their model reliably reproduce the observed SFRs and quiescent fractions over time, especially in overdense regions in SDSS (although not necessarily cluster cores, as we are only using UniverseMachine interloper galaxies, described in the following paragraph). A key aspect of the UniverseMachine model is that SFRs are stochastic – they fluctuate over time – and are linked to the merger history of the halo. Behroozi et al. (2019) found that without such scatter the quiescent fractions of satellites would be too high (relative to centrals). Specifically, higher SFRs are assigned to halos with higher levels of halo growth, parameterised by the relative logarithmic growth in $v_{\rm max}$, over the past dynamical time (where $v_{\rm max}$ is the maximum circular velocity of the halo). The stochasticity has two components: a short timescale component ($\sim 10 - 100$ Myr) representing internal processes affecting local galactic cold gas, and the second component linked to the dynamical time (~ 1 Gyr). This stochasticity will be a key difference in our comparison to other infall models (which use smooth star formation histories). A galaxy can transition between quiescent and star-forming, as long as the overall quiescent fraction and other properties are matched to the various observations they used, in a self-consistent manner.

We construct a PPS catalogue using the UniverseMachine simulation results at $z = 0$, assuming arbitrarily that the z-axis is the observational line-of-sight. For each of

the 144 UniverseMachine simulation sub-volumes, galaxies were selected from around central haloes ('UPID'==-1) with halo masses $\log(M_{\rm vir}/{\rm M}_\odot) > 14$. All galaxies (including centrals) are selected so that their projected radius is $R < 2.5$ and projected velocity is $V < 2$, where the PPS coordinates (R, V) are defined as described previously in Section 3.2.1. True interlopers and satellites, as opposed to interlopers and satellites as defined in PPS, are identified with 3D cuts of $R > 2.5$ and $R < 2.5$, respectively.

3.2.4 SDSS dataset

For the observed sample of galaxies, we build on the sample used by Oman et al. (2021) for their quenching analysis. As in Oman et al. (2021), we use the SDSS Data Release 7 catalogue (Abazajian et al., 2009), supplemented with SFRs (Brinchmann et al., 2004; Salim et al., 2007) and stellar masses (Mendel et al., 2014), which were used in Oman et al. (2021) for estimating galaxy subhalo masses using subhalo abundance matching. We also use the spectroscopic sample of galaxies, which we note suffers from fiber collisions, although Oman et al. (2021) determine through a detailed exploration that the impact of this should be minimal.

We use the mass-weighted ages, as well as the accompanying stellar mass estimates, of Comparat et al. (2017), who performed full spectral fitting of galaxy properties using FIREFLY (Wilkinson et al., 2017). We compare their stellar masses with those of Mendel et al. (2014) and confirm that offsets in the stellar masses do not affect our results. In particular, we use the fits done using the stellar population models of Maraston & Strömbäck (2011), a Chabrier (2003) IMF, and the MILES stellar library (Sánchez-Blázquez et al., 2006; Falcón-Barroso et al., 2011; Beifiori et al., 2011) for the mass-weighted ages ('CHABRIER_MILES_age_massW'), and stellar masses ('CHABRIER_MILES_stellar_mass').

For simplicity, we focus on high-mass cluster haloes, $\log(M_{\rm vir}/{\rm M}_\odot) > 14$, where environmental effects should be most extreme. As in Oman et al. (2021), we select candidate satellite galaxies around groups and clusters from the Lim et al. (2017) and Von Der Linden et al. (2007) catalogues, with cluster virial masses peaking at $\sim 3 \times 10^{13}{\rm M}_\odot$ and $\sim 3 \times 10^{14}{\rm M}_\odot$, respectively. We exclude groups with redshifts $z < 0.01$, as their members are generally too bright to be covered by SDSS spectroscopy. We note that the two group catalogues are constructed with different algorithms. Von Der Linden et al. (2007) look for overdensities of galaxies with similar colours, while Lim et al. (2017) use a friends-of-friends group finding algorithm. This does not significantly affect our analysis as we only use the cluster masses, centres, and line of sight velocities from the catalogues, rather than membership information. Satellite velocity offsets are normalized using cluster velocity

dispersions, calculated from the virial masses of the clusters in the catalogues. The velocity dispersions are similar to the dark matter particle velocity dispersion of the systems (within $\lesssim 10$ per cent; see Munari et al., 2013, table 1); this is important since the velocity dispersion of dark matter particles in the host halo is used to normalize the velocity offsets of satellite haloes in the simulations that the Oman et al. (2021) orbit library is derived from (see Section 3.2.2). Host halo masses are calculated following eq. 1 of Von Der Linden et al. (2007) and eq. 4 of Lim et al. (2017). These are converted to virial masses assuming an NFW density profile (Navarro et al., 1997) and mean mass-concentration relation from Ludlow et al. (2014), with differences between assumed cosmologies accounted for. The mean enclosed density is then used to define the virial radii,

$$r_{\rm vir} = \left(\frac{3}{4\pi} \frac{M_{\rm vir}}{\Delta_{\rm vir}(z)\Omega_m(z)\rho_{\rm crit}(z)} \right)^{\frac{1}{3}}, \tag{3.3}$$

where $\Delta_{\rm vir}(z)$ is the virial overdensity in terms of the mean matter density $\Omega_m(z)\rho_{\rm crit}(z)$, with critical density $\rho_{\rm crit} = 3H^2/(8\pi G)$. Group velocity dispersions are defined following Biviano et al. (2006), but with redshift dependence from Bryan & Norman (1998); explicitly this is

$$\frac{\sigma_{\rm 1D}}{\rm km\ s^{-1}} = \frac{0.0165}{\sqrt{3}} \left(\frac{M_{\rm vir}}{\rm M_\odot} \right)^{\frac{1}{3}} \left(\frac{\Delta_{\rm vir}(z)}{\Delta_{\rm vir}(0)} \right)^{\frac{1}{6}} (1+z)^{\frac{1}{2}}. \tag{3.4}$$

We use two stellar mass bins, $9 < \log(M_\star/{\rm M_\odot}) < 10$ and $10 < \log(M_\star/{\rm M_\odot}) < 10.5$. We note that for $\log(M_\star/{\rm M_\odot}) > 10.5$ there are too few star forming galaxies to yield robust results, so we do not consider this mass range in this paper.

Quiescent fraction trends in PPS around SDSS clusters

Our first source of information for deriving quenching timescales is the quiescent fraction in SDSS clusters. As we are using the same observational data sample as Oman & Hudson (2016) and Oman et al. (2021), we define define star-forming and passive galaxies using the same cut, namely

$$\log({\rm sSFR/yr^{-1}}) = -0.4 \log(M_\star/{\rm M_\odot}) - 6.6, \tag{3.5}$$

with star-forming (quiescent) galaxies lying above (below) the specific star formation rate (sSFR) relation.

We illustrate the quiescent fraction trends in PPS for $9 < \log(M_\star/{\rm M_\odot}) < 10$ galaxies in Fig. 3.2. In the figure we see well-known observed trends of decreasing $f_{\rm Q}$ with increasing

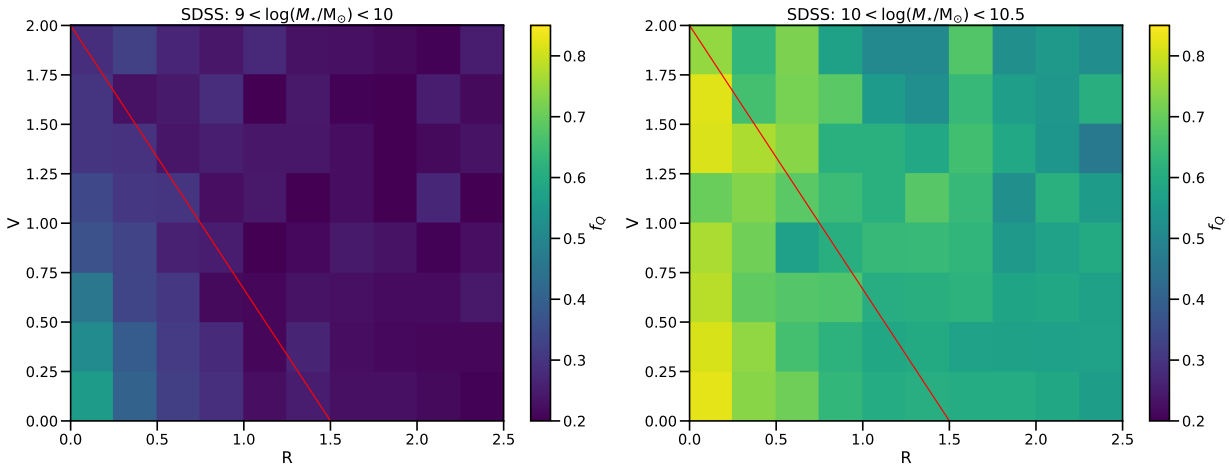

Figure 3.2: Quiescent fraction of SDSS galaxies in the stellar mass ranges $9 < \log(M_\star/\mathrm{M}_\odot) < 10$ (left) and $10 < \log(M_\star/\mathrm{M}_\odot) < 10.5$ (right) in clusters with host halo mass $\log(M_{\rm vir}/\mathrm{M}_\odot) > 14$, binned in PPS coordinates. The quiescent fraction is significantly higher in cluster centres than in their outskirts ($\gtrsim 30$ per cent). For the lower stellar mass bin, regions within the ~ 50 per cent interloper (red diagonal) line, show at least modestly elevated quiescent fractions, with little evidence of enhanced quenching immediately outside of (above) this line. For the higher stellar mass bin, some higher velocity galaxies within the virial radius also show somewhat elevated quiescent fractions.

distance from cluster centre as well as higher $f_{\rm Q}$ for galaxies with lower velocity offsets. We draw a line indicating roughly where $\sim$ 50 per cent of galaxies are interlopers, with galaxies above this line increasingly dominated by interlopers, moving from lower to higher R and V coordinates. Enhanced quenching largely falls within the region bounded by this 50 per cent interloper line in PPS. Contrasting with the field results of Oman et al. (2021, see upper right panel of e.g. fig. 10 to see star-forming fraction versus stellar mass for the SDSS field), with field defined as the average overall SDSS population, we see that the interloper quiescent fraction is higher than the field by 0.05 and 0.09 for our lower and higher stellar mass bins, respectively.

Having information on how quenching depends on both the radial position and velocity relative to host cluster centre gives us very useful information on when and where quenching occurs. It's clear in Fig. 3.2 that most quenching of infalling star forming galaxies occurs well within the virial radius. Modestly enhanced quenching up to high velocities indicates quenching is at least beginning to occur within the first infall or just after first pericentre. Although we have some useful information from $f_{\rm Q}$ in PPS, this information alone results in significant degeneracies between time of quenching onset and duration of quenching, as we will clearly show later in this work (see Section 3.3.2). To break this timescale information degeneracy we must turn to another independent observable as a function of its position in PPS.

Mass-weighted age – stellar mass relation

For the stellar ages of SDSS galaxies we use a simple proxy to capture when the bulk of the stellar mass in a galaxy was formed, namely the mass-weighted age (MWA). We include only quiescent galaxies for our MWA-based measurements, since the emission lines of star-forming galaxies fill in the age-sensitive Balmer absorption lines, making them rather unreliable as an age indicator. In this subsection, we note a trend in MWA with stellar mass in both the observationally-derived SDSS values and the UniverseMachine simulated galaxies. As we are only interested in the differential change in MWA relative to an infalling population, we first describe how we control for the MWA–$M_\star$ effect in this work. After this, we will briefly illustrate observed MWA trends in PPS in Section 3.2.4.

We show the trend in MWA with stellar mass for both the observationally-derived SDSS values and the UniverseMachine (Behroozi et al., 2019) simulated galaxies side-by-side in Fig. 3.3. The mean and median trends that we see for SDSS and UniverseMachine are qualitatively similar, but the UniverseMachine galaxies are offset in overall MWA such that they are younger than SDSS MWAs by $\sim$ 3 Gyr on average. We note that mass-weighted ages derived from spectra depend on the assumed star formation history. For

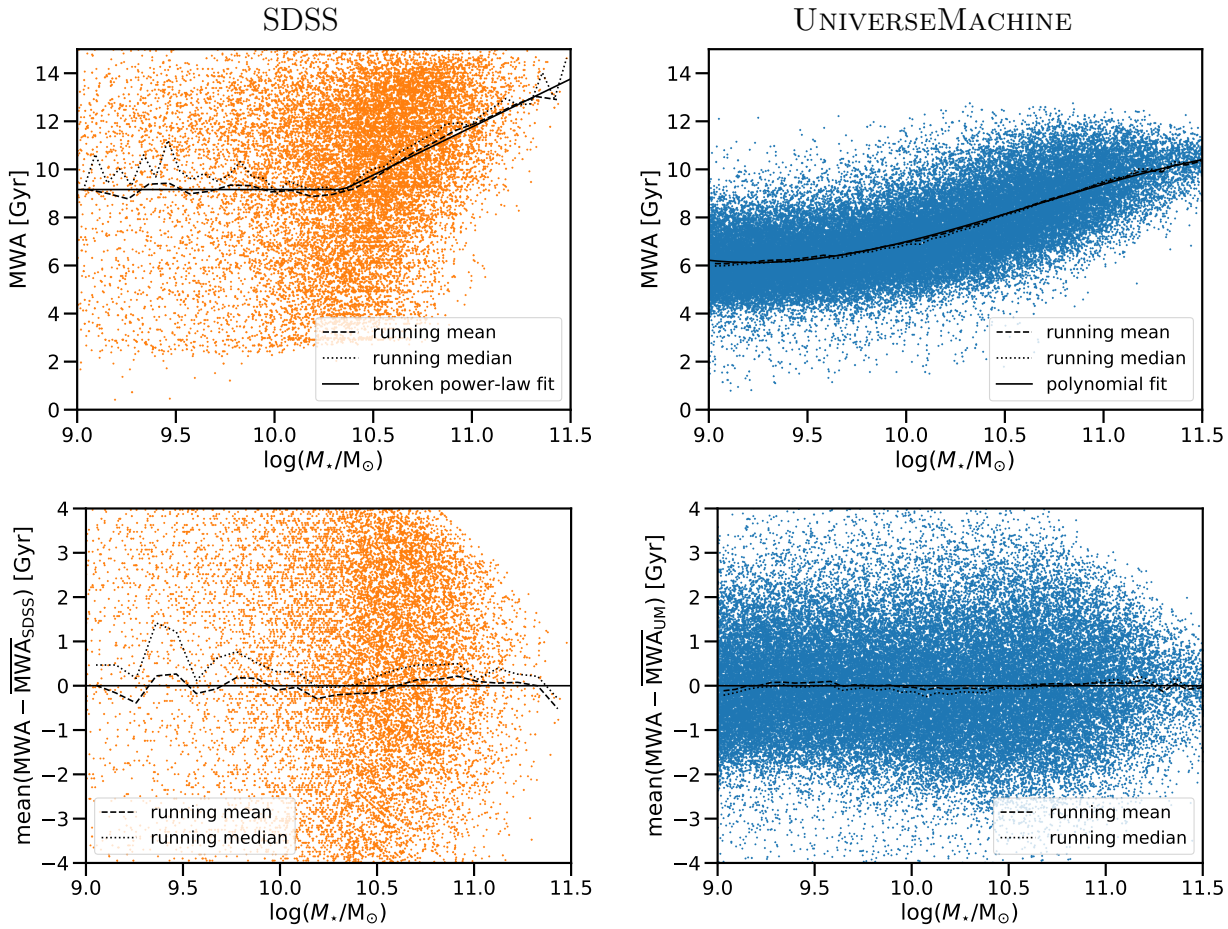

Figure 3.3: *Top panels:* SDSS observationally-derived mass-weighted ages for quiescent galaxies (left) exhibit a high degree of scatter and trend older with increasing galaxy stellar mass. UniverseMachine simulated galaxies (right) show a similar trend in mass-weighted age with stellar mass, albeit with a ~ 3 Gyr offset and significantly less scatter (see Section 3.2.4 for discussion). SDSS points indicate the best-fitting mass-weighted ages for SDSS galaxies from Wilkinson et al. (2017, stellar masses are from Comparat et al., 2017), with the running mean (median) shown as a dashed (dotted) line. The functional fits of the mean MWA–$M_\star$ relation used in the analysis of this work is fit to the running mean mass-weighted age at a given stellar mass and is shown with the solid black curves. *Bottom panels:* Residual MWA from the respective MWA–$M_\star$ functional fits for SDSS (left) and UniverseMachine (right) is shown along with the running mean (dashed) and median (dotted) of the residual.

example, Allanson et al. (2009) showed that a range of star formation histories can fit the observed stellar absorption lines equally well in quiescent cluster galaxies, yielding mass-weighted ages that range from 5 Gyr (single burst) to 8 Gyr (exponentially declining star formation history) to 12.8 Gyr ('frosting' model) for the lowest-mass cluster galaxies. Since we use ages only in a differential sense in our analysis, i.e. comparing the difference in MWA in the cluster core to the infalling regions in PPS, any systematic offset in the ages due to different star-formation history assumptions will not affect our analysis. For SDSS, the MWA–$M_\star$ relation is approximately flat, with MWA ~ 9 Gyr for $9 < \log(M_\star/\mathrm{M}_\odot) \lesssim 10.5$ galaxies, which then increases for $\log(M_\star/\mathrm{M}_\odot) \gtrsim 10.5$ to $\sim$ 12-13 Gyr for the highest stellar mass galaxies, $\log(M_\star/\mathrm{M}_\odot) > 11$. The increase in MWA for UniverseMachine galaxies from lowest to highest stellar masses shown in Fig. 3.3 is similar in magnitude to that for SDSS (~ 4 Gyr), albeit with a more steadily increasing monotonic trend, i.e. a non-flat trend in MWA below $\log(M_\star/\mathrm{M}_\odot) < 10.5$. The scatter is also quite noticeably different – the SDSS scatter can be thought of as the natural distribution of galaxies (shown modeled here by the UniverseMachine) convolved with the scatter induced in estimated MWAs from uncertainties in SED-fitting the galaxy spectra.

To remove the systematic trend in MWA with stellar mass and the ~ 3 Gyr offset between the SDSS observationally-derived MWAs and the simulated UniverseMachine MWAs so that we can focus solely on the effect of environment on galaxy MWAs, we look at the mean MWA residual from the mean MWA–$M_\star$ relation. This allows us to measure the differential effect between inner cluster regions and cluster outskirts (i.e. controlled for stellar mass). In particular, we use interloper galaxies as our reference infalling (already pre-processed) population.

For a simple clean proxy interloper sample that can be easily compared between UniverseMachine and SDSS, we choose galaxies in the region of PPS given by

$$(1.5 < R < 2.5, 1.5 < V < 2) \cup (2 < R < 2.5, 1 < V < 1.5) \tag{3.6}$$

as illustrated in Fig. 3.1 (see also Section 3.3.1). Based on statistics from the orbit library of Oman et al. (2021), this region of PPS provides a sample that is made up of $\gtrsim 97$ per cent true interlopers. Correcting for the ~ 3 per cent impurity is unnecessary for our purposes.

For SDSS, we parameterise the mean MWA–$M_\star$ relation (fit and residual shown as black curve in the left panels of Fig. 3.3) for (predominantly interloper) galaxies with $R < 2.5$ and $V < 2$ in the stellar mass range $10^9 < M_\star/\mathrm{M}_\odot < 10^{12}$ using the function

$$\overline{\mathrm{MWA}}_{\mathrm{SDSS}} = A \log\left[\left(\frac{M_\star}{M_{\mathrm{crit}}}\right)^{\alpha} + \left(\frac{M_\star}{M_{\mathrm{crit}}}\right)^{\beta}\right] + b, \tag{3.7}$$

where $A = 0.1$ Gyr is the normalization, $b = 9.16$ Gyr is the vertical offset, $M_{\rm crit} = 10^{10.35}\,{\rm M}_\odot$ is the location of the break in slopes, and $\alpha = 0$ and $\beta = 40$ specify the lower and higher stellar mass slopes, respectively. The fit is chosen to minimize the residual between the running mean MWA–$M_\star$ relation and the curve, and an offset is added so that the interloper population has mean(MWA$-\overline{\rm MWA}_{\rm SDSS}$) = 0 by construction. This was done rather than fit the interloper MWA–$M_\star$ relation directly since the interloper population had relatively few galaxies to give a good fit across the whole stellar mass range.

For the UniverseMachine simulated sample, a polynomial is fit to the ∼pure interloper population (Eq. 3.6) to the running mean MWA (fit and residual shown as the black curve in the right panels of Fig. 3.3). The polynomial fit has the following form:

$$\overline{\rm MWA}_{\rm UM} = -0.301 + 9.83x - 105x^2 + 370x^3; \tag{3.8}$$

where $x \equiv \log(M_\star/{\rm M}_\odot)$ and the coefficients have units of Gyr.

Trends in the mean deviation of mass-weighted age in PPS

We present a binned map of the deviation in mass-weighted age from the mean MWA–$M_\star$ relation of the SDSS interloper proxy sample, mean(MWA $-\overline{\rm MWA}_{\rm SDSS}$) (see previous section), as a function of the PPS coordinates R and V in Fig. 3.4. Errors on the mean values are calculated by bootstrapping over clusters. The figure shows that mean(MWA $-\overline{\rm MWA}_{\rm SDSS}$) is enhanced for galaxies at lower radii and velocities. This is particularly clear for the higher stellar mass bin. Within the 50 per cent interloper line shown in the figure, we calculate mean(MWA $-\overline{\rm MWA}_{\rm SDSS}$) $= 0.76^{+0.12}_{-0.14}$ and mean(MWA $-\overline{\rm MWA}_{\rm SDSS}$) $= 0.66^{+0.08}_{-0.09}$ for the lower and higher stellar mass bins, respectively. Our higher stellar mass bin is consistent with Kim et al. (2022), who find that populations in PPS around clusters at $0.3 < z < 1.4$ identified as 'early infall' were older on average by 0.71 ± 0.4 Gyr than comparable 'recent infall' galaxies.

In the following section we will show that the distribution of modeled mean(MWA $-\overline{\rm MWA}_{\rm UM}$), ΔMWA, in PPS differs from that of $f_{\rm Q}$ (shown previously in Fig. 3.2, Section 3.2.4). These differences in observed f_Q and ΔMWA distributions will provide us with a distinct set of preferred values for time of quenching onset and the duration of quenching timescales.

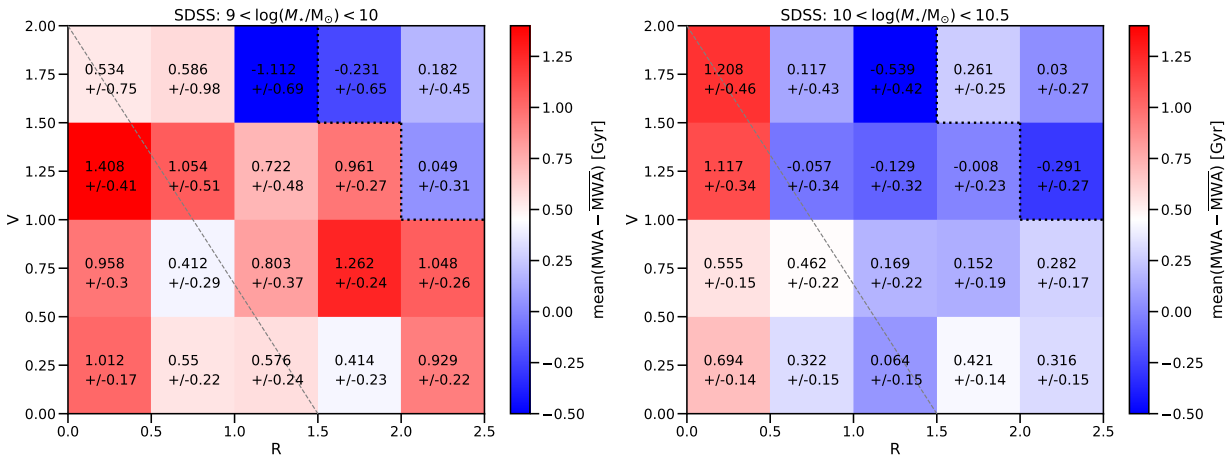

Figure 3.4: Mean deviation in MWA from the MWA–$M_\star$ relation of an SDSS interloper proxy sample (top right three bins; outlined by dotted black lines), mean(MWA $-$ $\overline{\mathrm{MWA}}_{\mathrm{SDSS}}$), for quiescent $9 < \log(M_\star/\mathrm{M}_\odot) < 10$ (left) and $10 < \log(M_\star/\mathrm{M}_\odot) < 10.5$ (right) SDSS galaxies as a function of PPS coordinates. Errors on the mean values were calculated by bootstrapping over clusters, rather than individual galaxies. We note that the zero-point for this figure, defined by the three PPS bins in the top right corner are 97 per cent interloper galaxies according the orbit library of Oman et al. (2021). The dashed grey diagonal line indicates where approximately 50 per cent of galaxies are interlopers.

3.3 Modelling and Results

Our goal is to model the effects of infall quenching on two SDSS observables, f_Q and mean ΔMWA, in PPS around $z \sim 0$ galaxy clusters, and then use these results to constrain the associated quenching timescales. In this section, we first describe our infall quenching model in detail in Section 3.3.1. We show our model results for f_Q in Section 3.3.2 and for ΔMWA in Section 3.3.3. Finally, we combine our modelling results for both f_Q and ΔMWA to find a joint constraint on our model's two quenching timescales in Section 3.3.4.

3.3.1 The model

To model the effects of infall quenching on both f_Q and mean ΔMWA, we use the UniverseMachine semi-analytic model, as described in Section 3.2.3, as a representative model of star formation histories for galaxies in the infall region around a given cluster. A simple, smooth parametric model could be used, but such models don't have any intrinsic scatter in their star formation histories. We will see that this scatter has an impact on the bimodality in the star formation rates of the galaxy population (see Section 3.4.2). The UniverseMachine simulation also provides us with a pre-processed infall sample.

Using a galaxy cluster PPS orbit library from Oman et al. (2021), as described in Section 3.2.2, we sample the infall time distribution of galaxies in PPS in galaxy clusters, including the interloper fraction across PPS. With these tools in hand, we describe in Section 3.3.1 how we construct an infall quenching model to predict f_Q and ΔMWAs as a function of position in PPS. For the sake of intuition, we visually illustrate some basic trends in f_Q and ΔMWA with our quenching parameters in Section 3.3.1.

Description of our satellite quenching model

We take the previously defined interloper sample as the infalling population, which will naturally include any pre-processing of galaxies in infalling structures (e.g. groups or filaments), as captured by the UniverseMachine model. Our model assumes that star formation histories of $z = 0$ cluster satellite galaxies are the same as the $z = 0$ infalling population of galaxies, but with the addition of a quenching mechanism on infall, as described below. Galaxies that fall into the cluster begin suppression of their SFR when a time interval of $t_{\rm delay}$ has elapsed after their first pericentre passage. Defining the model this way means that we are modeling the mean quenching timescales for the population of galaxies as a whole, over all possible infall orbits (e.g. circular versus eccentric/plunging),

giving us robust mean observed properties, insensitive to the choice between stochastic or smooth star formation histories (see Section 3.4.2 for discussion of this point).

For UniverseMachine galaxies, we use the same sSFR cut to separate quiescent/star forming galaxies as Behroozi et al. (2019), namely

$$\log(\mathrm{sSFR}/\mathrm{yr}^{-1}) = -11, \tag{3.9}$$

where star-forming (quiescent) galaxies are defined as lying above (below) the cut. The UniverseMachine interloper population and SDSS interloper population differ slightly in their quiescent fractions (see e.g. Fig. B.1), but we are only interested in the differential quenching effect (f_{Q} in the cluster versus some infall population). To find the timescales associated with infall quenching, we will fit for the infalling f_{Q}. In Appendix B.3 we will confirm that our results are robust to adjusting the UniverseMachine infalling star formation histories such that the infalling galaxies closely match the SDSS $f_{\mathrm{Q}} - M_{\star}$ trend.

In the literature, some variation of a 'delayed-then-rapid' quenching scenario is common, like that proposed and explored in Wetzel et al. (2013). Exponentially declining SFR (e.g. Wetzel et al., 2013; Roberts et al., 2019) or linearly declining quiescent fraction (such as in Oman et al., 2021) are common assumptions. To facilitate comparison with previous work, we choose a model with an exponential suppression of the SFR on a timescale, τ_{env}, that starts after some time delay, t_{delay}, relative to the time of first pericentre t_{fp} (we note that this allows for negative values of t_{delay}, i.e. quenching onset prior to t_{fp}).

Galaxies with a given stellar mass and time of first pericentre are Monte Carlo sampled from satellites in the orbital library of Oman et al. (2021). This gives, for each part of PPS, some mix of interloper galaxies, as well as in-cluster galaxies, which have a distribution of infall times depending on position in PPS. The star formation history for a random interloper with the closest stellar mass to that just drawn is then also drawn from UniverseMachine , which gives the star formation history of this Monte Carlo-simulated galaxy. Each of these simulated satellite galaxies have quenching applied by starting the decline in the SFR at the time $t_{\mathrm{fp}} + t_{\mathrm{delay}}$, i.e. $\mathrm{SFR}_{\mathrm{sat}} = \mathrm{SFR}_i q(t)$, where $q(t)$ is the multiplicative quenching envelope,

$$q(t; t_{\mathrm{delay}}, \tau_{\mathrm{env}}) = \begin{cases} 1, & t < t_{\mathrm{fp}} + t_{\mathrm{delay}}, \\ e^{-(t - t_{\mathrm{delay}} - t_{\mathrm{fp}})/\tau_{\mathrm{env}}}, & t \geq t_{\mathrm{fp}} + t_{\mathrm{delay}}, \end{cases} \tag{3.10}$$

where i refers to a given Monte Carlo-sampled interloper (infalling galaxy) star formation history. In Fig. 3.5, we illustrate the effect of the multiplicative envelope on the stochastic star formation histories of the UniverseMachine galaxies.

We then define our model of the quiescent fraction in a given PPS bin as

$$f_{\mathrm{Q,model}}(t_{\mathrm{delay}}, \tau_{\mathrm{env}}, f_{\mathrm{Q,infall}}) = \Delta f_{\mathrm{Q}}(t_{\mathrm{delay}}, \tau_{\mathrm{env}}) + f_{\mathrm{Q,infall}}, \tag{3.11}$$

where Δf_Q is the increase in quenching from our model and $f_{\mathrm{Q,infall}}$ is left as a free parameter of the infalling population's quiescent fraction to account for systematic differences between UniverseMachine and the SDSS data.

To determine the stellar masses of any galaxy at $z = 0$, the UniverseMachine SFRs are integrated numerically according to eq. 21 and eq. 22 in Behroozi et al. (2019). Explicitly, this gives a final stellar mass of

$$M_\star(t_{\mathrm{now}}) = \int_0^{t_{\mathrm{now}}} \frac{\mathrm{d}M}{\mathrm{d}t}\,\mathrm{d}t \tag{3.12}$$

$$= \int_0^{t_{\mathrm{now}}} \mathrm{SFR}(t)(1 - f_{\mathrm{loss}}(t_{\mathrm{now}} - t))\,\mathrm{d}t, \tag{3.13}$$

where $f_{\mathrm{loss}}(t) = 0.05 \ln\left(1 + t/1.4\mathrm{Myr}\right)$ and t_{now} is the age of the Universe at $z = 0$.

Integrated true (simulated) stellar masses are offset to give 'observed' stellar masses, according to the prescription in Behroozi et al. (2019, eq. 25 and eq. 27), namely by offsetting them by $\mu = \mathrm{SM_{obs}} - \mathrm{SM_{true}} = \mu_0 + \mu_a(1-a)$ [dex] (where $a = 1/(1+z)$ is the cosmological scale factor) and additionally adding Gaussian scatter of $\sigma_{\mathrm{SM,obs}} = \min(\sigma_{\mathrm{SM,z}}(1+z), 0.3)$ [dex]. Best-fitting values associated with UniverseMachine catalogues available online[2] were used for these stellar mass adjustments, namely $\mu_0 = 5.6 \times 10^{-3}$ and $\mu_a = -0.03$ used for the offset and $\sigma_{\mathrm{SM,z}} = 0.069$ for the Gaussian scatter parameter, respectively.

Mass-weighted ages are integrated numerically from the stellar mass calculations, using the midpoints between the simulation snapshot timesteps and $\mathrm{d}M/\,\mathrm{d}t$ between two snapshots' timesteps,

$$\mathrm{MWA} = t_{\mathrm{now}} - \frac{1}{M_{\mathrm{true}}} \int_0^{t_{\mathrm{now}}} t\left(\frac{\mathrm{d}M}{\mathrm{d}t}\right) \mathrm{d}t, \tag{3.14}$$

where M_{true} is the total simulated stellar mass at the present time without any corrections for observational effects. Note that MWA is expressed as a lookback time.

The MWA predicted by our quenching model is then

$$\mathrm{MWA}_Q = t_{\mathrm{now}} - \frac{1}{M_{\mathrm{true}}} \int_0^{t_{\mathrm{now}}} t\left(\frac{\mathrm{d}M}{\mathrm{d}t}\right) q(t; t_{\mathrm{delay}}, \tau_{\mathrm{env}})\,\mathrm{d}t, \tag{3.15}$$

[2] UniverseMachine data release 1 catalogues using the *Bolshoi-Planck* dark matter simulation, including catalogues for complete star formation histories, are available on the following page of Peter Behroozi's website: https://www.peterbehroozi.com/data.html.

Similar to f_Q in Eq. 3.11 above, we define the ΔMWA observable of our model in a given PPS bin for each galaxy as

$$\Delta\mathrm{MWA}(t_{\mathrm{delay}}, \tau_{\mathrm{env}}, \delta\mathrm{MWA}_{\mathrm{infall}}) = \mathrm{MWA}_{Q,\mathrm{model}}(t_{\mathrm{delay}}, \tau_{\mathrm{env}}) \tag{3.16}$$

$$- \overline{\mathrm{MWA}}_{\mathrm{UM}}$$

$$+ \delta\mathrm{MWA}_{\mathrm{infall}}, \tag{3.17}$$

where $\mathrm{MWA}_Q(t_{\mathrm{delay}}, \tau_{\mathrm{env}})$ is the MWA from our quenching model, $\delta\mathrm{MWA}_{\mathrm{infall}}$ is a floating offset to allow for the possibility that the infalling population's MWA may be different than that of the interloper phase space bins in equation 3.6, and $\overline{\mathrm{MWA}}_{\mathrm{UM}}$ is the MWA expected from the mean MWA–$M_\star$ relation as defined in Eq. 3.8 for UniverseMachine galaxies. We use the mean ΔMWA in a given PPS bin in the rest of this work.

Simple illustration of our quenching model

Now that we have described our infall quenching model, we illustrate our predictions for trends in f_{Q} and ΔMWA in PPS. In particular, we start by exploring the effect of varying the quenching time delay relative to a satellite galaxy's first pericentre passage, t_{delay}, assuming instantaneous quenching (i.e. $\tau_{\mathrm{env}} = 0$). We first illustrate this visually in Fig. 3.6 for t_{delay} ranging from $t_{\mathrm{delay}} = -2$ Gyr (i.e. prior to first pericentre) to $t_{\mathrm{delay}} = 4$ Gyr. We include contaminating interlopers.

For $t_{\mathrm{delay}} = -2$ Gyr, quiescent fractions are very high, $\gtrsim 0.75$ throughout most of the region dominated by satellites (i.e. below the ~ 50 per cent interloper line, indicated by the same diagonal line as in Figs. 3.2 and 3.4). ΔMWA reaches ~ 1.1 Gyr for $V < 0.5$ in the cluster core ($R < 0.5$). f_{Q} and ΔMWA values increase with decreasing radius and also generally increase with decreasing velocity offset (albeit less strongly than with radius).

As t_{delay} increases, there is a decrease in both f_{Q} and ΔMWA, as intuitively expected. f_{Q} is still clearly enhanced relative to the interloper population within the ~ 50 per cent interloper line, even for a t_{delay} as long as 4 Gyr. ΔMWA reaches $\lesssim 0.25$ Gyr at all (R, V) bins for $t_{\mathrm{delay}} = 4$ Gyr. For an even longer $t_{\mathrm{delay}} \gtrsim 6$ Gyr (not shown), f_Q continues to drop and ΔMWA drops to ~ 0 Gyr.

With this physical intuition in mind, we now carry out a quantitative analysis of our model for f_{Q} and ΔMWA in turn, as well as the joint constraint that observed SDSS f_Q and ΔMWA values place on our model. We will see in the subsections that follow, differences in the trends for these two observables will enable us to break degeneracy in the t_{delay} and τ_{env} model parameters.

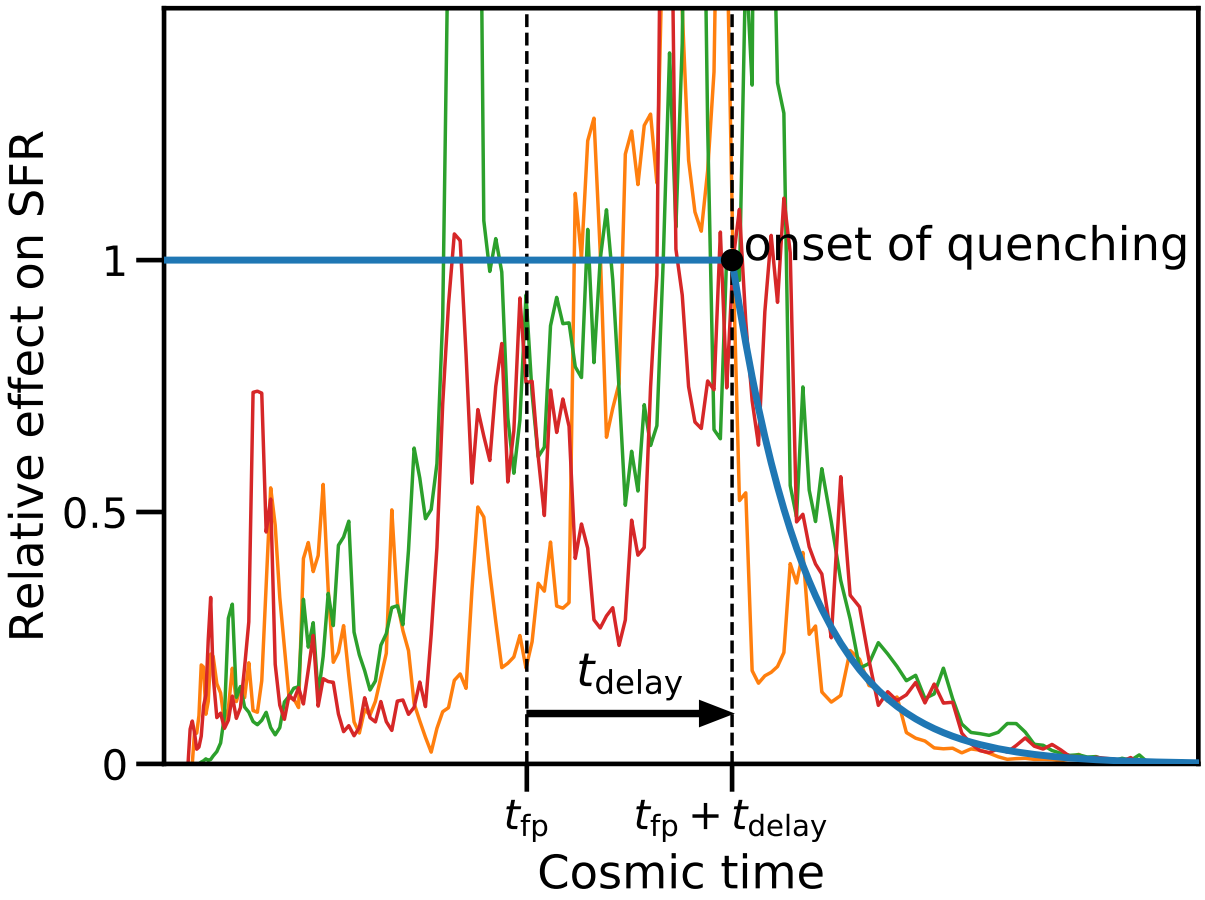

Figure 3.5: Illustration of the effect of our delayed-then-exponential envelope (thick blue line) on SFR, where at some time delay, t_{delay}, after time of first pericentre upon infall into a cluster, t_{fp}, SFR is quenched exponentially by a multiplicative envelope with timescale, τ_{env}.

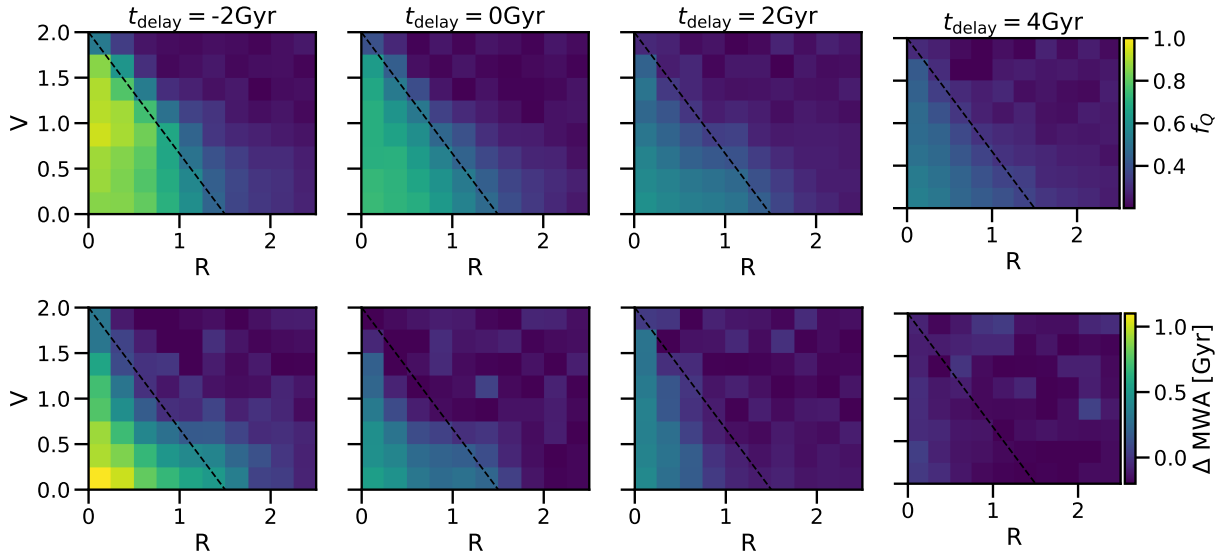

Figure 3.6: Delayed-then-rapid (instantaneous quenching, i.e. $\tau_{\rm env} = 0$) model predictions for a range of delay times, $t_{\rm delay}$, after time of first pericentre (a negative $t_{\rm delay}$ corresponds to quenching prior to $t_{\rm fp}$). For these illustrative plots, we use the UniverseMachine 'observed' interloper proxy sample as defined in Section 3.2.4, for clusters with $\log(M_{\rm vir}/{\rm M}_{\odot}) > 14$. *Top row:* predicted quiescent fractions, $f_{\rm Q}$, in PPS. The diagonal dashed line, $V = -(4/3)R + 2$, marks the location where ~ 50 per cent of galaxies are interlopers. *Bottom row:* quiescent mass-weighted age predictions in PPS.

3.3.2 Quiescent fraction: comparison of models and data

We plot $f_{\rm Q}$ model predictions as a function of time of quenching onset relative to the first pericentre, $t_{\rm delay}$, for a range of $\tau_{\rm env}$ values (different coloured curves) in Fig. 3.7 for $9 < \log(M_\star/{\rm M}_\odot) < 10$ galaxies. For the equivalent plot for $10 < \log(M_\star/{\rm M}_\odot) < 10.5$ galaxies at $z \sim 0$, see Fig. B.2 in Appendix B.4. For reference, we show the mean $f_{\rm Q}$ (grey horizontal line) and the bootstrapped error on the mean (shaded gray region) for the SDSS sample in each PPS bin. When finding the best-fitting $t_{\rm delay}$ values (see Section 3.3.4 for this), we also fit for the infalling population's $f_{\rm Q}$ as a nuisance parameter, to account for possible systematic differences between the quenching from UniverseMachine and the actual infall population, that we will then marginalize over. For the infalling galaxies, our fits prefer $f_{\rm Q,infall} = 0.16 \pm 0.01$ ($f_{\rm Q,infall} = 0.48 \pm 0.01$) for $9 < \log(M_\star/{\rm M}_\odot) < 10$ ($10 < \log(M_\star/{\rm M}_\odot) < 10.5$) galaxies, shown in Table 3.1, which are offset -0.06 ± 0.01 (0.09 ± 0.01) relative to the infall/interloper population's MWAs predicted by the UniverseMachine model.

We now turn our attention to the trends in $f_{\rm Q}$ with $t_{\rm delay}$ and $\tau_{\rm env}$, by focussing on the region of PPS where the infall quenching effect in our model is most pronounced, namely the innermost parts of clusters. In e.g. the $R < 0.5, V < 0.5$ bin we see no effect on $f_{\rm Q}$ for very long quenching times ($t_{\rm delay} \sim 10$ Gyr), as expected. $f_{\rm Q}$ then steadily increases with decreasing time delay up until a point at which it begins decreasing again, at e.g. $t_{\rm delay} \sim -3$ Gyr. This turnover feature comes about because the star formation histories of infalling galaxies are being truncated so aggressively that many quenched galaxies are dropping out of our stellar mass range, with increasing numbers of quenched galaxies having $\log(M_\star/{\rm M}_\odot) < 9$. Since there are fewer high stellar mass galaxies, truncated higher stellar mass galaxies dropping into the bin are not enough to compensate for those dropping below $\log(M_\star/{\rm M}_\odot) = 9$. The effect is most pronounced for instantaneous quenching, $\tau_{\rm env} = 0$, and less pronounced for longer star formation suppression timescales, $\tau_{\rm env} > 0$; $\tau_{\rm env}$ acts to smooth out dependencies of $f_{\rm Q}$ on $t_{\rm delay}$. This delay in quenching due to longer $\tau_{\rm env}$ values also results in an offset between the maximum possible $f_{\rm Q}$ as a function of $t_{\rm delay}$. This offset effect is such that for higher values of $\tau_{\rm env}$ the maximum possible $f_{\rm Q}$ (the turnover point) requires much earlier quenching, significantly before the time of first pericentre. Features on shorter timescales (i.e. bumps and wiggles) shown in our model curves are due to the discrete snapshot times of the N-body simulation used for the orbit library in Oman et al. (2021).

We contrast this with the methodology of Oman et al. (2021), where stellar masses were not truncated by quenching, since for simplicity they did not make use of star formation histories. In that case, there is no turnover effect in $f_{\rm Q}$ as a function of $t_{\rm delay}$ since galaxies

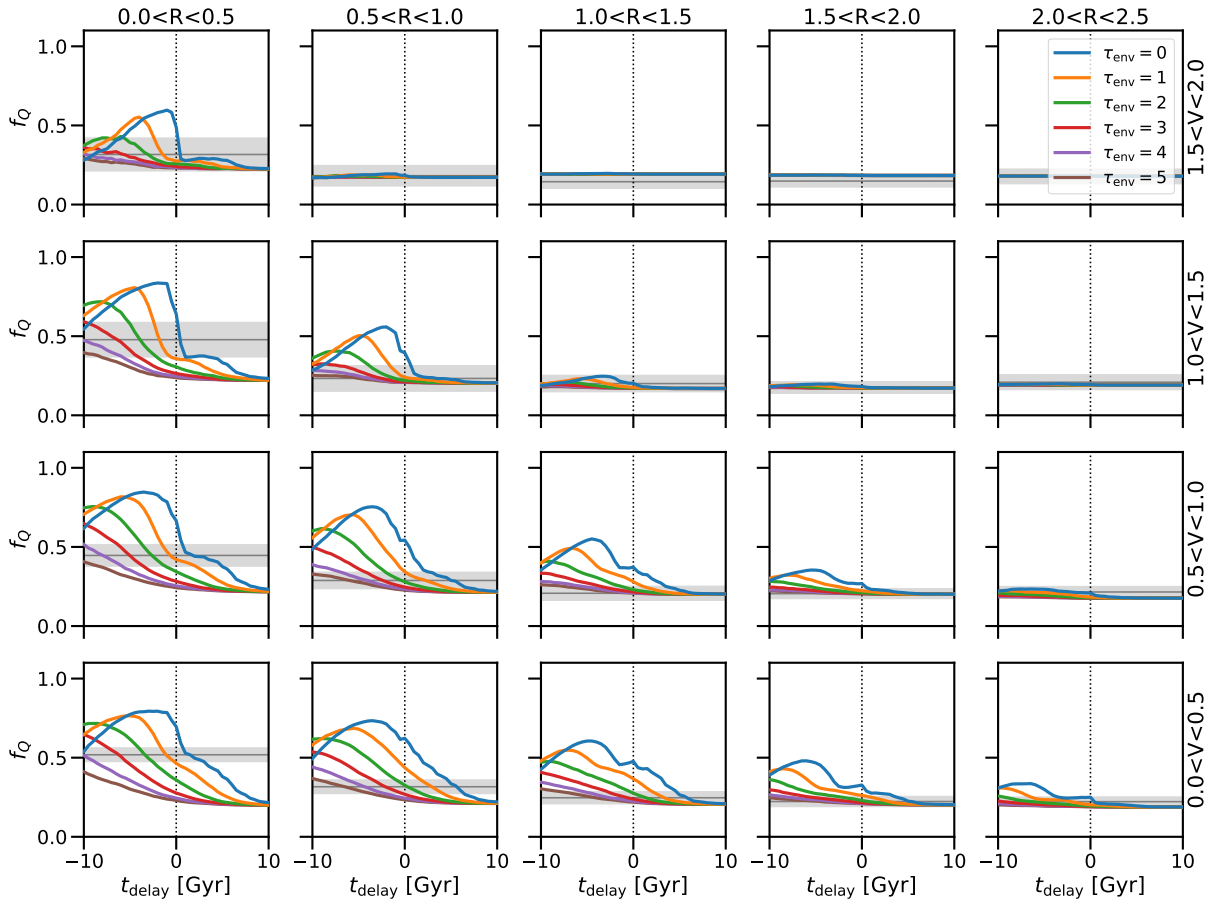

Figure 3.7: Quiescent fraction, $f_{\rm Q}$, predictions for $9 < \log(M_\star/{\rm M}_\odot) < 10$ galaxies for a range of models where galaxies quench after some delay time, $t_{\rm delay}$, relative to the time of first pericentre. We show models for a range of exponential suppression timescales. The SDSS mean $f_{\rm Q}$ values are shown as grey lines, with the shaded regions showing the bootstrapped (over clusters) uncertainty in the mean.

are not dropping out of the stellar mass range. That said, the $f_{\rm Q}$ data do not prefer excessively negative values of $t_{\rm delay}$ and so the shift in preferred delay time compared to our choice of truncating stellar masses is rather minimal: it simply causes an offset of ~ 0.5 Gyr (earlier) relative to our model.

In PPS, the models reproduce the general trends in $f_{\rm Q}$ visible in the SDSS data, but there is clearly significant degeneracy in the preferred model (i.e. which $t_{\rm delay}$, $\tau_{\rm env}$ combination is preferred). In order to break this degeneracy, we need another observable beyond the quiescent fraction to constrain $t_{\rm delay}$ and $\tau_{\rm env}$. As mentioned earlier, we will use observationally-derived stellar ages of galaxies for this purpose. We explore model predictions for stellar ages of galaxies in PPS in the next section.

3.3.3 Stellar ages: comparison of models and data

We now compare our models of stellar age to the SDSS data. As in the previous section, in Fig. 3.8, we plot the mean ΔMWAs as a function of $t_{\rm delay}$ in bins of PPS coordinates R and V for $9 < \log(M_\star/{\rm M}_\odot) < 10$. For the equivalent plot for $10 < \log(M_\star/{\rm M}_\odot) < 10.5$ galaxies, see Fig. B.2 in Appendix B.4. We note that for the infalling galaxies, we find that our fits prefer offsets of $\delta{\rm MWA}_{\rm infall} = 0.59 \pm 0.12$ Gyr and $\delta{\rm MWA}_{\rm infall} = 0.47 \pm 0.07$ Gyr for $9 < \log(M_\star/{\rm M}_\odot) < 10$ and $10 < \log(M_\star/{\rm M}_\odot) < 10.5$ galaxies (shown in Table 3.1), which correspond to infalling MWAs of $6.70^{+0.11}_{-0.13}$ Gyr and 7.63 ± 0.07 Gyr.

As in the previous section, looking at e.g. the innermost, low-velocity bin ($R < 0.5, V < 0.5$), we see no effect on ΔMWA for very long quenching delay times, with the effect on ΔMWA usually increasing with decreasing $t_{\rm delay}$ (earlier onset of quenching). This general trend, for the most part, is similar for different values of $\tau_{\rm env}$, but with shallower slopes for higher values of $\tau_{\rm env}$. Or, put another way, a longer timescale for the suppression of star formation (a higher value of $\tau_{\rm env}$) would require an earlier onset of quenching to have the same degree of impact on the stellar age. Interestingly, the trend in higher ΔMWA for earlier onset of quenching relative to time of first pericentre is not monotonic for all values of $\tau_{\rm env}$: for example, for $\tau_{\rm env} \sim 0$ (instantaneous or almost-instantaneous suppression of star formation) around $t_{\rm fp}$ that there is a small $\sim 0.1 - 0.3$ Gyr dip. This dip is most pronounced for the higher velocity bins, as this is where galaxies reaching their first pericentre will preferentially be located in PPS – close to the cluster core and moving at a high velocity. Since the figure is only showing the mean ΔMWA of quiescent galaxies, and this region of PPS is dominated by galaxies on their first infall, the influx of recently quenched galaxies lowers the mean ΔMWA relative to values of $t_{\rm delay}$ slightly earlier/later than $t_{\rm delay} \sim -1$ Gyr (the deepest part of the dip). Longer suppression timescales blur out

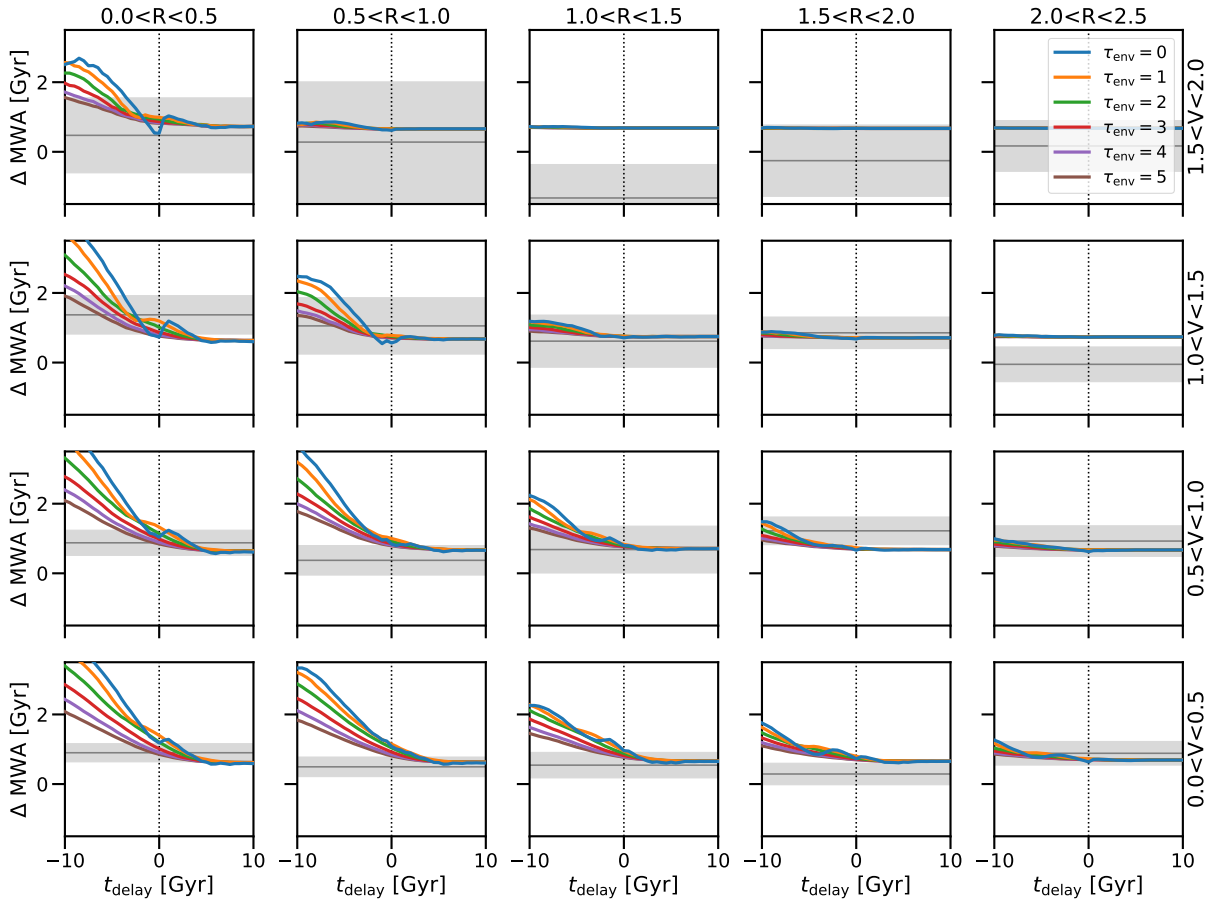

Figure 3.8: Mean ΔMWA predictions for quiescent $9 < \log(M_\star/\mathrm{M}_\odot) < 10$ galaxies for a range of models where galaxies quench after some delay time, relative to time of first pericentre. We show models run for a range of exponential suppression timescales. The SDSS mean ΔMWA values are shown as grey lines, with the shaded regions showing the bootstrapped (over clusters) uncertainty in the mean. Note that our models include an additional offset to allow for the possibility that the infalling population may be different than that of the interloper phase space bins in Eq. 3.6.

Parameter	$9 < \log(M_\star/\mathrm{M}_\odot) < 10$	$10 < \log(M_\star/\mathrm{M}_\odot) < 10.5$
t_{delay}	$3.5^{+0.6}_{-0.9}$ Gyr	$-0.3^{+0.8}_{-1.0}$ Gyr
τ_{env}	≤ 1.0 Gyr†	$2.3^{+0.5}_{-0.4}$ Gyr
$f_{\mathrm{Q,infall}}$	0.16 ± 0.01	0.48 ± 0.01
$\delta\mathrm{MWA}_{\mathrm{infall}}$	0.59 ± 0.12	0.47 ± 0.07

Table 3.1: Best-fitting quenching model parameters, given as the 50$^{\mathrm{th}}$ percentile for each respective marginal posterior probability distribution. Upper and lower uncertainties are the 84$^{\mathrm{th}}$ and 16$^{\mathrm{th}}$ percentiles of the marginal distributions. *Top rows:* The time delay until the onset of quenching relative to the time of a galaxy's first pericentre (t_{delay}), and the exponential star formation suppression timescale after the onset of quenching (τ_{env}). These are the best-fitting values indicated by the black diamond markers for t_{delay} and τ_{env} on the subplots of Fig. 3.9. *Bottom rows:* Best-fitting infalling population values, as described for f_{Q} in Eq. 3.11 and ΔMWA in Eq. 3.16. † indicates that the value is a 95$^{\mathrm{th}}$-percentile upper limit.

this effect. Since the lower velocity regions in the cluster core ($R < 0.5$) are dominated by galaxies that entered the cluster a long time ago, this effect is washed out.

Although the uncertainties on ΔMWA are larger than for f_{Q}, our model still predicts clear trends for ΔMWA across PPS. Because the ΔMWA trends with the timescale parameters differ from those obtained from f_{Q}, we explore the constraints that arise from combining f_{Q} and ΔMWA in the next section.

3.3.4 Fitting and joint constraints of time delay and exponential quenching timescale

By running our model across a range of t_{delay} and τ_{env} values we can jointly constrain these timescale parameters by using the information contained in the trends of f_{Q} and ΔMWA as a function of the PPS coordinates. For each τ_{env} we perform χ^2 fitting to determine the best-fitting t_{delay} value, by minimizing

$$\chi^2 = \sum_i \left(\frac{y_{\mathrm{obs},i} - y_{\mathrm{model},i}}{\sigma_i} \right)^2 . \tag{3.18}$$

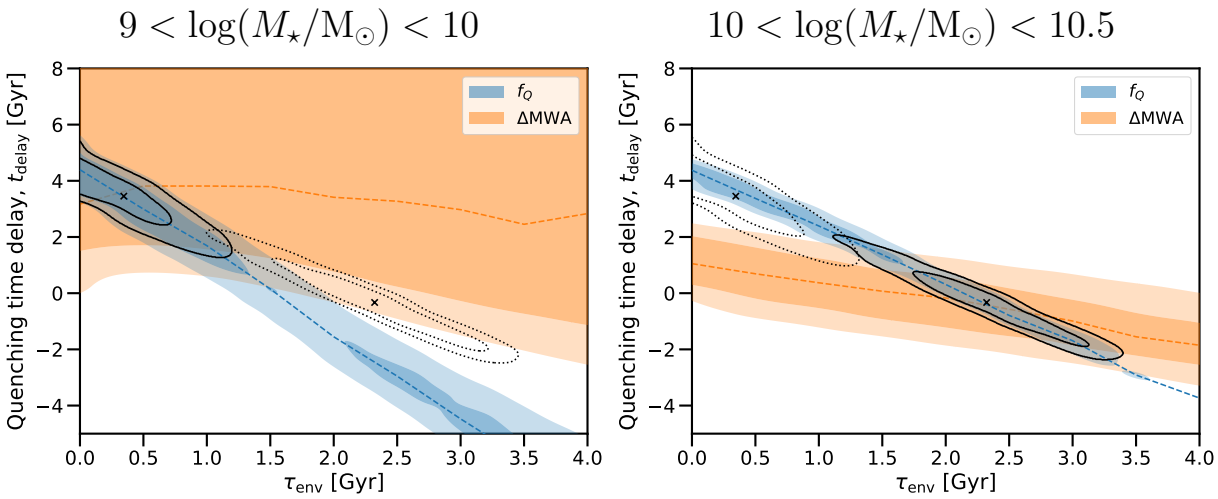

Figure 3.9: Marginal best-fitting parameter values on our model's quenching timescales for the two observables, f_{Q} (blue), mean ΔMWA for quiescent galaxies (orange), as well as joint (black lines/grey shading) for $9 < \log(M_\star/\mathrm{M}_\odot) < 10$ galaxies (left) and $10 < \log(M_\star/\mathrm{M}_\odot) < 10.5$ (right). Uncertainties on the best-fitting parameters are shown with corresponding shaded regions (darker and lighter shaded regions corresponding to the 68% and 95% confidence regions, respectively). The parameters fit here are the quenching delay time relative to time of first pericentre, t_{delay}, and the exponential suppression of star formation timescale, τ_{env}. Dashed lines indicate the best-fitting t_{delay} at a given τ. The joint 68% and 95% confidence region from both observables for t_{delay} and τ_{env} are shown overlaid with black contours. The joint best fitting model, i.e. the location with the peak joint probability, is indicated with a cross symbol. For each plot, the other stellar mass bin's joint constraint is overlaid (black cross and dotted contours). Marginal best-fitting values and uncertainties from the joint constraints are tabulated in Table 3.1.

$y_{\mathrm{obs},i}$ and σ_i are the mean observed SDSS data value and its uncertainty, respectively, for either f_Q or MWA, in a given PPS bin i. $y_{\mathrm{model},i}$ is the modeled value, as defined in Eq. 3.11 and Eq. 3.16, respectively, and is a function of t_{delay}, τ_{env}, and the infall population. The sum is over all PPS bins. We find that the uncertainties on the data may be underestimated, since for the $20 - 3 = 17$ degrees of freedom (20 PPS bins, three free parameters) we find the following reduced χ^2 values: $\chi^2_{\mathrm{red}}(f_{\mathrm{Q}}) \approx 2.75$ and $\chi^2_{\mathrm{red}}(\Delta\mathrm{MWA}) \approx 2.47$ for $9 < \log(M_\star/\mathrm{M}_\odot) < 10$. Similarly, for $10 < \log(M_\star/\mathrm{M}_\odot) < 10.5$ we find $\chi^2_{\mathrm{red}}(f_{\mathrm{Q}}) \approx 1.38$ and $\chi^2_{\mathrm{red}}(\Delta\mathrm{MWA}) \approx 1.25$. A high χ^2 leads to parameter constraints that may be too tight, so to be conservative we inflate the uncertainties on the observed SDSS mean f_{Q} and mean ΔMWA in each PPS bin by a factor of $\sqrt{\chi^2_{\mathrm{red}}}$. We note that uncertainties on the models are negligible as they can be made arbitrarily small simply by sampling more UniverseMachine galaxies.

We present our best-fitting values for t_{delay} as a function of τ_{env} for our observables f_{Q} and ΔMWA in Fig. 3.9, for both $9 < \log(M_\star/\mathrm{M}_\odot) < 10$ (left panel) and $10 < \log(M_\star/\mathrm{M}_\odot) < 10.5$ (right panel) stellar mass bins. Consistent with the PPS results presented in Section 3.3.3, ΔMWA provides a constraint on t_{delay} that depends only weakly on τ_{env}. For f_{Q} there is a steeper trend between the fit t_{delay} for a given τ_{env}. These relations make sense intuitively: as f_{Q} depends on the distributions of SFRs at a given moment in time, it can be greatly impacted by any change in the timescale of SFR suppression, τ_{env}. ΔMWA, on the other hand, will not change significantly with τ_{env} since the bulk of stellar mass growth occurred in the past and will mainly depend on the time at which a galaxy has quenched.

Also shown in Fig. 3.9 are contours showing the confidence intervals for t_{delay} and τ_{env} jointly when combining f_{Q} and ΔMWA. We list our best-fitting joint values with uncertainties (16^{th} and 84^{th} percentiles) defined by the t_{delay} and τ_{env}'s marginal probability distributions in Table 3.1.

Looking first at the $9 < \log(M_\star/\mathrm{M}_\odot) < 10$ bin in Fig. 3.9 (left panel), quenching time delay relative to time of first pericentre is preferred to be $t_{\mathrm{delay}} = 3.5^{+0.6}_{-0.9}$ Gyr. We find a relatively rapid suppression of star formation once quenching has started, with a best-fitting $\tau_{\mathrm{env}} \leq 1.0$ Gyr (95% confidence level used as an upper bound). We choose to use a one-sided upper limit for τ_{env} for the lower stellar mass bin, as the probability distribution for τ_{env} is not Gaussian, peaking at $\tau_{\mathrm{env}} \sim 0$ and the 50^{th}-percentile occurring at $\tau_{\mathrm{env}} = 0.3$ Gyr.

Turning to the higher stellar mass bin, $10 < \log(M_\star/\mathrm{M}_\odot) < 10.5$ (bottom panel), a different fit is preferred: an earlier onset of quenching, $t_{\mathrm{delay}} = -0.3^{+0.8}_{-1.0}$ Gyr, corresponding to the onset of quenching beginning close to the time of first pericentre. The corresponding

best-fitting $\tau_{\rm env}$ is $2.3^{+0.5}_{-0.4}$ Gyr, indicating a significantly slower suppression of star formation.

3.4 Discussion

We now discuss the meaning of our modelling results and how they contrast with previous literature. For a discussion of the robustness of our results to changes in the overall UniverseMachine star formation histories, see Appendix B.3.

We first compare with the work that we have directly built upon, namely that of Oman et al. (2021) (see also: Oman et al., 2013; Oman & Hudson, 2016). We then compare our results to the alternative framework proposed in the seminal work of Wetzel et al. (2013), followed by other observational studies: Taranu et al. (2014) which made use of stellar age-related spectral indices and Rhee et al. (2020) which used PPS information. Finally, we compare to a study examining the predictions of hydrodynamical simulations (Wright et al., 2022; Lotz et al., 2019).

For the purposes of our discussion, we define a quantity, $t_{\rm Q}$, as the average time for a star-forming galaxy with median sSFR (of a star-forming galaxy) to exponentially decline in SFR until it crosses the UniverseMachine quenching threshold of $10^{-11}\,{\rm yr}^{-1}$. For our lower (higher) stellar mass bin this difference in sSFR is ~ 1.0 dex (~ 0.8 dex). Assuming a constant stellar mass for simplicity, the quenching timescale is $t_{\rm Q} = t_{\rm delay} + 2.33\tau_{\rm env}$ ($t_{\rm Q} = t_{\rm delay} + 1.82\tau_{\rm env}$). These timescales are summarized in Table 3.2 and their contours are also plotted in Fig. 3.10.

3.4.1 Oman et al. (2021)

The satellite quenching model of Oman et al. (2021), based on modelling quiescent fractions in PPS, employs a maximum likelihood model constraining four parameters: the quiescent fraction of an infalling population ($f_{\rm before}$), the final quiescent fraction of galaxies after satellite quenching has taken place ($f_{\rm after}$, set to zero for their core analysis), the time at which half of the drop in quiescent fraction is complete ($t_{\rm mid}$, relative to time of first pericentre), and the timescale to go from the initial to final quiescent fraction (Δt). For the purpose of consistency across the following discussion sections, we will refer to the quenching time as $t_{\rm Q}$ rather than $t_{\rm mid}$.

We've previously discussed how the preferred time of quenching in Oman et al. (2021)

Study	Quantity	Lower $M_\star$ bin	Higher $M_\star$ bin
This work (best)	$\boldsymbol{t_Q}$	$\mathbf{4.3 \pm 0.4}$ **Gyr**	$\mathbf{3.9 \pm 0.2}$ **Gyr**
This work ($t_{\rm delay} \equiv 0$)*	$\boldsymbol{t_Q}$	$\mathbf{3.7 \pm 0.4}$ **Gyr**	$\mathbf{4.0 \pm 0.2}$ **Gyr**
Oman+2021	t_Q	3.7 ± 0.2 Gyr	3.4 ± 1.0 Gyr
Wetzel+2013	t_Q	2.4 Gyr	1.5 Gyr
Taranu+2014	t_Q	—	5.0 Gyr
Rhee+2020	t_Q	4.2 Gyr	2.5 Gyr
Wright+2022	t_Q	1.1 Gyr	2.3 Gyr
This work (best)	$\boldsymbol{\tau_{\rm env}}$	$\mathbf{\leq 1.0}$ **Gyr**†	$\mathbf{2.3^{+0.5}_{-0.4}}$ **Gyr**
This work ($t_{\rm delay} \equiv 0$)*	$\boldsymbol{\tau_{\rm env}}$	$\mathbf{1.6 \pm 0.2}$ **Gyr**	$\mathbf{2.2 \pm 0.1}$ **Gyr**
Wetzel+2013	$\tau_{\rm Q,fade}$	0.8 ± 0.2 Gyr	0.5 ± 0.2 Gyr
Taranu+2014	$\tau_{\rm post}$	—	3 Gyr
Rhee+2020	$\tau_{\rm cluster}$	$1.7^{+0.2}_{-0.3}$ Gyr	$1.1^{+0.3}_{-0.2}$ Gyr
Wright+2022	τ	0.4 Gyr	0.9 Gyr

Table 3.2: Comparison of timescales from various literature results to our work; in each table section they are listed in the order in which they appear in Section 3.4. 'Lower' and 'higher' stellar mass bins refer to $9 < \log(M_\star/\mathrm{M}_\odot) < 10$ and $10 < \log(M_\star/\mathrm{M}_\odot) < 10.5$, respectively. *Upper section:* average time t_Q until quenching, relative to time of first pericentre. *Lower section:* exponential timescales τ compared to our exponential suppression best-fitting timescale as well as with the conditional assumption ($*$) that quenching begins at time of first pericentre ($t_{\rm delay} \equiv 0$), using the f_Q contour only. † indicates use of the upper 95% confidence level as an upper bound. Note that definitions of τ in the literature vary; the respective discussion sections should be consulted when making comparisons between τ values.

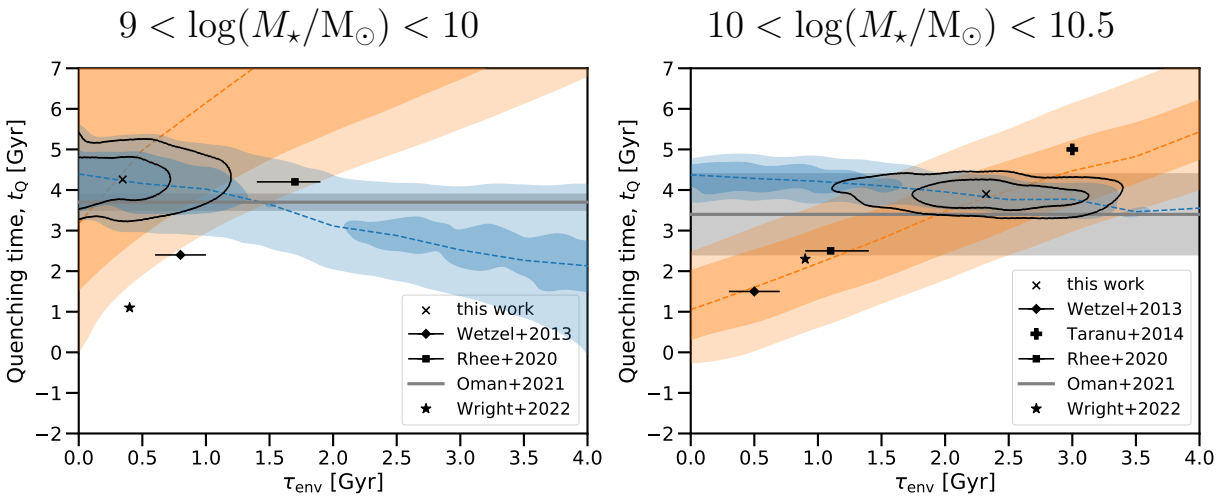

Figure 3.10: Marginal and joint best-fitting parameter values on overall quenching time, t_Q, and τ_{env} for the two observables, f_Q (blue) and quiescent ΔMWA (orange) for $9 < \log(M_\star/\mathrm{M}_\odot) < 10$ galaxies (left) and $10 < \log(M_\star/\mathrm{M}_\odot) < 10.5$ (right), analogous to Fig. 3.9. As well, we have overlaid the t_Q literature values from Table 3.2 with the various points and lines shown in the legend. We omit error bars where it was not straightforward to determine them.

is offset to be $\lesssim 0.5$ Gyr later than ours, since for simplicity they assumed galaxy star formation histories are not truncated by premature quenching.

They find a nearly flat $t_{\rm Q}$ relation with stellar mass (excluding $\log(M_\star/{\rm M}_\odot) \gtrsim 10.5$), with $t_{\rm Q} = 3.7 \pm 0.2$ Gyr and $t_{\rm Q} = 3.4 \pm 1.0$ Gyr for our lower and higher stellar mass bins, respectively. We find consistent overall quenching times ($t_{\rm Q}(t_{\rm delay} = 0) = 3.7 \pm 0.4$ Gyr and $t_{\rm Q}(t_{\rm delay} = 0) = 3.9 \pm 0.2$ Gyr, respectively). Relaxing this assumption, our model is still consistent with theirs, although the lower stellar mass bin $t_{\rm Q}$ increases slightly, by ~ 0.5 Gyr.

Oman et al. (2021) were unable to provide strong constraints on their Δt parameter; they find that it tends to be underestimated, e.g. with the median value (based on the probability density from the model) underestimated by up to ~ 1 Gyr at lower stellar masses. They note that this effect is due to resolution issues in the N-body simulation resulting in low-mass satellite haloes being disrupted too early. Values of $\Delta t \sim 1 - 1.5$ Gyr were preferred by their modelling, but with very large uncertainties, which they marginalized over for their primary analysis to get their tight constraints on $t_{\rm Q}$ and the quiescent fraction parameters. They note that the resolution effect could mask a decreasing trend in $t_{\rm Q}$, which could likewise occur in our modelling.

3.4.2 Wetzel et al. (2013)

Wetzel et al. (2013) found that satellites falling into a cluster experience 'delayed-then-rapid' quenching. One difference between their model and ours is that although Wetzel et al. (2013) fits a delayed-then-rapid model with an exponentially declining sSFR (specifically, their parameters are: time delay, $t_{\rm Q,delay}$, and 'fading timescale', $\tau_{\rm fade}$), our model relies on the star formation histories of UniverseMachine which are stochastic rather than a simple smooth analytical function.

Another important difference in the models is the treatment of pre-processing of galaxies prior to entering the cluster. In our model, a simulated infalling population is used to account for pre-processing, whereas in Wetzel et al. (2013) the infall quenching 'clock' for a given galaxy starts on first infall into any larger halo, i.e. when a central becomes a satellite. Because of this, one would expect their (average) quenching time delay to be longer, as their quenching time delay includes the time spent in smaller groups prior to infalling into the main cluster progenitor. The magnitude of the median difference between time of first infall into any halo and infall into the final cluster is 3.2 Gyr (their fig. 2; assuming $\log M_{\rm 200c/M_\odot}(z = 0) = 14.2$ – our median host halo mass).

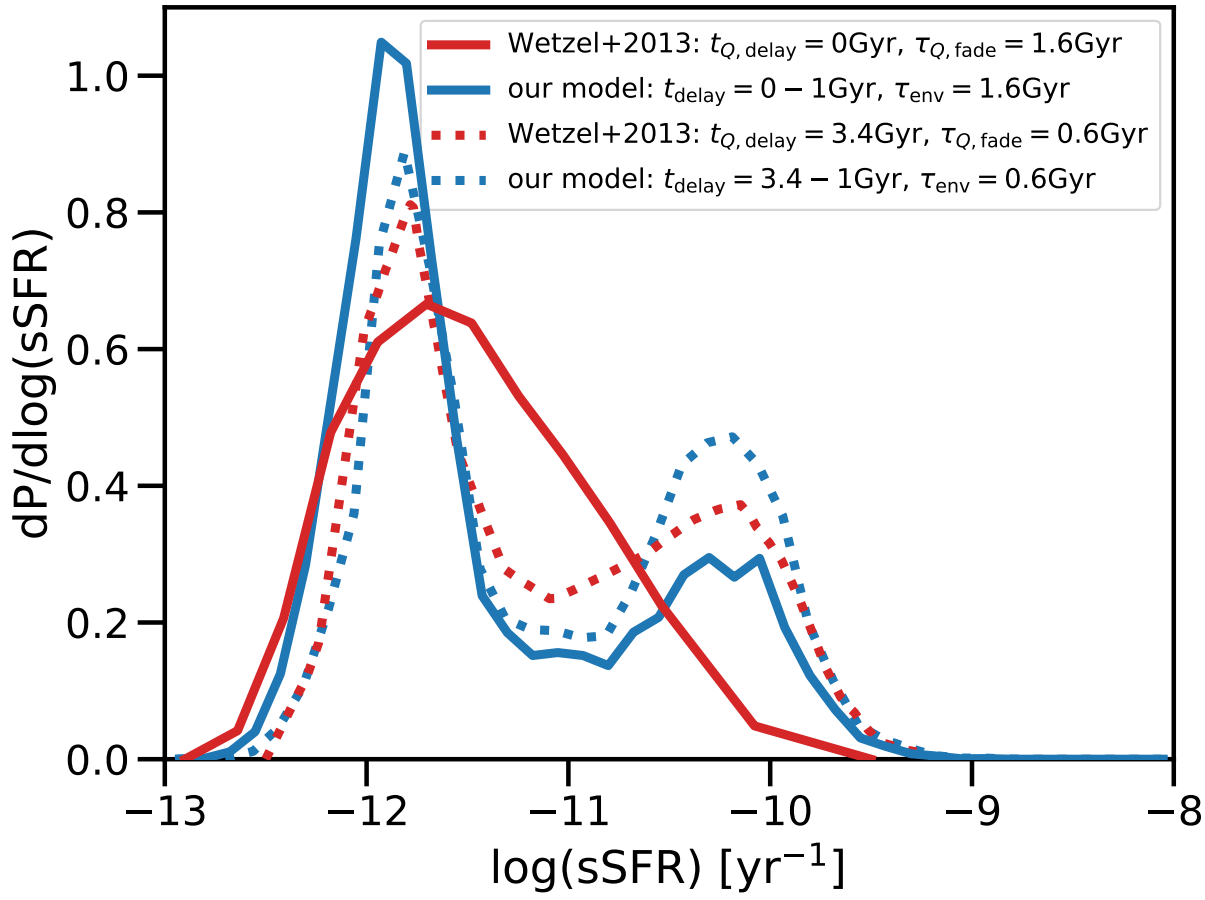

Figure 3.11: Our model displays a persistent bimodality in sSFR distribution, regardless of SFR suppression timescale, whereas Wetzel et al. (2013) finds a unimodal distribution for long suppression times (contrast the red solid line for their model with the blue solid line for our model). This arises because of our use of a stochastic star formation history, whereas they use smooth star formation histories. In particular, we are contrasting with fig. 9 in Wetzel et al. (2013), for our $10 < \log(M_\star/\mathrm{M}_\odot) < 10.5$ stellar mass bin and their $10.1 < \log(M_\star/\mathrm{M}_\odot) < 10.5$ stellar mass bin. A correction of -1 Gyr is added to be comparable to their average infall time, which has the time zero-point set at r_{vir}. Additionally, for ease of comparison with Wetzel et al. (2013), who claimed need for a short exponential suppression timescale to reproduce the bimodality, we include only galaxies within $r_{200\mathrm{c}} \approx 0.73 r_{360\mathrm{m}}$ and add log-normal scatter with mean $\log(\mathrm{sSFR}/\mathrm{yr}^{-1}) = -12$ and 0.25 dex variance to all galaxies with $\log(\mathrm{sSFR}/\mathrm{yr}^{-1}) < -12$.

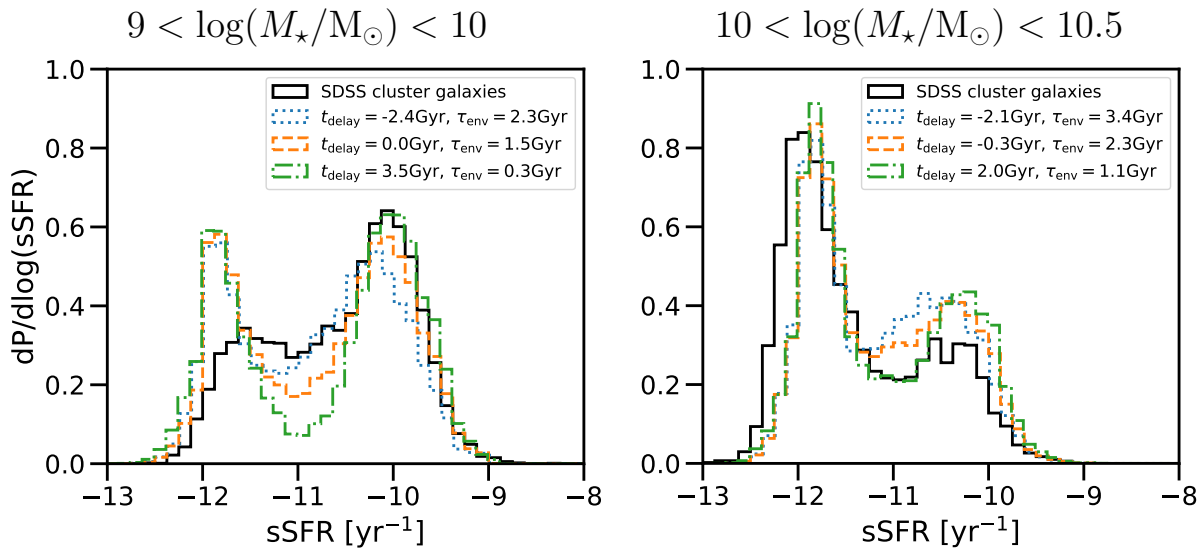

Figure 3.12: Similar to Fig. 3.11, except we now demonstrate how we can reproduce the bimodality in the sSFR distributions of the SDSS data (solid black histogram) for a range of relevant models with different exponential quenching timescales (coloured lines) for our two stellar mass bins, $9 < \log(M_\star/\mathrm{M}_\odot) < 10$ (left) and $10 < \log(M_\star/\mathrm{M}_\odot) < 10.5$ (right). The left panel shows three scenarios, which are (in the order that they are listed in the legend): (i) long τ equal to that preferred for our higher stellar mass bin, but $t_{\rm delay}$ taken from along the $f_{\rm Q}$ error contour, (ii) a scenario where $t_{\rm delay} = 0$, with $\tau_{\rm env}$ chosen to minimize χ^2 (see Fig. 3.9), (iii) 50$^{\rm th}$ percentile of our timescale parameters. The right panel is similar, showing: (i) rightward end of the 95% confidence level ellipse, (ii) best-fitting timescale parameters, (iii) leftward end of the 95% confidence level ellipse. It is worth noting that there is an offset in $f_{\rm Q}$ not factored into the above model histograms, equal to that described in Section 3.3.2, and that the quenching sSFR cut for SDSS has some stellar mass dependence, rather than a simple sSFR $= 10^{-11}\,\mathrm{yr}^{-1}$cut.

Quenching delay time

To compare their model with ours, we must account for the two populations of galaxies falling into clusters which will have different quenching times relative to time of first pericentre in the $z \sim 0$ cluster: those that are already satellites in some smaller halo which have had their quenching clock start at some earlier time (A) and those that are falling into a larger halo for the first time (B). For case (A), according to the fits of Wetzel et al. (2013) for a $9 < \log(M_\star/\mathrm{M}_\odot) < 10$ galaxy, the full time until quenching for a galaxy that became a satellite in a $\log(M_{\rm vir}/\mathrm{M}_\odot) > 14$ cluster is ~ 5.7 Gyr (interpolated). Taking the median time between first infall and infall into the cluster to be ~ 3.2 Gyr (see fig. 2 of Wetzel et al., 2013) and time from $r_{\rm vir}$ to first pericentre in the final $\log(M_{\rm vir}/\mathrm{M}_\odot) > 14$ cluster to be ~ 1 Gyr (Oman et al., 2013), we would expect such galaxies to quench $\bar{t} \sim 1.5$ Gyr after first pericentre on average. We note that these pre-processed galaxies are quenching earlier than they would in a scenario where quenching occurs only due to infall into the final cluster host. For case (B), according to their fits for galaxies falling into $\log(M_{\rm vir}/\mathrm{M}_\odot) > 14$ clusters, the full time until quenching is $t_{\rm Q} \sim 4.8$ Gyr for $9 < \log(M_\star/\mathrm{M}_\odot) < 10$ galaxies, or about ~ 3.8 Gyr after first pericentre. The relative proportions of the (A) and (B) scenarios are ~ 0.6 and ~ 0.4, respectively (see Wetzel et al., 2013, fig. 1).

These approximations give an average quenching time, relative to time of first pericentre, of $t_{\rm Q} \sim 0.6(1.5\,\mathrm{Gyr}) + 0.4(3.8\,\mathrm{Gyr}) \sim 2.4\,\mathrm{Gyr}$. The same calculation for our higher stellar mass bin gives $t_{\rm Q} \sim 1.5$ Gyr. These are shorter, by ~ 1.9 Gyr and ~ 2.4 Gyr, than our quenching times of $t_{\rm Q} = 4.3 \pm 0.4$ Gyr and $t_{\rm Q} = 3.9 \pm 0.2$ Gyr, for our lower and higher stellar mass bins, respectively.

Fading time and sSFR bimodality

Wetzel et al. (2013) claim that in order for the bimodality in the sSFR distribution to persist across environments, including in the most massive clusters, infall-induced quenching requires a short exponential timescale, $\tau_{\rm Q,fade} < 1$ Gyr (they find $\tau_{\rm Q,fade} = 0.8 \pm 0.2$ Gyr and $\tau_{\rm Q,fade} = 0.5 \pm 0.2$ Gyr for our lower and higher stellar mass bins, respectively). For longer SFR fading timescales (~ 2 times their best-fitting $\tau_{\rm fade}$), their model predicts no bimodality in the sSFR distribution, but rather a unimodal distribution peaking near the centre of the 'green valley' ($\log(\mathrm{sSFR}) \sim -11.2$ for $\log(M_\star/\mathrm{M}_\odot) < 10.5$ galaxies), which we illustrate in Fig. 3.11. This occurs because their model assumes a smooth exponentially-declining star formation history for the infalling galaxies, and a gentle fading leads to galaxies passing through the green valley too slowly to maintain the bimodality.

We find our lower stellar mass bin exponential timescale ($\tau_{\rm env} \leq 1.0$ Gyr) is consistent with theirs, but our higher stellar mass bin value of $\tau_{\rm env} = 2.3^{+0.5}_{-0.4}$ Gyr is significantly longer than their $\tau_{\rm Q,fade} \sim 0.5 \pm 0.2$ Gyr. However, these fading times are different quantities: $\tau_{\rm Q,fade}$ in Wetzel et al. (2013) represents the fading time of an individual galaxy, whereas our $\tau_{\rm env}$ is a population-wide fading 'envelope' which multiplies the stochastic star formation histories of individual UniverseMachine galaxies. The stochasticity in star formation histories is due to significant variations in SFR of UniverseMachine galaxies, which occur by design: in this model, SFR tracks the accretion rate of baryonic matter, as well having a random variability on short timescales ($\sim 10-100$ Myr). This stochasticity allows the sSFR distribution to be bimodal even in the case of a long $\tau_{\rm env}$. Because of the rapid changes in SFR for UniverseMachine galaxies, they do not spend significant amounts of time in the green valley, whether or not their SFRs are forced to decline by our exponential suppression envelope (visually illustrated in Fig. 3.5). The SFRs of infalling galaxies undergoing satellite quenching drop below the sSFR quenched threshold much more abruptly than a suppressed smooth star formation history, so longer fading/suppression envelopes are allowed.

From a qualitative comparison of the scenarios in Fig. 3.12, a longer $\tau_{\rm env} \gtrsim 2.3$ Gyr is preferred by the depth of the green valley for $9 < \log(M_\star/{\rm M}_\odot) < 10$ galaxies, rather than a short $\tau_{\rm env} \leq 1.0$ Gyr preferred by the $f_{\rm Q}$ and ΔMWA constraints. We note that the location of the star forming peak of the sSFR distribution is better fit by e.g. $t_{\rm delay} = 0$ Gyr and $\tau_{\rm env} \sim 1.5$ Gyr. For $10 < \log(M_\star/{\rm M}_\odot) < 10.5$ galaxies, we find that the relative depth of the green valley implies a preference for longer $\tau_{\rm env}$, e.g. $\tau_{\rm env} \gtrsim 2.3$ Gyr, which is our best-fitting result.

A robust quantitative comparison of infall quenching models using additional sSFR distribution features, aside from f_Q, clearly requires controlling for type of star formation history. The depth of the green valley depends on whether the assumed star formation histories are smooth or stochastic and the specific choice of stochasticity made in UniverseMachine is not unique. Additionally, measured star formation rates of quiescent galaxies have high systematic uncertainties regardless of how they are obtained (Brinchmann et al., 2004; Salim et al., 2007; Wetzel et al., 2012; Hayward et al., 2014), meaning that much of the shape of the quiescent bump is determined by observational systematics, rather than quenching physics. As such, we do not utilize additional features of the sSFR distribution beyond f_Q, as they do not appear informative or robust in constraining our infall quenching model and comparing it to e.g. Wetzel et al. (2013).

3.4.3 Taranu et al. (2014)

Using an approach broadly similar to our work, Taranu et al. (2014) combined a star formation and quenching model with information from a library of subhalo orbits from N-body simulations of 4 rich clusters with $\log(M_{200c}/\mathrm{M}_\odot) > 15$, with median stellar masses in their sample of $\log(M_\star/\mathrm{M}_\odot) = 10.4$. They compared model predictions to observed bulge and disc colours and are one of the only previous studies (see also Upadhyay et al., 2021, for an attempt with a spectroscopic sample of 11 galaxies) to make use of age-sensitive stellar absorption line-strength indices for constraining cluster infall quenching times using radial information. Since galaxy disc colours are particularly affected by environment, they can be used to constrain the quenching timescale and location of quenching onset in the cluster using their median trends in cluster-centric radius. They used the age-sensitive Balmer lines of luminous passive cluster galaxies, which are more sensitive to older stellar populations than disc colours.

From their set of models, they found that quenching starting shortly before the time of first pericentre (within a quenching radius of $0.5r_{200c}$, which is ~ 0.5 Gyr prior to the time of first pericentre for a galaxy on first infall) produced the best fits to disc colours as a function of radius. They found that delayed-then-rapid models lead to an excessively large slope in galaxy disc colour versus cluster-centric radius, and also overpredict the strength of the Balmer lines. Instead, their preferred model is one with a gentle exponential quenching timescale of $\tau_{\mathrm{post}} \sim 3$ Gyr, consistent with the τ_{env} that we find for the higher stellar mass bin. This corresponds to a total quenching time of $t_{\mathrm{Q}} \sim 5$ Gyr, longer than ours by ~ 0.7 Gyr (see Table 3.2).

3.4.4 Rhee et al. (2020)

Rhee et al. (2020) fit a quenching model to disc galaxies in $z = 0.08$ clusters. Infall is defined as when a galaxy first crosses $1.5R_{\mathrm{vir}}$. They follow an approach similar to ours, parametrizing quenching with a time delay followed by an exponential suppression of star formation, but instead of modelling the quiescent fraction they model the full SFR distribution of galaxies as a function of position in PPS.

They find that the time delay from infall until the onset of quenching is 2 Gyr for all stellar masses $\log(M_\star/\mathrm{M}_\odot) > 9.5$. The time for a galaxy to fall from their infall definition of $1.5R_{\mathrm{vir}}$ to first pericentre is ~ 1.3 Gyr. We can then subtract this from their quenching time since infall (as presented as t_{Q} in their table 1 for similar stellar mass bins), giving $5.45\,\mathrm{Gyr} - 1.3\,\mathrm{Gyr} \sim 4.2\,\mathrm{Gyr}$ and $\sim 3.8\,\mathrm{Gyr(interpolated)} - 1.3\,\mathrm{Gyr} = 2.5\,\mathrm{Gyr}$ for our lower

and higher stellar mass bins, respectively. This is consistent with our lower stellar mass bin (we find $t_{\rm Q} \sim 4.3 \pm 0.4$ Gyr) but earlier for our higher stellar mass bin by ~ 1.4 Gyr (our $t_{\rm Q} \sim 3.9 \pm 0.2$ Gyr).

This difference in trend with stellar mass between our results and those of Rhee et al. (2020) is not due to a difference in delay times, but rather is due to their SFR suppression timescale, $\tau_{\rm cluster}(z = 0)$, which declines with increasing stellar mass over our stellar mass range, whereas we find the opposite trend. We note that they add a redshift-dependent factor to their quenching timescale $\tau_{\rm cluster}(z_{\rm inf}) = \tau_{\rm cluster,0}(1+z)^{-\alpha}$ and to the quenching time delay timescale (due to the redshift evolution of the dynamical time in clusters), $t_{\rm d}(z_{\rm inf}) = t_{\rm d,0}(1 + z_{\rm inf})^{-1.5}$. This only results in a small correction (a decrease by ~ 10 per cent if we use e.g. $z = 0.5$, the time at which an average galaxy has fallen into the cluster). For $z = 0$, they find $\tau_{\rm cluster,0} = 1.7^{+0.2}_{-0.3}$ Gyr and $\tau_{\rm cluster,0} \sim 1.1^{+0.3}_{-0.2}$ Gyr for our lower and higher stellar mass bins, respectively. This is consistent with our lower stellar mass bin's $\tau_{\rm env}(t_{\rm delay} = 0) = 1.6 \pm 0.2$ Gyr, but more rapid than our higher stellar mass bin's $\tau_{\rm env}(t_{\rm delay} = 0) = 2.2 \pm 0.1$ Gyr, respectively.

3.4.5 Comparison with hydrodynamical simulations

A study directly comparable to ours, which examines quenching in the EAGLE hydrodynamical simulations, is that of Wright et al. (2022). Their work provides an orbital analysis of galaxies' gas inflow, stripping, star formation and quenching. Stripping of infalling galaxies' hot gas begins at 2–3 virial radii from the host and takes longer for high-mass satellites ($\log(M_\star/{\rm M}_\odot) > 10$). This begins the process of starvation and the removal of the hot gas 'buffer', resulting in galaxies becoming vulnerable to cold gas stripping. They refer to the hot gas halo as having a protective effect, as they observe that the onset of significant cold gas stripping only begins after stripping of the hot gas halo is complete. In their work, they include both HI and molecular hydrogen in the mass of cold gas in a galaxy.

For low-mass satellites ($\log(M_\star/{\rm M}_\odot) < 10$), they find that suppression of gas cooling onto the galaxy becomes permanent after hot gas stripping, normally occurring around the time of first pericentre. Some high-mass satellites, on the other hand, retain small hot gas reservoirs, and continue to cool gas for star-formation after first pericentre. Cold gas stripping is shown to be periodic, being strongest for galaxies near pericentre, as that is when density and velocity is at a maximum, hence maximizing the ram-pressure force ($P_{\rm ram} \propto \rho_{\rm ICM} v^2$). All of this results in the following: low mass satellites experience very efficient ram-pressure stripping of cold gas, leading to rapid quenching, whereas high mass satellites experience less efficient stripping and a more gradual starvation-like scenario after their first pericentre.

In terms of quenching, we note that Wright et al. (2022) remove pre-processed infalling satellites, namely those galaxies which were satellites in a host halo with $\log(M_{200}/\mathrm{M}_\odot) \geq 12$ prior to falling into the current host (≈ 30 per cent of infalling galaxies). This handling of pre-processing is somewhat different from ours, as we fit the pre-processed quiescent fraction for infalling galaxies and focus on the differential quenching (relative to the infalling population) in the final $z = 0$ cluster.

To compare our quenching timescales with Wright et al. (2022), we compare the time required for a galaxy of average sSFR (see their fig. 7) to cross the quenching threshold and assume $t_{\rm delay} = 0$ to find an approximate average quenching time relative to the time of first pericentre. Wright et al. (2022) finds median quenching times $0.25\langle T_{\rm orb}\rangle = 0.25(4.5\,\mathrm{Gyr}) = 1.1$ Gyr and $0.65\langle T_{\rm orb}\rangle = 0.65(3.5\,\mathrm{Gyr}) = 2.3$ Gyr relative to the time of first pericentre, for their $9 < \log(M_\star/\mathrm{M}_\odot) < 10$ and $10 < \log(M_\star/\mathrm{M}_\odot) < 11$ bins, respectively. For the higher stellar mass galaxies, the majority (~ 80 per cent) are quenched by second pericentre. We find longer quenching times of $t_{\rm Q} = 3.7 \pm 0.4$ Gyr for $9 < \log(M_\star/\mathrm{M}_\odot) < 10$ galaxies and $t_{\rm Q} = 4.0 \pm 0.2$ Gyr for $10 < \log(M_\star/\mathrm{M}_\odot) < 10.5$ galaxies. Using similar reasoning, their SFR suppression is equivalent to an exponential suppression time of $\tau \sim 0.4$ Gyr and ~ 0.9 Gyr for our lower and higher stellar mass bins, respectively. Taking $t_{\rm delay} = 0$, our $\tau_{\rm env}$ is significantly longer, by 1.2 Gyr and 1.3 Gyr, respectively. Relaxing $t_{\rm delay} = 0$, we find little to no change in preferred $t_{\rm Q}$, but results in our preferred exponential suppression timescale being consistent with theirs for lower stellar mass galaxies.

Based on this discussion, we conclude that we prefer significantly longer total quenching timescales than Wright et al. (2022). If we assume $t_{\rm delay} = 0$, as their models predict, then we find that our star formation suppression timescales, $\tau_{\rm env}$, are longer than theirs by $1.2 - 1.3$Gyr.

A similar previous study is that of Lotz et al. (2019), which instead examined $z \sim 0$ quiescent fractions in the Magneticum Pathfinder hydrodynamical simulation. They found that most $\log(M_\star/\mathrm{M}_\odot) < 10.5$ galaxies are quenched within ~ 1 Gyr of crossing r_{200c} (i.e. around the time of first pericentre), with the relatively small fraction of galaxies with tangential orbits and very high stellar masses able to maintain star formation after first pericentre. This quenching is significantly earlier than we find for both of our stellar mass bins, and all of the results examined in our discussion above.

3.4.6 Towards a consistent model of quenching

There is ample observational evidence that ram pressure stripping of the cold gas starts at or just before first pericentre. For example, Smith et al. (2010) found that ram-pressure

stripped tails of Coma cluster galaxies were prevalent within half of the cluster virial radius and that most of these tails pointed away from the cluster, indicating that the stripping was occurring on infall, i.e. just before pericentre. Studies of the distribution of HIabundance as a function of the PPS coordinates (Jaffé et al., 2015; Oman et al., 2021) find that HIdepletion begins close to pericentre, i.e within $0.5r_{200c}$, in agreement with Smith et al. (2010). However, quenching is not instantaneous and likely proceeds from outside inwards if it is due to ram-pressure stripping (Boselli et al., 2022). Owers et al. (2019) studied cluster galaxies with spatially resolved spectroscopy and uncovered a population of galaxies with strong Hδ absorption – indicative of recent quenching – in their outskirts, but these same galaxies had ongoing star formation in their centres. They modeled the distribution of these galaxies in PPS, finding indications that galaxies with a recent quenching event in their outskirts are within 1 Gyr of entering within $0.5r_{200c}$ of the cluster centre.

That quenching should start at (or just before) pericentre is supported by our results for our higher stellar mass bin ($t_{\rm delay} = -0.3\pm^{+0.8}_{-1.0}$ Gyr) but is at odds with our results for low stellar mass galaxies. For these we find that the onset of quenching occurs well past pericentre $t_{\rm delay} = 3.5\pm^{+0.6}_{-0.9}$ Gyr and with a fast quenching envelope ($\tau_{\rm env} \leq 1.0$ Gyr). Such a short quenching timescale, however, would predict a deep 'green valley' in the sSFR distribution, inconsistent with the observed shallow depth (see Fig. 3.12). For the lower stellar mass bin, quenching starting at pericentre ($t_{\rm delay} = 0$) is permitted by the quiescent fraction but disfavoured by the stellar ages at the $\gtrsim 2\sigma$ level (see Fig. 3.9). This preference is driven by there being little-to-no gradient in ΔMWA between galaxies in the cluster core and those infalling, as shown in Fig. 3.4. This result, however, appears to be driven partly by the very lowest stellar mass galaxies: if we restrict analysis to $9.5 < \log(M_\star/{\rm M}_\odot) < 10$, we find somewhat better compatibility with $t_{\rm delay} = 0$. If we fix $t_{\rm delay} = 0$, as suggested by other observational and theoretical evidence, then, for the lower stellar mass bin, we find slower quenching with $\tau_{\rm env} = 1.6 \pm 0.2$ Gyr. This timescale is in better agreement with the sSFR distribution in Fig. 3.12. For the higher stellar mass sample, the quenching timescale is longer, with $\tau_{\rm env} = 2.2 \pm 0.1$ Gyr, and is in reasonable agreement with the sSFR distribution. While the SFR suppression timescales that we find are longer than those found in hydrodynamical simulations (see Section 3.4.5), they are shorter than the gas depletion timescales of 3.5–4 Gyr for field galaxies of comparable stellar mass (Boselli et al., 2014).

Taking all of these results together suggests a picture in which ram pressure stripping starts close to pericentre and is effective in a satellite galaxy's outskirts (where the restoring force is low compared to the force due to ram pressure) but may not be fully effective in their more tightly bound inner regions. For gas in the inner regions, while there may be no inflow of new cold gas (due to the complete stripping of the hot gas in the halo), the

remaining cold gas will then be consumed by star formation. This consumption timescale is shorter than in the field for two reasons: first, because there is less cold gas available due to the stripping in the outskirts; and second, because ram pressure stripped galaxies have modestly-enhanced star formation rates at fixed stellar mass, compared to similar galaxies in the field, of 0.2–0.3 dex (Roberts & Parker, 2020; Roberts et al., 2022).

3.5 Conclusions

We have combined SDSS photometry and spectroscopy, orbital information from tracking haloes in an N-body simulation, and simulated galaxies from the UniverseMachine empirical model to constrain a simple model that suppresses star-formation histories of galaxies that have fallen into clusters. In the model, an infalling galaxy will have its star formation rate suppressed by an exponential envelope with timescale $\tau_{\rm env}$ after some delay time $t_{\rm delay}$, relative to the time of the first pericentre. The parameter fits from this modeling give the mean quenching timescales for the infalling population as a whole. We jointly fit these model parameters using both the quiescent fraction and mean deviation from the mean MWA–$M_\star$ relation (ΔMWA) of the infalling population in projected phase space. Doing so allows us to break the degeneracy between time of quenching onset and quenching duration that was present in previous models. The method accounts for interloper galaxies (which appear in projection, but are not physically in the cluster), and the pre-processing of infalling galaxies, allowing us to isolate the quenching effect of the (most recent) infall into a massive cluster. Our main results can be summarized as follows:

- The mean mass-weighted stellar age depends on location in projected phase space, with cluster member-dominated regions being older (by $\lesssim 1$ Gyr) relative to an interloper-dominated region.
- Overall quenching times for our two stellar mass bins are driven by the quiescent fraction and are consistent with Oman et al. (2021), whose methodology we build on directly: $t_{\rm Q} = 4.3 \pm 0.4$ Gyr and $t_{\rm Q} = 3.9 \pm 0.2$ Gyr for our lower and higher stellar mass bins, respectively. We find longer overall quenching timescales than other works in the literature where only star-formation rates are modeled, but agree with Taranu et al. (2014), who make additional use of the age-sensitive Balmer lines of quiescent galaxies.
- Using mass-weighted ages allows us to break the degeneracy between $t_{\rm delay}$ and $\tau_{\rm env}$. We find that the onset of quenching occurs at $t_{\rm delay} = 3.5^{+0.6}_{-0.9}$ Gyr and $t_{\rm delay} =$

$-0.3^{+0.8}_{-1.0}$ Gyr, relative to time of first pericentre, for galaxies in our $9 < \log(M_\star/\mathrm{M}_\odot) < 10$ and $10 < \log(M_\star/\mathrm{M}_\odot) < 10.5$ stellar mass bins, respectively. The models prefer a short SFR suppression timescale, $\tau_{\mathrm{env}} \leq 1.0$ Gyr (consistent with ram-pressure stripping), for our lower stellar mass bin, and a longer $2.3^{+0.5}_{-0.4}$ Gyr (consistent with strangulation) for our higher stellar mass bin.

- In contrast to Wetzel et al. (2013), our model is able to reproduce the SFR bimodality even with long exponential suppression timescales, thanks to the stochasticity of the UniverseMachine star formation histories that we employ (as opposed to using smooth analytic star formation histories). We note that, for our lower stellar mass bin, the depth of the green valley prefers values of $\tau_{\mathrm{env}} \gtrsim 1.5$ Gyr and $t_{\mathrm{delay}} \sim 0$, in slight tension with the later quenching onset preferred by ΔMWAs.

Based on these findings and on our detailed discussion of the literature, we argue that satellites infalling into clusters experience ram pressure stripping of cold gas starting close to pericentre, which is only effective in the galaxy's outskirts, at least on the first pericentre passage. This leaves reduced cold gas available for continued star formation, resulting in star formation suppression timescales of $\tau_{\mathrm{env}} \sim 2$ Gyr – longer than if galaxies were fully stripped on their first pericentre passage, but shorter than a simple starvation scenario.

Future surveys like the Bright Galaxy Survey of the Dark Energy Spectroscopic Instrument (DESI) will provide a large increase in sample size over that of the one million galaxies in the SDSS DR14 main galaxy sample (Ruiz-Macias et al., 2021). An increase in sample size of galaxies with spectroscopically-derived MWAs should reduce the errors on ΔMWA significantly. Using spectroscopically-derived quantities more sensitive to recent SFR suppression or quenching, such as the time at which 90 per cent of the stellar mass has formed (Webb et al., 2020; Upadhyay et al., 2021), could also provide additional constraining power on infall-related and general quenching models. The models could also be improved by using a physically-motivated model of ram-pressure stripping, rather than a generic timescale for SFR decline. Such a model could involve radius and velocity at first pericentre, as suggested in a simple model by Owers et al. (2019, see also Roberts et al., 2019 for a quenching model depending on ICM density). With these various improvements, tighter constraints on time of quenching onset and duration via infall quenching as a function of stellar mass should be possible in the future.

Chapter 4

How many stars form in major mergers?

4.1 Introduction

Understanding the impact of the merging of galaxies is essential to formulating a complete picture of hierarchical galaxy evolution in the ΛCDM framework (Kauffmann et al., 1993; Navarro et al., 1996; Somerville & Davé, 2015). Mergers, both major and minor, are an intrinsic part of the build-up of stellar and dark matter mass to form the galaxies we see in today's Universe, especially given their highly pronounced role early in the Universe's history (e.g. Conselice et al., 2003; Hopkins et al., 2010). Mergers are not only additive, but also transformative: they are believed to trigger central starbursts (Heckman et al., 1990; Hopkins et al., 2008c; Perez et al., 2011), accelerate the feeding of gas to supermassive black holes (Di Matteo et al., 2005; Hopkins et al., 2008b), and can transform a galaxy's morphology (Barnes & Hernquist, 1996b). Much observational work has been done verifying qualitative predictions of simulations over a range of redshifts (e.g. Kennicutt et al., 1987; Barton et al., 2000; Conselice et al., 2003; Koss et al., 2010; Xu et al., 2012; Cotini et al., 2013; Ellison et al., 2019, to name a few). Despite extensive study, a detailed and fully quantified picture of the merger process and its impacts on various galaxy properties remains a challenge – a carefully matched control sample is needed to separate effects of various parts of the merger process from intrinsic trends in galaxy populations (Perez et al., 2009; Ellison et al., 2013b; Bickley et al., 2022).

Terminology related to mergers varies and can easily lead to confusion. For consistency and clarity, we describe the stages of the merger sequence with our preferred terminology

as follows. Galaxies first orbit each other as a pair that becomes closer (on average) with time due to dynamical friction – we refer to this as the "inspiral" phase. As the pair becomes even closer, it may appear as a single disturbed galaxy but with a double nucleus. We consider a pair to have coalesced when there is a single nucleus. Galaxies that have coalesced but can still be identified morphologically as a merger product (from disturbed or tidal features) are referred to in this work as *post-coalescence mergers*.

Large systematic galaxy surveys, in particular the Sloan Digital Sky Survey (SDSS) of approximately one million nearby galaxies, have enabled much more detailed statistical study of mergers via close pairs. Studies have found bluer bulge colours (Ellison et al., 2010; Patton et al., 2011; Lambas et al., 2012), enhanced star formation rates (Nikolic et al., 2004; Alonso et al., 2006; Li et al., 2008; Ellison et al., 2013b; Scudder et al., 2012; Patton et al., 2013; Lackner et al., 2014; Pan et al., 2019), a modest reduction in metallicity (e.g. Scudder et al., 2012; Thorp et al., 2019), enhanced HI gas (e.g. Scudder et al., 2015; Dutta et al., 2018; Ellison et al., 2018), increased AGN activity/fraction (e.g. Ellison et al., 2011; Lackner et al., 2014; Weston et al., 2017), etc. In particular, modest but significant enhancement of star formation is present in galaxy pairs that have a separation $r_p < 150h_{70}^{-1}$ kpc (Patton et al., 2013), with star formation rates matching control galaxies beyond this ($150h_{70}^{-1}$kpc $< r_p <$ 1Mpc), indicating enhanced star formation on the order of a Gyr or more prior to merging (Kitzbichler & White, 2008; Jiang et al., 2014).

While much of the observational merger literature has focused on close pairs or pre-coalescence mergers with two visible nuclei, little work has been done on post-coalescence mergers. As a result, the amount of stellar mass formed during the final burst remains highly uncertain. A major difficulty has been identifying a large sample of post-coalescence mergers in a consistent way.

Post-starburst galaxies (PSBs), quenched galaxies with a significant population of type-A stars, indicative of a burst of star formation in the last ~ 1 Gyr (González Delgado et al., 1999), are often assumed to be mostly post-coalescence merger galaxies, at least at low redshifts, where starbursts should otherwise be uncommon. Observationally, $50 - 90$ per cent of post-starbursts feature tidal features or disturbed morphologies (e.g. Pawlik et al., 2016; Sazonova et al., 2021). Ellison et al. (2022) find a 30–60x excess of PSBs in post-coalescence mergers (but not for close pairs), lending further support to this connection, but make it clear that less than a majority of post-coalescence mergers are PSBs. By selecting PSBs based on the presence of a strong burst, they may not be representative of the post-coalescence merger population as a whole.

Few attempts have been made to observationally quantify the amount of stellar mass formed in galaxy mergers. Samples of PSBs find large stellar mass burst fractions of

~ 0.30 (e.g. French et al., 2018). Hopkins et al. (2008c) found a stellar mass burst fraction of ~ 0.25 by fitting excess central light in a sample of ~ 50 morphologically-identified gas-rich post-coalescence merger candidates. Very recently, Yoon et al. (2023) use stellar ages for a small sample of galaxies with any morphologically-identified tidal features and find a burst fraction of up to 7 per cent for their $10.6 < \log(M_\star/\mathrm{M}_\odot) < 11.1$ galaxies.

The goal of this work is to model the stellar mass burst during merging using galaxy stellar ages. To measure the stellar mass created in the starburst from the coalescence stage of a typical major merger in a systematic and unbiased way, a sample must ideally have high purity (high fraction of genuine mergers) and high completeness or representative sample of post-coalescence mergers. By using the machine learning-identified but visually confirmed post-coalescence mergers of Bickley et al. (2022), we expect to have a highly pure and representative sample of post-coalescence mergers.

The outline of this paper is as follows. In Section 4.2 we describe the SDSS observational data and sample selections of post-coalescence mergers and controls. Then in Section 4.3 we present our core results: observed properties of merger galaxies, particularly stellar ages compared to controls, as well as our star formation history modeling of both the inspiral phase and stellar mass excess from the final burst of star-formation during coalescence. In Section 4.4, we discuss the robustness of these results and contrast them with gas mass fractions and works in the literature. We conclude in Section 4.5.

Unless otherwise specified, the following assumptions and conventions are used. Uncertainties are estimated from the 16th-84 percentile interval (equivalent to 1-σ for a Gaussian-distributed variable). Logarithms with base 10 ($\log_{10}$) are written simply as 'log' throughout this work. A flat ΛCDM cosmology consistent with the Planck 2015 cosmological parameters (Planck Collaboration et al., 2016a) is assumed, namely $H_0 = 68$ km s^{-1} Mpc^{-1}, $\Omega_m = 0.31$, and $\Omega_\Lambda = 0.69$. A Chabrier (2003) initial mass function (IMF) is assumed throughout. 'Age' of a galaxy refers specifically to mass-weighted age, expressed as a look-back time. Finally, we define the stellar mass ratio of a pair of galaxies as $\mu \equiv M_{\star,1}/M_{\star,2}$ (primary to secondary stellar mass ratio) and use this throughout.

4.2 Data and sample selection

4.2.1 Observational data: SDSS

Stellar masses and ages

We use stellar masses and mass-weighted ages (hereafter simply 'ages') of the value-added catalogue Comparat et al. (2017), who performed full spectral fitting of galaxy properties from the Sloan Digital Sky Survey (SDSS) Data Release 14 (Abolfathi et al., 2018) using FIREFLY (Wilkinson et al., 2017). The SDSS data are limited to a Petrosian r-band magnitude $m_r < 17.77$. We only include objects whose spectra Comparat et al. (2017) classified as a 'GALAXY'. Note that this excludes objects classified as a 'QSO' – quasi-stellar objects. We compare their stellar masses with those of Mendel et al. (2014) and confirm that offsets in the stellar masses do not affect our results. In particular, we use the fits of Comparat et al. (2017) that were done using the M11 stellar population models of Maraston & Strömbäck (2011), a Chabrier IMF (Chabrier, 2003), and the MILES stellar library (Sánchez-Blázquez et al., 2006; Falcón-Barroso et al., 2011; Beifiori et al., 2011) for the mass-weighted ages ('CHABRIER_MILES_age_massW'), stellar masses ('CHABRIER_MILES_stellar_mass'), and SFRs from (Brinchmann et al., 2004; Salim et al., 2007).

Post-coalescence merger sample

We select galaxies with $0.01 \leq z \leq 0.2$, $\log(M_\star/\mathrm{M}_\odot) > 10$, and that have a match to the FIREFLY catalogue by Wilkinson et al. (2017), from the visually-confirmed post-coalescence merger catalogue of Bickley et al. (2022) which also have SDSS spectroscopy-derived stellar ages, yielding 445 galaxies out of their total 699 post-coalescence mergers catalogue (with a similar reduction in numbers from excluding objects with QSO spectra and the redshift cut). The mean redshift of the merger sample is 0.13 and since the SDSS fibre aperture is 3 arcsec, the SDSS fibres cover a radius of 3.6 kpc. We discuss the impact of this effect in our robustness discussion in Section 4.4.1.

We choose the visually-confirmed sample, confirmed by full consensus of three of their co-authors, because expert visual classifications have long been the preferred way of identifying and confirming post-coalescence mergers. Bickley et al. (2022) identified initial candidates from the deep r-band imaging of the Canada-France Imaging Survey (Ibata et al., 2017, now part of UNIONS[1]) using a convolutional neural network (CNN) developed in

[1] https://www.skysurvey.cc/

Bickley et al. (2021). In their visually-confirmed sample, only morphologically-disturbed galaxies that appear to be coalesced, i.e. that do not have a double nuclei, are included. In order to interpret our results employing their catalogue, it is important to understand the training set used for their CNN. We highlight a few key points here (for a detailed discussion of the CNN architecture and training methodology, see Bickley et al., 2021). To train the CNN, they convert IllustrisTNG cosmological magnetohydrodynamical simulation galaxies into mock observations using the observational realism code RealSimCFIS, a customized version of RealSIM (Bottrell et al., 2019). In particular, the training set is composed of post-coalescence merger and non-post-coalescence merger galaxies from the 100-1 (100^3 Mpc^3) run of the IllustrisTNG simulation (Marinacci et al., 2018; Naiman et al., 2018; Nelson et al., 2018; Pillepich et al., 2018; Springel et al., 2018; Nelson et al., 2019), with post-coalescence mergers identified as having completed a merger within the most recent simulation snapshot ($\sim$170 Myr temporal resolution). Mergers were required to have stellar mass ratios of $1 \leq \mu \leq 10$ in the stellar mass range 10^{10}–10^{12} M$_\odot$ at $z \leq 1$. Non-mergers in this training set were selected to have not experienced a merger in the last 2 Gyr. Using their trained CNN, they only included candidates assessed by the CNN as having a high probability of being a post-coalescence merger, namely a 'decision threshold' greater than 0.7, to ensure high purity and best match the SFR enhancements in the ground-truth of the simulation.

Merger control sample

To construct a control sample for the post-coalescence mergers, we closely follow the control sample selection methodology of Ellison et al. (2013b). Explicitly, the overall collection of all possible control galaxies are those that appear to be isolated, having no spectroscopic companion within $80h^{-1}$kpc and with a relative velocity of Δv within 10 000 km s^{-1}. From these galaxies, we then select matching control galaxies for each post-coalescence merger within a redshift tolerance of $\Delta z = 0.005$, a mass tolerance of $\Delta \log M_\star = 0.1$ dex, and a normalized local density difference of $\log(1 + \delta_5) = 0.1$ dex. Normalized densities, δ_5, are computed relative to the median local environmental density,

$$\Sigma_n = \frac{n}{\pi d_n^2} \, ,$$

within $\Delta z \pm 0.01$, where d_n is the projected physical distance to the n-th nearest neighbour within $\pm$1000 km s^{-1}. As in Ellison et al. (2013b), we use $n = 5$.

We require that there are at least 5 control galaxies per post-coalescence merger. If there are fewer than this, we increase the tolerance limits (additively) by another $\Delta z = 0.005$

in redshift, $\Delta \log M_\star = 0.1$ dex in stellar mass, and $\Delta \log(1 + \delta_5) = 0.1$ dex in normalized local density. Only 0.7 per cent of post-coalescence mergers require more than one loop to find more than 5 control galaxies. We end up with $\sim 79\,000$ control galaxies total.

4.2.2 Observed post-coalescence merger properties

We note some observed properties of the post-coalescence merger sample. In the top subplot of Figure 4.2, we see that the log of the running mean SFR of the overall post-coalescence merger sample (black) declines less steeply with stellar mass than for the control sample, but only modestly so. By breaking down the sample into star forming (blue) and quiescent (red), we see that the difference in trend is primarily due to the post-coalescence merger sample having a modestly lower (< 10 per cent lower) quiescent fraction (Figure 4.2). The distribution of post-coalescence merger SFRs is shown in the bottom subplot. The quiescent post-coalescence mergers have higher sSFRs than quiescent controls. Furthermore, the median star forming merger has a lower sSFR than the median star-forming control. In this sense, the mergers populate the "green valley" to a greater extent than the controls. Nevertheless, because of an excess of mergers with much higher star formation rates ($\log \text{sSFR} \gtrsim -9.8$), we still reproduce the mean ~ 0.27 dex enhancement in star formation rate for star forming galaxies, as measured in Bickley et al. (2022), who used the same post-coalescence merger sample. We additionally note that the fraction of quiescent galaxies is consistent between mergers and controls (Figure 4.1).

In Figure 4.3, we compare the running mean of the post-coalescence mergers (including both quiescent and star forming galaxies) sample with their corresponding control sample. The well-known ages-$\log(M_\star/\mathrm{M}_\odot)$ trend (e.g. Nelan et al., 2005; Graves et al., 2007) is apparent for both the post-coalescence mergers and controls sample. The mean age of the post-coalescence merger sample is significantly younger, particularly at lower stellar masses, by up to $\Delta A \sim 3$ Gyr for $\log(M_\star/\mathrm{M}_\odot) \sim 10$. We note that breaking the galaxies down into quiescent or star forming subsets does not change the results, as is expected because Comparat et al. (2017) mask the emission lines (both nebular and AGN) when performing their FIREFLY fitting of the SDSS spectroscopy.

4.3 Modeling and Results

Our goal is to determine the burst fraction from major mergers by measuring the fraction of the stellar mass from the starburst that can account for the difference in age as seen in

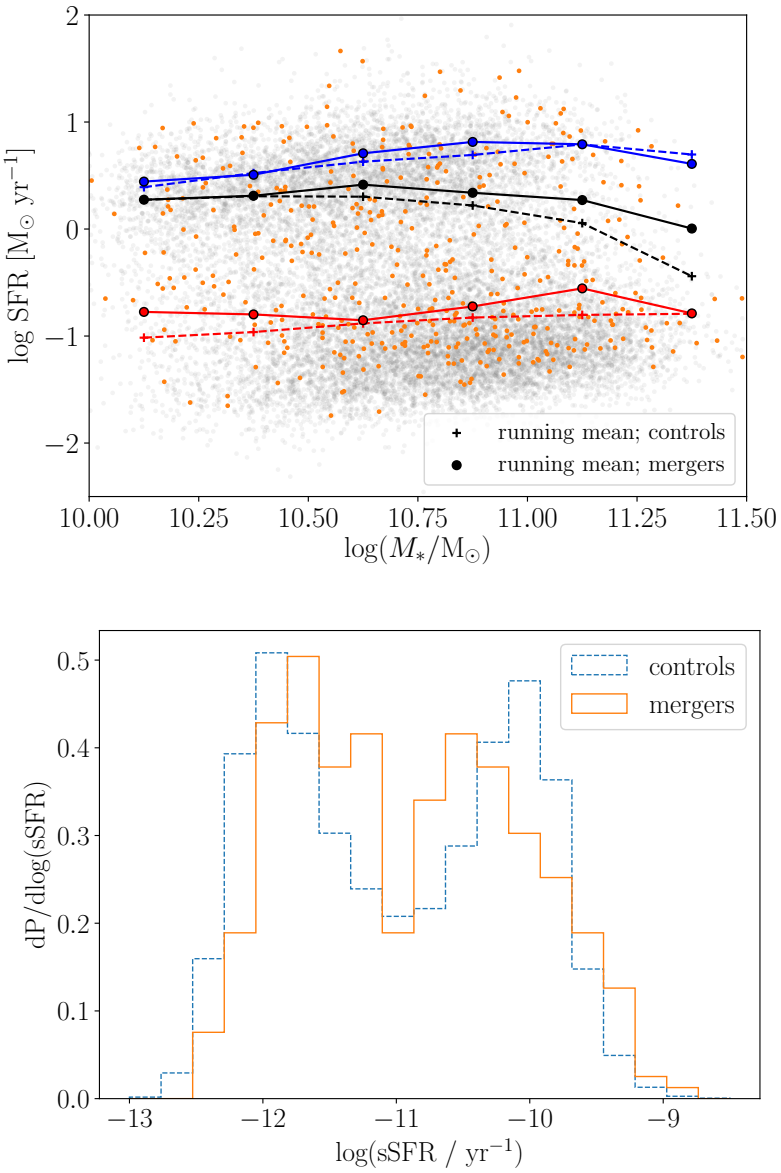

Figure 4.1: **Top:** Running average SFR for SDSS post-coalescence mergers (circular points connected by solid lines) and controls ('+' symbols connected by dashed lines), broken down by total (black), star forming (blue), and quiescent (red). Each post-coalescence merger's $\log \mathrm{SFR} - M_\star$ value is additionally plotted (small orange points), as is a random subset of the overall SDSS sample (small grey points). **Bottom:** Histograms of the normalized sSFR for post-coalescence mergers (orange solid) and controls (blue dashed).

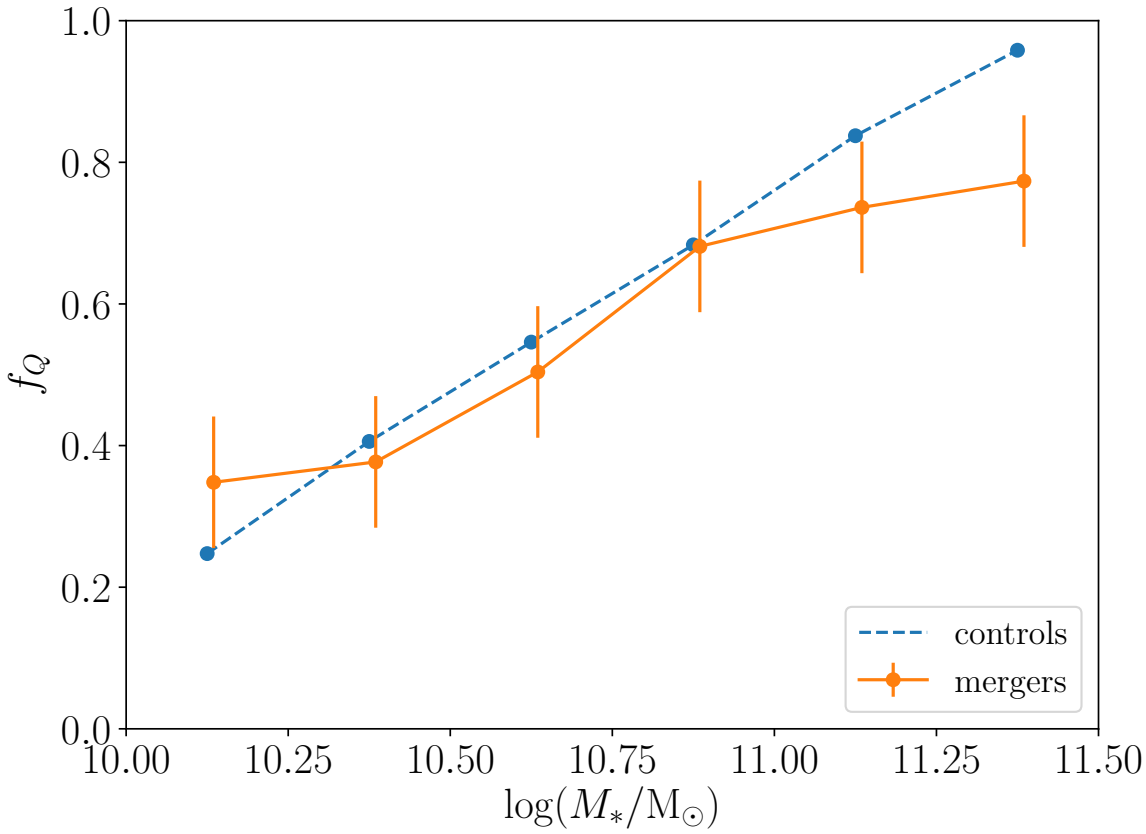

Figure 4.2: Quiescent fraction as a function of stellar mass for the post-coalescence merger sample (blue points connected by dashed line) and our control sample (orange points connected with solid line). Errorbars on the mergers are the bootstrapped error on the mean f_Q; because of the large control sample, errors on the controls' f_Q values are negligible.

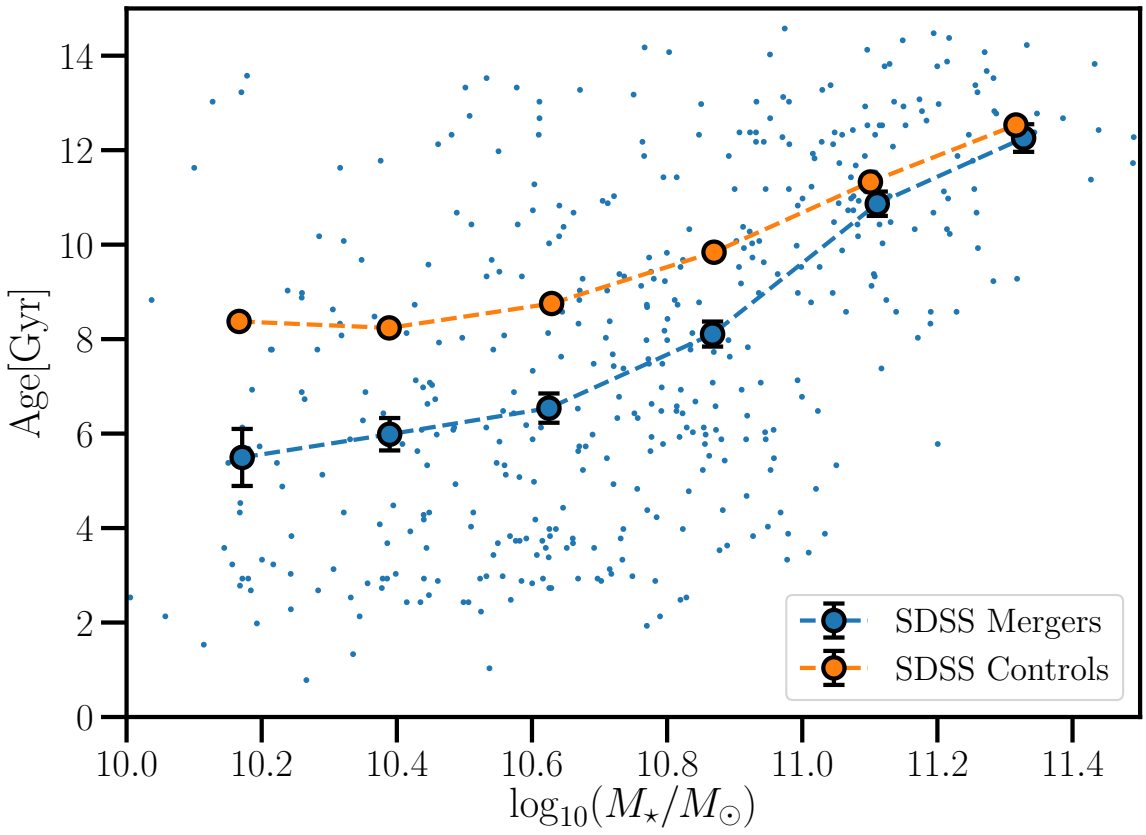

Figure 4.3: Running mean of the SDSS-derived ages as a function of stellar mass for the merger sample of Bickley et al. (2022) (large blue circles) contrasted with our control sample (orange). Post-coalescence mergers are younger than control galaxies by $\sim 2-3$ Gyr for $10 < \log(M_\star/\mathrm{M}_\odot) < 11$. Error bars shown are the bootstrapped standard error on the mean. All age–$M_\star$ values of the post-coalescence merger sample are shown (small blue points) to give an indication of the scatter in the SDSS ages.

Figure 4.3. Note that for $\log(M_\star/\mathrm{M}_\odot) > 11$, there is no significant age difference, so we restrict the analysis to $10 < \log(M_\star/\mathrm{M}_\odot) < 11$. We do so by adding a recent burst of star formation to the SFR of the pre-merger progenitors, which we model with an analytic SFH, as described in Section 4.3.1. We will also need to model the additional star formation during the inspiral phase and so we use published close pair SFR enhancement ratios as a function of pair separation, integrated over inspiral timescales derived from these separations; we present this aspect of the modeling and results in Section 4.3.2. Finally, in Section 4.3.3, we present our modeled stellar age results and best-fitting stellar mass burst fraction.

4.3.1 Control star formation histories

For a set of control galaxy star formation histories, we use functions which are log-normal in time, which have been shown to be excellent fits for individual galaxies for most star formation histories, with the exception being the small fraction of galaxies suddenly quenched shortly after becoming satellites (Diemer et al., 2017, see also Gladders et al. (2013)). Following Diemer et al. (2017), we parameterize our control galaxy star formation histories as

$$\mathrm{SFR}_{\mathrm{con}}(t) = \frac{B}{\sqrt{2\pi\tau^2} \times t} \exp\left(- \frac{(\ln(t) - T_0)^2}{2\tau^2} \right), \tag{4.1}$$

where B, T_0, τ are free parameters. We note that our results are robust to the particular choice of analytic SFH, as we discuss in Section 4.4.1.

We determine B from the total stellar mass of the galaxy we wish to model, i.e. from their equation 2, $M_{\mathrm{final}} = B \times 10^9 \times f_{\mathrm{ret}}$, where $f_{\mathrm{ret}} = 0.6$ is the stellar mass retention factor (similar to that assumed by Gladders et al., 2013, and that found for IllustrisTNG in Diemer et al. (2017)).

To solve for the other parameters, we assume the peak time-width relation Diemer et al. (2017) find for their Illustris sample, namely $\sigma_{\mathrm{SFR}} = 0.83 t_{\mathrm{peak}}^{3/2}$ (their equation 7), where $\sigma_{\mathrm{SFR}} = 2 t_{\mathrm{peak}} \sinh \sqrt{2 \ln 2} \tau$ is the full width at half maximum in linear time for the SFH. Let A_{con} be the mass-weighted age of the control galaxy. By noting that t_{peak} is simply the mode of the log-normal distribution, i.e. $t_{\mathrm{peak}} = \exp(T_0 - \tau^2/2)$, and that $t_{\mathrm{now}} - A_{\mathrm{con}}$ is simply the first moment of the distribution, i.e. $t_{\mathrm{now}} - A_{\mathrm{con}} = \exp(T_0 + \tau^2/2)$, we find the following expression that can be solved numerically for τ using the mass-weighted age

as an input:

$$0 = 0.83(t_{\rm now} - A_{\rm con})^{\frac{1}{2}} \exp\left(\frac{-3\tau^2}{4}\right) - 2\sinh(\sqrt{2\ln 2}\tau). \tag{4.2}$$

With τ now in hand, we can then simply solve for T_0 using the definition of the first-moment, $t_{\rm now} - A_{\rm con} = \exp(T_0 + \tau^2/2)$.

We show example log-normal star formation histories for a range of stellar masses, $10 < \log(M_\star/{\rm M}_\odot) < 11$, as the solid smooth curves in Figure 4.4, using the SDSS control galaxies' age–$M_\star$ relation in Figure 4.3 to solve for the SFH parameters for each stellar mass shown.

Since we will be modifying these control star formation histories for our merger analysis, rather than use the input stellar mass and age for a given star formation history, we numerically integrate the star formation history. The stellar masses of a galaxy at the average observed redshift of $z = 0.13$, is calculated as

$$M_\star(t_{\rm now}) = \int_0^{t_{\rm now}} \frac{{\rm d}M_\star}{{\rm d}t}\,{\rm d}t \tag{4.3}$$

$$= f_{\rm ret} \int_0^{t_{\rm now}} {\rm SFR}(t)\,{\rm d}t, \tag{4.4}$$

where $t_{\rm now} = 12.05$ Gyr. Similarly, ages are calculated as

$$A_{\rm con} = t_{\rm now} - \frac{1}{M_\star(t_{\rm now})} \int_0^{t_{\rm now}} t\left(\frac{{\rm d}M_\star}{{\rm d}t}\right){\rm d}t \tag{4.5}$$

$$= t_{\rm now} - \frac{f_{\rm ret}}{M_\star(t_{\rm now})} \int_0^{t_{\rm now}} t\,{\rm SFR}(t)\,{\rm d}t\,; \tag{4.6}$$

we note it is written this way since it is a mass-weighted age, which is expressed as a lookback time.

4.3.2 SFR enhancement during the inspiral phase using close pairs

Previous studies have shown that star formation in the close pair "inspiral" phase of the merger is enhanced, as summarised, for example, in table 1 of Behroozi et al. (2015). To compute the increase in stellar mass during inspiral, we use the empirically-determined

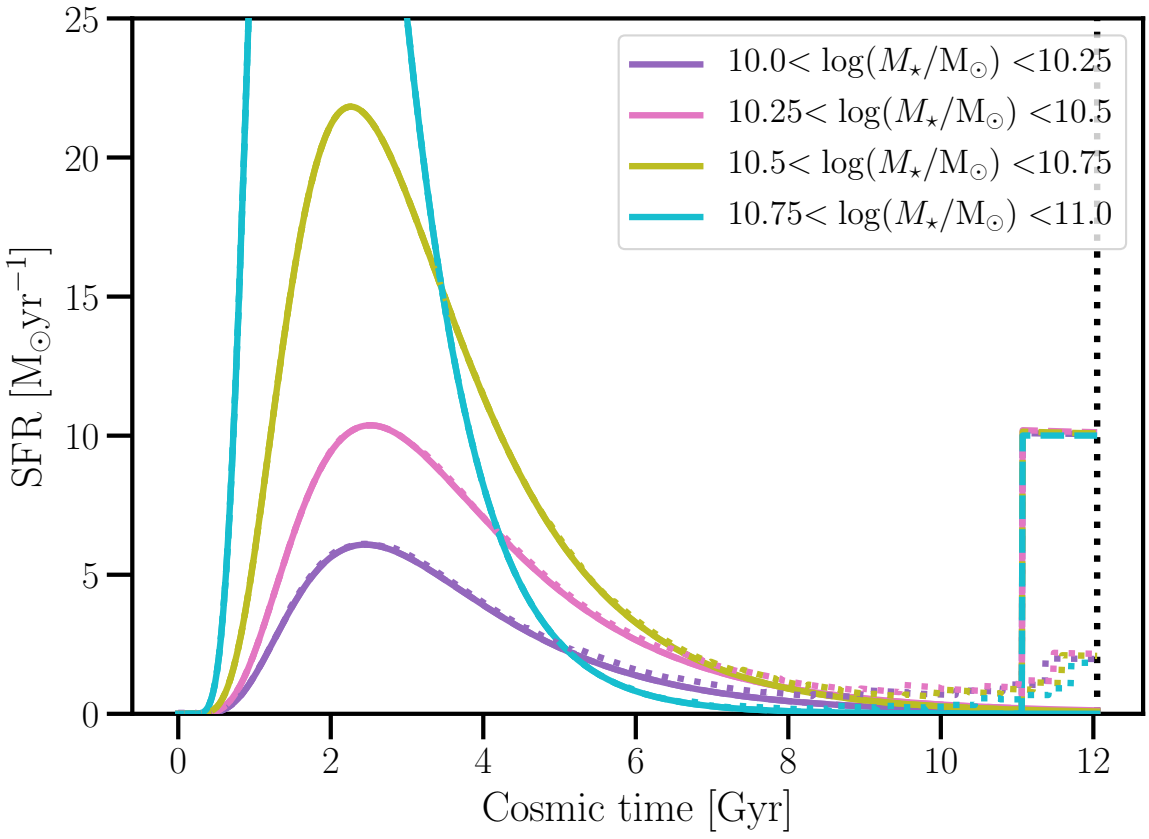

Figure 4.4: Mean log-normal control galaxy star formation histories (solid lines) overlaid with estimated enhanced SFR due to inspiral (dashed lines) binned by stellar mass, as well as an example $\Delta t_{\rm burst} = 1$ Gyr additive SFR burst of $\rm SFR_{burst} = 10$ M$_\odot$yr^{-1}. Enhanced SFR from the inspiral phase was calculated using the SFR-r_p galaxy pair results of Patton et al. (2013), with radii converted to average inspiral timescales using Equation 4.3.2. Note that star formation histories in this figure are shown up until the average observed redshift, $t_{\rm merge}(z = 0.13) \sim 12$ Gyr.

relative enhancement in SFR (a ratio to control galaxies) vs r_p relation from figure 1 of Patton et al. (2013). We convert the projected separation bins to merging timescales by assuming galaxies at a given radius will take some increment of time to fall from one r_p bin to the next, $dt_i = t_{i+1} - t_i$, where t_i is the average infall time for some r_p bin and t_{i+1} is the average infall time for the next farthest r_p bin. The average infall time for a given bin, $r_{p,i}$ is given by $t_i = t_{\rm merge}(r_{p,i})$, where

$$t_{\rm merge}(r_p) = 2.2 \text{ Gyr} \frac{r_p}{50 \text{ kpc}} \left(\frac{\mu}{4}\right) \left(\frac{M_\star}{4 \times 10^{10} h^{-1} \mathrm{M}_\odot}\right)^{-0.3} \left(1 + \frac{z}{8}\right),$$

which is adapted from equation 10 of Kitzbichler & White (2008) with an extra multiplicative term μ as found in the fit relation from Jiang et al. (2014), normalized to $\mu = 4$. The extra term is included to correct for Kitzbichler & White (2008) not examining the dependence of merging time on a pair's mass-ratio (this led to their original expression only matching that of Jiang et al. (2014) for $\mu = 4$), which is a significant effect. We note that the mean μ depends weakly on stellar mass (using only the range $1 < \mu < 10$), decreasing from $\mu = 3.25$ to $\mu = 2.8$ from $\log(M_\star/\mathrm{M}_\odot) \sim 10$ to $\log(M_\star/\mathrm{M}_\odot) \sim 11$.

Whether we compute $t_{\rm merge}$ using the mean μ for a given stellar mass bin or whether we calculate the mean $t_{\rm merge}$ for a whole distribution of observed pair μ values does not impact our results. We find that for 2/3 of pairs $t_{\rm merge} < 1$ Gyr.

The excess stellar mass from the inspiral phase prior to merging is then

$$\Delta M_\star = f_{\rm ret} \sum_i \Delta \text{ SFR}_i \times \text{SFR}_{\rm con}(t_i) dt_i,$$

where Δ SFR$_i$ is the ratio in star formation rate between galaxies that are close pairs and their corresponding controls. SFR$_{\rm con}$ is simply the mean SFR of an SDSS galaxy with the control galaxy's stellar mass. The result from this choice is robust as long as most of an inspiral's excess star formation occurs in the last few Gyr, which we will shortly show. We again assume $f_{\rm ret} = 0.6$.

In Figure 4.4, we illustrate the effect of this additional star formation on the overall modeled star formation history due to the inspiral phase (dotted line). Most importantly for this work is the impact on stellar ages from the inspiral phase, which we show with black arrows in the subplots in Figure 4.5. The enhanced star formation results in younger stellar ages for galaxies, with the effect largest (~ 1.5 Gyr) for the lowest stellar mass bin ($10 < \log(M_\star/\mathrm{M}_\odot) < 10.25$), and smallest ($\sim 0.6$ Gyr) for the highest stellar mass bin ($10.75 < \log(M_\star/\mathrm{M}_\odot) < 11$). Interestingly, this removes the trend in ΔA with stellar mass, leaving $\Delta A \sim -1.7$ Gyr at all considered stellar mass bins to be explained by a starburst during coalescence.

4.3.3 Starburst during coalescence

We can explain the remaining difference in stellar ages via a simple star-formation burst during coalescence, i.e. upon two galaxies merging. To do this, we model the enhanced star formation during coalescence as an additive burst with a flat SFR, parametrized by the duration of the burst, $\Delta t_{\rm burst}$, and the burst fraction for the resulting merged object, $f_{\rm burst} \equiv (M_{\star,\rm merger} - M_{\star,\rm con})/M_{\star,\rm merger}$. $M_{\star,\rm con}$ is the mass of the two merged galaxies without a burst (where 'con' is short for 'control'), and $M_{\star,\rm merger}$ is the final merged object with the burst. We illustrate a simple example $\Delta t_{\rm burst} = 1$ Gyr long burst of SFR = 10 $\rm M_\odot yr^{-1}$ in Figure 4.4.

This modeling requires an iterative computation to find the input control galaxy's stellar mass. Since our SFH model for control galaxies takes in age as an input, to estimate an age for a trial control galaxy given some stellar mass, we fit the mean age–$M_\star$ relation for controls with a tight-fitting fourth-order polynomial and flat relation below $x = \log(M_\star/\rm M_\odot) = 10.2$. We put in a flat trend instead of the polynomial for the lower stellar mass end as there are few post-coalescence mergers (and therefore few matched controls) below $\log(M_\star/\rm M_\odot) \sim 10.2$ and the overall trend for SDSS galaxies is approximately flat below this. We iterate through control masses (the stellar mass of the merged galaxies without the starburst added) until we find the needed control stellar mass to give the desired burst fraction.

For our model, we plot the change in age, $\Delta A = A_{\rm merger} - A_{\rm con}$ as a function of $f_{\rm burst}$ for our four stellar mass bins in Figure 4.5. For each stellar mass bin we additionally plot the measured difference in age between the post-coalescence mergers and control sample as a horizontal (grey) band, shifted by the modeled inspiral ΔA results of the previous section.

Earlier works find short star formation bursts. For example (Di Matteo et al., 2008) find bursts of up to 500 Myr long at most, with average durations of 200–300 Myr. With this in mind, we show two models with burst durations of $\Delta t_{\rm burst} = 0$ Gyr (instantaneous; blue line) and $t_{\rm burst} = 1$ Gyr (long duration extreme case; orange line), which display nearly identical linear declining trends, with a maximum difference between the ΔA of the two models of ~ 0.5 Gyr for high burst fractions, as expected from the difference in age of the two bursts. Additionally, if we perform a simple back-of-the-envelope calculation for an instantaneous burst and assume the control stellar mass is simply the same as the merger, i.e. $f_b = (A_{\rm merger} - A_{\rm con})/A_{\rm merger}$, then we would expect that $\Delta A = -A_{\rm con} f_{\rm burst}$, which is a very similar linear trend in ΔA as a function of $f_{\rm burst}$ to our plotted $\Delta t_{\rm burst} = 0$ Gyr model.

Assuming the uncertainties on the SDSS ages are normally distributed, we compute the best-fitting $f_{\rm burst}$ with uncertainties in each stellar mass bin, which we show in Figure 4.6

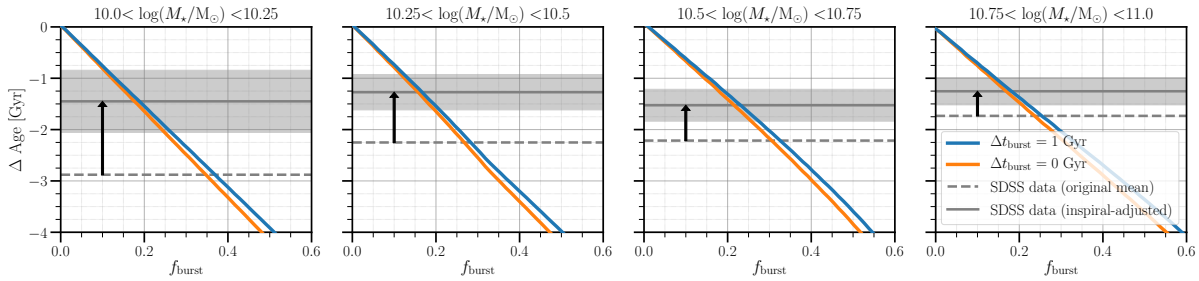

Figure 4.5: Change in modeled merger age, $\Delta A = A_{\rm merger} - A_{\rm con}$, relative to a control galaxy as a function of burst fraction, $f_{\rm burst} = (M_{\rm merger} - M_{\rm con})/M_{\rm merger}$, for four stellar mass bins. On each subplot we show two models: one with an instantaneous burst ($\Delta t_{\rm burst} = 0$ Gyr) and a model using $\Delta t_{\rm burst} = 1$ Gyr. In solid grey we plot the mean ΔA from the SDSS data shifted by the modeled inspiral phase using close pairs data (black arrow indicates the shift), with the shaded region indicating the bootstrapped error on the mean.

for both models. There is a small systematic offset in best-fitting $f_{\rm burst}$, such that the $\Delta t_{\rm burst} = 1$ Gyr is higher by ~ 0.02, a difference which is significantly smaller than the uncertainties. We find no trend in $f_{\rm burst}$ with stellar mass. The mean stellar mass fraction across our four stellar mass bins is $f_{\rm burst} = 0.18 \pm 0.02$ ($f_{\rm burst} = 0.19 \pm 0.03$ for $\Delta t_{\rm burst} = 1$ Gyr).

4.4 Discussion

The inspiral phase of galaxy mergers has received significant attention in the literature, in both observational and simulation work, thanks to the ease of observationally identifying close pairs. Since post-coalescence mergers have received relatively little focus in observational work, we focus our discussion primarily on our modeled starburst at the time of coalescence.

4.4.1 Robustness of measured burst fraction

In this section we explore the robustness of our measured stellar mass burst fraction. In particular, we check, in turn, the effects of the SDSS fibre aperture, the impact of choosing the whole post-coalescence merger sample versus only quenched galaxies, and whether our modeling is sensitive to choice of star formation history.

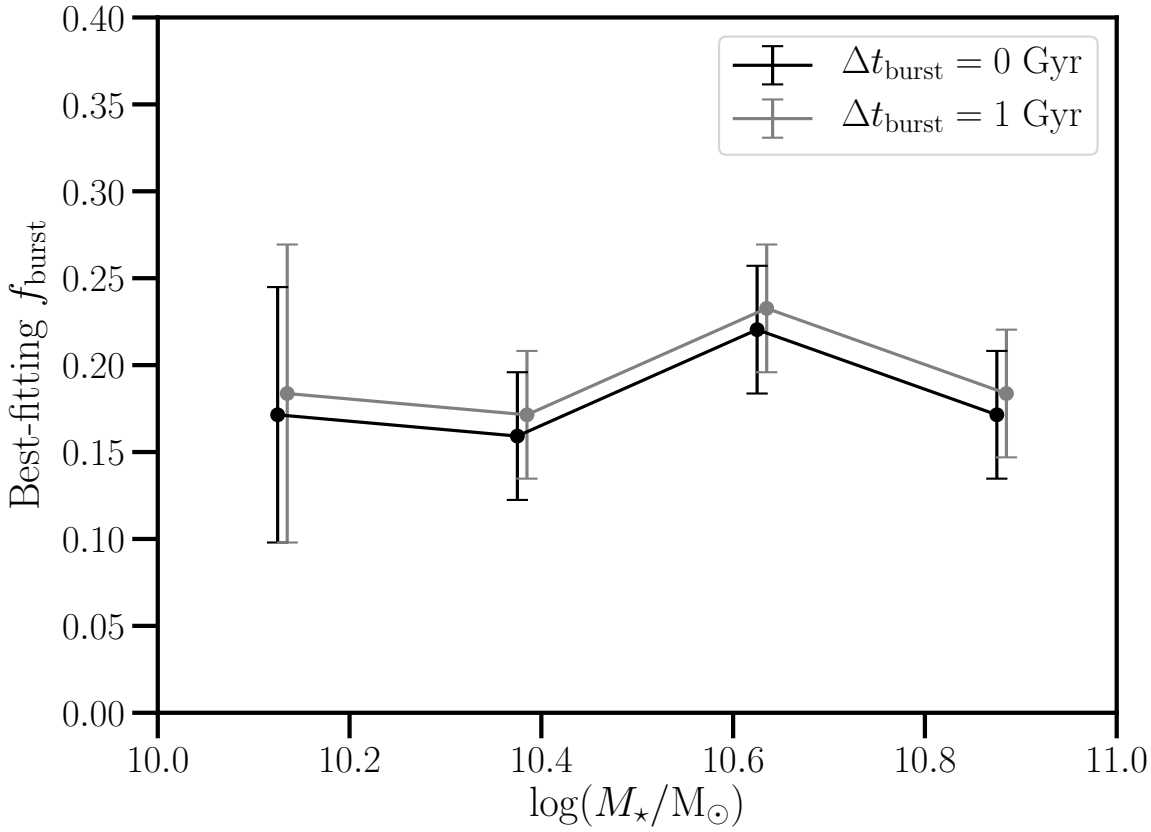

Figure 4.6: Best-fitting burst fraction, $f_{\rm burst} = (M_{\rm merger} - M_{\rm con})/M_{\rm merger}$ (for an instantaneous burst), as a function of stellar mass. We show both models from Figure 4.5: the one with an instantaneous burst ($\Delta t_{\rm burst} = 0$ Gyr) and a model using $\Delta t_{\rm burst} = 1$ Gyr.

As noted earlier, the mean redshift of the merger sample is 0.13, for which the SDSS fibres cover a radius of 3.6 kpc. Since the stellar burst is likely mainly in the central regions of the galaxy, most of the burst should fit within the fibre, but some of the galaxy's non-nuclear stellar mass may be cut off. Assuming that the luminosity distribution is proportional to the stellar mass distribution and assuming that mergers ultimately form ellipticals, one can use the relation between the half-light radius, $R_{\rm e}$, and $M_\star$, from figure 8 of Hyde & Bernardi (2009). The largest effect is for $\log(M_\star/{\rm M}_\odot) \sim 11$ galaxies, where $R_{\rm e} \sim 3$ kpc, so for those objects the SDSS fibres are only seeing half of the light and hence stellar mass. This suggests that for the most massive galaxies in this paper, the burst fraction may be overestimated by a factor of up to ~ 2. For the less massive galaxies the impact of the fibre is negligible: for $\log(M_\star/{\rm M}_\odot) \sim 10$, $R_{\rm e} \sim 1$ kpc, for which the fibre will capture most of the light (see e.g. figure 1 of Graham & Driver, 2005).

The merger and control samples have no restrictions on their observed SFRs. For those post-coalescence mergers that are still forming stars at the time at which they are observed, one might expect them to continue doing so for some time after. In that case, the observed burst fraction may underestimate the final burst fraction. This can be checked by using only quiescent galaxies in the analysis. However, restricting to only quiescent galaxies reduces our post-coalescence merger sample from 442 galaxies to 258, with very few galaxies remaining below $\log(M_\star/{\rm M}_\odot) < 10.5$. For the full stellar mass range we find $f_{\rm burst} = 0.16 \pm 0.04$, with a higher value of 0.24 ± 0.04 for $\log(M_\star/{\rm M}_\odot) > 10.5$, both consistent with our best-fitting value of $f_{\rm burst} = 0.18 \pm 0.02$ for the full sample including both star forming and quiescent galaxies.

We expect our modeling results to be robust to changes in the SFH, as long as the control SFH results in the correct control galaxy stellar mass and age. As a test of the robustness of our best-fitting burst fractions to the choice of SFH, we replace our controls' log-normal SFH with a delayed-tau SFH model,

$$\mathrm{SFH}_{\rm con}(t) = \begin{cases} B \exp\left(-\frac{t-t_i}{\tau}\right), & t \geq t_i \\ 0, & t < t_i, \end{cases} \tag{4.7}$$

where $B = M_{\star,{\rm con}}/(10^9 f_{\rm ret}\tau)$ normalizes the star formation history to give the control galaxy's stellar mass. We set $t_i = 1$ Gyr as suggested by Simha et al. (2014), and τ is chosen such that we reproduce the SDSS controls' age.

Using the delayed-τ SFH instead of a log-normal SFH results in a lower modeled post-coalescence merger ΔA by up to 0.09 Gyr, or a lower $f_{\rm burst}$ by up to 0.01, for a given value of $f_{\rm burst}$ or ΔA, respectively. This effect is greatest for the lower stellar mass bins and negligible for the highest stellar mass bin. From this test it is clear that swapping out

our original SFH model with delayed-τ has no significant impact on our conclusions. We expect this to hold for any reasonable choice of analytic SFH.

4.4.2 Dependence on the merger progenitors

Unlike close pairs, with post-coalescence mergers it is impossible to identify the masses, morphological types, and gas fractions of the progenitors of an individual merger. This problem can be studied statistically, however.

The CNN used to identify the post-coalescence merger sample was trained with merger mass ratios, $1 < \mu < 10$, with $\overline{\mu} \sim 3$. What remains uncertain, however, is whether the visual-confirmation step is biased to mass ratios closer to unity. For a post-merger galaxy with $\log(M_\star/\mathrm{M}_\odot) \sim 10.2$ with a 20% burst of stars one might then expect the progenitors to have stellar masses of $\log(M_\star/\mathrm{M}_\odot) \sim 10.0$ and 9.5. These would typically be gas-rich, star-forming galaxies in the "blue cloud" and so the merger would be gas-rich or "wet". Once the progenitors have stellar masses above $\log(M_\star/\mathrm{M}_\odot) \sim 10.5$, the probability that they will be gas rich drops rapidly. Thus for post-merger remnants with $\log(M_\star/\mathrm{M}_\odot) \gtrsim 10.7$, we expect the burst fraction to drop rapidly as these mergers become "dry". Indeed, as shown in Figure 4.3, for $\log(M_\star/\mathrm{M}_\odot) > 11$, the age difference between mergers and controls is consistent with zero (and hence so is the burst fraction).

4.4.3 Comparison to other f_{burst} values in the literature

Most prior work modeling the stellar mass created in a merger starburst have been in complex hydrodynamical simulations or semi-analytic models, but a few works derive stellar mass burst fractions directly from observations of post-coalescence mergers.

In particular, Yoon et al. (2023) use FIREFLY to fit star formation histories to MaNGA integral field unit spectroscopic data of 193 early-type galaxies (ETGs; visually identified using the SDSS g, r, and i band imaging), 44 of which (23 per cent) display tidal features. Tidal features were identified visually in the deeper coadded imaging of the Stripe 82 region of SDSS, ~ 2 mag. deeper than the rest of SDSS. They found that ETGs with tidal tail features have younger stellar ages than those without by $1-2$ Gyr for our stellar mass range, shorter than the $2-3$ Gyr we see between post-coalescence mergers and controls.

They find the fraction of stellar mass formed in ETGs with tidal features in the past 2 Gyr is 2 ± 1 and 7 ± 3 percent higher than those without, at $\log(M_\star/\mathrm{M}_\odot) \leq 10.6$ and $10.6 \leq \log(M_\star/\mathrm{M}_\odot) \leq 11.1$, respectively. This is substantially lower than the burst

fractions that we find, possibly due to a few important factors. Selecting only for ETGs may bias towards galaxies that have less cold gas than our sample which may contain a proportion of disc galaxies (discs can re-form post-merger, e.g. Hopkins et al., 2008c). Including faint tidal features in their selection may also bias the sample towards minor mergers, which are much more common than major mergers that our sample was trained on. Finally, whereas the sample we use is primarily of recent post-coalescence mergers, Yoon et al. (2023) select on generic tidal features which may include all stages of the merger process (for the deeper SDSS imaging in Stripe 82 Yoon & Lim, 2020), from small satellites stretched out into a tidal stream after first pericentre to major mergers that occurred up to ~ 3 Gyr ago (although see also Desmons et al., 2023, who suggest galaxies selected by tidal features alone are mostly post-coalescence mergers). We note that compared to our inspiral-period excess stellar mass estimate, their result is lower than our ~ 7 per cent for $\log(M_\star/\mathrm{M}_\odot) \leq 10.6$ galaxies and higher than our ~ 1 per cent for $10.6 \leq \log(M_\star/\mathrm{M}_\odot) \leq 11.1$ galaxies.

Hopkins et al. (2008c) studied morphologically-identified gas-rich merger candidates and then fitted surface brightness profiles to quantify the excess central light created by a recent starburst(s) from Rothberg & Joseph (2004). 40 out of 52 of the galaxies are classified as fully violently relaxed in Rothberg & Joseph (2004), although our conclusion from their result is not changed whether we include/exclude those with relaxation classified as 'incomplete'. In other words, their sample and result should be representative of recently coalesced gas-rich mergers. They find an average best-fitting excess light fraction of $f_e = 0.25 \pm 0.03$ for galaxies with $\log(M_\star/\mathrm{M}_\odot) \sim 11$, consistent with our burst fraction of 0.18 ± 0.04 at this stellar mass (including the inspiral period of ~ 0.01). Systematic factors such as overestimation of burst mass to burst light fraction, due to reliance on one photometric band, may have resulted in modest overestimation of the stellar mass burst fraction.

French et al. (2018) perform detailed SED-fitting and modeling of post-starburst galaxies, objects for which a substantial fraction appear to be post-coalescence mergers (e.g. Sazonova et al., 2021; Ellison et al., 2022; Wilkinson et al., 2022). We note that post-starburst galaxies are only a minority ($\sim$ 20 per cent) of our post-coalescence merger sample (Ellison et al., 2022). Therefore, it is perhaps not surprising that they find a much higher mean burst stellar mass fraction of ~ 0.5 for $\log(M_\star/\mathrm{M}_\odot) \sim 10$ galaxies (versus our 0.28 ± 0.07 value including the inspiral period). For more massive galaxies with $\log(M_\star/\mathrm{M}_\odot) > 10.5$ their burst stellar mass fraction of 0.21 ± 0.02 is consistent with ours.

It is also interesting to compare our results with the predictions from hydrodynamical simulations. The IllustrisTNG hydrodynamical simulation was used to train the CNN used by Bickley et al. (2022) to identify the post-coalescence mergers used in our work.

Hani et al. (2020) examined post-coalescence merger galaxies in IllustrisTNG and found a modest $\sim$ 2 factor increase in SFR, which quickly declines, resulting in only a small $f_{\rm burst} \sim 0.5$ per cent. Their result is in clear contradiction with ours and the papers discussed above, apart from Yoon et al. (2023). Moreno et al. (2019) used the Feedback in Realistic Environments 2 (FIRE-2) hydrodynamical simulations to study pairs of merging galaxies at a 1 pc resolution. Star formation becomes enhanced around the time of first pericentre, followed by a significant (mostly central) starburst with SFR ~ 10 $\mathrm{M_\odot yr^{-1}}$ beginning at second pericentre, $\lesssim 250$ Myr prior to coalescence. Integrating the excess SFR for their 3×10^{10} $\mathrm{M_\odot}$ and 1.2×10^{10} $\mathrm{M_\odot}$ simulated progenitor galaxies (combined stellar mass of $\log(M_\star/\mathrm{M_\odot}) \sim 10.6$), we find 5 per cent of the post-coalescence merger's final stellar mass comes from the inspiral period (prior to second pericentre) and 8 per cent from the burst. This is consistent with our inspiral period's excess stellar mass fraction, but less than half of our best-fitting stellar mass burst fraction for the starburst.

4.4.4 Starburst duration

We can constrain the duration of the starburst during coalescence, if the typical SFR during the starburst is known. Luminous infrared galaxies (LIRGs, Sanders & Mirabel, 1996) are believed to be starburst galaxies, with SFR > 10 $\mathrm{M_\odot yr^{-1}}$ (similar SFRs to a typical starburst sample, French et al., 2018), usually inferred from IR luminosity (although we note that in principle AGN could be contributing to this, e.g. Iwasawa et al., 2011; Petric et al., 2011). As described earlier, the vast majority of low-z starburst/post-starburst galaxies may be due to mergers (see Section 4.1). LIRGs/ULIRGs have substantial young stellar populations (≤ 100 Myr), and appear to have gone through a period of enhanced star formation prior to their current burst. There is also some correlation with being late-stage inspiraling pairs and especially with coalescing/coalesced merger galaxies (e.g. Gao et al., 1997; Rodríguez Zaurín et al., 2010; Stierwalt et al., 2013; Larson et al., 2016).

Because of the likelihood at least the majority of LIRGs are due to mergers, we use a sample of 52 late-stage inspiraling LIRGs' SFRs from Shangguan et al. (2019) to measure the typical merger SFR and so constrain the starburst duration. We choose the subset of these morphologically identified by Stierwalt et al. (2013) as having two nuclei in a common envelope.

We fit a power-law to the SFR–$M_\star$ trend for this subset of objects (see objects labeled '(d)', e.g. in their figure 5), finding $\mathrm{SFR} = (29 \pm 13) M_\star^{0.53 \pm 0.17}$. Since our modeled burst

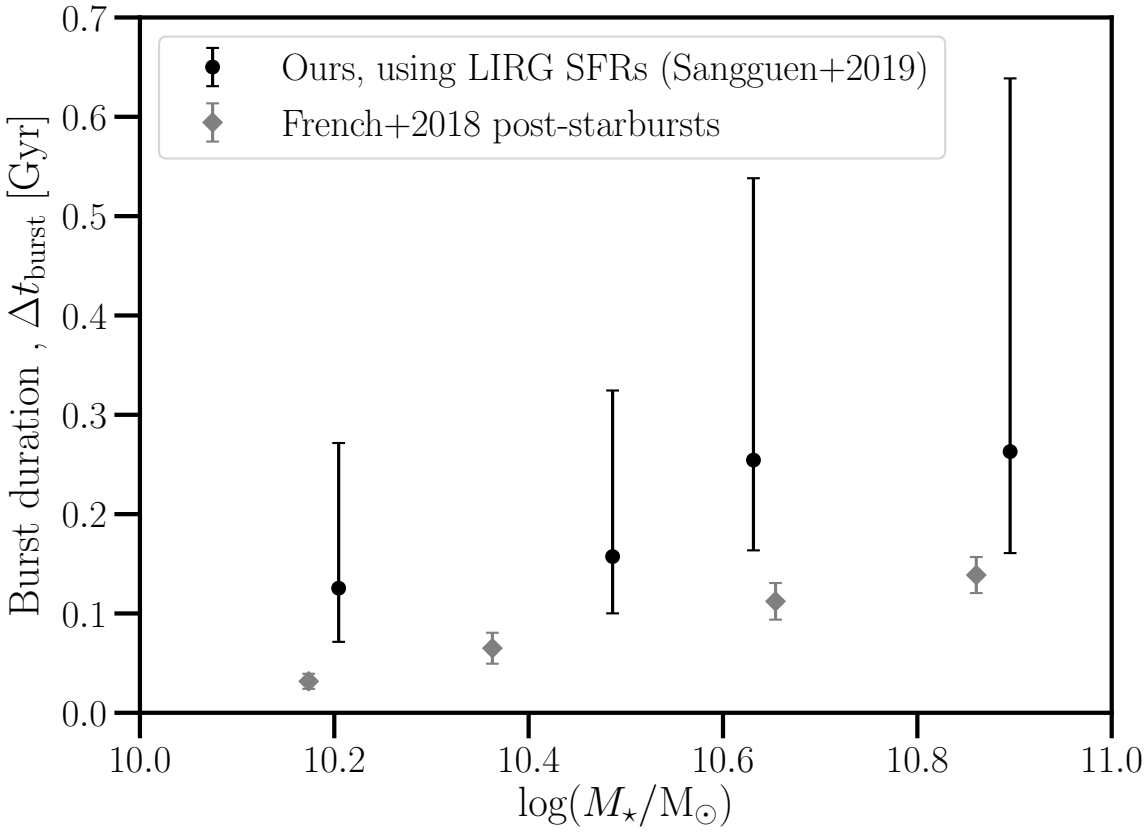

Figure 4.7: Estimated starburst duration, $\Delta t_{\rm burst}$, as a function of stellar mass, estimated by assuming $f_{\rm burst}$ from Figure 4.6 (black points) and the 'late-stage' inspiraling LIRG SFRs from Shangguan et al. (2019) (a presumed population of starburst galaxies).

fraction result is quite insensitive to choice of $\Delta t_{\rm burst}$, we can constrain the burst duration

$$\Delta t_{\rm burst} = \frac{\Delta M_\star}{f_{\rm ret} \times {\rm SFR}_{\rm LIRGs}}. \tag{4.8}$$

We show the result of this calculation in Figure 4.7. We see $\Delta t_{\rm burst} \sim 120$ Myr for the lowest stellar mass bin, increasing to $\Delta t_{\rm burst} \sim 250$ Myr for the highest stellar mass bins, albeit with large uncertainties from the LIRG SFR–$M_\star$ relation. We note our burst times are similar to the free-fall or violent relaxation time at the outer edge of the disk.

French et al. (2018), who studied post-starburst galaxies, found an average duration of 103 ± 23 Myr for $10 < \log(M_\star/{\rm M}_\odot) < 11$ galaxies. Their starburst duration increases with stellar mass, from 30 Myr for $\log(M_\star/{\rm M}_\odot) \sim 10$ to 140 Myr for $\log(M_\star/{\rm M}_\odot) \sim 11$, and is systematically shorter than our estimate, as shown in Figure 4.7.

Hani et al. (2020) trace their Illustris TNG100-1 $\log(M_\star/{\rm M}_\odot) > 10$ simulated post-coalescence merger sample forward in time and find that significant enhancements in SFR last for $100-250$ Myr post-coalescence (with uncertainty coming from the 162 Myr temporal resolution for the simulation), with a total decay time of ~ 0.5 Gyr for this enhancement. This effect was independent of the merger mass ratio. Their timescale is consistent with our estimate. Their SFR burst peaks at a factor only ~ 2 higher than their control galaxy, much lower than the factors of 40 – 100 seen in LIRGs. In the higher resolution FIRE-2 merger simulations, Moreno et al. (2019, 2021) find a longer burst duration than we do: 0.5 Gyr (beginning at second pericentre and therefore finishing 250 Myr after coalescence) for their $\log(M_\star/{\rm M}_\odot) \sim 10.6$ simulated merger.

4.4.5 Is there enough cold gas to fuel the burst?

The general picture of cold gas in mergers is as follows. Atomic gas in the galaxy outskirts flows inwards, due to decreased angular momentum from gravitational torques, resulting in rapidly increased cold gas density in the central region. This cold atomic gas condenses into molecular clouds, with collision-induced pressure possibly accelerating the formation of additional molecular gas from atomic (HI) gas (Moster et al., 2011a). This additional molecular gas in the core then leads to intense star formation in the galaxy nucleus (Mihos & Hernquist, 1996; Di Matteo et al., 2008; Renaud et al., 2014). Turbulence induced by gravitational torques during interactions, particularly at the start of coalescence, may also lead to gas fragmentation, forming massive and dense molecular clouds, fueling the intense star formation of a starburst (see e.g. Teyssier et al., 2010; Bournaud et al., 2011).

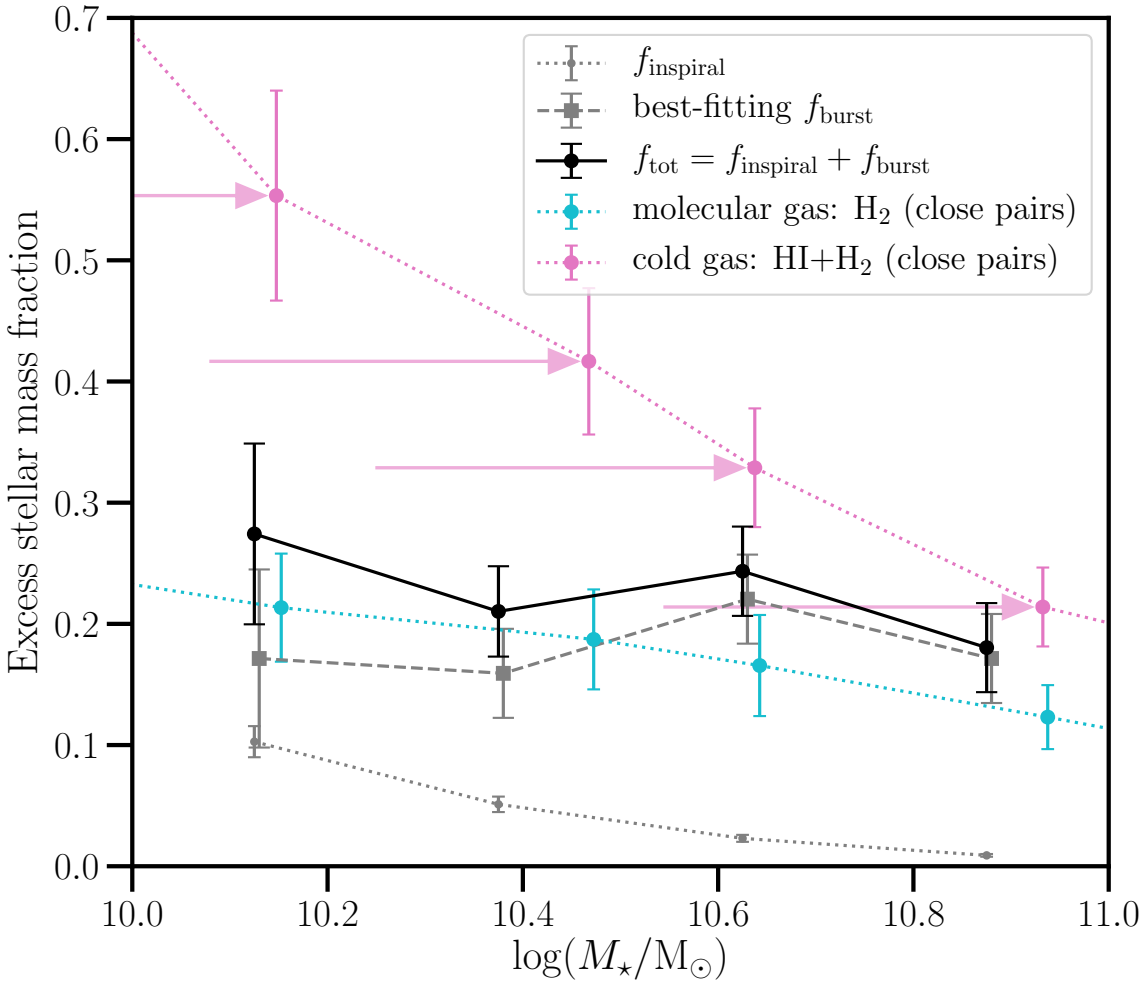

Figure 4.8: Comparison of estimated stellar mass burst fractions from our modeling of the inspiral phase (small grey circles), best-fitting $f_{\rm burst}$ (grey squares), and the total excess stellar mass from these two contributions (black points). Also shown are molecular (blue diamonds) and total cold gas (pink circles) converted into the equivalent mass fraction of long-lived stars by multiplying by $f_{\rm ret} = 0.6$. Pink arrows show the stellar mass shift for close pairs gas fractions (so they can be compared to post-coalescence merger quantities), which is applied to both molecular and atomic gas; see text for details.

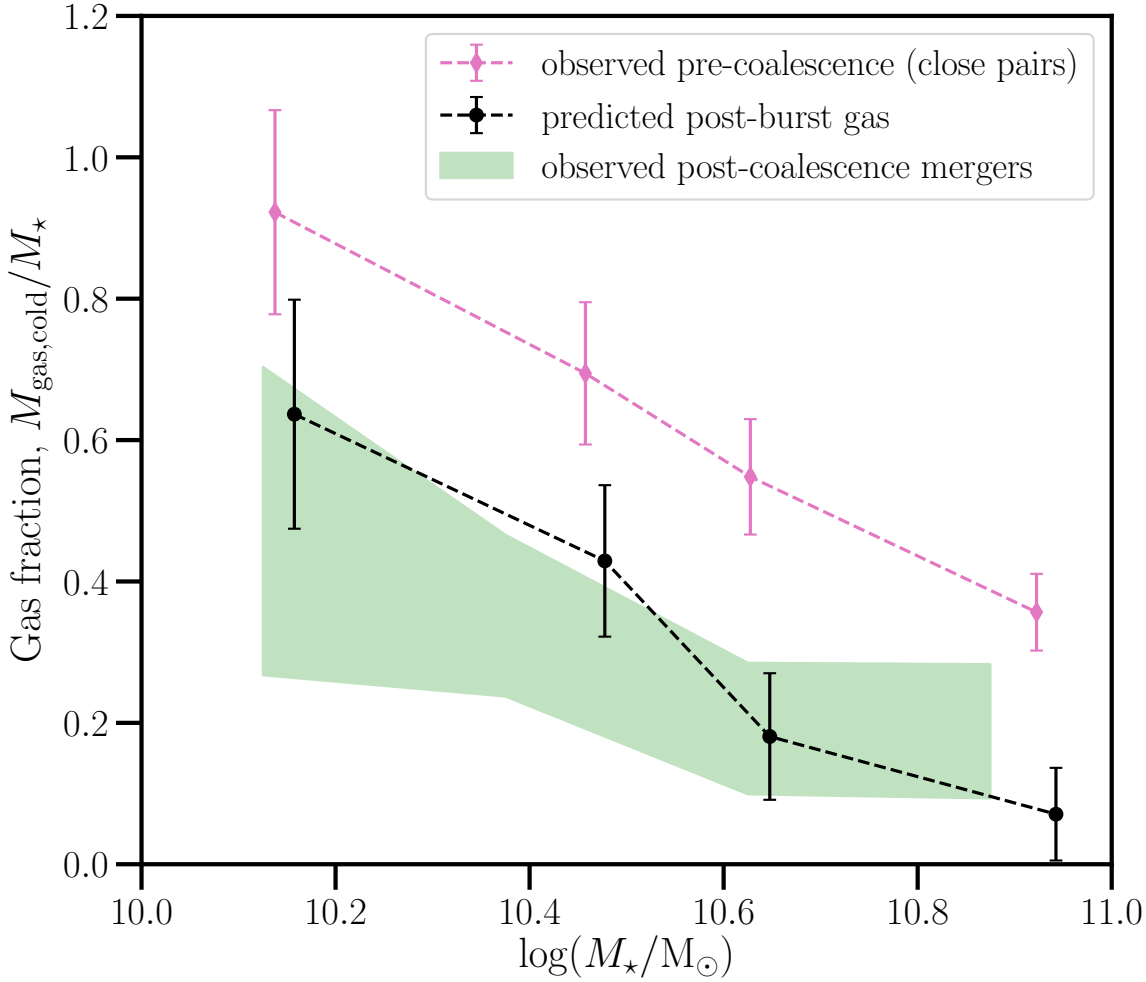

Figure 4.9: Comparison of cold gas before (pink points) and after coalescence (green), as well as our prediction for remaining cold gas after the burst (black points), all as a fraction of the final merger stellar mass. Our prediction is simply the cold gas before minus the gas consumed during star formation (any gas ejected in supernovae is assumed to be hot). For the post-coalescence mergers we use the HI gas masses from Ellison et al. (2018) and H_2 gas masses from various samples of post-starburst galaxies (French et al., 2015; Rowlands et al., 2015; Otter et al., 2022, see text for details).

Such a picture is seen in detailed hydrodynamical simulations. In the FIRE-2 simulations, Moreno et al. (2021) find a 0.8–1 dex enhancement of cool atomic and 1.1–1.2 dex enhancement of cold-dense molecular gas mass in the central regions ($r < 1$ kpc) at time of second pericentre, coming from the galaxy outskirts ($r = 1$–10 kpc). This excess gas in the central region rapidly declines, back to the baseline of the two galaxies evolving in isolation, during the duration of the starburst (~ 0.5 Gyr).

A key question is then whether there is enough cold gas fuel available to form the excess mass of stars formed, namely $\sim 0.2 M_{\star,\rm merger}$, and if so, how much gas remains after the burst? To examine this question, we look at cold gas measurements for pairs of galaxies to estimate the amount of cold gas available to form stars at the start of coalescence.

We take cold gas fraction measurements of HI and H_2 from the XCOLD GASS survey (as presented in Saintonge et al., 2017), a systematic survey of $0.01 < z < 0.05$ galaxies selected from SDSS to be representative down to $10^9 M_\odot$ in stellar mass. We then adjust these gas masses by the relative enhancements in the proportions of the cold gas components for close pairs. In particular, we note that HI does not appear significantly different from controls in recent samples of several dozen pair galaxies, with some debate as to the exact impact (Ellison et al., 2015; Yu et al., 2022). For pre-coalescence HI gas masses, we simply use the unmodified Saintonge et al. (2017) HI masses. For H_2, we take the H_2 gas mass enhancements, relative to controls, of very close pairs from Pan et al. (2018) (most have stellar mass ratios $1 \leq \mu \leq 10$) and we multiply their figure 8 value (projected separation $r_p < 30$ kpc) by the ratio of gas masses for $10 < \log(M_\star/M_\odot) < 11$ galaxies to their whole sample, to find a mean molecular gas fraction ($M_{H_2}/M_\star$) enhancement of 0.62 ± 0.07 dex (see also Casasola et al., 2004; Violino et al., 2018). Such an enhancement increases the H_2 mass fraction of the cold gas from $M_{H_2}/(M_{\rm HI} + M_{H_2}) = 0.08$ – 0.11 for the general field sample of Saintonge et al. (2017) to $M_{H_2}/(M_{\rm HI} + M_{H_2}) = 0.39$ – 0.58 for close pairs (with higher gas fractions in these given ranges being for lower stellar mass galaxies). We note their result is consistent with Lisenfeld et al. (2019), when this latter work is corrected to account for He and metals. Such a large increase in molecular gas during the inspiral process is also consistent with data from LIRGS that are morphologically-defined as having double nuclei in the pre-coalescence stage of merging (Larson et al., 2016).

The relevant gas fraction for a merger involves not the stellar mass of the final merger product but rather the gas fractions expected from the progenitors and summed together appropriately. The final stellar mass is then the sum of the stellar masses of the progenitors (close pairs) plus the retained stellar mass after the cold gas is converted to stars. To compare gas fractions with the stellar mass burst fraction, we therefore shift the stellar mass bins of the gas fractions by doubling their mass and appropriately adding in the stellar mass burst, i.e. $M'_\star = 2M_\star/(1 - f_{\rm burst})$. We note that whether we assume equal mass

mergers or a more realistic e.g. $\mu = 3$, the impact on the gas fractions for our stellar mass range is negligible. We show these gas fractions overlaid with our best-fitting $f_{\rm burst}$ values in Figure 4.8. Assuming $f_{\rm ret} = 0.6$, we find there is just enough molecular gas available prior to coalescence to form the stellar mass burst, but only if either there is ~ 100 per cent efficiency in converting existing molecular gas to stars or if more molecular gas is formed during coalescence. Using instead the total cold gas content (molecular and atomic) prior to coalescence, the gas consumption efficiency of $e = (f_{\rm burst} M_{\star,\rm merger}/f_{\rm ret})/M_{\rm gas,cold}$ ranges from 30–80 per cent, increasing in efficiency from the lowest to highest stellar mass bin.

A similar comparison has been performed for post-starburst galaxies. In particular, French et al. (2018, see also Rowlands et al. 2015) find a significant decline in molecular gas to stellar mass fraction with increasing post-burst age, which persists after controlling for fraction of stellar mass produced in the recent burst. Assuming an exponentially declining gas fraction, they find a best-fitting timescale of $117 - 230$ Myr and best-fitting initial molecular gas fractions of 0.4–0.7 at a post-burst age of zero (lower end of this range is consistent with Pan et al., 2018). Based on their fit relation, for a post-starburst about 0.5 Gyr after the beginning of the burst (their mean found for post-starbursts with SED fitting), a post-starburst has $M_{\rm H_2}/M_\star \sim 0.05$. The difference between their results and ours is likely driven by the difference in sample selection, since as noted earlier, only ~ 20 per cent of post-coalescence mergers are post-starbursts (Ellison et al., 2022).

Subtracting the gas consumed in the burst from the total expected cold gas fraction in the merging pair pre-coalescence, we predict a residual post-burst cold gas fraction as shown in Figure 4.9 (black points). Specifically, our prediction assumes all gas ejected by supernovae (i.e. the $(1\text{-}f_{\rm ret}) = 0.4$ fraction of cold gas not retained as stellar mass) is in the form of hot gas. Is this consistent with observed gas fractions in post-coalescence mergers?

For HI gas, we use reported HI gas enhancements in Ellison et al. (2018) of median atomic gas-to-stellar mass ratios in observed post-coalescence mergers (see their figure 4). They find enhancements, relative to xGASS stellar mass-matched controls, of ~ 0.2 dex when including only detections above their adopted threshold level (which we refer to as their "HI upper estimate") and ~ 0.4 dex ("HI lower estimate") when including both detections and upper limits on HI gas masses. We show this range, including uncertainties, as the green shaded region in Figure 4.9. For H_2 gas masses, there are no published values for post-coalescence mergers yet in the literature. Instead, we adopt a compilation of post-starburst H_2 gas masses (French et al., 2015; Rowlands et al., 2015; Otter et al., 2022) in the stellar mass range $\log(M_\star/{\rm M}_\odot) = [10, 11]$. We combine the HI and H_2 gas fractions into a post-coalescence merger cold gas fraction, shown in green on Figure 4.9 (with the shaded vertical range including the range in possible HI values as well as uncertainties on the gas fractions). Our predicted cold gas fraction is consistent with this range, lending

further credence to our estimated burst to stellar mass fraction.

As to why this cold gas remains after the burst, suppression of the burst before gas can be depleted by star formation has been proposed to be due to enhanced turbulence from the merging process, as well as from shocks and/or outflows from star formation and (non-QSO) AGN feedback (e.g. Veilleux et al., 2013; Sell et al., 2014; Rich et al., 2014; Mortazavi & Lotz, 2019). These effects could make the ISM stable against gravitational collapse even if cold gas is abundant (Alatalo et al., 2015; Smercina et al., 2018; van de Voort et al., 2018). A sample of resolved molecular gas observations of MaNGA post-starbursts in the recent work of Otter et al. (2022) supports this, they find compact but highly disturbed molecular gas unable to form stars efficiently.

4.5 Conclusions

In this work, we used the morphologically selected and visually-confirmed post-coalescence merger catalog of Bickley et al. (2022) combined with available SDSS photometric and spectroscopic data to directly model the stellar mass formed in the starburst during coalescence. To fit for the stellar mass burst fraction, we forward model the difference in mean age–$M_\star$ relation between post-coalescence mergers and a control sample, controlling for stellar mass, local density, and redshift. In particular, we model the star formation history of control galaxies in four bins across $10 < \log(M_\star/\mathrm{M}_\odot) < 11$, the inspiral (pre-merger close pair) star formation enhancement, and the final starburst from coalescence. Our main results and conclusions are as follows:

- Post-coalescence merger galaxies are younger than control galaxies by $2-3$ Gyr, with a smaller age difference for higher stellar mass galaxies.
- We find a mean stellar mass burst fraction of $f_{\mathrm{burst}} = 0.18 \pm 0.02$, independent of stellar mass and with only a very weak dependence on burst duration.
- Our burst fraction is consistent with some observationally-derived values, namely Hopkins et al. (2008c) measurement of gas rich post-mergers and the higher stellar mass end of post-starbursts (French et al., 2018). We find a notably higher burst fraction than another recent study using stellar ages, Yoon et al. (2023), which may be due to differences in sample selection; our sample is trained on major mergers of any morphological type, whereas theirs includes any tidally-disturbed ETG, potentially including minor mergers or pre-coalescence disturbances.

- Compared to simulations, our burst fraction is twice that of the hydrodynamical FIRE-2 simulation and much greater than that of the cosmological hydrodynamical IllustrisTNG simulation, which finds a negligible starburst.

- Using the star formation rates of published LIRGs that were morphologically-identified as late-stage inspiraling pairs (i.e. not yet coalesced), we estimate the starburst duration for post-coalescence mergers is $\Delta t_{\rm burst} \sim 120$ Myr for $\log(M_\star/{\rm M}_\odot) < 10.25$ galaxies and increasing to $\Delta t_{\rm burst} \sim 250$ Myr for $\log(M_\star/{\rm M}_\odot) > 10.5$ galaxies. This is longer than found in the literature for observed post-starburst galaxies, consistent with the Illustris TNG100-1 hydrodynamical simulation, and $\sim$ half as long as for the high-resolution FIRE-2 hydrodynamical simulation.

- We find there is enough molecular gas present in close pairs to fuel the starburst that we measure, assuming a high efficiency in converting molecular gas into stars. Assuming both molecular and atomic gas are available as fuel for star formation during the burst (consistent with our burst timescale being $\sim$ the free-fall time at the edge of the disc), we predict a remaining cold gas fraction that is consistent with observations.

Based on our results and discussion, we conclude there is clearly a significant stellar mass burst during galaxy mergers. Crucially important when comparing results is how the morphological selection of post-coalescence galaxies is performed. Samples relying on faint features could easily include minor mergers, which likely have a much smaller burst fraction than for major mergers.

Additionally, cold gas measurements, particularly of H_2 for post-coalescence mergers, are needed to quantify the mass of cold gas remaining after a galaxy merger. As seen in portions of our work, derived burst fractions and timescales for post-starbursts are not always representative of all post-coalescence mergers. To measure H_2 gas masses, a CO survey of at least one to two dozen post-coalescence galaxies, e.g. using a subset of the post-coalescence merger sample of Bickley et al. (2022), is feasible with the Atacama Large Millimeter/submillimeter Array (ALMA).

Chapter 5

Conclusion

5.1 Synthesis of thesis works and additional context since publication

Understanding the physical processes underlying galaxy evolution can be studied through naturally controlled 'experiments', i.e. contrasting environmental effects on galaxies with what is observed for galaxies in different environments or isolated galaxies. Star formation and quenching of star formation remain challenging to model accurately across environmental effects, galaxy mass, and redshift. This thesis studied several such 'natural experiments' to probe the physics of star formation and quenching. I summarize the three studies I presented in the previous chapters and particularly for the summary of Chapter 2 and Chapter 3, adding additional context, including from new GOGREEN works, that has become clear since publication.

5.1.1 Chapter 2 – study of quenching in high-z GOGREEN groups

In Chapter 2, GOGREEN groups were confirmed and they, as well as other high-redshift ($1 < z < 1.5$) galaxy groups, were studied. We found an enhancement, relative to the field, of the quiescent fraction for galaxies with stellar masses $\log(M_\star/\mathrm{M}_\odot) \gtrsim 10.7$. For high stellar mass galaxies, with $\log(M_\star/\mathrm{M}_\odot) \gtrsim 11$, essentially all group members were quenched rather than only half of these being quiescent in an average field volume. When we put these group results in the context of previously published GOGREEN $1 < z < 1.5$ clusters (by van der Burg et al., 2020) and lower redshift samples, we determined that the

environmental quiescent fraction excess depends on halo mass with a logarithmic slope of $\mathrm{d(QFE)/dlog}(M_{\mathrm{halo}}) \sim 0.24 \pm 0.04$, at a fixed stellar mass. This is slightly steeper than e.g. Woo et al. (2013) who found a slope of ~ 0.15–0.18 for a fixed stellar mass at $z \sim 0$. It was found, however, that, unlike at low redshift, at high redshift the dependencies of quenching on stellar and halo mass are not separable. The most natural explanation for quenching across all of these scales, especially in group mass halos, was concluded to be the shutoff of cosmological accretion of gas onto satellite galaxies (starvation). Baxter et al. (2022) followed-up with more detailed modeling of infall quenching in GOGREEN clusters, using accretion histories for $z \sim 1$ IllustrisTNG simulated galaxy clusters to constrain quenching timescales and compare them to cold gas depletion times. They came to similar conclusions regarding infall quenching in their work as well in a follow-up modeling work, Baxter et al. (2023), where they build on this model and incorporate a radial location of quenching onset.

Comparing to the BAHAMAS hydrodynamical simulations at $z \sim 1$ in Chapter 2, it was clear that BAHAMAS is able to reproduce the trend of quiescent fraction with halo mass, but predicts a declining trend with stellar mass – the opposite of observations. This is a problem that is much less pronounced in hydrodynamical simulations at $z \sim 0$. It was concluded that this likely indicates an incomplete model of subgrid feedback and/or star formation at galaxy scales. Follow-up work by Kukstas et al. (2023) look at a suite of hydrodynamical simulations of galaxy clusters at $z \sim 1$ and confirm this problem for BAHAMAS/MACSIS (McCarthy et al., 2017; Barnes et al., 2017), Hydrangea (Bahé et al., 2017), as well as TNG300 (Gu et al., 2020). All of these simulations struggle with overquenching low-mass satellite galaxies in clusters, resulting in a factor of two or more quenching than seen in the GOGREEN data for $\log(M_\star/\mathrm{M}_\odot) \lesssim 10$.

The GOGREEN group and cluster quenching results were then fit with toy infall quenching models, contrasting a pre-processing scenario (infall-induced quenching starting when a galaxy falls into any halo for the first time) with a scenario without pre-processing (infall-induced quenching starting only upon infall into the final galaxy cluster's halo or main progenitor halo). With this analysis it was clear that the time delay until quenching due to infall is strongly dependent on stellar mass, decreasing with stellar mass. The difference in quenching time delay between groups and clusters, at a fixed stellar mass, was far larger in the case with no pre-processing (~ 1.5 Gyr longer for groups, vs only ~ 0.5 Gyr longer for groups with the pre-processing model). In these models it was found that the discrepancy between modeled and observed quiescent mass-weighted ages was minimized by the pre-processing model, although some discrepancy remained, suggesting that quiescent galaxies in $1 < z < 1.5$ clusters are still older than can be explained by this pre-processing model. This would possibly indicate a head-start for galaxy quenching in

cluster galaxies versus galaxies in the general field or groups, as suggested in van der Burg et al. (2020) and supported by slightly older cluster ages found in Webb et al. (2020).

A similar picture of quenching to that at low redshifts, where massive centrals quench prior to entering clusters, became clear in the work of Werner et al. (2022), who found that satellite quenching is not especially important for $z \sim 1$ GOGREEN clusters, as most quenching occurred prior to infall. They come to this conclusion by looking at quenching in the infalling regions around GOGREEN clusters, noting that there are far more massive quiescent galaxies in the infalling region than a field control sample, likely simply due to groups being much more common in the infall region of clusters than the general field. Instead of starvation being the dominant driver of quenching in cluster satellite galaxies, it appears that massive galaxies quenched prior to infall as centrals of group halos, while many lower mass galaxies experienced pre-processing in group halos (e.g. via starvation) prior to infall into $z \sim 1$ clusters. Baxter et al. (2022) confirm this effect for high mass galaxies, finding $\sim 65-80$ per cent of $\log(M_\star/\mathrm{M}_\odot) > 11$ galaxies quenched prior to infall.

In summary, it is clear that environment and environmental pre-processing, particularly through host halo mass, play an important role in quenching up to at least $z \sim 1.5$. It is important even in lower mass halos and likely not due to ram pressure stripping of cold gas reservoirs, since such physics would most impact low-mass rather than massive galaxies. It appears possible that most 'pre-processing' of massive galaxies that end up in clusters at $z \sim 1$ occurs during their time spent in group mass halos (including as centrals) and/or denser protocluster environments. A clearer understanding of this will require careful systematic study of protocluster environments at $z > 2$, work which has only recently begun thanks to the James Webb Space Telescope (Valentino et al., 2023).

5.1.2 Chapter 3 – infall quenching timescales in galaxy clusters from stellar ages

As noted in the previous subsection, taking account of pre-processing prior to infall into clusters is essential to quantify the intensity of quenching after infall. Chapter 3 continues a line of work (Oman & Hudson, 2016; Oman et al., 2021) that models infall quenching in $z \sim 0$ clusters using statistical information in projected phase space and use an infall region as an already pre-processed control sample. In order to break degeneracies between the delay until quenching onset and the duration of the star formation rate suppression, the work of Chapter 3 breaks the degeneracy by adding (in addition to f_Q) another observable in projected phase space: stellar ages of galaxies. By assuming the empirically-motivated stochastic star formation histories from the UniverseMachine model (Behroozi et al.,

2019) and the statistical infall time distribution of cluster galaxies using an orbit library derived from N-body simulations (Oman et al., 2013, 2021), we forward model the impact of infall quenching on star formation histories using using a delayed then exponentially declining star formation rate suppression, relative to time of first pericentre.

We found the mean deviation in MWA from the mean MWA–$M_\star$ relation depends on position in projected phase space, up to about ~ 1 Gyr older in the cluster core than an interloper-dominated region. Our overall quenching times are ~ 4 Gyr for a delayed-then-instantaneous quenching model for our lower ($9 < \log(M_\star/\mathrm{M}_\odot) < 10$) and higher stellar mass ($10 < \log(M_\star/\mathrm{M}_\odot) < 10.5$) bins. In a detailed literature comparison, we show that our overall ~ 4 Gyr quenching timescales are consistent with Oman et al. (2021) which we build upon, but are longer than other modeling works that only use quiescent fraction and may also be underestimating the amount of pre-processing prior to infall. Our higher stellar mass bin results are consistent with Taranu et al. (2014) who use age-sensitive Balmer lines of quiescent galaxies rather than quiescent fractions.

Using our full model, we found that quenching starts at or shortly before first pericentre, with a short ≤ 1 Gyr exponential suppression timescale for our lower stellar mass bin and a longer ~ 2.3 Gyr exponential suppression timescale for our higher stellar mass bin. This result contrasts with prior modeling papers, such as the work of Wetzel et al. (2013), who found only short star formation suppression timescales are possible – otherwise the observed bimodality in star formation rates is not maintained for galaxies in clusters. Their result, however, depends on their assumption of a smooth star formation history. We have shown that assuming a stochastic star formation history, where galaxies can transition between being quiescent and star forming, allows for a much longer timescale for environmental quenching.

Our model's preference for quenching starting close to first pericentre suggests ram-pressure stripping as the quenching mechanism. However, our overall quenching timescale of 4.0 Gyr is much longer than timescales often given for aggressive ram pressure stripping in the literature (< 1 Gyr, see Cortese et al., 2021), and is actually consistent with a simple starvation scenario (~ 4 Gyr). This could indicate that ram-pressure stripping is primarily of the hot gas halo and not of the cold gas in the disc. It's also possible that a partially cold-gas stripped galaxy could retain a sizeable reservoir of hot halo gas that could cool, in which case there likely is a degeneracy between the amount of cold and hot gas stripped for a given quenching timescale. Future works should aim to address this, for example using a semi-analytic model (or hydro sims), where quenching times are forward-modeled (determined) from the amount of cold gas and hot gas stripping.

If we scale the total quenching time of a $10 < \log(M_\star/\mathrm{M}_\odot) < 10.5$ galaxy from Chap-

ter 3, namely 4.9 Gyr (3.9 Gyr plus $\sim$ 1 Gyr for the average time for a galaxy to travel from R_{200c} to time of first pericentre), by the evolution in the dynamical time to $z = 1.25$ we would expect a quenching timescale of 2.7 Gyr. This timescale is consistent with that predicted by the infall model with pre-processing presented in Chapter 2. Wetzel et al. (2013), on the other hand, would find their very short 2.4 Gyr and 1.5 Gyr timescales scaled to 1.3 Gyr and 0.8 Gyr for a $\log(M_\star/\mathrm{M}_\odot) \sim 10$ and $\log(M_\star/\mathrm{M}_\odot) \sim 10.5$ galaxy, respectively. This is consistent with Baxter et al. (2022) at $z \sim 1.08$ (see also Baxter et al., submitted). There is clearly a tension between my results and e.g. Wetzel et al. (2013) and Baxter et al. (2022). The reason for the tension with Wetzel et al. (2013) is clear from the discussion in Chapter 3 – they are artificially constraining their fits by assuming a need for short timescales to preserve the galaxy SFR bimodality. With Baxter et al. (2022), the reason for the difference remains unclear.

Popping et al. (2015a) (note also the erratum Popping et al., 2015b) found a starvation time of 2.4 Gyr for a $\log(M_\star/\mathrm{M}_\odot) \sim 10.3$ galaxy at $z \sim 1$–1.5. At $z \sim 0$, using cold gas masses and SFRs from Saintonge et al. (2017), the implied starvation timescale is $\sim$ 4.2 Gyr. My results are clearly consistent with this starvation timescale. The differing modeling approaches in works like e.g. Wetzel et al. (2013) and Baxter et al. (2022), results in them instead favouring a more aggressive quenching scenario, where there is significant cold gas stripping occurring upon infall, rather than primarily stripping of hot gas.

5.1.3 Chapter 4 – how many stars form during a galaxy merger?

The usefulness of mass-weighted ages in constraining quenching timescales, demonstrated in Chapter 3, inspired their use with a recently released dataset of morphologically-identified post-coalescence mergers by Bickley et al. (2022). In particular, in Chapter 4 we found that these post-coalescence mergers are 2–3 Gyr younger than controls and we used this information to address the outstanding difficulty in measuring the stellar mass burst fraction from galaxy mergers by forward modelling the stellar ages given a burst fraction. This allowed us to constrain the burst fraction due to a recent merger as 0.18 ± 0.02.

Mergers are considered a possible quenching avenue and therefore could constitute a source of pre-processing. Such a quenching pathway could be particularly influential since mergers are most common in group environments, which are very common surrounding galaxy clusters.

Interestingly, we found that quenching is not enhanced in post-coalescence mergers compared to control galaxies. While we found a substantial burst, it was not sufficient to consume all of the available cold gas, leaving behind a gas fraction that is consistent with

observations. The amount of cold gas available post-merger is similar to that for a general field galaxy, indicating there should be little impact on the cold gas depletion timescale. That said, the remaining cold gas is quite dense, and should collapse to form more stars, unless it is supported e.g. by turbulence, as we speculated at the end of Chapter 4. In galaxies unable to reform discs from fresh cold gas, i.e. early-type galaxies created by these mergers, the turbulence could keep galaxies quenched even if there is additional inflows/cooling of cold gas (morphological quenching). Given the increased prevalence of mergers in groups, this could be a source of the extra quenching seen in higher mass group galaxies, including those examined in Chapter 2. Further study of the evolution of galaxies in high-resolution hydro sims (with turbulence), up to e.g. 1–2 Gyr post-coalescence, could help elucidate what happens to gas depletion post-merger.

5.2 Open questions and future work

5.2.1 Modeling and theoretical work

A key research question requiring further work is whether redshift evolution in quenching timescale is due to evolution in group/cluster properties or whether a separate quenching mechanism is dominant at each epoch.

It would be ideal to constrain what fraction of galaxies are quenched by e.g. ram-pressure stripping. Such constraints could come from building on the infall quenching modeling in projected phase space performed in my work and similar works by incorporating post-starbursts, observed radial/PPS trends of jelly-fish galaxies in deep imaging, and/or stellar ages from stellar population synthesis fitting sensitive to recent star formation (such as outputting the time at which 90 percent of stellar mass has formed). Alternatively (or additionally), since galaxies quenched by ram pressure stripping of cold gas appear to quench outside-in (Bluck et al., 2020; Wang et al., 2022), HI gas measurements could be combined with resolved star formation maps. Such a model would likely greatly improve the ability to constrain when and where such quenching in clusters occurs (and maybe for what fraction of galaxies). Building on hydrodynamic simulations of gas-stripping in galaxies could refine plausible scenarios linking quenching to galaxy and cluster halo mass. Simulation work, like e.g. the study of jellyfish galaxies in TNG50 in Rohr et al. (2023), indicates that star formation can persist until approximately 98 per cent of their cold gas is stripped.

Other areas requiring improvement are the dependence on halo mass as well as further work on preprocessing. Accounting for the role of pre-processing (broadly speaking, includ-

ing evolution as centrals) up to the infall region around clusters, including for high $z > 1$ redshifts, appears more important than previously assumed, especially for higher stellar mass galaxies. Doing so changes preferred timescales for quenching to be longer in clusters. A single consistent model applied to datasets at a range of redshifts accounting for this is highly desirable, as this would make much more clear the impact of evolution with redshift. More specific modeling of the infall populations should also examine whether the evolution in infall region region might impact projected phase space and radius-dependence modeling results, since the infall region will have evolved in the $1 - 2$ Gyr between what we see and when they will actually fall into the cluster – this effect may be especially important at higher redshifts (e.g. $z \gtrsim 1$ Werner et al., 2022).

Finally, improved detailed fitting and modeling of the star formation histories of galaxies is still needed. In particular, better understanding is needed of how stochastic star formation is for individual galaxies, since as Chapter 3's work employing stochastic star formation histories showed, such assumptions can change our conclusions about timescales, and therefore the processes involved, in environmental quenching. Stellar ages and star formation histories derived by fitting stellar populations to photometry/spectroscopy remains crude and considerable work remains that could improve our understanding of environmental quenching processes.

5.2.2 Future surveys and observations

Optical/near-IR observations

Essential to future progress in the study of environmental quenching will be future homogeneous surveys with large telescopes across swaths of the electromagnetic spectrum.

At high redshift, particularly above $z \sim 1.5$, large spectroscopic surveys of large homogeneous samples of galaxies are needed. As well, delayed-then-rapid quenching appears to be disfavoured at low redshift for $\log(M_\star/\mathrm{M}_\odot) > 10$ by my work in Chapter 3, but it remains to be confirmed or ruled out at higher redshifts. Surveys like GOGREEN have effectively maxed out the capabilities of existing large telescopes like Gemini – it is prohibitively expensive to integrate long enough on a sizable sample of faint lower mass galaxies. The Prime Focus Spectrograph (PFS Tamura et al., 2016; Greene et al., 2022) on the 8.2m Subaru telescope or the planned 11.25m Maunakea Spectroscopic Explorer (The MSE Science Team et al., 2019) should fill this need, as they are able to collect and integrate the spectra of thousands of targets simultaneously. This could enable infall quenching modelling using both quiescent fractions and mass-weighted ages in projected phase space at GOGREEN redshifts, like we have explored at low redshifts.

Special focus on measuring redshifts of known or suspected protocluster regions at $z > 2$ would also be especially informative to understand prior quenching in the earliest overdense environments. Targeted deep spectroscopy and imaging by the James Webb Space Telescope will also be key to understanding the processes behind this in detail and to be complete down to lower stellar masses. In particular, this could be carried out with JWST's microshutter array on its NIRSpec imager, which has an on-sky field of view similar to the size of a galaxy cluster at $z \sim 1$–1.5. NIRSpec is able to capture $\gtrsim 100$ spectra simultaneously (Ferruit et al., 2012) to a better signal-to-noise ratio than GOGREEN in $\lesssim 2$ hours telescope time instead of ~ 15 hours (for galaxies with lower stellar masses). Galaxy groups would especially benefit from a larger and more complete spectroscopic survey, as the sampling with GOGREEN was rather limited due to number of slits and integration time costs for lower stellar mass galaxies.

When fitting stellar ages, higher signal-to-noise than GOGREEN (e.g. S/N$>$ 20 instead of S/N $\sim$ 5–10) possible with JWST or the next generation of ground-based telescopes will be highly desirable. As well, it would be worth outputting additional stellar age measures sensitive to recent quenching/bursts (such as time at which a galaxy has formed 90 per cent of its stellar mass), as they will likely greatly help with fitting e.g. infall-quenching models.

Larger high-quality post-coalescence merger catalogues, such as an expanded version of that by Bickley et al. (2022), will shortly be possible upon the completion of the UNIONS survey (Ibata et al., 2017). Using morphological features in additional color bands may also help with machine learning classification, rather than relying on a single colour band. Deeper multi-band wide field imaging from Euclid could also upon available imaging data for the northern parts of the sky (Laureijs et al., 2011; Euclid Collaboration et al., 2022), where there is the systematic spectroscopic coverage needed for determining stellar ages and other properties.

Cold gas observations

From my mergers work presented in Chapter 4, a clear next step for studying mergers will be to measure the H_2 gas masses of a modest sample of one–two dozen post-coalescence mergers. Such a survey should be relatively straightforward now that sizable samples of post-coalescence mergers have been identified. In particular, this take the form of a CO survey of one–two dozen objects from the Bickley et al. (2022) sample using the Atacama Large Millimeter/submillimeter Array (ALMA). Larger samples of integrated H_2 measurements for close pairs would also be highly desirable, as H_2 gas masses for close pairs remain relatively poorly quantified.

Going forward, in the years ahead, it's clear that for the local Universe we need larger systematic surveys of cold gas (sub-mm and radio) in galaxies in pairs and mergers. With the ability to generate samples of hundreds or more morphologically-identified post-mergers, we can now target not only samples of close interacting pairs with increasingly large surveys, but also post-mergers. The Square Kilometre Array (SKA), due to come online in 2028 or 2029, will completely revolutionize our available data as it will map integrated HI emission in billions of galaxies via 21cm mapping out to the edge of the visible Universe. It will also be capable of detailed HI mapping. This data will be immensely useful in understanding the mechanisms fueling star formation and causing quenching generally, from low redshifts all the way to extremely high redshifts (effectively the edge of the observable Universe). A smaller scale survey of the $z \lesssim 0.26$ Universe, the Widefield ASKAP L-band Legacy All-sky Blind surveY (WALLABY), is currently being conducted as a stepping stone toward the SKA by using the Australian Square Kilometer Array Pathfinder (ASKAP), with informative early results are already being released (Deg et al., 2022).

5.3 Concluding remarks

We have answered some questions regarding infall quenching and the use of differences in stellar ages to robustly add information for constraining environmental effects on galaxy's star formation histories. In the process of answering these questions, we have raised new ones as well. What are the remaining sources of discrepancies in quenching timescales at high redshifts? Can the modeling framework of Oman & Hudson (2016), Oman et al. (2021), and Reeves et al. (2023) (including additional observables like stellar ages or cold gas fractions) clarify our understanding of infall quenching at higher redshifts? Are we on the cusp of identifying a consistent infall quenching mechanism up to high redshifts, or is this even possible, given the possible degeneracy between the amount of ram pressure stripping of hot and cold gas for a given quenching timescale? Additionally, understanding why not all of the cold disc gas (in very close pairs) is converted into stars during the starburst phase of a major merger is a question that requires further investigation.

Significantly improved survey data and high redshift spectroscopy from a new generation of telescopes will continue in the coming years, which can be used to help address these and other questions. It is essential to employ consistent modeling approaches across various redshifts to fully exploit the new and existing data for improving our understanding of environmental quenching mechanisms and their evolution through the history of the Universe.

References

Abazajian K. N., et al., 2009, ApJS, 182, 543

Abolfathi B., et al., 2018, ApJS, 235, 42

Ade P. A., et al., 2014, Astronomy & Astrophysics, 571, A16

Alatalo K., et al., 2015, ApJ, 812, 117

Alatalo K., et al., 2016, ApJ, 827, 106

Allanson S. P., Hudson M. J., Smith R. J., Lucey J. R., 2009, ApJ, 702, 1275

Almaini O., et al., 2017, MNRAS, 472, 1401

Alonso M. S., Tissera P. B., Lambas D. G., Coldwell G., 2006, in Revista Mexicana de Astronomia y Astrofisica Conference Series. p. 187

Andreon S., 2008, MNRAS, 386, 1045

Armus L., et al., 2009, PASP, 121, 559

Arnouts S., Cristiani S., Moscardini L., Matarrese S., Lucchin F., Fontana A., Giallongo E., 1999, MNRAS, 310, 540

Avila S., et al., 2014, MNRAS, 441, 3488

Bahé Y. M., McCarthy I. G., 2015, MNRAS, 447, 969

Bahé Y. M., McCarthy I. G., Balogh M. L., Font A. S., 2013, MNRAS, 430, 3017

Bahé Y. M., et al., 2017, MNRAS, 470, 4186

Baldry I. K., Glazebrook K., Brinkmann J., Ivezić Ž., Lupton R. H., Nichol R. C., Szalay A. S., 2004, ApJ, 600, 681

Baldry I. K., Balogh M. L., Bower R. G., Glazebrook K., Nichol R. C., Bamford S. P., Budavari T., 2006, MNRAS, 373, 469

Baldry I. K., et al., 2012, MNRAS, 421, 621

Balogh M. L., Morris S. L., Yee H. K. C., Carlberg R. G., Ellingson E., 1999, ApJ, 527, 54

Balogh M. L., Navarro J. F., Morris S. L., 2000, ApJ, 540, 113

Balogh M., et al., 2004a, MNRAS, 348, 1355

Balogh M. L., Baldry I. K., Nichol R., Miller C., Bower R., Glazebrook K., 2004b, ApJ, 615, L101

Balogh M. L., McCarthy I. G., Bower R. G., Eke V. R., 2008, MNRAS, 385, 1003

Balogh M., McGee S., Parker L., Bower R., Mulchaey J., Finoguenov A., Wilman D., Connelly J., 2010, The transition of galaxy groups from an invigorating environment to a suffocating one, NOAO Proposal

Balogh M. L., et al., 2014, MNRAS, 443, 2679

Balogh M. L., et al., 2016, MNRAS, 456, 4364

Balogh M. L., et al., 2017, MNRAS, 470, 4168

Balogh M. L., et al., 2021, MNRAS, 500, 358

Barger A. J., Aragon-Salamanca A., Ellis R. S., Couch W. J., Smail I., Sharples R. M., 1996, MNRAS, 279, 1

Barnes J. E., Hernquist L. E., 1991, ApJ, 370, L65

Barnes J. E., Hernquist L., 1996a, ApJ, 471, 115

Barnes J. E., Hernquist L., 1996b, ApJ, 471, 115

Barnes D. J., Kay S. T., Henson M. A., McCarthy I. G., Schaye J., Jenkins A., 2017, MNRAS, 465, 213

Barton E. J., Geller M. J., Kenyon S. J., 2000, ApJ, 530, 660

Baxter D. C., et al., 2022, MNRAS, 515, 5479

Baxter D. C., et al., 2023, arXiv e-prints, p. arXiv:2306.09404

Behroozi P. S., Wechsler R. H., Wu H.-Y., 2013a, ApJ, 762, 109

Behroozi P. S., Wechsler R. H., Wu H.-Y., Busha M. T., Klypin A. A., Primack J. R., 2013b, ApJ, 763, 18

Behroozi P. S., Wechsler R. H., Conroy C., 2013c, ApJ, 770, 57

Behroozi P. S., Wechsler R. H., Conroy C., 2013d, ApJ, 770, 57

Behroozi P. S., Wechsler R. H., Lu Y., Hahn O., Busha M. T., Klypin A., Primack J. R., 2014, ApJ, 787, 156

Behroozi P. S., et al., 2015, MNRAS, 450, 1546

Behroozi P., Wechsler R. H., Hearin A. P., Conroy C., 2019, MNRAS, 488, 3143

Beifiori A., Maraston C., Thomas D., Johansson J., 2011, A&A, 531, A109

Bekki K., Couch W. J., Shioya Y., 2002, ApJ, 577, 651

Bekki K., Couch W. J., Shioya Y., Vazdekis A., 2005, MNRAS, 359, 949

Bell E. F., McIntosh D. H., Katz N., Weinberg M. D., 2003, ApJS, 149, 289

Bell E. F., et al., 2004a, ApJ, 600, L11

Bell E. F., et al., 2004b, ApJ, 608, 752

Benson A. J., 2010, Phys. Rep., 495, 33

Bergvall N., Marquart T., Way M. J., Blomqvist A., Holst E., Östlin G., Zackrisson E., 2016, A&A, 587, A72

Bernardi M., Nichol R. C., Sheth R. K., Miller C. J., Brinkmann J., 2006, AJ, 131, 1288

Berrier J. C., Stewart K. R., Bullock J. S., Purcell C. W., Barton E. J., Wechsler R. H., 2009, ApJ, 690, 1292

Bickley R. W., et al., 2021, MNRAS, 504, 372

Bickley R. W., Ellison S. L., Patton D. R., Bottrell C., Gwyn S., Hudson M. J., 2022, MNRAS, 514, 3294

Bigiel F., Leroy A., Walter F., Brinks E., de Blok W. J. G., Madore B., Thornley M. D., 2008, AJ, 136, 2846

Biviano A., Murante G., Borgani S., Diaferio A., Dolag K., Girardi M., 2006, A&A, 456, 23

Biviano A., et al., 2021, arXiv e-prints, p. arXiv:2104.01183

Bluck A. F. L., et al., 2020, MNRAS, 499, 230

Boselli A., Gavazzi G., 2006, PASP, 118, 517

Boselli A., Cortese L., Boquien M., Boissier S., Catinella B., Lagos C., Saintonge A., 2014, A&A, 564, A66

Boselli A., et al., 2016, A&A, 596, A11

Boselli A., Fossati M., Sun M., 2022, A&ARv, 30, 3

Bottrell C., et al., 2019, MNRAS, 490, 5390

Bouché N., et al., 2010, ApJ, 718, 1001

Bournaud F., Powell L. C., Chapon D., Teyssier R., 2011, Proceedings of the International Astronomical Union, IAU Symposium, 271, 160

Bower R. G., Benson A. J., Malbon R., Helly J. C., Frenk C. S., Baugh C. M., Cole S., Lacey C. G., 2006, MNRAS, 370, 645

Bower R. G., Schaye J., Frenk C. S., Theuns T., Schaller M., Crain R. A., McAlpine S., 2017, MNRAS, 465, 32

Bradshaw E. J., et al., 2013, MNRAS, 433, 194

Brammer G. B., van Dokkum P. G., Coppi P., 2010, EAZY: A Fast, Public Photometric Redshift Code (ascl:1010.052)

Brammer G. B., et al., 2011, ApJ, 739, 24

Brammer G. B., et al., 2012, The Astrophysical Journal Supplement Series, 200, 13

Brinchmann J., Charlot S., White S. D. M., Tremonti C., Kauffmann G., Heckman T., Brinkmann J., 2004, MNRAS, 351, 1151

Brodwin M., et al., 2013, ApJ, 779, 138

Brown M. J. I., et al., 2009, ApJ, 703, 150

Bruzual G., Charlot S., 2003, MNRAS, 344, 1000

Bryan G. L., Norman M. L., 1998, ApJ, 495, 80

Budzynski J. M., Koposov S. E., McCarthy I. G., McGee S. L., Belokurov V., 2012, MNRAS, 423, 104

Butcher H., Oemler A. J., 1978, ApJ, 219, 18

Butcher H., Oemler A. J., 1984, ApJ, 285, 426

Cales S. L., Brotherton M. S., 2015, MNRAS, 449, 2374

Cales S. L., et al., 2013, ApJ, 762, 90

Canalizo G., Stockton A., 2001, ApJ, 555, 719

Cappellari M., et al., 2011, MNRAS, 413, 813

Cappellari M., et al., 2013, MNRAS, 432, 1862

Carnall A. C., McLure R. J., Dunlop J. S., Davé R., 2018, MNRAS, 480, 4379

Carnall A. C., Leja J., Johnson B. D., McLure R. J., Dunlop J. S., Conroy C., 2019, ApJ, 873, 44

Casasola V., Bettoni D., Galletta G., 2004, A&A, 422, 941

Cattaneo A., Dekel A., Faber S. M., Guiderdoni B., 2008, MNRAS, 389, 567

Chabrier G., 2003, PASP, 115, 763

Chan J. C. C., et al., 2019, ApJ, 880, 119

Chan J. C. C., et al., 2021, ApJ, 920, 32

Chevallard J., Charlot S., 2016, MNRAS, 462, 1415

Chiappetti L., et al., 2013, MNRAS, 429, 1652

Chung A., van Gorkom J. H., Kenney J. D. P., Crowl H., Vollmer B., 2009, AJ, 138, 1741

Cirasuolo M., McLure R. J., Dunlop J. S., Almaini O., Foucaud S., Simpson C., 2010, MNRAS, 401, 1166

Coil A. L., et al., 2011, The Astrophysical Journal, 741, 8

Comparat J., et al., 2017, arXiv e-prints, p. arXiv:1711.06575

Conroy C., 2013, ARA&A, 51, 393

Conroy C., Gunn J. E., 2010a, FSPS: Flexible Stellar Population Synthesis (ascl:1010.043)

Conroy C., Gunn J. E., 2010b, ApJ, 712, 833

Conroy C., Wechsler R. H., Kravtsov A. V., 2006, ApJ, 647, 201

Conroy C., Gunn J. E., White M., 2009a, ApJ, 699, 486

Conroy C., Gunn J. E., White M., 2009b, ApJ, 699, 486

Conselice C. J., Bershady M. A., Dickinson M., Papovich C., 2003, AJ, 126, 1183

Cool R. J., et al., 2013, The Astrophysical Journal, 767, 118

Cooper M. C., et al., 2006, MNRAS, 370, 198

Cooper M. C., et al., 2007, MNRAS, 376, 1445

Cortese L., Catinella B., Smith R., 2021, Publ. Astron. Soc. Australia, 38, e035

Cotini S., Ripamonti E., Caccianiga A., Colpi M., Della Ceca R., Mapelli M., Severgnini P., Segreto A., 2013, MNRAS, 431, 2661

Cowie L. L., Songaila A., Hu E. M., Cohen J. G., 1996, AJ, 112, 839

Cox T. J., Jonsson P., Somerville R. S., Primack J. R., Dekel A., 2008, MNRAS, 384, 386

Crawford S. M., Bershady M. A., Hoessel J. G., 2009, ApJ, 690, 1158

Cressie N., 1993, Wiley-Interscience

Damen M., Labbé I., Franx M., van Dokkum P. G., Taylor E. N., Gawiser E. J., 2009, ApJ, 690, 937

Darg D. W., et al., 2010, MNRAS, 401, 1552

Darvish B., Mobasher B., Sobral D., Rettura A., Scoville N., Faisst A., Capak P., 2016, ApJ, 825, 113

Davé R., Finlator K., Oppenheimer B. D., 2012, MNRAS, 421, 98

Davidzon I., et al., 2016, A&A, 586, A23

Davis T. A., van de Voort F., Rowlands K., McAlpine S., Wild V., Crain R. A., 2019, MNRAS, 484, 2447

De Lucia G., et al., 2004, ApJ, 610, L77

De Lucia G., et al., 2007, MNRAS, 374, 809

De Lucia G., Weinmann S., Poggianti B. M., Aragón-Salamanca A., Zaritsky D., 2012, MNRAS, 423, 1277

Deg N., et al., 2022, Publ. Astron. Soc. Australia, 39, e059

Dekel A., Birnboim Y., 2006a, MNRAS, 368, 2

Dekel A., Birnboim Y., 2006b, MNRAS, 368, 2

Desmons A., Brough S., Martínez-Lombilla C., De Propris R., Holwerda B., López Sánchez Á. R., 2023, arXiv e-prints, p. arXiv:2305.17894

Dewdney P. E., Hall P. J., Schilizzi R. T., Lazio T. J. L. W., 2009, IEEE Proceedings, 97, 1482

Di Matteo T., Springel V., Hernquist L., 2005, Nature, 433, 604

Di Matteo P., Bournaud F., Martig M., Combes F., Melchior A. L., Semelin B., 2008, A&A, 492, 31

Diemer B., More S., Kravtsov A. V., 2013, ApJ, 766, 25

Diemer B., Sparre M., Abramson L. E., Torrey P., 2017, ApJ, 839, 26

Donnari M., et al., 2019, MNRAS, 485, 4817

Donnari M., Pillepich A., Nelson D., Marinacci F., Vogelsberger M., Hernquist L., 2020, arXiv e-prints, p. arXiv:2008.00004

Donnari M., et al., 2021, MNRAS, 500, 4004

Dressler A., 1980, ApJ, 236, 351

Du W., Luo A. L., Prugniel P., Liang Y. C., Zhao Y. H., 2010, MNRAS, 409, 567

Dutta R., Srianand R., Gupta N., 2018, MNRAS, 480, 947

Ebeling H., Stephenson L. N., Edge A. C., 2014, ApJ, 781, L40

Efstathiou G., Davis M., White S. D. M., Frenk C. S., 1985, ApJS, 57, 241

Ellison S. L., Patton D. R., Simard L., McConnachie A. W., 2008, AJ, 135, 1877

Ellison S. L., Patton D. R., Simard L., McConnachie A. W., Baldry I. K., Mendel J. T., 2010, MNRAS, 407, 1514

Ellison S. L., Patton D. R., Mendel J. T., Scudder J. M., 2011, MNRAS, 418, 2043

Ellison S. L., Mendel J. T., Scudder J. M., Patton D. R., Palmer M. J. D., 2013a, MNRAS, 430, 3128

Ellison S. L., Mendel J. T., Patton D. R., Scudder J. M., 2013b, MNRAS, 435, 3627

Ellison S. L., Fertig D., Rosenberg J. L., Nair P., Simard L., Torrey P., Patton D. R., 2015, MNRAS, 448, 221

Ellison S. L., Catinella B., Cortese L., 2018, MNRAS, 478, 3447

Ellison S. L., Viswanathan A., Patton D. R., Bottrell C., McConnachie A. W., Gwyn S., Cuillandre J.-C., 2019, MNRAS, 487, 2491

Ellison S. L., et al., 2022, MNRAS, 517, L92

Euclid Collaboration et al., 2022, A&A, 662, A112

Faber S. M., et al., 1997, AJ, 114, 1771

Faber S. M., et al., 2007, ApJ, 665, 265

Falcón-Barroso J., Sánchez-Blázquez P., Vazdekis A., Ricciardelli E., Cardiel N., Cenarro A. J., Gorgas J., Peletier R. F., 2011, A&A, 532, A95

Falkenberg M. A., Kotulla R., Fritze U., 2009, MNRAS, 397, 1954

Fang J. J., Faber S. M., Koo D. C., Dekel A., 2013, ApJ, 776, 63

Ferruit P., et al., 2012, in Clampin M. C., Fazio G. G., MacEwen H. A., Oschmann Jacobus M. J., eds, Society of Photo-Optical Instrumentation Engineers (SPIE) Conference Series Vol. 8442, Space Telescopes and Instrumentation 2012: Optical, Infrared, and Millimeter Wave. p. 84422O, doi:10.1117/12.925810

Fillingham S. P., Cooper M. C., Wheeler C., Garrison-Kimmel S., Boylan-Kolchin M., Bullock J. S., 2015, MNRAS, 454, 2039

Finlator K., Davé R., 2008, MNRAS, 385, 2181

Finoguenov A., et al., 2010, MNRAS, 403, 2063

Foltz R., et al., 2018, ApJ, 866, 136

Font A. S., et al., 2008, MNRAS, 389, 1619

Fontana A., et al., 2004, A&A, 424, 23

Foreman-Mackey D., Hogg D. W., Lang D., Goodman J., 2013, PASP, 125, 306

Forrest B., et al., 2020, ApJ, 903, 47

Fossati M., et al., 2017, ApJ, 835, 153

Fossati M., et al., 2018, A&A, 614, A57

Franx M., van Dokkum P. G., Schreiber N. M. F., Wuyts S., Labbé I., Toft S., 2008, The Astrophysical Journal, 688, 770

French K. D., 2021, PASP, 133, 072001

French K. D., Yang Y., Zabludoff A., Narayanan D., Shirley Y., Walter F., Smith J.-D., Tremonti C. A., 2015, ApJ, 801, 1

French K. D., Zabludoff A. I., Yoon I., Shirley Y., Yang Y., Smercina A., Smith J. D., Narayanan D., 2018, ApJ, 861, 123

Fujita Y., 2004, PASJ, 56, 29

Furlong M., et al., 2015, MNRAS, 450, 4486

Furusawa H., et al., 2008, The Astrophysical Journal Supplement Series, 176, 1

Gallazzi A., Charlot S., Brinchmann J., White S. D. M., Tremonti C. A., 2005, MNRAS, 362, 41

Gao Y., Gruendl R., Lo K. Y., Hwang C. Y., Veilleux S., 1997, in Holt S. S., Mundy L. G., eds, American Institute of Physics Conference Series Vol. 393, The Seventh Astrophysical Conference: Star formation, near and far. pp 319–322 (arXiv:astro-ph/9612153), doi:10.1063/1.52748

Garrison-Kimmel S., et al., 2018, MNRAS, 481, 4133

Gavazzi G., Consolandi G., Gutierrez M. L., Boselli A., Yoshida M., 2018, A&A, 618, A130

Genel S., et al., 2008, ApJ, 688, 789

George M. R., et al., 2011, ApJ, 742, 125

Gerke B. F., et al., 2007, MNRAS, 376, 1425

Gilbank D. G., Yee H. K. C., Ellingson E., Gladders M. D., Loh Y. S., Barrientos L. F., Barkhouse W. A., 2008, ApJ, 673, 742

Giodini S., et al., 2012, A&A, 538, A104

Gladders M. D., Oemler A., Dressler A., Poggianti B., Vulcani B., Abramson L., 2013, ApJ, 770, 64

Gobat R., et al., 2019, A&A, 629, A104

Gómez P. L., et al., 2003, ApJ, 584, 210

González Delgado R. M., Leitherer C., Heckman T. M., 1999, ApJS, 125, 489

Gonzalez A. H., Zaritsky D., Zabludoff A. I., 2007, ApJ, 666, 147

Gozaliasl G., et al., 2019, MNRAS, 483, 3545

Graham A. W., Driver S. P., 2005, Publ. Astron. Soc. Australia, 22, 118

Graves G. J., Faber S. M., Schiavon R. P., Yan R., 2007, ApJ, 671, 243

Greene J. E., Setton D., Bezanson R., Suess K. A., Kriek M., Spilker J. S., Goulding A. D., Feldmann R., 2020, ApJ, 899, L9

Greene J., Bezanson R., Ouchi M., Silverman J., the PFS Galaxy Evolution Working Group 2022, arXiv e-prints, p. arXiv:2206.14908

Gu M., et al., 2020, arXiv e-prints, p. arXiv:2010.04166

Guglielmo V., et al., 2019, A&A, 625, A112

Gunn J. E., Gott J. Richard I., 1972, ApJ, 176, 1

Haan S., et al., 2011, AJ, 141, 100

Haines C. P., et al., 2013, ApJ, 775, 126

Haines C. P., et al., 2015, ApJ, 806, 101

Han S., Smith R., Choi H., Cortese L., Catinella B., Contini E., Yi S. K., 2018, ApJ, 866, 78

Hani M. H., Gosain H., Ellison S. L., Patton D. R., Torrey P., 2020, MNRAS, 493, 3716

Harker G., Cole S., Helly J., Frenk C., Jenkins A., 2006, MNRAS, 367, 1039

Harris C. R., et al., 2020, Nature, 585, 357

Harrison C. M., 2017, Nature Astronomy, 1, 0165

Hartley W. G., et al., 2008, MNRAS, 391, 1301

Haynes M. P., Giovanelli R., Chincarini G. L., 1984, ARA&A, 22, 445

Hayward C. C., et al., 2014, MNRAS, 445, 1598

Hearin A. P., et al., 2017, The Astronomical Journal, 154, 190

Heavens A., Panter B., Jimenez R., Dunlop J., 2004, Nature, 428, 625

Heckman T. M., Armus L., Miley G. K., 1990, ApJS, 74, 833

Helly J. C., Cole S., Frenk C. S., Baugh C. M., Benson A., Lacey C., 2003, MNRAS, 338, 903

Hernquist L., 1989, Nature, 340, 687

Hirschmann M., De Lucia G., Fontanot F., 2016, MNRAS, 461, 1760

Hopkins P. F., 2012, MNRAS, 420, L8

Hopkins P. F., Hernquist L., Cox T. J., Di Matteo T., Robertson B., Springel V., 2006, ApJS, 163, 1

Hopkins P. F., Hernquist L., Cox T. J., Kereš D., 2008a, ApJS, 175, 356

Hopkins P. F., Hernquist L., Cox T. J., Kereš D., 2008b, ApJS, 175, 356

Hopkins P. F., Hernquist L., Cox T. J., Dutta S. N., Rothberg B., 2008c, ApJ, 679, 156

Hopkins P. F., Cox T. J., Dutta S. N., Hernquist L., Kormendy J., Lauer T. R., 2009, ApJS, 181, 135

Hopkins P. F., et al., 2010, ApJ, 724, 915

Hopkins P. F., Cox T. J., Hernquist L., Narayanan D., Hayward C. C., Murray N., 2013, MNRAS, 430, 1901

Hou A., Parker L. C., Harris W. E., 2014, MNRAS, 442, 406

Hu W., Kravtsov A. V., 2003, The Astrophysical Journal, 584, 702

Hubble E. P., 1925, ApJ, 62, 409

Hubble E. P., 1926, ApJ, 63, 236

Hubble E., 1929, Proceedings of the National Academy of Science, 15, 168

Hunter J. D., 2007, Computing in Science & Engineering, 9, 90

Hwang J.-S., Park C., 2015, ApJ, 805, 131

Hyde J. B., Bernardi M., 2009, MNRAS, 394, 1978

Ibata R. A., et al., 2017, ApJ, 848, 128

Ilbert O., et al., 2006, A&A, 457, 841

Iwasawa K., et al., 2011, A&A, 529, A106

Jaffé Y. L., Smith R., Candlish G. N., Poggianti B. M., Sheen Y.-K., Verheijen M. A. W., 2015, MNRAS, 448, 1715

Jaffé Y. L., et al., 2018, MNRAS, 476, 4753

Jiang L., Helly J. C., Cole S., Frenk C. S., 2014, MNRAS, 440, 2115

Johnson B. D., Leja J. L., Conroy C., Speagle J. S., 2019a, Prospector: Stellar population inference from spectra and SEDs (ascl:1905.025)

Johnson B. D., Leja J. L., Conroy C., Speagle J. S., 2019b, Prospector: Stellar population inference from spectra and SEDs (ascl:1905.025)

Just D. W., et al., 2019, ApJ, 885, 6

Karim A., et al., 2011, The Astrophysical Journal, 730, 61

Kartaltepe J. S., et al., 2010, ApJ, 721, 98

Kauffmann G., Haehnelt M., 2000, MNRAS, 311, 576

Kauffmann G., White S. D. M., Guiderdoni B., 1993, MNRAS, 264, 201

Kauffmann G., et al., 2003, MNRAS, 346, 1055

Kauffmann G., White S. D. M., Heckman T. M., Ménard B., Brinchmann J., Charlot S., Tremonti C., Brinkmann J., 2004, MNRAS, 353, 713

Kawata D., Mulchaey J. S., 2008, ApJ, 672, L103

Kawinwanichakij L., et al., 2016, The Astrophysical Journal, 817, 9

Kawinwanichakij L., et al., 2017, ApJ, 847, 134

Keel W. C., et al., 2012, MNRAS, 420, 878

Kelkar K., Gray M. E., Aragón-Salamanca A., Rudnick G., Jaffé Y. L., Jablonka P., Moustakas J., Milvang-Jensen B., 2019, MNRAS, 486, 868

Keller B. W., Wadsley J., Benincasa S. M., Couchman H. M. P., 2014, MNRAS, 442, 3013

Kennicutt Robert C. J., 1998, ApJ, 498, 541

Kennicutt R. C., Evans N. J., 2012, ARA&A, 50, 531

Kennicutt Robert C. J., Keel W. C., van der Hulst J. M., Hummel E., Roettiger K. A., 1987, AJ, 93, 1011

Kereš D., Katz N., Weinberg D. H., Davé R., 2005, MNRAS, 363, 2

Kewley L. J., Rupke D., Zahid H. J., Geller M. J., Barton E. J., 2010, ApJ, 721, L48

Khullar G., et al., 2022, ApJ, 934, 177

Kim S., Contini E., Choi H., Han S., Lee J., Oh S., Kang X., Yi S. K., 2020, ApJ, 905, 12

Kim K. J., et al., 2022, arXiv e-prints, p. arXiv:2207.12491

Kimm T., et al., 2009, MNRAS, 394, 1131

Kitzbichler M. G., White S. D. M., 2008, MNRAS, 391, 1489

Klypin A., Yepes G., Gottlöber S., Prada F., Heß S., 2016, MNRAS, 457, 4340

Knobel C., et al., 2013, ApJ, 769, 24

Kodama T., Bower R. G., 2001, MNRAS, 321, 18

Koss M., Mushotzky R., Veilleux S., Winter L., 2010, ApJ, 716, L125

Kovač K., et al., 2010, ApJ, 708, 505

Kovač K., et al., 2014, MNRAS, 438, 717

Kravtsov A. V., Borgani S., 2012, ARA&A, 50, 353

Kriek M., van Dokkum P. G., Labbé I., Franx M., Illingworth G. D., Marchesini D., Quadri R. F., 2009, ApJ, 700, 221

Kroupa P., 2001, MNRAS, 322, 231

Kukstas E., et al., 2023, MNRAS, 518, 4782

Lackner C. N., et al., 2014, AJ, 148, 137

Lambas D. G., Alonso S., Mesa V., O'Mill A. L., 2012, A&A, 539, A45

Larson R. B., Tinsley B. M., Caldwell C. N., 1980, ApJ, 237, 692

Larson K. L., et al., 2016, ApJ, 825, 128

Lauer T. R., et al., 1995, AJ, 110, 2622

Laureijs R., et al., 2011, arXiv e-prints, p. arXiv:1110.3193

Leauthaud A., et al., 2010, ApJ, 709, 97

Leauthaud A., et al., 2012, The Astrophysical Journal, 746, 95

Lee-Brown D. B., et al., 2017, ApJ, 844, 43

Lee J., et al., 2014, MNRAS, 445, 4197

Lee J., et al., 2018, ApJ, 864, 69

Legrand L., et al., 2019, MNRAS, 486, 5468

Leja J., Johnson B. D., Conroy C., van Dokkum P. G., Byler N., 2017a, ApJ, 837, 170

Leja J., Johnson B. D., Conroy C., van Dokkum P. G., Byler N., 2017b, ApJ, 837, 170

Leja J., Carnall A. C., Johnson B. D., Conroy C., Speagle J. S., 2019, ApJ, 876, 3

Lemaux B. C., et al., 2019, MNRAS, 490, 1231

Leonardi A. J., Rose J. A., 1996, AJ, 111, 182

Leroy A. K., Walter F., Brinks E., Bigiel F., de Blok W. J. G., Madore B., Thornley M. D., 2008, AJ, 136, 2782

Li C., Kauffmann G., Heckman T. M., Jing Y. P., White S. D. M., 2008, MNRAS, 385, 1903

Li Z., French K. D., Zabludoff A. I., Ho L. C., 2019, ApJ, 879, 131

Lilly S. J., Carollo C. M., Pipino A., Renzini A., Peng Y., 2013, ApJ, 772, 119

Lim S. H., Mo H. J., Lu Y., Wang H., Yang X., 2017, MNRAS, 470, 2982

Lin L., et al., 2010, ApJ, 718, 1158

Lintott C. J., et al., 2009, MNRAS, 399, 129

Lisenfeld U., Xu C. K., Gao Y., Domingue D. L., Cao C., Yun M. S., Zuo P., 2019, A&A, 627, A107

Liu C. T., Green R. F., 1996, ApJ, 458, L63

Łokas E. L., Mamon G. A., 2001, MNRAS, 321, 155

Lotz J. M., Jonsson P., Cox T. J., Primack J. R., 2008, MNRAS, 391, 1137

Lotz M., Remus R.-S., Dolag K., Biviano A., Burkert A., 2019, MNRAS, 488, 5370

Ludlow A. D., Navarro J. F., Angulo R. E., Boylan-Kolchin M., Springel V., Frenk C., White S. D. M., 2014, MNRAS, 441, 378

Lynden-Bell D., 1967, MNRAS, 136, 101

Mac Low M.-M., Klessen R. S., 2004, Reviews of Modern Physics, 76, 125

Madau P., Dickinson M., 2014, ARA&A, 52, 415

Mahajan S., Mamon G. A., Raychaudhury S., 2011, MNRAS, 416, 2882

Maraston C., Strömbäck G., 2011, MNRAS, 418, 2785

Marinacci F., et al., 2018, MNRAS, 480, 5113

Martig M., Bournaud F., Teyssier R., Dekel A., 2009, ApJ, 707, 250

Masters D. C., Stern D. K., Cohen J. G., Capak P. L., Rhodes J. D., Castander F. J., Paltani S., 2017, ApJ, 841, 111

Masters D. C., et al., 2019, ApJ, 877, 81

Mathews W. G., Brighenti F., 2003, ARA&A, 41, 191

McBride J., Fakhouri O., Ma C.-P., 2009, MNRAS, 398, 1858

McCarthy I. G., Frenk C. S., Font A. S., Lacey C. G., Bower R. G., Mitchell N. L., Balogh M. L., Theuns T., 2008a, MNRAS, 383, 593

McCarthy I. G., Frenk C. S., Font A. S., Lacey C. G., Bower R. G., Mitchell N. L., Balogh M. L., Theuns T., 2008b, MNRAS, 383, 593

McCarthy I. G., et al., 2010, MNRAS, 406, 822

McCarthy I. G., Schaye J., Bird S., Le Brun A. M. C., 2017, MNRAS, 465, 2936

McCarthy I. G., Bird S., Schaye J., Harnois-Deraps J., Font A. S., van Waerbeke L., 2018, MNRAS, 476, 2999

McCracken H., et al., 2012, Astronomy & Astrophysics, 544, A156

McElroy R., et al., 2022, MNRAS, 515, 3406

McGee S. L., Balogh M. L., Bower R. G., Font A. S., McCarthy I. G., 2009, MNRAS, 400, 937

McGee S. L., Balogh M. L., Wilman D. J., Bower R. G., Mulchaey J. S., Parker L. C., Oemler A., 2011, MNRAS, 413, 996

McGee S. L., Bower R. G., Balogh M. L., 2014, MNRAS, 442, L105

McLeod D. J., McLure R. J., Dunlop J. S., Cullen F., Carnall A. C., Duncan K., 2021, MNRAS,

McLure R. J., et al., 2013, MNRAS, 428, 1088

McNab K., et al., 2021, MNRAS, 508, 157

McNamara B. R., Nulsen P. E. J., 2007, ARA&A, 45, 117

McNamara B. R., Nulsen P. E. J., 2012, New Journal of Physics, 14, 055023

Mehta V., et al., 2018, The Astrophysical Journal Supplement Series, 235, 36

Melnyk O., et al., 2013, A&A, 557, A81

Mendel J. T., Simard L., Palmer M., Ellison S. L., Patton D. R., 2014, ApJS, 210, 3

Mihos J. C., Hernquist L., 1994, ApJ, 427, 112

Mihos J. C., Hernquist L., 1996, ApJ, 464, 641

Mo H., van den Bosch F. C., White S., 2010, Galaxy Formation and Evolution

Mok A., et al., 2013, MNRAS, 431, 1090

Momcheva I. G., et al., 2016, The Astrophysical Journal Supplement Series, 225, 27

More S., Diemer B., Kravtsov A. V., 2015, ApJ, 810, 36

Moreno J., et al., 2019, MNRAS, 485, 1320

Moreno J., et al., 2021, MNRAS, 503, 3113

Mortazavi S. A., Lotz J. M., 2019, MNRAS, 487, 1551

Moster B. P., Macciò A. V., Somerville R. S., Naab T., Cox T. J., 2011a, MNRAS, 415, 3750

Moster B. P., Somerville R. S., Newman J. A., Rix H.-W., 2011b, The Astrophysical Journal, 731, 113

Moster B. P., Naab T., White S. D. M., 2013, MNRAS, 428, 3121

Moster B. P., Naab T., White S. D. M., 2018, MNRAS, 477, 1822

Muñoz-Cuartas J. C., Macciò A. V., Gottlöber S., Dutton A. A., 2011, MNRAS, 411, 584

Munari E., Biviano A., Borgani S., Murante G., Fabjan D., 2013, MNRAS, 430, 2638

Muñoz-Cuartas J., Maccio A., Gottlober S., Dutton A., 2010, Spin and Shape,[1007.0438] Preprint

Muzzin A., et al., 2012, ApJ, 746, 188

Muzzin A., et al., 2013a, The Astrophysical Journal Supplement Series, 206, 8

Muzzin A., et al., 2013b, The Astrophysical Journal, 777, 18

Muzzin A., et al., 2014, ApJ, 796, 65

Naab T., Ostriker J. P., 2017, ARA&A, 55, 59

Naiman J. P., et al., 2018, MNRAS, 477, 1206

Nantais J. B., et al., 2016, Astronomy & Astrophysics, 592, A161

Nantais J. B., et al., 2017, MNRAS, 465, L104

Navarro J. F., Frenk C. S., White S. D. M., 1996, ApJ, 462, 563

Navarro J. F., Frenk C. S., White S. D. M., 1997, ApJ, 490, 493

Neistein E., Dekel A., 2008, MNRAS, 388, 1792

Nelan J. E., Smith R. J., Hudson M. J., Wegner G. A., Lucey J. R., Moore S. A. W., Quinney S. J., Suntzeff N. B., 2005, ApJ, 632, 137

Nelson D., et al., 2018, MNRAS, 475, 624

Nelson D., et al., 2019, Computational Astrophysics and Cosmology, 6, 2

Nevin R., Blecha L., Comerford J., Simon J., Terrazas B. A., Barrows R. S., Vázquez-Mata J. A., 2023, arXiv e-prints, p. arXiv:2303.06249

Nikolic B., Cullen H., Alexander P., 2004, MNRAS, 355, 874

Noble A. G., Webb T. M. A., Yee H. K. C., Muzzin A., Wilson G., van der Burg R. F. J., Balogh M. L., Shupe D. L., 2016, ApJ, 816, 48

Noguchi M., 1987, MNRAS, 228, 635

Noguchi M., 1988, A&A, 203, 259

Obreschkow D., Rawlings S., 2009, MNRAS, 394, 1857

Oesch P. A., et al., 2016, ApJ, 819, 129

Old L. J., et al., 2020, MNRAS, 493, 5987

Oman K. A., Hudson M. J., 2016, MNRAS, 463, 3083

Oman K. A., Hudson M. J., Behroozi P. S., 2013, MNRAS, 431, 2307

Oman K. A., Bahé Y. M., Healy J., Hess K. M., Hudson M. J., Verheijen M. A. W., 2021, MNRAS, 501, 5073

Omand C. M. B., Balogh M. L., Poggianti B. M., 2014, MNRAS, 440, 843

Ono Y., et al., 2010, MNRAS, 402, 1580

Otter J. A., et al., 2022, ApJ, 941, 93

Owers M. S., et al., 2019, ApJ, 873, 52

Paccagnella A., et al., 2016, ApJ, 816, L25

Pallero D., Gómez F. A., Padilla N. D., Torres-Flores S., Demarco R., Cerulo P., Olave-Rojas D., 2019, MNRAS, 488, 847

Pan H.-A., et al., 2018, ApJ, 868, 132

Pan H.-A., et al., 2019, ApJ, 881, 119

Panter B., Heavens A. F., Jimenez R., 2003, MNRAS, 343, 1145

Papovich C., et al., 2018, ApJ, 854, 30

Pasquali A., Gallazzi A., Fontanot F., van den Bosch F. C., De Lucia G., Mo H. J., Yang X., 2010, MNRAS, 407, 937

Pasquali A., Smith R., Gallazzi A., De Lucia G., Zibetti S., Hirschmann M., Yi S. K., 2019, MNRAS, 484, 1702

Patton D. R., Ellison S. L., Simard L., McConnachie A. W., Mendel J. T., 2011, MNRAS, 412, 591

Patton D. R., Torrey P., Ellison S. L., Mendel J. T., Scudder J. M., 2013, MNRAS, 433, L59

Patton D. R., Qamar F. D., Ellison S. L., Bluck A. F. L., Simard L., Mendel J. T., Moreno J., Torrey P., 2016, MNRAS, 461, 2589

Pawlik M. M., Wild V., Walcher C. J., Johansson P. H., Villforth C., Rowlands K., Mendez-Abreu J., Hewlett T., 2016, MNRAS, 456, 3032

Pawlik M. M., et al., 2018, MNRAS, 477, 1708

Pearson W. J., et al., 2019, A&A, 631, A51

Peng Y.-j., et al., 2010, ApJ, 721, 193

Peng Y.-j., Lilly S. J., Renzini A., Carollo M., 2012, ApJ, 757, 4

Peng Y., Maiolino R., Cochrane R., 2015, Nature, 521, 192

Pentericci L., McLure R. J., Franzetti P., Garilli B., the VANDELS team 2018, arXiv e-prints, p. arXiv:1811.05298

Pérez F., Granger B. E., 2007, Computing in Science and Engineering, 9, 21

Perez J., Tissera P., Padilla N., Alonso M. S., Lambas D. G., 2009, MNRAS, 399, 1157

Perez J., Michel-Dansac L., Tissera P. B., 2011, MNRAS, 417, 580

Petric A. O., et al., 2011, ApJ, 730, 28

Pillepich A., et al., 2018, MNRAS, 473, 4077

Pintos-Castro I., Yee H. K. C., Muzzin A., Old L., Wilson G., 2019, ApJ, 876, 40

Planck Collaboration et al., 2016a, A&A, 594, A13

Planck Collaboration et al., 2016b, A&A, 594, A24

Planck Collaboration et al., 2020, A&A, 641, A6

Poggianti B. M., Smail I., Dressler A., Couch W. J., Barger A. J., Butcher H., Ellis R. S., Oemler Augustus J., 1999, ApJ, 518, 576

Poggianti B. M., et al., 2006, ApJ, 642, 188

Poggianti B. M., et al., 2016, AJ, 151, 78

Pop A.-R., Pillepich A., Amorisco N. C., Hernquist L., 2018, MNRAS, 480, 1715

Popping G., Behroozi P. S., Peeples M. S., 2015a, MNRAS, 449, 477

Popping G., Caputi K. I., Somerville R. S., Trager S. C., 2015b, MNRAS, 452, 169

Pracy M. B., Kuntschner H., Couch W. J., Blake C., Bekki K., Briggs F., 2009, MNRAS, 396, 1349

Pracy M. B., Owers M. S., Couch W. J., Kuntschner H., Bekki K., Briggs F., Lah P., Zwaan M., 2012, MNRAS, 420, 2232

Pracy M. B., et al., 2013, MNRAS, 432, 3131

Presotto V., et al., 2012, A&A, 539, A55

Price-Whelan A., et al., 2018, The Astronomical Journal, 156, 123

Prieto J. L., et al., 2016, ApJ, 830, L32

Puchwein E., Sijacki D., Springel V., 2008, ApJ, 687, L53

Qu Y., et al., 2017, MNRAS, 464, 1659

Quadri R. F., Williams R. J., Franx M., Hildebrandt H., 2012, ApJ, 744, 88

Quilis V., Planelles S., Ricciardelli E., 2017, MNRAS, 469, 80

Quintero A. D., et al., 2004, ApJ, 602, 190

Reddick R. M., Wechsler R. H., Tinker J. L., Behroozi P. S., 2013, ApJ, 771, 30

Reeves A. M. M., et al., 2021, MNRAS, 506, 3364

Reeves A. M. M., Hudson M. J., Oman K. A., 2023, MNRAS,

Renaud F., Bournaud F., Kraljic K., Duc P. A., 2014, MNRAS, 442, L33

Renzini A., 2016, MNRAS, 460, L45

Rhee J., Smith R., Choi H., Contini E., Jung S. L., Han S., Yi S. K., 2020, ApJS, 247, 45

Rich J. A., Torrey P., Kewley L. J., Dopita M. A., Rupke D. S. N., 2012, ApJ, 753, 5

Rich J. A., Kewley L. J., Dopita M. A., 2014, ApJ, 781, L12

Rich J. A., Kewley L. J., Dopita M. A., 2015, ApJS, 221, 28

Roberts I. D., Parker L. C., 2020, MNRAS, 495, 554

Roberts I. D., Parker L. C., Brown T., Joshi G. D., Hlavacek-Larrondo J., Wadsley J., 2019, ApJ, 873, 42

Roberts I. D., et al., 2021, A&A, 650, A111

Roberts I. D., et al., 2022, MNRAS, 509, 1342

Robitaille T. P., et al., 2013, Astronomy & Astrophysics, 558, A33

Rodriguez-Gomez V., et al., 2015a, MNRAS, 449, 49

Rodriguez-Gomez V., et al., 2015b, MNRAS, 449, 49

Rodríguez-Puebla A., Behroozi P., Primack J., Klypin A., Lee C., Hellinger D., 2016, MNRAS, 462, 893

Rodríguez-Puebla A., Primack J. R., Avila-Reese V., Faber S. M., 2017, MNRAS, 470, 651

Rodríguez Zaurín J., Tadhunter C. N., González Delgado R. M., 2010, MNRAS, 403, 1317

Rohr E., Pillepich A., Nelson D., Zinger E., Joshi G. D., Ayromlou M., 2023, MNRAS, 524, 3502

Rothberg B., Joseph R. D., 2004, AJ, 128, 2098

Rowlands K., Wild V., Nesvadba N., Sibthorpe B., Mortier A., Lehnert M., da Cunha E., 2015, MNRAS, 448, 258

Ruiz-Macias O., et al., 2021, MNRAS, 502, 4328

Saintonge A., Catinella B., 2022, ARA&A, 60, 319

Saintonge A., et al., 2013, ApJ, 778, 2

Saintonge A., et al., 2017, ApJS, 233, 22

Salim S., et al., 2007, ApJS, 173, 267

Sánchez Almeida J., Elmegreen B. G., Muñoz-Tuñón C., Elmegreen D. M., 2014, A&ARv, 22, 71

Sánchez-Blázquez P., et al., 2006, MNRAS, 371, 703

Sanders D. B., Mirabel I. F., 1996, ARA&A, 34, 749

Sanders D. B., Soifer B. T., Elias J. H., Madore B. F., Matthews K., Neugebauer G., Scoville N. Z., 1988, ApJ, 325, 74

Sanders D. B., Scoville N. Z., Zensus A., Soifer B. T., Wilson T. L., Zylka R., Steppe H., 1989, A&A, 213, L5

Saro A., Mohr J. J., Bazin G., Dolag K., 2013, ApJ, 772, 47

Sazonova E., et al., 2021, ApJ, 919, 134

Schaye J., et al., 2010, MNRAS, 402, 1536

Schechter P., 1976, The Astrophysical Journal, 203, 297

Schreiber C., et al., 2015, A&A, 575, A74

Scudder J. M., Ellison S. L., Torrey P., Patton D. R., Mendel J. T., 2012, MNRAS, 426, 549

Scudder J. M., Ellison S. L., Momjian E., Rosenberg J. L., Torrey P., Patton D. R., Fertig D., Mendel J. T., 2015, MNRAS, 449, 3719

Sell P. H., et al., 2014, MNRAS, 441, 3417

Serra P., et al., 2012, MNRAS, 422, 1835

Shangguan J., Ho L. C., Li R., Zhuang M.-Y., Xie Y., Li Z., 2019, ApJ, 870, 104

Shioya Y., Bekki K., Couch W. J., De Propris R., 2002, ApJ, 565, 223

Shuntov M., et al., 2022, A&A, 664, A61

Silva A., Marchesini D., Silverman J. D., Martis N., Iono D., Espada D., Skelton R., 2021, ApJ, 909, 124

Simet M., McClintock T., Mandelbaum R., Rozo E., Rykoff E., Sheldon E., Wechsler R. H., 2017, MNRAS, 466, 3103

Simha V., Weinberg D. H., Conroy C., Dave R., Fardal M., Katz N., Oppenheimer B. D., 2014, arXiv e-prints, p. arXiv:1404.0402

Skelton R. E., et al., 2014, ApJS, 214, 24

Smercina A., et al., 2018, ApJ, 855, 51

Smith G. P., Treu T., Ellis R. S., Moran S. M., Dressler A., 2005, ApJ, 620, 78

Smith R. J., Hudson M. J., Lucey J. R., Nelan J. E., Wegner G. A., 2006, MNRAS, 369, 1419

Smith R. J., Lucey J. R., Hudson M. J., 2009, MNRAS, 400, 1690

Smith R. J., et al., 2010, MNRAS, 408, 1417

Smith R. J., Lucey J. R., Price J., Hudson M. J., Phillipps S., 2012, MNRAS, 419, 3167

Smith G. P., et al., 2016, MNRAS, 456, L74

Snyder G. F., Cox T. J., Hayward C. C., Hernquist L., Jonsson P., 2011, ApJ, 741, 77

Sobral D., Best P. N., Smail I., Geach J. E., Cirasuolo M., Garn T., Dalton G. B., 2011, MNRAS, 411, 675

Somerville R. S., Davé R., 2015, ARA&A, 53, 51

Sparre M., Hayward C. C., Feldmann R., Faucher-Giguère C.-A., Muratov A. L., Kereš D., Hopkins P. F., 2017, MNRAS, 466, 88

Speagle J. S., Steinhardt C. L., Capak P. L., Silverman J. D., 2014, ApJS, 214, 15

Springel V., 2005, MNRAS, 364, 1105

Springel V., Hernquist L., 2003, MNRAS, 339, 289

Springel V., Frenk C. S., White S. D. M., 2006, Nature, 440, 1137

Springel V., et al., 2018, MNRAS, 475, 676

Srisawat C., et al., 2013, MNRAS, 436, 150

Stierwalt S., et al., 2013, ApJS, 206, 1

Stott J. P., Smail I., Edge A. C., Ebeling H., Smith G. P., Kneib J. P., Pimbblet K. A., 2007, ApJ, 661, 95

Strateva I., et al., 2001, AJ, 122, 1861

Strauss M. A., et al., 2002, AJ, 124, 1810

Strazzullo V., et al., 2019, A&A, 622, A117

Tacchella S., Dekel A., Carollo C. M., Ceverino D., DeGraf C., Lapiner S., Mandelker N., Primack Joel R., 2016, MNRAS, 457, 2790

Tacconi L. J., et al., 2013, ApJ, 768, 74

Tamura N., et al., 2016, in Evans C. J., Simard L., Takami H., eds, Society of Photo-Optical Instrumentation Engineers (SPIE) Conference Series Vol. 9908, Ground-based and Airborne Instrumentation for Astronomy VI. p. 99081M (arXiv:1608.01075), doi:10.1117/12.2232103

Taranu D. S., Hudson M. J., Balogh M. L., Smith R. J., Power C., Oman K. A., Krane B., 2014, MNRAS, 440, 1934

Taylor E. N., et al., 2015, MNRAS, 446, 2144

Tempel E., et al., 2014, A&A, 566, A1

Teyssier R., Chapon D., Bournaud F., 2010, ApJ, 720, L149

The MSE Science Team et al., 2019, arXiv e-prints, p. arXiv:1904.04907

Thomas D., Maraston C., Bender R., Mendes de Oliveira C., 2005, ApJ, 621, 673

Thorp M. D., Ellison S. L., Simard L., Sánchez S. F., Antonio B., 2019, MNRAS, 482, L55

Tinker J. L., Wetzel A. R., 2010, ApJ, 719, 88

Tinker J. L., Leauthaud A., Bundy K., George M. R., Behroozi P., Massey R., Rhodes J., Wechsler R. H., 2013, ApJ, 778, 93

Tomczak A. R., et al., 2014, ApJ, 783, 85

Tomczak A. R., et al., 2016, ApJ, 817, 118

Toomre A., Toomre J., 1972, ApJ, 178, 623

Trager S. C., Faber S. M., Worthey G., González J. J., 2000, AJ, 119, 1645

Trudeau A., et al., 2020, Astronomy & Astrophysics, 642, A124

Ueda J., et al., 2021, ApJS, 257, 57

Upadhyay A. K., Oman K. A., Trager S. C., 2021, A&A, 652, A16

van den Bosch F. C., 2002, MNRAS, 331, 98

van den Bosch F. C., Aquino D., Yang X., Mo H. J., Pasquali A., McIntosh D. H., Weinmann S. M., Kang X., 2008, MNRAS, 387, 79

van der Burg R. F. J., et al., 2013, A&A, 557, A15

van der Burg R. F. J., McGee S., Aussel H., Dahle H., Arnaud M., Pratt G. W., Muzzin A., 2018, A&A, 618, A140

van der Burg R. F. J., et al., 2020, A&A, 638, A112

van de Voort F., et al., 2018, MNRAS, 476, 122

Valentino F., et al., 2020, ApJ, 889, 93

Valentino F., et al., 2023, ApJ, 947, 20

Van Rossum G., Drake Jr F. L., 1995, Python tutorial. Centrum voor Wiskunde en Informatica Amsterdam, The Netherlands

Veilleux S., et al., 2013, ApJ, 776, 27

Vikhlinin A., Kravtsov A., Forman W., Jones C., Markevitch M., Murray S. S., Van Speybroeck L., 2006, ApJ, 640, 691

Violino G., Ellison S. L., Sargent M., Coppin K. E. K., Scudder J. M., Mendel T. J., Saintonge A., 2018, MNRAS, 476, 2591

Virtanen P., et al., 2020, Nature Methods, 17, 261

Voit G. M., Bryan G. L., 2001, Nature, 414, 425

Von Der Linden A., Best P. N., Kauffmann G., White S. D. M., 2007, MNRAS, 379, 867

Vulcani B., et al., 2011, MNRAS, 412, 246

Vulcani B., et al., 2013, A&A, 550, A58

Vulcani B., et al., 2018, ApJ, 866, L25

Wang J., Bose S., Frenk C. S., Gao L., Jenkins A., Springel V., White S. D. M., 2020, Nature, 585, 39

Wang D., et al., 2022, MNRAS, 516, 3411

Wang J., et al., 2023, ApJ, 944, 102

Webb K., et al., 2020, MNRAS, 498, 5317

Wechsler R. H., Tinker J. L., 2018, ARA&A, 56, 435

Wechsler R. H., Bullock J. S., Primack J. R., Kravtsov A. V., Dekel A., 2002, ApJ, 568, 52

Weigel A. K., et al., 2017, ApJ, 845, 145

Weinmann S. M., van den Bosch F. C., Yang X., Mo H. J., 2006, MNRAS, 366, 2

Weinmann S. M., Kauffmann G., von der Linden A., De Lucia G., 2010, MNRAS, 406, 2249

Werner N., McNamara B. R., Churazov E., Scannapieco E., 2019, Space Sci. Rev., 215, 5

Werner S. V., Hatch N. A., Muzzin A., van der Burg R. F. J., Balogh M. L., Rudnick G., Wilson G., 2022, MNRAS, 510, 674

Wes McKinney 2010, in Stéfan van der Walt Jarrod Millman eds, Proceedings of the 9th Python in Science Conference. pp 56 – 61, doi:10.25080/Majora-92bf1922-00a

Weston M. E., McIntosh D. H., Brodwin M., Mann J., Cooper A., McConnell A., Nielsen J. L., 2017, MNRAS, 464, 3882

Wetzel A. R., 2011, MNRAS, 412, 49

Wetzel A. R., Tinker J. L., Conroy C., 2012, MNRAS, 424, 232

Wetzel A. R., Tinker J. L., Conroy C., van den Bosch F. C., 2013, MNRAS, 432, 336

Wetzel A. R., Tollerud E. J., Weisz D. R., 2015, ApJ, 808, L27

Wheeler C., Phillips J. I., Cooper M. C., Boylan-Kolchin M., Bullock J. S., 2014, MNRAS, 442, 1396

Whitaker K. E., et al., 2011, ApJ, 735, 86

Whitaker K. E., Kriek M., van Dokkum P. G., Bezanson R., Brammer G., Franx M., Labbé I., 2012, ApJ, 745, 179

Whitaker K. E., et al., 2014, ApJ, 795, 104

White S. D. M., Frenk C. S., 1991, ApJ, 379, 52

White S. D. M., Rees M. J., 1978, MNRAS, 183, 341

Wild V., Heckman T., Charlot S., 2010, MNRAS, 405, 933

Wild V., Almaini O., Dunlop J., Simpson C., Rowlands K., Bowler R., Maltby D., McLure R., 2016, MNRAS, 463, 832

Wild V., et al., 2020, MNRAS, 494, 529

Wilkinson D. M., Maraston C., Goddard D., Thomas D., Parikh T., 2017, MNRAS, 472, 4297

Wilkinson S., Ellison S. L., Bottrell C., Bickley R. W., Gwyn S., Cuillandre J.-C., Wild V., 2022, MNRAS, 516, 4354

Williams R. J., Quadri R. F., Franx M., van Dokkum P., Labbé I., 2009, ApJ, 691, 1879

Wilman D. J., et al., 2005, MNRAS, 358, 88

Woo J., et al., 2013, MNRAS, 428, 3306

Wright R. J., Lagos C. d. P., Davies L. J. M., Power C., Trayford J. W., Wong O. I., 2019, MNRAS, 487, 3740

Wright R. J., Lagos C. d. P., Power C., Stevens A. R. H., Cortese L., Poulton R. J. J., 2022, MNRAS, 516, 2891

Xu C. K., Zhao Y., Scoville N., Capak P., Drory N., Gao Y., 2012, ApJ, 747, 85

Yang Y., Zabludoff A. I., Zaritsky D., Mihos J. C., 2008, ApJ, 688, 945

Yang X., Mo H. J., van den Bosch F. C., Zhang Y., Han J., 2012, ApJ, 752, 41

Yoon Y., Lim G., 2020, ApJ, 905, 154

Yoon Y., Ko J., Kim J.-W., 2023, ApJ, 946, 41

Yu Q., Fang T., Feng S., Zhang B., Xu C. K., Wang Y., Hao L., 2022, ApJ, 934, 114

Zabludoff A. I., Mulchaey J. S., 1998, ApJ, 498, L5

Zhang C., et al., 2019, ApJ, 884, L52

Zinger E., Dekel A., Kravtsov A. V., Nagai D., 2018, MNRAS, 475, 3654

Zolotov A., et al., 2015, MNRAS, 450, 2327

APPENDICES

Appendix A

Appendices for Chapter 2 - GOGREEN Galaxy Groups

A.1 Acknowledgements

We thank the native Hawaiians for the use of Mauna Kea, as observations from Gemini, CFHT, and Subaru were all used as part of our survey.

Data products were used from observations made with ESO Telescopes at the La Silla Paranal Observatory under ESO programme ID 179.A-2005 and on data products produced by TERAPIX and the Cambridge Astronomy Survey Unit on behalf of the UltraVISTA consortium. As well, this study makes use of observations taken by the 3D-HST Treasury Program (GO 12177 and 12328) with the NASA/ESA HST, which is operated by the Association of Universities for Research in Astronomy, Inc., under NASA contract NAS5-26555. MB gratefully acknowledges support from the NSERC Discovery Grant program. BV acknowledges financial contribution from the grant PRIN MIUR 2017 n.20173ML3WW_001 (PI Cimatti) and from the INAF main-stream funding programme (PI Vulcani). GW acknowledges support from the National Science Foundation through grant AST-1517863, HST program number GO-15294, and grant number 80NSSC17K0019 issued through the NASA Astrophysics Data Analysis Program (ADAP). Support for program number GO-15294 was provided by NASA through a grant from the Space Telescope Science Institute, which is operated by the Association of Universities for Research in Astronomy, Incorporated, under NASA contract NAS5-26555. GR thanks the International Space Science Institute (ISSI) for providing financial support and a meeting facility that inspired insightful discussions for team "COSWEB: The Cosmic Web and Galaxy Evolution". GR acknowl-

edges support from the National Science Foundation grants AST-1517815, AST-1716690, and AST-1814159, NASA HST grant AR-14310, and NASA ADAP grant 80NSSC19K0592. GR also acknowledges the support of an ESO visiting science fellowship. This work was supported in part by NSF grants AST-1815475 and AST-1518257.

We thank M. Salvato for allowing us to use the master spectroscopic catalog used within the COSMOS collaboration.

This work made use of data products derived from Prospector (Leja et al., 2017a; Johnson et al., 2019b), python-fsps and FSPS (Conroy & Gunn, 2010a; Conroy et al., 2009b). We also used the following Python (Van Rossum & Drake Jr, 1995) software packages: Astropy (Robitaille et al., 2013; Price-Whelan et al., 2018), matplotlib (Hunter, 2007), scipy (Virtanen et al., 2020), ipython (Pérez & Granger, 2007), numpy (Harris et al., 2020), pandas (Wes McKinney, 2010), and emcee (Foreman-Mackey et al., 2013).

A.2 Data availability

Group catalogues are publicly available for both the COSMOS and SXDF group samples in the 'supplementary data' section at https://academic.oup.com/mnras/article/483/3/3545/5211093 and in Finoguenov et al. (2010), respectively.

The photometric datasets used for the $1 < z < 1.5$ groups analysis in this work are from sources in the public domain; UltraVISTA DR1 and DR3 at `http://ultravista.org/`, and SPLASH SXDF at `https://homepages.spa.umn.edu/~mehta074/splash/`.

Spectroscopic release information and datasets are also available in the public domain, 3D-HST at `https://archive.stsci.edu/prepds/3d-hst/`, UDSz at `https://www.nottingham.ac.uk/astronomy/UDS/UDSz/`, XMM-LSS survey at `https://heasarc.gsfc.nasa.gov/W3Browse/all/xmmlssclas.html`, VANDELS at `https://www.eso.org/sci/publications/announcements/sciann17248.html`. The compilation of published redshifts in the COSMOS field was obtained from a catalogue curated by M. Salvato; further information about a future public release of this catalogue can be found at `https://cosmos.astro.caltech.edu/page/specz`.

Access to the GOGREEN and GCLASS data release of spectroscopy, photometry, and derived data products, including jupyter python3 notebooks for reading and using the data, is available at the CADC (`https://www.cadc-ccda.hia-iha.nrc-cnrc.gc.ca/en/community/gogreen`), and NSF's NOIR-Lab (`https://datalab.noao.edu/gogreendr1/`). Future releases, science results and other updates will be announced via the GOGREEN

website at http://gogreensurvey.ca/. The full posteriors of Webb et al. (2020)'s PROSPECTOR fits are available from the Canadian Advanced Network for Astronomical Research (CANFAR), at www.canfar.net/storage/list/AstroDataCitationDOI/CISTI.CANFAR/20.0009/data; DOI:10.11570/20.0009.

A.3 Photometric redshift calibration and selection

A.3.1 De-biasing photometric redshifts using available spectroscopic redshifts

In Figure A.1 we show the correlation between $\Delta z/(1+z_{\rm spec})$ and $1+z_{\rm spec}$, for all galaxies in COSMOS and SXDF with available spectroscopic redshifts, where $\Delta z = z_{\rm phot} - z_{\rm spec}$. These include deep spectroscopy focused on the $1 < z < 1.5$ regime by GOGREEN (Balogh et al., 2021). For UltraVISTA DR3 (not shown), there is no significant bias, up to $z \sim 2$. Both UltraVISTA DR1 and SXDF show a small bias, such that the photometric redshift is lower than the spectroscopic redshift for $1 < z < 2$. This difference increases modestly with redshift.

To correct for this we fit a quadratic function to this correlation. We find a fit of $z_{\rm phot} = -0.085z_{\rm spec}^2 + 1.121z_{\rm spec} - 0.044$ for UltraVISTA DR1 and $z_{\rm phot} = 0.087z_{\rm spec}^2 + 0.737z_{\rm spec} + 0.150$ for SPLASH-SXDF. We remove the bias by subtracting off the difference of this relation from a linear one-to-one relation between spectroscopic and photometric redshifts. Galaxies with photometric redshifts outside 2–4 σ (depending on dataset) are considered outliers, and iteratively removed from the fit. The lower and upper 68% photometric redshift uncertainties are also corrected to reflect this shift in photometric redshift. We note that this does not entirely eliminate the bias from SPLASH-SXDF, as photometric redshifts at $z \sim 1.3$ are still too small, on average, by ~ 0.04 after the correction.

For each galaxy, we also apply a small redshift-dependent stellar mass correction, to account for the corresponding change in luminosity distance. This adjustment is by a factor of $\left[D_L(z_{\rm pert})/D_L(z_{\rm true})\right]^2$. $D_L(z)$ is the luminosity distance at a given redshift and $z_{\rm pert}$ and $z_{\rm true}$ are the redshifts of the galaxy originally and after being perturbed, respectively[1].

[1]To see how this factor comes about, consider that the original "$M_{\rm true}$" of the galaxy in the UltraVISTA dataset was $M_{\rm true} = 4\pi D_L^2(z_{\rm true})F[M/L]$, with F being the observed flux of the galaxy and M/L being the mass/luminosity ratio of the galaxy. The recovered stellar mass of that galaxy after having its photometric redshift perturbed will be $M_{\rm rec} = 4\pi D_L^2(z_{\rm pert})F[M/L]$. Taking the ratio of $M_{\rm rec}/M_{\rm true}$ then gives the desired result.

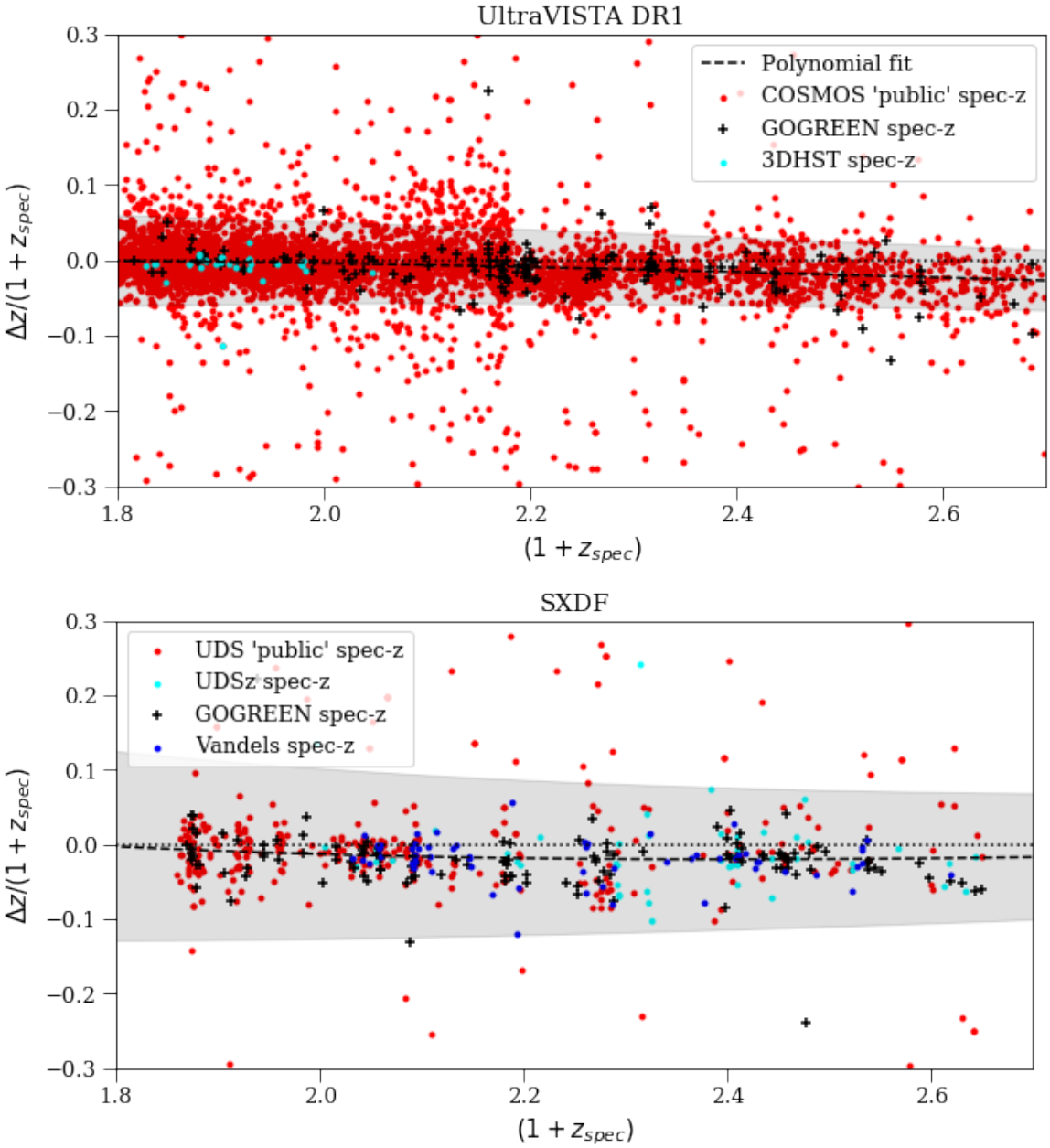

Figure A.1: The difference between catalogued photometric and spectroscopic redshifts for UltraVISTA DR1 (top) and SPLASH-SXDF (bottom) is shown as a function of spectroscopic redshifts. The final quadratic fit (solid blue curve) is based on the points within the shaded region, which we determine by an iterative sigma-clipping procedure.

A.3.2 Photometric redshift selection

As described in §2.3.1, group members are first selected to lie within a photometric redshift range of width $\Delta z = 0.126$, prior to applying a statistical background subtraction. Plots of available spectroscopic redshifts matched to photometric redshifts (for UltraVISTA DR1 and SPLASH-SXDF) are shown in Figure A.2, following van der Burg et al. (2013). This Figure demonstrates how the size of this cut compares with the photometric redshift scatter, for galaxies with available spectroscopic redshifts.

The choice of $\Delta z = 0.126$ is made as it corresponds to $\Delta z = 2\times\text{median}(z_{u68} - z_{\text{peak}})$ for UltraVISTA DR1 and DR3. Here, z_{u68} is the 84th percentile of the photometric redshift probability distribution and z_{peak} is the peak of that distribution (i.e. z_{u68} is the upper 1-sigma confidence interval) . Although SPLASH-SXDF has smaller photometric redshift uncertainties, thanks to greater depth in several bands, there is still a remaining bias at $z \sim 1.2 - 1.3$ that is not fully removed from the debiasing described in Appendix A.3.1. Therefore we conservatively adopt the same $\Delta z = 0.126$ for all systems, to help mitigate this.

A.3.3 Field stellar mass functions

In Figure A.3 we show our field stellar mass functions, which were fit and described in §2.3.1. We plot Schechter fits using the best fit parameters in Table 2.2 and contrast our field fits with those from Muzzin et al. (2013b), which exclusively measured stellar mass functions using the UltraVISTA survey region. We find similar stellar mass functions and our fits are consistent with theirs, within 2σ. The similarity in fit is expected, given that much of our survey area is UltraVISTA. We note that the Schechter fit for the quiescent population doesn't quite fit the very high mass end as well as the Muzzin et al. (2013b) fits. This explains why the quiescent fraction curves, as plotted in Figure 2.5, turn over rather than flattening out for the two highest stellar mass bins. As well for the quiescent population, there is some deviation from the fit in the lowest stellar mass points. These small discrepancies in fit do not significantly affect any of our results, discussion, or conclusion.

A.4 Spectroscopy and GOGREEN spectroscopic groups

Nine of the groups in our $1 < z < 1.5$ redshift range were observed with Gemini-GMOS by the GOGREEN spectroscopic survey (Balogh et al., 2021): four from COSMOS and five

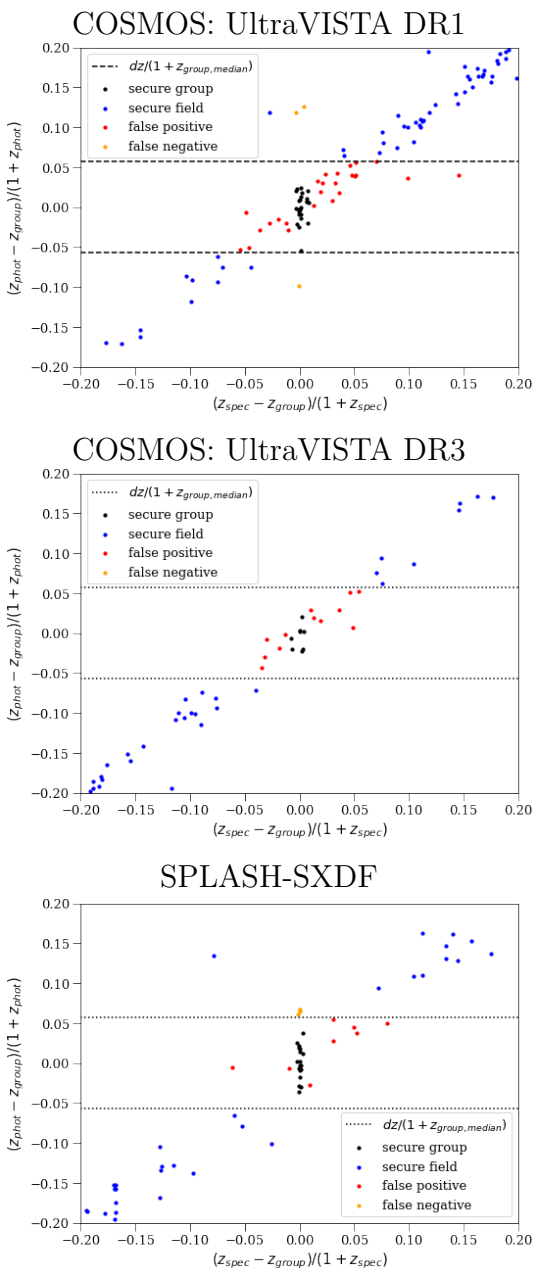

Figure A.2: Verification of the photometric redshift cuts for COSMOS (UltraVISTA DR1 and DR3 UltraDeep) and SXDF using the spectroscopic redshifts. The COSMOS: UltraVISTA DR1 subplot shown here contains all 23 $1 < z < 1.5$ groups, regardless of quality flag, to maximize the spectroscopic and photometric redshift matches. Dashed horizontal lines show the photometric redshift cut that was chosen.

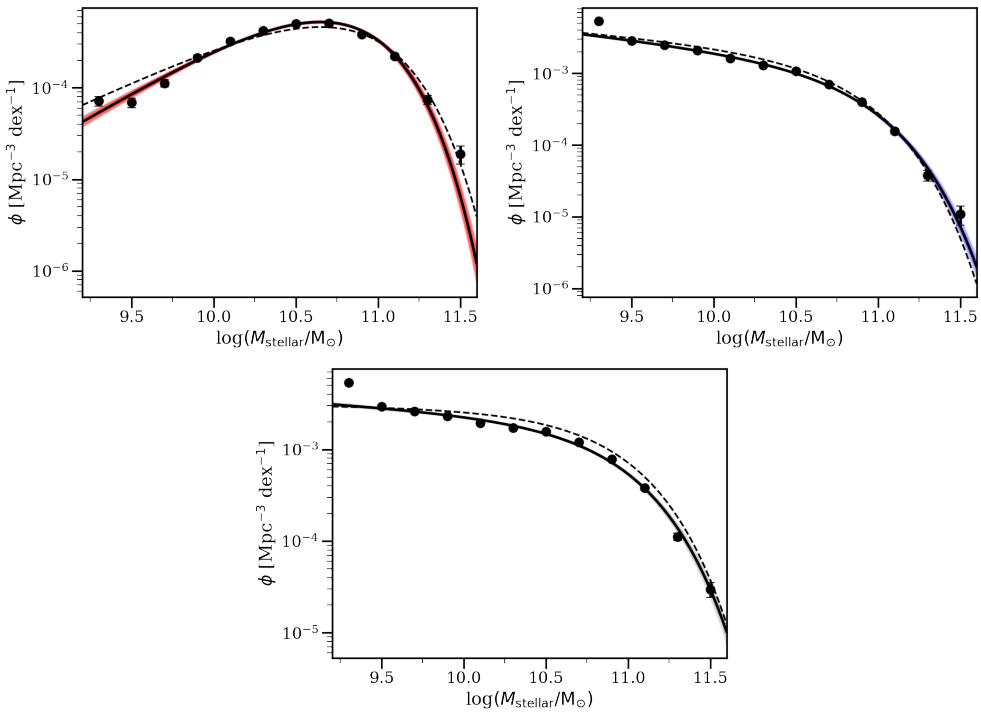

Figure A.3: Stellar mass function of quiescent (top panel), star-forming (middle), and total (bottom) field galaxies at $1 < z < 1.5$. Error bars shown represent the Poisson shot noise. Overlaid on each plot are the Schechter function fits (solid line), normalized to match the number of field galaxies per Mpc^3 per dex (bin size $\Delta \log(M_{\rm stellar}/{\rm M}_\odot) = 0.2$), and with shaded regions indicating the 68% confidence interval on the fit parameters, computed as described in the text. The best fit from Muzzin et al. (2013b) is shown as a dashed line.

from SXDF, as listed in Table 2.1. The names given to the GOGREEN-identified groups are the same as those used in the original COSMOS (Gozaliasl et al., 2019) and SXDF (Finoguenov et al., 2010) group catalogues. For simplicity we will refer to individual groups using a shortened name comprised of the last three digits in the formal name appended to the appropriate catalogue (e.g. COSMOS-28 instead of COSMOS-20028). Here we present additional details of the spectroscopic datasets used (Appendix A.4.1), definition of our field sample at $1 < z < 1.5$ (Appendix A.4.2), as well as analysis of the dynamics (in particular, confirming the group membership and dynamical masses for a subset of our groups in Appendix A.4.3), and description of the spectroscopically-determined mass-weighted ages used for a subset of our group sample (Appendix A.4.4).

A.4.1 Spectroscopy

Our primary source for redshifts is the GOGREEN survey (Balogh et al., 2021). This sample was selected from galaxies with $z' < 24.25$ within a $5.5' \times 5.5'$ area around nine targets in these two fields. A broad colour selection was applied to reduce foreground and background galaxies. The survey provides redshifts for an average $\sim 45\%$ of the parent cluster population within 500 kpc, unbiased with respect to galaxy type for stellar masses $M_{\rm stellar} > 10^{10.2}$ $\mathrm{M}_{\odot}$ (Balogh et al., 2021). We use 173 robust redshifts in the COSMOS field, and 198 in the SXDF field, from GOGREEN. For more details we refer to Balogh et al. (2021).

In addition, for COSMOS we use the master spectroscopic redshift catalogue of publicly available redshifts in use within the COSMOS collaboration, curated by M. Salvato (priv. comm.). We also use available 3D-HST redshifts (Skelton et al., 2014; Brammer et al., 2012), but only for the purpose of checking and debiasing the photometric redshifts in Appendix A.3.1.

For the SXDF field we supplement the GOGREEN redshifts with data from UDSz (Bradshaw et al., 2013; McLure et al., 2013), the XMM-Large Scale Structure (XMM-LSS) survey (Melnyk et al., 2013; Chiappetti et al., 2013) and VANDELS (Pentericci et al., 2018). 3D-HST data are again used only for debiasing the photometric redshifts.

A.4.2 Field sample at redshift 1–1.5

For comparison with our sample of overdense galaxy systems, we define a reference "field" galaxy sample that is representative of the average galaxy population. We simply define our field sample as all galaxies in the UltraVISTA and SPLASH-SXDF catalogues with

photometric redshifts in the range of interest. This includes galaxies that make up our group sample, but as they only make up ~ 1 per cent of the total, this has a negligible effect on our analysis. Calculated field values are an area-weighted average. Such a sample includes overdense regions, and thus provides a lower contrast to our group sample than would a comparison with low-density regions (Peng et al., 2010; Kawinwanichakij et al., 2017; Papovich et al., 2018) or samples of "central" galaxies. It will also be influenced by cosmic variance (Kovač et al., 2010; Moster et al., 2011b), though this is small given the relatively large area of the combined surveys.

A.4.3 Group membership, dynamics and masses

In Figure A.4 we show the spatial and redshift distribution of galaxies with spectroscopic redshifts, in each of the 5′ GMOS fields of view, with respect to the X-ray contours. In addition to GOGREEN, we include spectroscopy from available public sources as described in §A.4.1. We calculate a new weighted centre for each group within 1 Mpc ($\sim 2R_{200c}$) of the catalogued position, and then rerun an iterative 2.5σ-clipping routine to calculate the final redshift and velocity dispersion. This procedure did not converge for two groups. In the case of COSMOS-125, the member candidates are spatially concentrated but redshift distribution does not show a clear peak. For COSMOS-63 it is the opposite, with a strong redshift overdensity but no spatial concentration of sources. Finally, for SXDF-76 we find two distinct groups along the line of sight. We keep both in the catalogue, and we have labelled them SXDF-76a and SXDF-76b.

We estimate dynamical halo masses from these velocity dispersion values using the relation presented in Saro et al. (2013). All galaxies within the 2.5σ velocity cut and within $2R_{200c}$ count as spectroscopic members for the purposes of Table 2.1, where we present all of these values. We also compute an average velocity dispersion by stacking all group galaxies in an ensemble. We find $\sigma_v = 352 \pm 32\,\mathrm{km\,s^{-1}}$, which has been corrected by subtracting in quadrature the estimated individual redshift uncertainty of $280\,\mathrm{km\,s^{-1}}$ observed-frame, from Balogh et al. (2021). This corresponds to a halo mass of $\log(M_{200c}/M_{\mathrm{solar}}) = 13.61\pm^{+0.11}_{-0.12}$, again using the Saro et al. (2013) relation. The distribution of the velocities in this ensemble is shown in A.6.

A.4.4 Mass-weighted ages

Formation times of quiescent galaxies in the GOGREEN spectroscopic sample, from Webb et al. (2020), are shown as a function of stellar mass in Figure A.7. This figure comple-

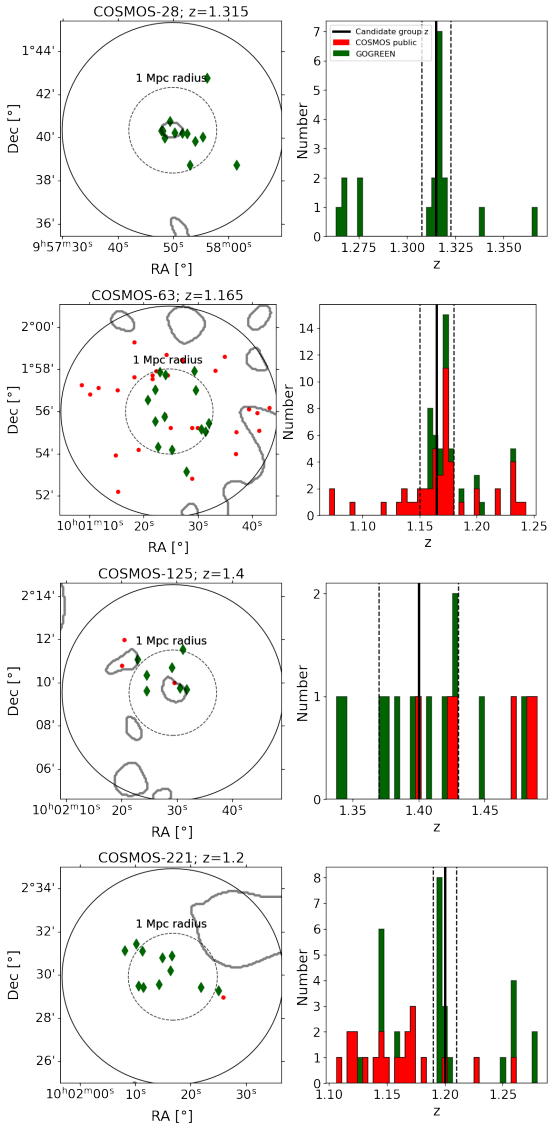

Figure A.4: Groups in the COSMOS field spectroscopically targeted by GOGREEN. Left subplots: spatial distribution of galaxies with a spectroscopic redshift centred on the identified group centre and within the iterative velocity dispersion cut. GOGREEN targets are indicated with green diamonds. The solid grey contours indicate smoothed X-ray emission. Right subplots: distribution of spectroscopic redshifts within the circular field of view (solid line) shown on the left. The dashed vertical lines indicates the redshift selection of galaxies that are displayed on the corresponding left subplot.

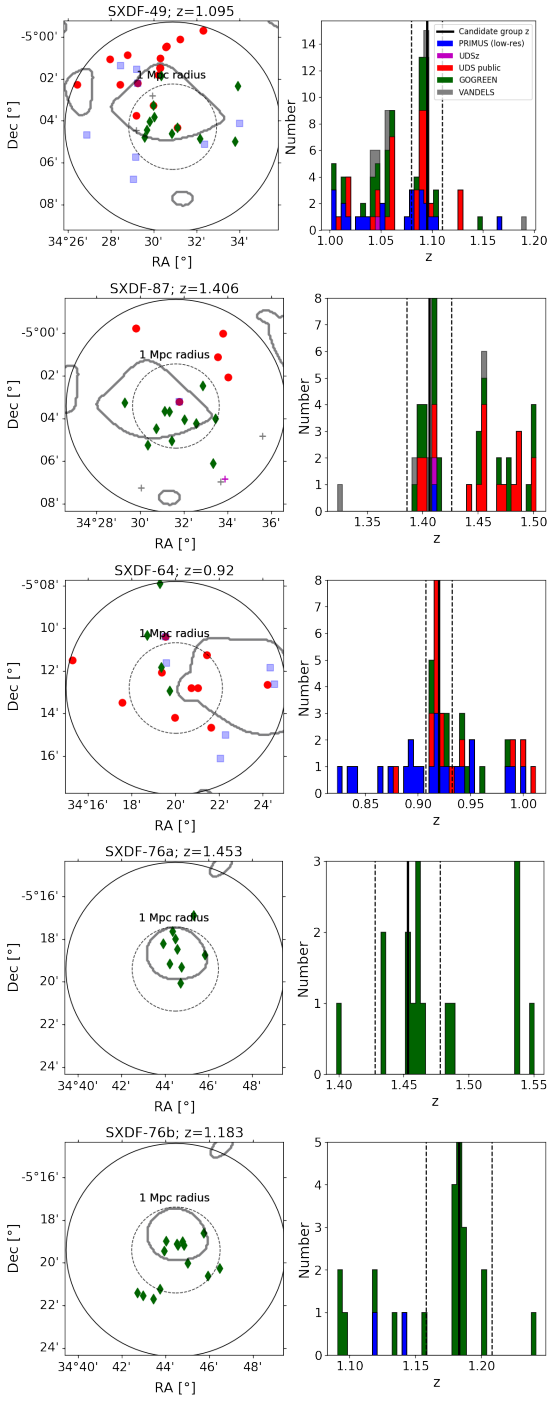

Figure A.5: SXDF GOGREEN spectroscopically targeted groups. Analogous to Figure A.4.

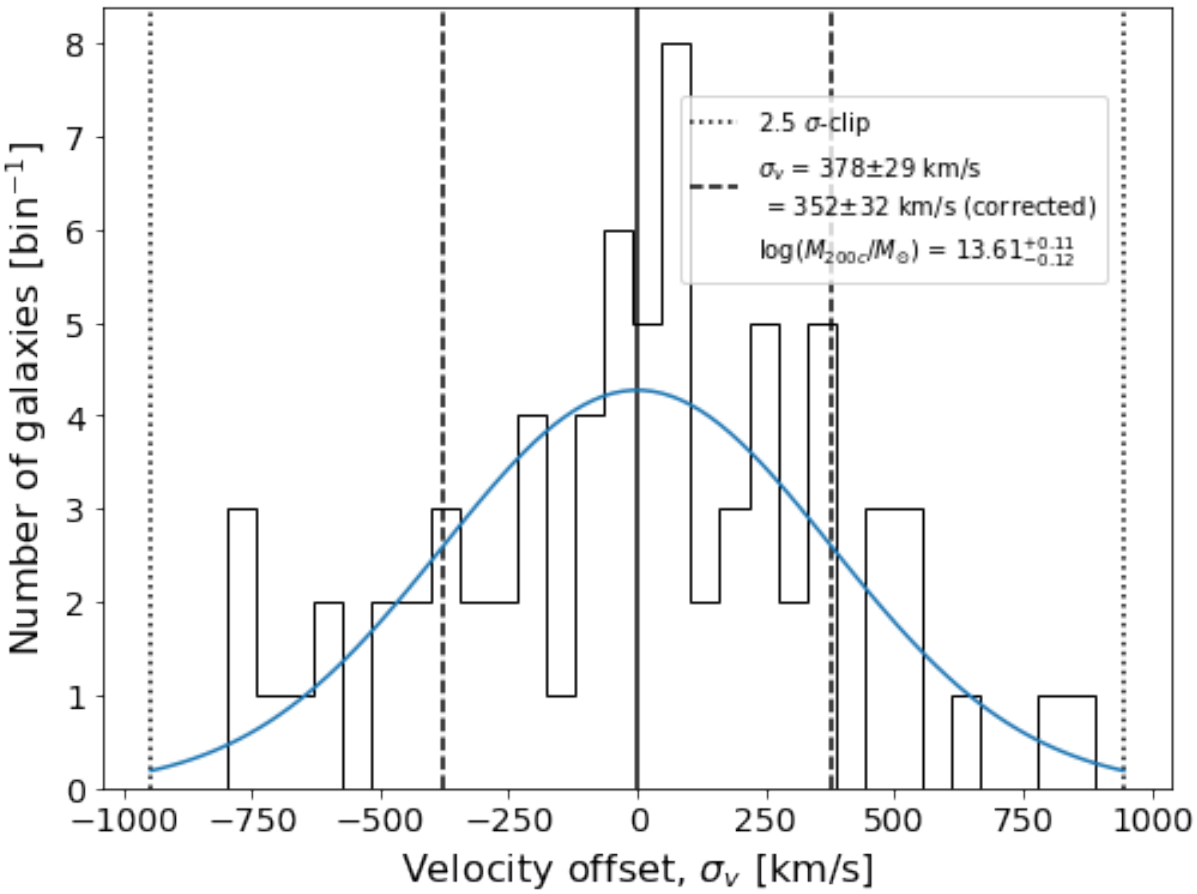

Figure A.6: Distribution of rest-frame galaxy velocities in the ensemble for all 83 spectroscopic group members in 9 GOGREEN groups. Vertical lines indicate the mean of $0\,\mathrm{km\,s^{-1}}$ (solid black), velocity dispersion (vertical dashed), and final 2.5σ cut (black dotted). Thirty evenly sized bins were used, corresponding to a bin width of $\sim 56\,\mathrm{km\,s^{-1}}$. The curved blue line indicates a Gaussian with mean 0 and standard deviation set to the velocity dispersion, normalized so the area corresponds to the total number of spectroscopic members.

ments Figure 2.11, which only shows differences with the field and omits the individual measurements for the sake of clarity. Formation times are computed from the time of observation and the mass-weighted age, as $t_{\rm form} = t_{\rm obs} - {\rm MWA}$. The running mean is additionally shown for the intermediate halo-mass bin used in the QFE vs halo mass analysis. The field, low-mass clusters, and high-mass clusters all show a declining trend of $t_{\rm form}$ with stellar mass. Both cluster sub-samples display ages about 200-300 Myr older than the field, as noted by Webb et al. (2020) for the entire cluster sample. The group sample, on the other hand, appears *younger* than the field by $\sim 150 - 200$ Myr, as noted in §2.4.2.

The small group sample has a high average galaxy stellar mass. To check that our results are not dominated by the most massive group galaxies, which could be central galaxies with a different formation history, we highlight these as green diamonds with black borders on Figure A.7. There is no evidence that the ages of these galaxies are significantly different from other group members.

A.5 Sensitivity of results to stellar mass binning

In §2.3.3 we consider the halo mass dependence of the QFE in two broad stellar mass bins (Figure 2.7), motivated by the qualitative change in QFE shown in Figure 2.6. Here we subdivide the lower mass bin into two, to demonstrate explicitly that the results are similar in both bins. We show both the QFE, and the f_Q values from which it is derived, in this binning in Figure A.8. As claimed, the halo mass dependence observed in the two lowest stellar mass bins is very similar. In particular, the unusually high QFE observed for the Planck clusters at intermediate redshifts persists in both stellar mass bins. As discussed in §2.3.3, we find the data in all three stellar mass bins are consistent with a QFE that depends on $\log(M_{\rm halo}/{\rm M}_\odot)$ with a slope of $m \approx 0.24 \pm 0.04$.

In Figure A.9 we show the BAHAMAS simulation results (originally shown in Figure 2.9) for the same quantities and binning. It is readily apparent here that, at fixed halo mass, the predicted f_Q and QFE in the simulations *decreases* with increasing stellar mass, in contrast with the observations. This behaviour is well-known and discussed further in Kukstas et al. (in preparation). Despite this, the correlation with halo mass is similar in both lower stellar mass bins – it increases up to a halo mass of $\sim 2 \times 10^{14} {\rm M}_\odot$ and becomes much shallower as halo mass increases further. This behaviour is not inconsistent with what we observe, with the possible exception of the intermediate redshift Planck-selected clusters.

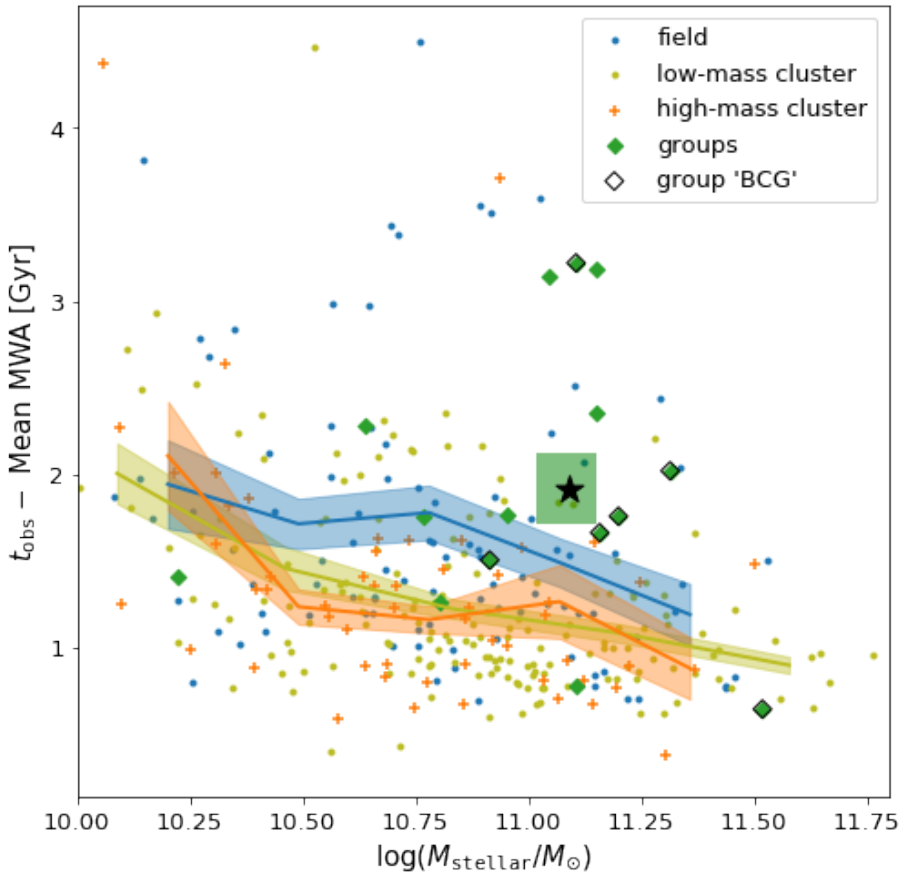

Figure A.7: This figure is a more detailed complement to Figure 2.11 in the main body of the paper. The points show measurements of $t_{obs}-$MWA as a function of stellar mass, from stellar population synthesis modelling of quiescent galaxies in the GOGREEN spectroscopic sample (Webb et al., 2020). Individual $t_{obs}-$MWA and stellar mass values are plotted for the field (blue dots), group (green diamonds), low-mass cluster (yellow dots), and high-mass cluster samples (small orange crosses). Groups, low-mass clusters, and high-mass clusters are the three halo mass bins explored at $1 < z < 1.5$ in §2.3.3. The most massive galaxy in each group ('BCGs') are indicated with a black diamond (two groups had only one quiescent galaxy). As well, a running mean with bootstrapped standard deviation on the mean is shown for the field and cluster samples. For the groups, there are only 15 quiescent spectroscopic members so we simply plot the mean $t_{obs}-$MWA and mean stellar mass of the full sample with a black star and a shaded region reflecting the bootstrapped errors. Quiescent galaxies in groups are not older than those in clusters, ruling out the predictions of our simple model without pre-processing.

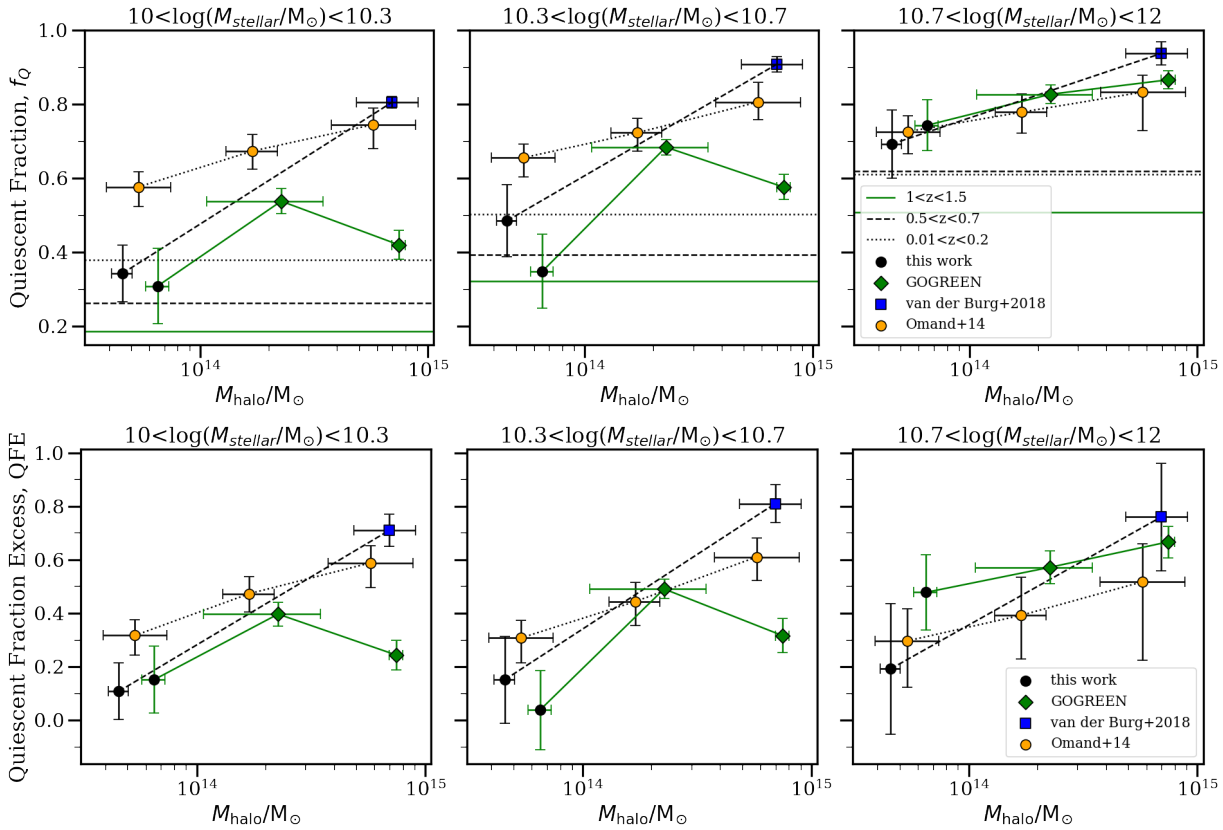

Figure A.8: Quiescent fraction (top row) and quiescent fraction excess (bottom row) are shown as a function of halo mass (M_{200c}), $M_{\rm halo}/{\rm M}_\odot$, for three galaxy stellar mass bins (one stellar mass bin per column), and for samples at three different redshift ranges, as indicated. Our new measurements of low-mass haloes at $1 < z < 1.5$ are shown as the green points connected by a green solid line. The other samples are described in §2.2.2. Horizontal lines represent the field at a given redshift range (errors are not significantly larger than the line widths on this plot). The bottom row is analogous to Figure 2.7, with a further subdivision of that Figure's lowest stellar mass bin.

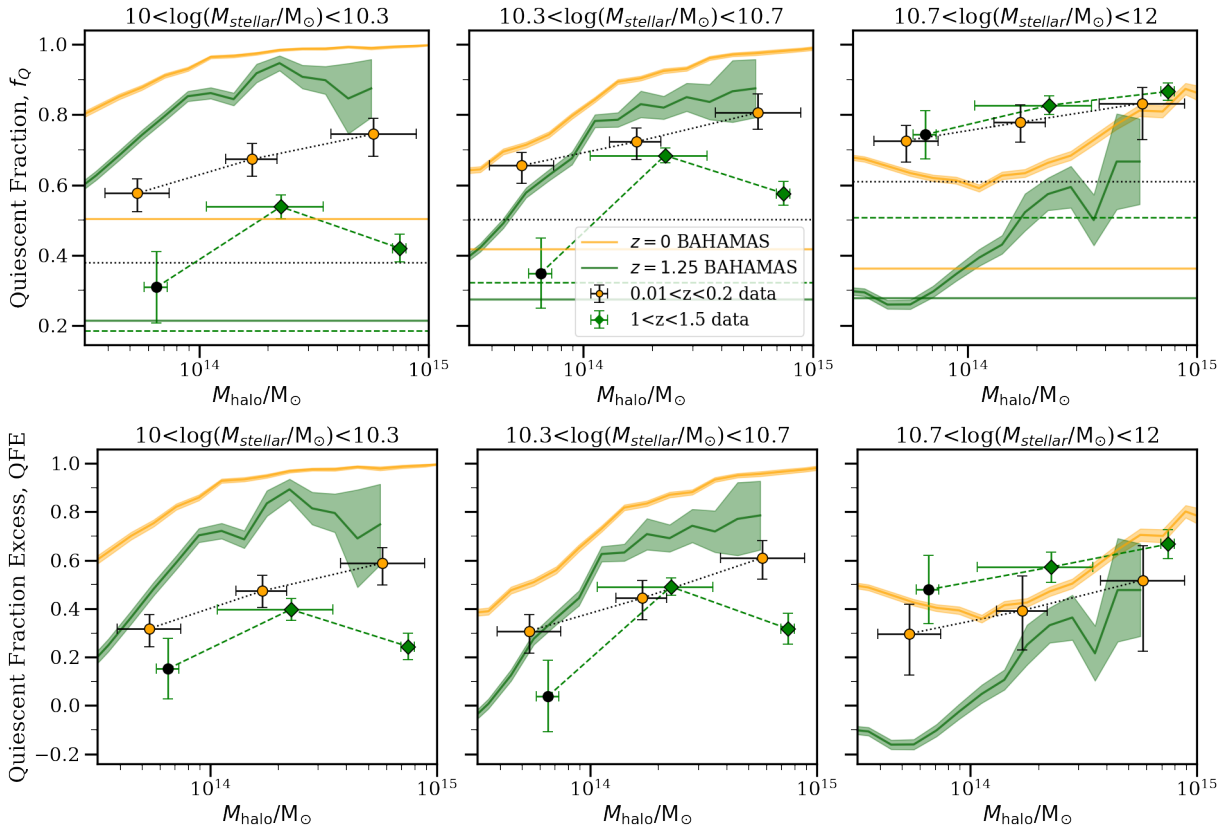

Figure A.9: We show results from the BAHAMAS hydrodynamic simulation, for the quiescent fraction (top) and quiescent fraction excess (bottom) as a function of stellar and halo mass, $M_{\rm halo}/{\rm M}_\odot$ at two redshifts as indicated, with the same stellar mass binning as in Figure A.8. The corresponding data from that Figure are shown, omitting the intermediate redshift sample for clarity. In the simulations, both f_Q and QFE decrease with increasing stellar mass, in contrast with the data. However, the correlation with halo mass and redshift is qualitatively similar to the trends observed in the data. The bottom row is analogous to Figure 2.9 in the main body of the paper, with the lowest stellar mass bin subdivided into two.

Appendix B

Appendices for Chapter 3 - Constraining satellite quenching with stellar ages

B.1 Acknowledgements

We thank the anonymous referee for their helpful comments. Addressing these clarified a number of key points for understanding this work. We thank S. Ellison for assistance with SDSS stellar masses and sSFRs. AMMR acknowledges support from a Queen Elizabeth II Graduate Scholarship in Science and Technology (QEII-GSST) from the province of Ontario. MJH acknowledges support from a NSERC Discovery Grant. KAO acknowledges support by the European Research Council (ERC) through Advanced Investigator grant to C. S. Frenk, DMIDAS (GA 786910), and by STFC through grant ST/T000244/1. This research has made use of NASA's Astrophysics Data System.

This work used the DiRAC@Durham facility managed by the Institute for Computational Cosmology on behalf of the STFC DiRAC HPC Facility (www.dirac.ac.uk). The equipment was funded by BEIS capital funding via STFC capital grants ST/K00042X/1, ST/P002293/1, ST/R002371/1 and ST/S002502/1, Durham University and STFC operations grant ST/R000832/1. DiRAC is part of the National e-Infrastructure.

The University of Waterloo acknowledges that much of our work takes place on the traditional territory of the Neutral, Anishinaabeg and Haudenosaunee peoples. Our main campus is situated on the Haldimand Tract, the land granted to the Six Nations that

includes six miles on each side of the Grand River. Our active work toward reconciliation takes place across our campuses through research, learning, teaching, and community building, and is centralized within the Office of Indigenous Relations.

Funding for the Sloan Digital Sky Survey (SDSS) has been provided by the Alfred P. Sloan Foundation, the Participating Institutions, the National Aeronautics and Space Administration, the National Science Foundation, the U.S. Department of Energy, the Japanese Monbukagakusho, and the Max Planck Society. The SDSS Web site is www.sdss.org.

The SDSS is managed by the Astrophysical Research Consortium (ARC) for the Participating Institutions. The Participating Institutions are The University of Chicago, Fermilab, the Institute for Advanced Study, the Japan Participation Group, The Johns Hopkins University, Los Alamos National Laboratory, the Max-Planck-Institute for Astronomy (MPIA), the Max-Planck-Institute for Astrophysics (MPA), New Mexico State University, University of Pittsburgh, Princeton University, the United States Naval Observatory, and the University of Washington.

B.2 Data Availability

The VVV simulation's initial conditions and snapshots are not currently publicly available. If they are needed, please ask the VVV authors for them. Alternatively, any N-body simulation of reasonably similar resolution and cosmology should yield the same results, statistically speaking. For satellite orbit and interloper data tables based on this simulation, request them from KAO (kyle.a.oman@durham.ac.uk). Alternatively, they may be created for any N-body simulation using the publicly available ROCKSTAR (bitbucket.org/gfcstanford/rockstar), CONSISTENT TREES (bitbucket.org/pbehroozi/consistent-trees) and ORBITPDF (github.com/kyleaoman/orbitpdf) codes.

The UNIVERSEMACHINE $z \sim 0$ simulation results using the *Bolshoi-Planck* dark matter simulation, including full star formation histories for all galaxies, are available in catalogue form via download from peterbehroozi.com/data.html.

The SDSS data used in this work is derived from Oman et al. (2021) and is available publicly as follows: Data Release 7 used in this work is available at skyserver.sdss.org/dr7; catalogues with stellar masses are available from VizieR (vizier.u-strasbg.fr), catalogue entry `J/MNRAS/379/867`; SFRs are available from wwwmpa.mpa-garching.mpg.de/SDSS/; the two group catalogues are separately available through VizieR (catalogue entry `J/MNRAS/379/867`)

and gax.sjtu.edu.cn/data/Group.html. The mass- and luminosity-weighted ages and their accompanying stellar mass estimates are available from sdss.org/dr16/spectro/galaxy_firefly.

B.3 Robustness of parameter constraints to changes in star formation history and floating infall parameters

An essential assumption for our modelling results and conclusions to be robust is that they are not particularly sensitive to changes in overall star formation history, for both $f_{\rm Q}$ as well as ΔMWA. Throughout this work, we simply allowed our infalling/interloper UniverseMachine galaxies' f_Q to float to match that of SDSS. As a test of these assumptions, we now consider a modified model where the UniverseMachine star formation histories are adjusted such that the infalling UniverseMachine galaxies have the same quiescent fraction as for SDSS.

The mismatch between the level of quenching observed in the infall region of UniverseMachine and SDSS clusters is particularly noticeable at stellar masses $\log(M_\star/{\rm M}_\odot) > 10$. To be specific, we now check whether we need to have star formation histories that match the $z \sim 0$, $f_{\rm Q} - M_\star$ relation of infalling UniverseMachine galaxies to that found for SDSS. For the purposes of this test we consider interlopers to be galaxies in the three upper-right bins in our PPS plots, namely the bins that define the infall region in e.g. Fig. 3.1.

Our quiescent fraction is several per cent too high at low stellar masses and several per cent too low at higher stellar masses, as apparent in Fig. B.1. Our floating $f_{\rm Q,infall}$ parameter removes this overall offset, leaving behind just the differential trends (across PPS) in $f_{\rm Q}$. This resolves possible issues due to differences in completeness between star forming and quiescent galaxies, particularly in the lower stellar mass bin. However, as a robustness check to see how much differences in $f_{\rm Q}$ might affect our measured timescales, we run a test where we modify the UniverseMachine star formation histories such that we closely match the $f_{\rm Q} - M_\star$ trend observed in SDSS. Star formation histories are suppressed by multiplying by an exponential function in time such that the UniverseMachine sSFR-$M_\star$ slope better matches the SDSS data and also better matches the SDSS $f_{\rm Q}$. Explicitly, this modified star formation history in terms of the unmodified UniverseMachine star formation history (SFH) as a function of cosmic time, t, is expressed as:

$$\mathrm{SFH}'(t) = \exp\left(\frac{t - t_{z=0}}{\tau}\right) \mathrm{SFH}(t), \tag{B.1}$$

where $t_{\rm now} = 13.8$ Gyr, $\tau = 1/k$, and $k = (\ln(10)/t_{\rm now}) \times -0.4(\log(M_\star/{\rm M}_\odot) - 10)$, with -0.4 coming from the slope of the SDSS sSFR cut. The value of this correction at $z = 0$ is such that the increase or decrease in SFR forms a broken power law with slope -1 for $\log(M_\star/{\rm M}_\odot) > 10$ and slope -0.7 for $\log(M_\star/{\rm M}_\odot) < 10$, with the value of the correction set to 1.0 at $\log(M_\star/{\rm M}_\odot) = 10.3$. This corresponds to a boost in the star formation histories for $\log(M_\star/{\rm M}_\odot) < 10.3$ and suppression for $\log(M_\star/{\rm M}_\odot) > 10.3$. The correction is applied to the 'true' rather than 'observed' UniverseMachine SFHs as well as the 'true' final SFRs and stellar masses (see Behroozi et al., 2019, for these definitions). A shift plus scatter is then applied to approximate observed versions of the quantities afterwards, according to the prescription used in Behroozi et al. (2019).

We find that this adjustment only results in minor effects on the best-fitting $t_{\rm delay}$ and $\tau_{\rm env}$ parameters. Specifically, the preferred $t_{\rm delay}$ changes by $+0.2$ Gyr and $\tau_{\rm env}$ by -0.2 Gyr for our lower stellar mass bin, or in terms of $t_{\rm Q}$, a shift of 0.5 Gyr. For the $10 < \log(M_\star/{\rm M}_\odot) < 10.5$ stellar mass bin, the corresponding shifts in $t_{\rm delay}$ and $\tau_{\rm env}$ are $+0.1$ Gyr and -0.5 Gyr, respectively. Given our uncertainties of ~ 0.5 Gyr for $\tau_{\rm env}$ and $\lesssim 1.0$ Gyr for $t_{\rm delay}$ (see Table 3.1), we conclude that any impact on our parameter constraints from changes in overall star formation history is negligible and therefore does not influence our discussion and qualitative conclusions.

B.4 Detailed modelling predictions for higher stellar mass bin

Analogous to Fig. 3.7 and Fig. 3.8, we show our detailed model predictions for $10 < \log(M_\star/{\rm M}_\odot) < 10.5$ galaxies in bins of PPS for $f_{\rm Q}$ and ΔMWA in Fig. B.2. Similar to our lower stellar mass bin, a somewhat different range of $t_{\rm delay}$ and $\tau_{\rm env}$ values are preferred by $f_{\rm Q}$ and ΔMWA. The joint best-fit for these parameters using both observables is given in Table 3.1, with the contours shown in Fig. 3.9.

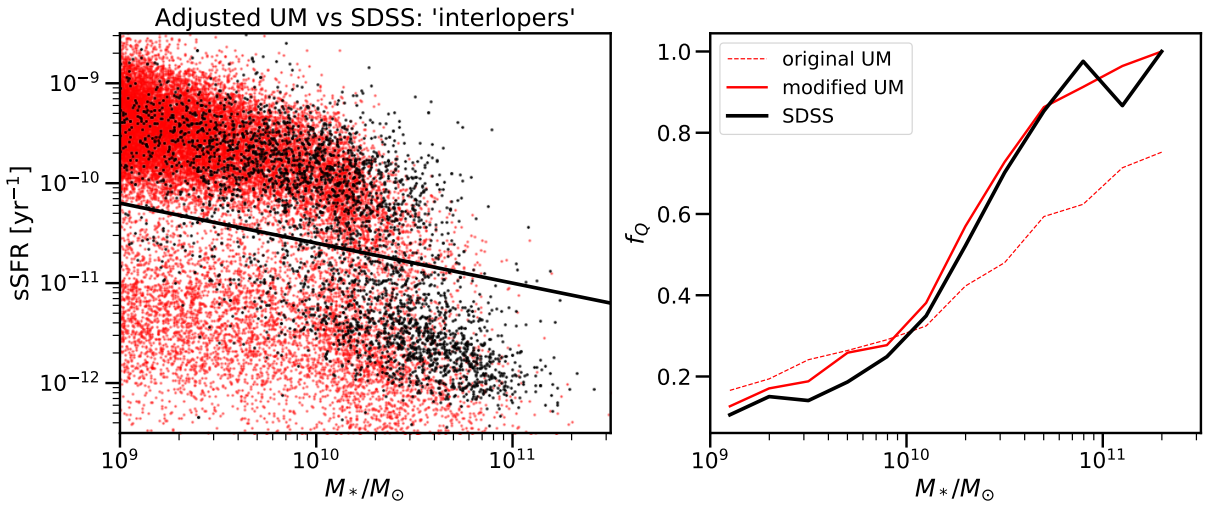

Figure B.1: Plots illustrating the adjusted UniverseMachine interlopers (red) relative to the SDSS data (black). Above $\log(M_\star/\mathrm{M}_\odot) = 10.2$, galaxies have had their star formation history suppressed to increase their f_Q to match the SDSS data, whereas galaxies below $\log(M_\star/\mathrm{M}_\odot) = 10.2$ have had their star formation boosted. *Left:* specific star formation rate plotted against stellar mass, with the adjusted UniverseMachine sSFR multiplied by 2.1 (vertical shift) for the purposes of comparing with SDSS data on this plot. The quiescent/star-forming cut used for both is shown with the solid black line. *Right:* quiescent fraction versus stellar mass. The adjusted UniverseMachine interloper sSFRs increase their f_Q (dashed red) up to that of the SDSS data for higher stellar masses. There is a small offset in the two curves as only the shape of the $f_\mathrm{Q} - \mathrm{M}_*$ relation was fit in this stellar mass binning and the absolute f_Q values were fit for stellar mass bins with edges at $\log(M_\star/\mathrm{M}_\odot) = (9, 10, 10.5, 11, 11.5)$.

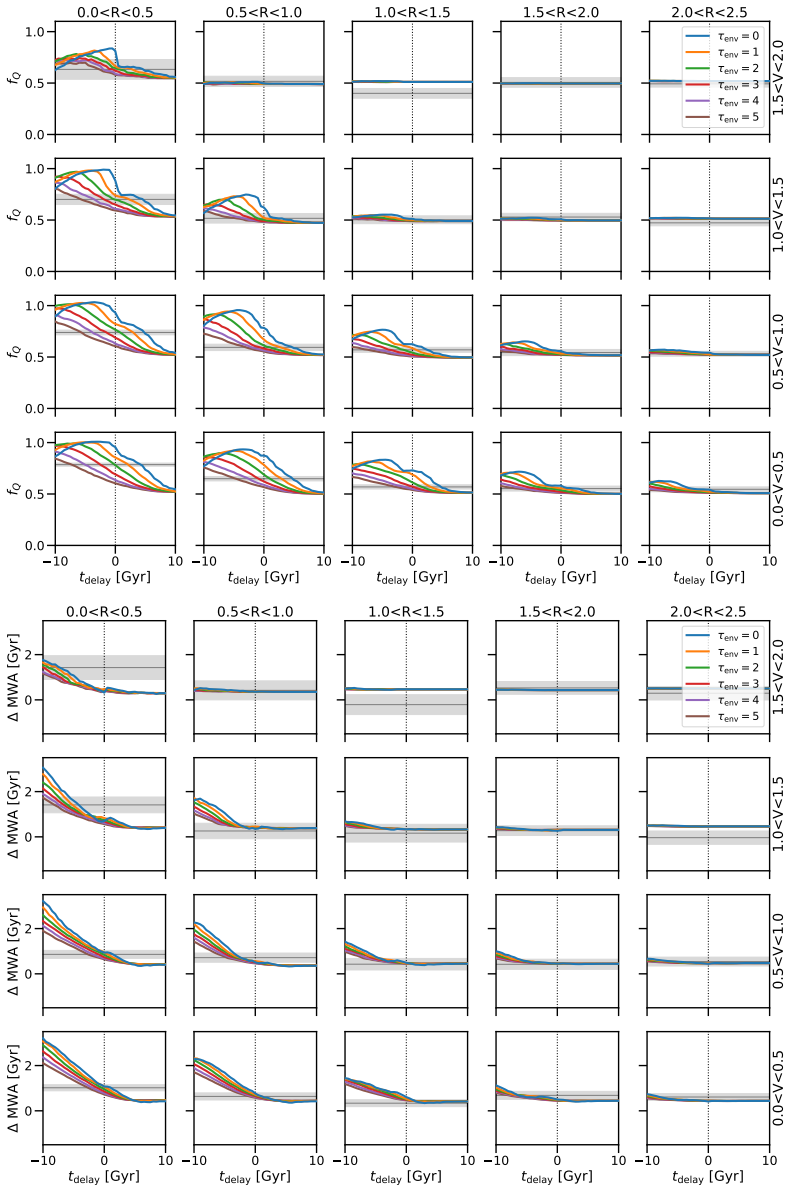

Figure B.2: $f_{\rm Q}$ (upper multi-paneled figure) and mean ΔMWA (lower figure) predictions for $10 < \log(M_\star/{\rm M}_\odot) < 10.5$ galaxies for a range of models where galaxies quench after some delay time, relative to time of first pericentre. We show models run for a range of exponential suppression timescales. The SDSS mean values are shown with grey lines, with the shaded region showing the bootstrapped (over clusters) error on the mean. Analogous to Figs. 3.7 and 3.8.

Appendix C

Appendices for Chapter 4 - How many stars form in major mergers?

C.1 Acknowledgements

We thank S. Ellison for assistance with the SDSS post-coalescence merger catalogue. We also thank Liza Sazonova for informative discussions on post-starburst galaxies, Kristy Webb for helpful insights into the impact of particular choices of SED fitting routines, and Prathamesh Tamhane for discussions regarding hot halo physics.

The University of Waterloo acknowledges that much of our work takes place on the traditional territory of the Neutral, Anishinaabeg, and Haudenosaunee peoples. Our main campus is situated on the Haldimand Tract, the land granted to the Six Nations that includes six miles on each side of the Grand River.

C.2 Data Availability

The visually-confirmed post-coalescence merger sample of Bickley et al. (2022) is available for download from the MNRAS web version of the Bickley et al. (2022) publication. The SDSS data used in this work is publicly available as follows: Data Release 14 used in this work is available at https://www.sdss4.org/dr14/data_access, and SFRs available from wwwmpa.mpa-garching.mpg.de/SDSS/, and mass- and luminosity-weighted ages and their accompanying stellar mass estimates are available from sdss.org/dr16/spectro/galaxy_firefly.